Integrable turbulence in optical fiber experiments: from local dynamics to statistics

Alexey Tikan

▶ **To cite this version:**

Alexey Tikan. Integrable turbulence in optical fiber experiments: from local dynamics to statistics. Physics [physics]. Université de Lille / Laboratoire PhLAM, 2018. English. NNT : . tel-02016080

HAL Id: tel-02016080
https://hal.science/tel-02016080

Submitted on 12 Feb 2019

HAL is a multi-disciplinary open access archive for the deposit and dissemination of scientific research documents, whether they are published or not. The documents may come from teaching and research institutions in France or abroad, or from public or private research centers.

L'archive ouverte pluridisciplinaire **HAL**, est destinée au dépôt et à la diffusion de documents scientifiques de niveau recherche, publiés ou non, émanant des établissements d'enseignement et de recherche français ou étrangers, des laboratoires publics ou privés.

UNIVERSITÉ DE LILLE
DOCTORAL THESIS

Integrable turbulence in optical fiber experiments: from local dynamics to statistics

Author:
Alexey TIKAN

Supervisors:
Prof. Pierre SURET
Prof. Stéphane RANDOUX

A thesis submitted in fulfillment of the requirements
for the degree of Doctor
in the domain of

Physics
Diluted media and fundamental optics

Thesis defended in front of jury:

Prof.	GUY MILLOT	University of Burgundy	(referee)
Prof.	SERGEI TURITSYN	Aston University	(referee)
Prof.	SERGE BIELAWSKI	University of Lille	(examiner)
Prof.	MARC DOUAY	University of Lille	(examiner)
Prof.	GENNADY EL	Northumbria University	(examiner)
Prof.	STEFANO TRILLO	University of Ferrara	(examiner)

November 15, 2018

Declaration of Authorship

I, Alexey TIKAN, declare that this thesis titled, "Integrable turbulence in optical fiber experiments: from local dynamics to statistics" and the work presented in it are my own. I confirm that:

- This work was done wholly or mainly while in candidature for a research degree at this University.
- Where any part of this thesis has previously been submitted for a degree or any other qualification at this University or any other institution, this has been clearly stated.
- Where I have consulted the published work of others, this is always clearly attributed.
- Where I have quoted from the work of others, the source is always given. With the exception of such quotations, this thesis is entirely my own work.
- I have acknowledged all main sources of help.
- Where the thesis is based on work done by myself jointly with others, I have made clear exactly what was done by others and what I have contributed myself.

Signed:

Date:

"Life at low intensity is dull."

Rick Trebino

UNIVERSITÉ DE LILLE

Abstract

Physics
Diluted media and fundamental optics

Integrable turbulence in optical fiber experiments: from local dynamics to statistics

by Alexey TIKAN

This work is dedicated to the investigation of the origin of statistical phenomena recently observed in the framework of integrable turbulence. Namely, experimental and numerical studies of the partially- coherent waves propagation in 1-D Nonlinear Schrödinger equation systems revealed a deviation from the Gaussian statistics. Focusing and defocusing regimes of propagation demonstrated qualitatively different behaviour: the probability of extreme events to appear in the focusing case is higher than it is predicted by normal law, while in defocusing it is lower.

We provided optical experiments well described by the 1-D Nonlinear Schrödinger equation in order to investigate this problem. We built two novel and complementary ultrafast measurement tools. Employing these tools we provided direct observation of coherent structures which appear at different stages of the propagation in both regimes.

Providing analysis of these structures, we determined dominating mechanisms in both focusing and defocusing regimes. In the focusing regime, we discovered the universal appearance of Peregrine soliton-like structures and made a link with the rigorous mathematical result obtained in the semi-classical regime. In the defocusing case, we showed that the mechanism of nonlinear interference of neighbour pulse-like structures defines the evolution of the partially-coherent initial conditions. We considered a simplified model which explained the presence of different scales in the recorded data.

Keywords: Nonlinear optics; Ultrafast phenomena - Measurement; Solitons; Optical fibers; Integrable turbulence; Nonlinear statistical optics; Nonlinear Schrödinger equation; Temporal imaging

UNIVERSITÉ DE LILLE

Résumé

Physique
Milieux dilués et optique fondamentale

Turbulence intégrable dans des expériences de fibres optiques: dynamique locale et statistique

par Alexey TIKAN

Ce travail est dédié à l'étude de l'origine des phénomènes statistiques récemment observés dans le cadre de la turbulence intégrable. Les études expérimentales et numériques de la propagation d'ondes partiellement cohérentes dans les systèmes décrits par l'équation de Schrödinger non linéaire à une dimension ont révélé un écart par rapport à la distribution gaussienne. Les régimes de propagation focalisant et défocalisant présentent un comportement qualitativement différent: la probabilité que des événements extrêmes apparaissent dans le cas focalisant est supérieure à la loi normale, alors que dans le régime défocalisant, elle y est inférieure.

Nous avons réalisé des expériences d'optique bien décrites par l'équation de Schrödinger non linéaire 1-D afin d'étudier ce problème. Nous avons construit deux outils de mesure nouveaux et complémentaires. En utilisant ces outils, nous avons réalisé une observation directe des structures cohérentes qui apparaissent à différents stades de la propagation dans les deux régimes.

En fournissant une analyse de ces structures, nous avons déterminé les mécanismes dominants dans les régimes focalisant et défocalisant. Dans le régime focalisant, nous avons mis en évidence le caractère universel de structures voisines des solitons de Peregrine et établi un lien avec un résultat mathématique rigoureux obtenu dans le régime semiclassique. Dans le régime défocalisant, nous avons montré que le mécanisme d'interférence non linéaire entre impulsions voisines définit l'évolution des conditions initiales partiellement cohérentes. Nous avons proposé un modèle simplifié qui explique la présence des différentes échelles dans les données enregistrées.

Mots clés: Optique non linéaire; Phénomènes ultra-rapides - Mesure; Solitons; Fibres optiques; Turbulence intégrable; Optique statistique non linéaire; Équation de Schrödinger non linéaire; Imagerie temporelle

Acknowledgements

First of all, I would like to thank all the members of the committee for their participation and contribution to the public defence of the current work. Namely, Prof. Guy Millot from the University of Burgundy and Prof. Sergei Turitsyn from Aston University for taking the role of referees; Prof. Serge Bielawski and Prof. Marc Douay from the University of Lille, Prof. Gennady El from Northumbria University and Prof. Stefano Trillo from the University of Ferrara for being my examiners. It is hard to imagine a better committee for this particular work.

This would not be possible without all the institutions and organisations involved. Namely, University of Lille directed by Jean-Christophe Camart; Laboratory PhLAM and its director Marc Douay; the Doctoral School SMRE with its coordinator Christophe Van Brussel and director Joël Cuguen, doctoral studies director Cristian Focsa and Majid Taki (former director); Labex CEMPI and particularly Marc Lefranc. Thereby, I would like to thank them.

I am afraid that it is barely possible to express all my gratitude to my supervisors Prof. Pierre Suret and Prof. Stephane Randoux. As we agreed, my PhD went in a rather non-usual way. Starting from the first day of my work in Lille, I always had amazingly interesting projects, non-stop. Looking back, I realize that every single moment was an important part of the plan and even working on individual projects I have never been alone. Despite all the variety of research directions you are working on, all the teaching and administrative work, you always always had time to discuss ideas, results or problems. You always shared your passion and will for discovery. I believe that an important basis for the future carer of a scientist is a scientific school. These three years in Lille were my school. It is very pity to leave you.

Also, I would like to thank all the group members who helped me. Among them Pierre Walczak who was my first example of the successful thesis defence. His thesis was an important reference that I often read. Another PhD from our team who I would like to thank is Rebecca El Koussaifi. We spent two nice years with Rebecca working side by side. Her ability to work hard is astonishing and at the same time very inspiring. I would like to thank the new generation PhD students: Giacomo Roberti, Adrien Kraych and Alexandre Label. Discussions with them helped me to look differently on the topics that I thought are completely understood. Special thank to Giacomo for explaining me the Boffetta-Osborne algorithm. It was a pleasure to have François Gustave as a postdoc in our team. I would like to thank him for the great job he did in creating a good atmosphere around as well as his help in the automation of our optical sampling oscilloscope. I wish the best to François Copie, a new lecturer, and the new division our team represented by Alberto Amo, Omar Jamadi and Bastian Real Elgueda.

Big thanks to all our collaborators! First of all, I would like to thank another team of PhLAM: Prof. Serge Bielawski, Prof. Christophe Szwaj and Clèment Evain. I learned a lot of things from you working on the Time Microscope. Also, I cannot forget the big help of Nunzia Savoia, Marc Le Parquier and Gauthier Dekyndt during this experiment. For almost everything I know about integrable systems, dispersive hydrodynamics and inverse scattering transform I would like to thank Prof. Gennady El. Special thanks for decoding of the Tovbis-Bertola result that was a basis of Chapter 3. I would like to thank Prof. Miguel Onorato for his clear and useful lectures. Also, I would like to thank Dmitry Agafontsev and Andrey Gelash for very helpful and interesting discussions.

Support of my friends is what always helped me to keep afloat. Particularly, I would like to thank Tobias Lipfert and Sabine Kopec for being my closest friends all these years and sharing with me all the successes and failures. I will never forget the Sunday Physics Club and Junheng Shi in particular. I hope our ways will cross again. I cannot forget about my Russian friends: Asya; Dima; Vital'ka, Oleg and Sashka; Misha, Igor and Evgen. There are a lot of people who were around and made this time in Lille better: Alexandra, Ambroise, Anna, Dana, Eva, Katharina, Lamyae and others.

It is hard to imagine my way in physics without my school teacher Arjamatova Nadejda Antonovna. The fire she has set many years ago is still shining. I hope you will bring to the World many new generations of people who love physics.

In the end, I would like to thank my little family for their unconditional and permanent support at my every step.

Contents

Declaration of Authorship iii

Abstract vii

Acknowledgements ix

1 Introduction 1
1.1 Integrable Turbulence . . . 1
1.1.1 Solitary waves and solitons . . . 1
1.1.1.1 Short history of solitons . . . 2
1.1.1.2 Equations that have solitonic solutions . . . 3
1.1.2 Integrable turbulence is not turbulence . . . 4
1.1.2.1 Wave turbulence . . . 4
1.1.2.2 Integrable turbulence . . . 5
1.1.3 Partially-coherent light . . . 6
1.1.3.1 Different initial states often considered in the framework of integrable turbulence . . . 6
1.1.3.2 Central limit theorem . . . 8
1.1.3.3 Statistical properties of partially-coherent waves 9
1.1.4 Rogue Waves . . . 10
1.1.4.1 Rogue Waves in ocean . . . 10
1.1.4.2 Rogue Waves in optics . . . 12
1.2 Nonlinear Schrödinger equation . . . 13
1.2.1 Universality of NLS equation . . . 13
1.2.1.1 NLS in optics and other physical systems . . 13
1.2.2 Basic properties of the focusing 1-D NLS . . . 15
1.2.2.1 Stationary solutions . . . 15
1.2.2.2 Modulation instability . . . 17
1.2.2.3 Solitons on the finite background and Rogue Waves . . . 19
1.2.3 Basic properties of the defocusing 1-D NLS . . . 20
1.2.3.1 Dark solitons . . . 21
1.2.3.2 Dispersive shock waves . . . 21
1.2.4 Inverse scattering transform . . . 22
1.2.4.1 Historical background of inverse scattering transform . . . 23
1.2.4.2 Inverse scattering transform of 1-D NLS: Zakharov-Shabat problem . . . 24
1.2.4.3 Finite-gap theory . . . 25
1.2.4.4 Examples of the IST spectra . . . 27

1.3 Problematic of the study . . . 30
1.3.1 State of the art: Theory . . . 30
1.3.2 State of the art: Experiment . . . 31
1.3.3 Motivation and objectives . . . 32

2 Ultrafast measurements of non-periodic optical waves using the Time Microscopy technique 35
2.1 Ultrafast measurements in optics . . . 35
2.2 Basics of the Time Microscopy . . . 41
2.2.1 Principles of temporal imaging . . . 41
2.2.1.1 Diffraction - dispersion analogy . . . 42
2.2.1.2 Thin lens - time lens analogy . . . 44
2.2.1.3 Spatial and temporal imaging with a lens . . . 45
2.2.1.4 Time Lens . . . 47
2.2.1.5 Spatial and temporal imaging with a microscope . . . 48
2.2.2 Experimental realization of the Time Microscope . . . 49
2.2.2.1 Pump laser . . . 49
2.2.2.2 Home-made femtosecond fiber laser . . . 51
2.2.2.3 Beam geometry . . . 51
2.2.2.4 Treacy compressor . . . 53
2.2.2.5 Sum frequency generation . . . 54
2.2.2.6 Single-shot spectrometer . . . 55
2.2.2.7 Camera specifications, settings and triggering 56
2.2.3 Power profile reconstruction and typical window of measurements . . . 56
2.2.3.1 The window of measurements . . . 58
2.2.4 Optimal resolution and compressor tuning . . . 58
2.2.5 Time calibration . . . 60
2.2.5.1 Numerical estimates of time-to-frequency conversion . . . 62
2.2.6 Aberrations analysis . . . 63
2.2.6.1 Influence of aberrations on the resolution estimates . . . 67
2.3 Heterodyne Time Microscope . . . 69
2.3.1 Extension of the Time Microscope for the heterodyne phase measurement . . . 70
2.3.1.1 Spatial encoding arrangement . . . 71
2.3.1.2 Setup . . . 72
2.3.1.3 Beam geometry . . . 72
2.3.1.4 CW source . . . 74
2.3.2 Heterodyne Time Microscope tuning . . . 75
2.3.2.1 What is the same in tuning . . . 75
2.3.2.2 Tuning at the 0^{th} order of diffraction grating . 76
2.3.2.3 Phase calibration. Importance of the right frequency choice . . . 76

2.3.3 2-D snapshot processing for phase and power reconstruction . . . 78
2.3.3.1 Intensity reconstruction . . . 79
2.3.3.2 Phase reconstruction . . . 80
2.3.4 Verification of the retrieval algorithm by reproducing the mean optical spectrum . . . 81
2.4 Removing aberrations. Spatial Encoding Arrangement with Hologram Observation for Recording in Single-shot the Electric field (SEAHORSE). . . . 82
2.4.1 Setup . . . 83
2.4.2 Phase sign and direction of time axis . . . 84
2.4.3 Comparison between HTM and SEAHORSE . . . 85

3 Peregrine soliton as a prototype of rogue waves in the integrable turbulence 89
3.1 Gradient catastrophe in the focusing NLS and its regularisation. Tovbis-Bertola theorem. . . . 89
3.1.1 Semi-classical limit of the focusing NLS . . . 90
3.1.2 Experimental evidence of the local Peregrine soliton emergence from deterministic initial conditions . . . 96
3.2 Role of Tovbis-Bertola scenario in dynamics of the partially-coherent waves . . . 103
3.2.1 Nonlinear propagation of the partially-coherent waves in optical fibre: ultrafast measurements with the HTM and SEAHORSE . . . 103
3.2.1.1 Numerical simulation of 1-D NLS with partially-coherent waves . . . 104
3.2.1.2 Adaptation of the HTM and SEAHORSE to the partially-coherent light measurements . . . 104
3.2.1.3 Partially-coherent light measurements with the HTM . . . 106
3.2.1.4 Comparison with the numerical simulations . . . 109
3.2.1.5 Partially-coherent light measurements with the SEAHORSE . . . 111
3.2.1.6 Nonlinear Digital Holography . . . 112
3.2.1.7 Comparison of statistical parameters . . . 116
3.2.2 Connection between local dynamics and statistics in focusing NLS . . . 116
3.2.2.1 Numerical estimation of ϵ distribution . . . 119
3.2.2.2 Calculation of the fourth moment of the PDF 119
3.2.2.3 Results of comparison . . . 120
3.3 IST analysis of the experimentally measured PS emerged from the integrable turbulence . . . 121
3.3.1 Fourier collocation method . . . 123
3.3.2 Global and local approaches to the IST . . . 124
3.3.2.1 Global IST with zero boundary conditions . . . 125
3.3.2.2 Interpretation of the Finite-gap spectrum . . . 125

3.3.2.3 Role of the window size 129
3.3.2.4 Role periodization in the local IST 130
3.3.3 IST Analysis of Tovbis-Bertola scenario 131
3.3.4 IST of the experimental data 135

4 Integrable turbulence in the defocusing NLS model 139
4.1 Numerical study of the 1-D defocusing NLS integrable turbulence 139
4.1.1 Simulations of the partially-coherent light propagation in 1-D defocusing NLS system 140
4.1.2 DSW and dark solitons as fundamental bricks of the 1-D defocusing NLS integrable turbulence 144
4.1.2.1 Black, grey and high order solitons 144
4.1.2.2 IST approach to the characterisation of the dark solitons 146
4.1.2.3 Dispersive Shock Wave formation via two pulse collision 146
4.1.2.4 Generation of the dark solitons 150
4.1.3 Statistical approach to the 1-D defocusing NLS integrable turbulence 151
4.2 Experimental investigation the defoctusing NLS integrable turbulence by using Heterodyne Time Microscope 153
4.2.1 Zoology in the defocusing regime of NLS integrable turbulence 154
4.2.2 Experimental data analysis 156

5 Conclusions and perspectives 161

A Thermal Lensing in the Treacy compressor 165

B Estimates of non-linear and dispersion coefficients of the PM fiber 167

C Change of variables in NLS equation 171

D Intrapulse stimulated Raman scattering effect on the random wave propagation 173

E Evolution of the spectra of the partially-coherent wave in defocusing system. 177

Bibliography 185

List of Figures

1.1 Example of partially-coherent initial condition with finite spectral width and periodic boundary conditions. (a) Representation in the Fourier space. Phase of each Fourier component is an uniformly distributed random variable varying from -π to π. Spectrum was chosen to be Gaussian. (b) Resulting representation in the real space. Creating the signal in the Fourier space we guaranteed periodicity in the real space. Phase experiences the π-jump in the points where power goes to zero. . . 8
1.2 Numerically computed distributions of different physical variables following from the Gaussian distribution of the real and imaginary parts of the function describing a random process. (a) Distributions of the real and imaginary part. (b) Uniform distribution of the phase. (c) Rayleigh distribution of the amplitude. (d) Exponential distribution of the intensity. 11
1.3 Two branches of stationary solutions of the focusing NLS equation. (top) The dn branch with values of s 0 (blue dotted line), 0.95 (black line), 1 (red dashed line). (bottom) The cn branch. Values of parameter s are the same. 16
1.4 Numerical simulation of the evolution of a plane wave with small noisy perturbation. All units are dimensionless. Brighter colours correspond to higher power. (left) Spatio-temporal diagram showing the modulation instability acting on the quasi-monochromatic wave. (right-top) Power profiles at three different cuts of the diagram. Colours are preserved. (right-bottom) Corresponding spectra. 18
1.5 Solitons on the finite background plotted using the exact analytical expression. (top-left) Akhmediev breather. (top-right) Kuznetsov-Ma soliton. (bottom) Peregrine soliton 20
1.6 Two dark solitons of different deepness. Black line corresponds to the quasi-black soliton with the value of B close to 1, red dashed line to the gray soliton with B=0.8. (top) Amplitude modulus square. (bottom) Phase profile. 22
1.7 Dispersive shock waves in the double-side dam break problem of 1-D defocusing NLS equation. 23
1.8 Example of the trace of the monodromy matrix as a function of the eigenvalue ξ. Gray rectangles depict the stable bands. . 27

1.9 Trace of the monodromy matrix of the dn branch of cnoidal solution of the 1-D focusing NLS equation shown in Fig. 1.3 (top). All colours are preserved. Blue and gray areas show the stable band for the dn(x,0) and dn(x,0.95) respectively. The band of the solitonic solution dn(x,1) converges to the two discrete points -0.5i and 0.5i. 28
1.10 IST spectra for the dn branch of cnoidal solution of the 1-D focusing NLS equation shown in Fig. 1.3 (top). All colours are preserved. The bands which correspond to dn(x,0) are depicted by blue,for dn(x,0.95) by black and two discrete points of dn(x,1) are depicted by red. 29
1.11 Schematic IST spectra of the solitons on the finite background of 1-D focusing NLS equation shown in Fig. 1.5. Arrangement of the figures is preserved. (top-left) Akhmediev breather. (top-right) Kuznetsov-Ma soliton. (bottom) Peregrine soliton. . . . 29

2.1 Schemes of the fast optical signal characterization methods. (Top) autocorrelation. A signal divided into two parts. One of them experiences a controllable temporal delay. Two parts are superimposed directly on the photodiode (field autocorrelation) or in a nonlinear crystal (intensity autocorrelation). (Middle) FROG. Similar to the intensity autocorrelation, but instead of the photodiode detection, the spectrum measurements are provided. The resulting FROG trace is a 2-D image of spectrum as a function of delay. (Bottom) SPIDER. A chirped replica of a signal is superimposed with its two copies. The spectrum of the resulting pattern allows to extract the phase and intensity. 37
2.2 Scheme of possible space-time duality realisations. Analogies between paraxial diffraction depicted as cross-section of a free space propagated beam and second-order dispersion in time represented as light beam propagated through a grating compressor or equally in optical fiber in linear regime. Effect of quadratic phase induced by conventional thin lens juxtaposed with nonlinear interaction of a chirped pulse with the studied signal. Also, a possibility of electro-optical phase modulation could be considered as an alternative approach. 42
2.3 Image formation with space and time lenses. D1 and D2 are dispersions of different values and signs. 46
2.4 Image formation with a thin lens. The case of magnification. . 46
2.5 Image formation with a microscope. 49
2.6 Scheme of the Time Microscope. 50
2.7 Spectrum of the pump laser after amplification. 50
2.8 Schematic illustration of the short pulse amplifier. Picture is taken from the user manual of the Spectra Physics Spitfire amplifier. 51
2.9 Scheme of the home-made fiber femtosecond laser. 52

2.10 Photography of the Treacy compressor. Input beam is depicted by red, output by blue. Beam (red) enters the compressor and reaches necessary hight by the first periscope. After passing through the grating pair (G1 and G2) beam changes its hight on the roof mirror. Reflected beam (blue) path back the grating pair and leaves the compressor by another periscope. Dispersion is controlled by adjusting the distance between the compressor with the high precision motorized translation stage. . 53
2.11 Scheme of two different monochromatic beams passing through the double-path grating compressor. The beams have close wavelengths λ_1 and λ_2. Here θ_i is initial angle 40°, $\theta_r(\lambda)$ - angle between reflected beam and normal to the grating surface. 55
2.12 Power profile reconstruction of the ASE signal. (a) A typical snapshot obtained with a Time Microscope. (b) Line with a maximum overall power (the 5^{th} line in the picture a). (c) Average TM response envelope of a corresponding set (green) and the maximum overall power line with subtracted background. 57
2.13 Window of measurements. (a) Result of division of the signal by the envelope the Fig. 2.12c. (b) Retrieved signal shrieked to the window of measurement. The window is chosen symmetrically from the maximum of the envelope. 59
2.14 Resolution curve. Dependence of pulse durations measured with the TM as a functions of distance between grating in the 1560 nm Treacy compressor. Input pulses are produced homemade femtosecond laser presented in the section 2.2.2.2. Each value has been determined by fitting with a Gaussian-like function. The minimum value corresponds to 250 fs for FWHM. . 60
2.15 Experimental measurements of ≈ 70 fs pulse with the TM. (a) Raw image recorded with the TM. (b) Pulse profile obtained making a cross-section of the image above. 61
2.16 (a)Time microscope response to a series of two pulses (700 fs long) with known spacing. This gives the correspondence between pixel spacing and time: 71 $fs/pixel$. Note that the lower scale has been defined after this calibration has been made. (b) Corresponding spectrum. The spectral width between 5 peaks is 0.89 THz, which gives the spacing 5.6 ps 62
2.17 Simulation of the Time Microscope. (a) blue pulses of 70 fs are taken as initial signal. Orange pulse of 30 fs is the pump. (b) the same signals experienced dispersion: 0.23 ps^2 for the pump and the same but negative for the signal. Usage of these parameters simulates experiments described in the articles [190, 200] 65

2.18 Simulation of the Time Microscope. Effect of the 3^{rd} order dispersion on the signal detection. (a,e) the ideal case, no higher order dispersion therm is added. (b,f) 3^{rd} order dispersion is added to the initial signal depicted by blue in the Fig. 2.17. (c,g) Show the effect when higher order dispersion term is added to the pump onlt. (d,h) depicts the case when 3^{rd} order dispersion is added to the signal and pump together. The value of the 3^{rd} order dispersion is always the same 5.14×10^{-4} ps^3. This value is computed with the formula 2.20. 66
2.19 (a)Root mean square of the pulses measured with the Time Microscope [200], versus distance between grating planes in the 1560 nm compressor. Input pulses are produced by a 70 fs Erbium doped fiber-laser. The minimum value corresponds to $\sim$250 fs at the full with at the half maximum. Blue dots show every RMS value taken into the account, (b-d) show the superposition of several pulses measured at the given grating distance (b-3.4 cm, c-3.85 cm, d-5.2 cm). 67
2.20 Simulation of the compressor tuning. (a-i) show the signal measured with a simulated Time Microscope with the different distance between gratings of the signal compressor, while the pump compressors stay untouched. Green dashed lines represent the ideal case when only the 2^{nd} order dispersion is added, black lines show the same, but with the presence of the 3^{rd} order dispersion. 3^{rd} order dispersion of the pump is fixed, while the dispersion coefficients of the signal were recomputed according to the formulas 2.16 and 2.20. 69
2.21 Experimentally measured dependence of the fifty highest amplitude pulses root mean square on its position on the recorded frame. Distance between the grating was varied from 3.37 cm to 5.15 cm. Optimal distance is 3.85 cm. Data correspond to one depicted in the Fig. 2.19a. The frame center is at 256^{th} pixel. 70
2.22 Typical snapshot obtained with a spatial encoding arrangement setup. Picture is generated numerically. 71
2.23 Experimental setup of Heterodyne Time Microscope arrangement for amplitude and phase measurement of arbitrary signals. (a) Complete setup. (b) Detailed 3-D view of the setup. . 73
2.24 Recorded spectra of the amplified continuous wave reference. The central wavelength is chosen at the maximum of amplified spontaneous emission noise. 75
2.25 Snapshots recorded at the zero order of the diffraction grating with the time microscope. (a) Line corresponding to the signal alone, (b) reference alone, (c) signal and reference together. The optimal tuning corresponds to symmetric line of the width close to 1 pixel. 76

2.26 Monochromatic wave phase measurements. Raw images (top) and retrieved phase evolutions (middle) obtained when the signal comes from a monochromatic laser source with various wavelengths, from left to right: λ_S = 1555.37 nm, λ_S = 1559.37 nm, λ_S = 1561.37 nm, λ_S = 1563.37 nm and λ_S = 1567.37 nm .In all cases the wavelength of the reference is fixed to λ_R = 1561.37 nm. Bottom layer shows the recovered intensity profile. The noise related to the interference of the spontaneous emission of amplifier and monochromatic signal. Corresponding spectra are depicted in the Fig. 2.24. 77
2.27 Intensity reconstruction. (a) 2-D snapshot obtained with the HTM. (b) Power profile before division by the envelope (red) and envelope (green). (c) Reconstructed power profile after division by envelope. 78
2.28 Phase reconstruction. (a) A 2D snapshot of a non-periodic signal. (b) Intensity profile along the green vertical line depicted above. (c) Corresponding Fourier spectra of the intensity profile. By the red dot highlighted the Fourier mode, argument of which is extracted. 80
2.29 Phase, amplitude and spectrum of partially coherent waves (ASE). a–f, The width $\Delta\nu$ of the (average) optical spectrum of the partially coherent light waves emitted by an ASE source is adjusted by using a programmable filter. Results correspond to $\Delta\nu$ = 0.1 THz (a,c,e,g) and $\Delta\nu$= 0.7 THz (b,d,f,h). a,b, Typical raw images recorded by the sCMOS camera of the HTM for ASE light with a spectral width $\Delta\nu$ = 0.1 THz (a) and $\Delta\nu$ = 0.7 THz (b). c,d, Phase retrieved from the interference pattern. e,f, Optical power normalized to the average power. In contrast to the raw signal in a and b, the signal in e and f is divided by the average power($P(t)/ < P >$). g,h, Optical spectra corresponding to $\Delta\nu$ = 0.1 THz and $\Delta\nu$ = 0.7 THz, respectively. Red stars represent the spectrum computed from the averaged Fourier transform of the envelope of the electric field recorded with the HTM. The spectrum recorded by the OSA is plotted with black lines for comparison. 82
2.30 Spatial Encoding Arrangement with Hologram Observation for Recording in Single shot the Electric field (SEAHORSE). (a) scheme of experimental setup adapted for the double pulse measurements. (b,c,d) Corresponding 2-D snapshot with the temporal hologram, retried phase and power. (e) The image reconstruction by adjusting the second order dispersion coefficient. (f) Reconstructed sharp image of the double-pulse signal. 84
2.31 Comparison between HTM and SEAHORSE. Single 70 fs pulse obtained with HTM (red) and SEAHORSE after reconstruction (black). 86

2.32 Interpolation of the SEAHORSE hologram. A 70 fs pulse recorded with the SEAHORSE. (Black line) pulse reconstructed directly from the hologram, the same as one depicted in Fig. 2.31. (Blue dots) 1024 points zero padding in the Fourier space. (Green dots) the same but with 8192 points. 87

3.1 Second derivative of the sech^2 function. 92
3.2 Dynamics of the bell-like shaped initial condition in the NLS system under the dispersionless limit. ρ and u profiles are displayed for ξ = 0, 0.35 and 0.5. Original figure can be found in [216]. 92
3.3 Analytical formula of the Peregrine soliton. (a) Spatio-temporal diagram. (b-c) Cross-section of amplitude and phase profile at the maximum compression point ($\xi = 0$). 94
3.4 Numerical simulation of the focusing NLS equation. Behaviour at the gradient catastrophe point. Parameter ϵ in the simulation is equal to 1/20. (a,b,c) Spatio-temporal diagram, amplitude and phase cross-section at the maximum compression point. $20sech(\tau)$ function is taken as initial condition. (d,e,f) the same but for the solitonless potential. $20sech(\tau)\exp[-i\mu\log(\cosh(\tau))]$, here $\mu = 2$. 95
3.5 Principal scheme of the experiment implying optical sampling oscilloscope. 97
3.6 Detailed scheme of optical sampling oscilloscope (top). Signal sampling via sum frequency generation (bottom). 98
3.7 Spectral filtering and propagated pulse spectrum. 99
3.8 Results of experimental measurement of a pulse profile at the point of the gradient catastrophe with the optical sampling oscilloscope. Blue circles and green stars show the measured data before propagation in the fiber and at the gradient catastrophe point, the black line is analytical Peregrine soliton formula applied without a fit, red line corresponds to numerical simulations of the experimental data taken as initial conditions while assuming a constant phase. 101
3.9 Measurements of a single pulse power and phase profiles in an optical fiber with the frequency-resolved optical gating technique. (top) FROG traces measured at different propagation distances using the cut-back technique. (middle and bottom) corresponding power and phase profiles. Measurements are provided in Institut FEMTO-ST, CNRS Université Bourgogne-Franche-Comté, Besançon, France. 102

3.10 Simulations of the random wave propagation in the focusing NLS system. Simulation parameters are close to the experimental: β_2 = -20 ps^2/km and γ = 2.4 $W^{-1}km^{-1}$, average power $P_0 = 2.6\ W$ and spectral width $\Delta\nu = 0.1\ THz$. (a) Spatio-temporal diagram. Green and orange lines correspond to 0 and 160 m respectively. Orange line shows the distance at which the first localised structure is appearing (-23 ps). (b) Power profile around the maximum of the first localised structure and initial conditions at the same time. Colours are conserved. An application of the Peregrine soliton formula is depicted with red lines. (c) The same (as b) for the phase profile. 105
3.11 Experimentally measured spectra. (a) Original spectrum of ASE light source (blue) and power spectral density of signals after filtering and amplification. (b) the same in the log-scale and zoomed around the 192 THz. 107
3.12 Recording of ASE emitted signal with the HTM. (a-d) Demonstrate the typical snapshots of the ASE signal and corresponding phase and power profiles. The spectral widths of the recorded signal were 0.05, 0.1, 0.5, 0.7 THz (depicted from left to right). 107
3.13 Experimentally measured spectra of the partially-coherent signal having the initial width 0.1 THz after propagation in the 400 m PM fiber. (a) Spectra of the output signal with different average powers (0.5, 1, 2.6 and 4 W) (b) same as in a, in log-scale. 109
3.14 Observation of the different stages of formation of the localized Peregrine soliton with HTM. Initial partially-coherent light has 0.05 THz spectral width and 0.5 W average power. Snapshots are recorded at the output of the 400 m PM fiber. 110
3.15 Nonlinear random waves measured with the HTM setup. (a) Scheme of experiment. Partially-coherent light filtered and amplified is injected into the PM fiber and detected with the HTM. (b-e) Snapshots of the random waves recorded with the HTM, recovered phase (blue) and amplitude (red) profiles. (f-i) Corresponding numerical simulations demonstrating the same power and phase profiles. 111
3.16 Partially-coherent light measurement with the SEAHORSE technique. The partially-coherent light after propagation in 400 m PM fiber having the same initial conditions as one depicted in the Fig. 3.15. The first row: 'temporal holograms' of random waves, recorded using the SEAHORSE. The second and third rows: extracted phase and intensity profiles without postprocessing. The power unit is here the number of electrons detected by sCMOS sensor. The fourth and fifth rows: numerically retrieved phase and intensity profiles by using the digital holography algorithm. 113

3.17 Nonlinear Digital Holography. Spatio-temporal diagram reconstruction using the experimentally recorded data with the HTM at the output of the 100 m PM fiber (a-f) and at the input (g-l). 115
3.18 Comparison of the probability density function computed for the partially-coherent light of 0.1 THz spectral width and 2.6 W average power. 117
3.19 Example of the initial conditions processing. 500 ps -long window of 0.05 THz spectral width and 2.6 W power. (Blue line) is the power profile of the partially-coherent wave. (Magenta dots) are detected maxima above the threshold (green dashed line). (Red and green stars) show the left and ring side of the structure at the level of FWHM. 120
3.20 Comparison of the Peregrine-soliton-like structure maximum compression point distribution and the M_4 moment at different propagation distances. Partially-coherent initial conditions 0.05 THz and 2.6 W. 121
3.21 Comparison of the Peregrine-soliton-like structure maximum compression point distribution and the M_4 moment at different propagation distances. Partially-coherent initial conditions 0.1 THz and 2.6 W. 122
3.22 Comparison of the Peregrine-soliton-like structure maximum compression point distribution and the M_4 moment at different propagation distances. Partially-coherent initial conditions 0.2 THz and 2.6 W. 122
3.23 Spatio-temporal diagram of two-soliton $u = 2sech(x)$ (top) and solitonless $u = 2sech(x)exp(-i2\mu\log(\cosh(x)))$ with $\mu = 2$ solutions of NLS. (Right) The cross-section of the spatio-temporal diagram for the power and phase. (green) initial conditions, (orange) maximum compression point. Simulations are presented using the normalization of Eq. 3.2. 126
3.24 ZS spectra of the two-soliton (green) and corresponding solitonless (red) potentials. The vertical axis corresponds to the imaginary part of ξ, while horizontal to its real part. 127
3.25 Spatio-temporal diagram of ten-soliton $u = 10sech(x)$ (top) and solitonless $u = 10sech(x)exp(-i10\mu\log(\cosh(x)))$ with $\mu = 2$ solutions of NLS. (Right) The cross-section of the spatio-temporal diagram for the power and phase. (green) initial conditions, (orange) maximum compression point. Simulations are presented using the normalization of Eq. 3.2. 128
3.26 ZS spectra of the two-soliton (green) and corresponding solitonless (red) potentials. The vertical axis corresponds to the imaginary part of ξ, while horizontal to its real part. 129
3.27 Artificially created IST spectra of the a complex solution of NLS (left) and the Peregrine soliton (right). 130

3.28 Effect of the window size on the IST spectra. (left)The Peregrine soliton truncated to the windows [-2,2] blue, [-5,5] green, [-10,10] red. (right) Corresponding IST spectra, the colour is preserved. The chosen window was periodized 30 times. The vertical axis corresponds to the imaginary part of ξ, while horizontal to its real part. 131
3.29 Effect of the periodization on the IST spectra. (left)The Peregrine soliton truncated to the window [-10,10]. (right) IST spectra of the signal. (blue dots) without periodization, (green stars) periodized 5 times and (red crosses) 10 times. The vertical axis corresponds to the imaginary part of ξ, while horizontal to its real part 132
3.30 Change of the IST spectrum with the evolution coordinate. (left) Initial amplitude profile $\psi(0,\tau) = sech(\tau)$ with $\epsilon = 0.02$-blue, amplitude profiles at different propagation points $\xi = 0.42, 0.53, 0.54, 0.543$-red and corresponding phase profile -blue. (left) IST analysis with at different positions with fixed window size and periodization number. Similar figure is presented in the book [216]. 133
3.31 Conservation of global IST. (left) spatio-temporal diagram for $\psi(0,\tau) = sech(\tau)$ with $\epsilon = 1/15$. (right-top) intensity profile of the initial condition (green) , at the maximum compression point (orange), truncated for the IST computation (red). (right-bottom) global (green, orange) and local (red) IST spectra. The vertical axis corresponds to the imaginary part of ξ, while horizontal to its real part. Colours are preserved. 134
3.32 Local IST spectra of the local high-amplitude structure which emerges as a regularisation of the gradient catastrophe with different solitonic content (from 3 to 17 solitons). (left) the full IST spectra, (right) zoomed around the unstable band. The vertical axis corresponds to the imaginary part of ξ, while horizontal to its real part. 135
3.33 IST of the experimental data. For the investigation the data from the Fig. 3.17c,d is taken. (left) normalized power profile (black) and the window for IST analysis (red). (right) corresponding IST spectrum. The vertical axis corresponds to the imaginary part of ξ, while horizontal to its real part. 136
3.34 Comparison of the local IST spectra of experimentally measured data and numerically obtained from deterministic initial conditions. (red dots) the same spectrum as in the Fig. 3.33, (blue crosses) from Fig. 3.32 for N =5. The spectra are scaled in order to provide the comparison. 137
3.35 IST of the experimental data. The data is taken from the Fig. 3.15e. (left) normalized power profile (black) and the window for IST analysis (red). (right) corresponding IST spectrum. The vertical axis corresponds to the imaginary part of ξ, while horizontal to its real part 137

4.1 Simulations of the partially-coherent wave propagation in the defocusing NLS system. Simulation parameters are close to the experimental ones: β_2 = 22 ps^2/km and γ = 3 $W^{-1}km^{-1}$, average power $P_0 = 4.5\ W$ and spectral width $\Delta\nu = 0.05\ THz$. (a) Spatio-temporal diagram. Green,orange and red lines correspond to 0, 0.5 and 1 km respectively. Orange line shows the distance at which the double shock happens. (b) Power profile is zoomed around the double shock area. Colours are preserved. (c) The same for the phase profile. 141
4.2 Simulations of the partially-coherent wave propagation in the defocusing NLS system. Simulation parameters are close to the experimental ones: β_2 = 22 ps^2/km and γ = 3 $W^{-1}km^{-1}$, average power $P_0 = 4.5\ W$ and spectral width $\Delta\nu = 0.1\ THz$. (a) Spatio-temporal diagram. Green,orange and red lines correspond to 0, 0.52 and 1 km respectively. Orange line shows the distance at which the double shock happens. (b) Power profile is zoomed around the double shock area. Colours are preserved. (c) The same for the phase profile. 142
4.3 Simulations of the partially-coherent wave propagation in the defocusing NLS system. Simulation parameters are close to the experimental ones: β_2 = 22 ps^2/km and γ = 3 $W^{-1}km^{-1}$, average power $P_0 = 4.5\ W$ and spectral width $\Delta\nu = 0.5\ THz$. (a) Spatio-temporal diagram. Green and red lines correspond to 0 and 1 km respectively. (b) Power profile is zoomed around the double shock area. Colours are preserved. (c) The same for the phase profile. 143
4.4 Simulations of the mulisoliton propagation in the defocusing NLS system, $u(0,x) = Ntanh(x)$ with $N = 4$ in this case. Simulations provided for the dimensionless 1-D NLS 4.2. (a) Spatio-temporal diagram. Green, orange and red lines correspond to 0, and 6 nonlinear lengths respectively. (b) Power profile around zoomed around the double shock area. Colours are preserved. (c) The same for the phase profile. 145
4.5 IST spectra of N soliton solutions 147
4.6 Simulations of the double pulse signal propagation in the defocusing NLS system. Simulation parameters are close to the experimental ones: β_2 = 22 ps^2/km and γ = 3 $W^{-1}km^{-1}$, peak power $P_0 = 5\ W$ and separation 30 ps. (a) Spatio-temporal diagram. Green, orange and red lines correspond to 0, 0.44 and 2 km respectively. (b) Power profile is zoomed around the double shock area. Colours are preserved. (c) The same for the phase profile 148

4.7 Simulations of the double pulse signal propagation in the defocusing NLS system. Simulation parameters are close to the experimental ones: $\beta_2 = 22\ ps^2/km$ and $\gamma = 3\ W^{-1}km^{-1}$, peak power $P_0 = 5\ W$ and separation 50 ps. (a) Spatio-temporal diagram. Green, orange and red lines correspond to 0, 0.75 and 2 km respectively. (b) Power profile is zoomed around the double shock area. Colours are preserved. (c) The same for the phase profile. 149
4.8 Simulations of the double pulse signal propagation in the defocusing NLS system. Simulation parameters are close to the experimental ones: $\beta_2 = 22\ ps^2/km$ and $\gamma = 3\ W^{-1}km^{-1}$, peak power $P_0 = 5\ W$ and separation 100 ps. (a) Spatio-temporal diagram. Green, orange and red lines correspond to 0, 1.4 and 4 km respectively. (b) Power profile is zoomed around the double shock area. Colours are preserved. (c) The same for the phase profile. 150
4.9 Typical scenario of generation of the dark soliton in the defocusing integrable turbulence. 151
4.10 The fourth order moments ($M_4[X] = E[(X)^4]/(E[(X)^2])^2$) of the partially-coherent initial condition as a function of the propagation distance. The average power is 4.5 W, spectral widths 0.05 (blue line), 0.1 (orange) and 0.5 (green) THz. 152
4.11 Comparison of he fourth order moment (orange) and the FWHM of the spectrum (blue) plotted as a function of the propagation distance. The average power of the partially-coherent initial conditions is 4.5 W, spectral widths - 0.1 THz. Black line shows the position of the maximum of the blue curve (z = 0.23 km). . 153
4.12 Experimentally recorded with HTM partially-coherent waves propagated in 900 m fiber with normal dispersion. The initial spectral with is 0.05 THz, average power 4.5 W. (first row) snapshots recorded directly with the HTM. (second and third rows) reconstructed phase and power profiles. 155
4.13 Experimentally recorded with HTM partially-coherent waves propagated in 900 m fiber with normal dispersion. Exactly the same experimental parameters as in Fig. 4.12 are used, however in this figure we present data that contains fast oscillating wavetrains. 156
4.14 Experimentally recorded with HTM partially-coherent waves propagated in 900 m fiber with normal dispersion. Spectral width is 0.1 THz, average power is 4.5 W. (first row) snapshots recorded directly with the HTM. (second and third rows) reconstructed phase and power profiles. 157
4.15 Experimentally recorded with HTM partially-coherent waves propagated in 900 m fiber with normal dispersion. Spectral width is 0.5 THz, average power is 4.5 W. (first row) snapshots recorded directly with the HTM. (second and third rows) reconstructed phase and power profiles. 157

4.16 Fit of the experimentally recorded data with the Eq. 4.3. The experimental data is recorded for the initial random wave having 0.05 THz and average power 4.5 W. Green lines show the fit for the black (a) and gray (b) soliton. 158
4.17 IST spectrum of the experimentally recorded data depicted in Fig. 4.16a 159

A.1 Average power 0.5 W. 165
A.2 Average power 2 W. 166
A.3 Average power 7.1 W. 166

B.1 168
B.2 Experimental and computed spectra, P_{max} of the pulse 3886 W. 168
B.3 Experimentally measured dispersion of the PMF Fibercore HB-1550T. Dashed line corresponds to the signal wavelength in the experiments. 169

C.1 Change of variables for NLS equation used in the manuscript. 171

D.1 Comparison of the numerical simulations and HTM measured signal. 174
D.2 Additional snapshot recorded with the HTM. Partially-coherent light having$P_0 = 4.5\ W\ \Delta\nu = 0.1\ THz$. 175
D.3 Additional snapshot recorded with the HTM. Partially-coherent light having$P_0 = 4.5\ W\ \Delta\nu = 0.1\ THz$. 175

E.1 Numerical studies of the evolution of the spectra in defocusing media. The average power of the partially-coherent initial conditions is 4.5 W, spectral widths - 0.1 THz. Distances 0, 0.27 and 1.9 km. Bottom plot shows the same data but in the log-scale. 178

List of Tables

2.1 Comparison of the existing ultra-short pulse measurements techniques. In the column Disadvantages we discuss reasons why this technique could not be applied to the partially-coherent waves measurements. For the primary sources of information see [134, 142, 146, 168, 172]. 40
2.2 Details of numerical simulations for the Fig. 2.18 65
2.3 Details of numerical simulations depicted in the Fig. 2.20. Parameters match exactly the configuration of the TM presented in [200]. 68
2.4 Summary of the estimated vertical and horizontal diameter of the pump, signal and reference beams inside the optical crystal. 74

List of Abbreviations

ASE	**A**mplified **S**pontaneous **E**mission
BBO	**B**eta **b**arium **b**orate
CW	**C**ontinuous **W**ave
DFT	**D**ispersive **F**ourier **T**ransform
DSW	**D**ispersive **S**hock **W**ave
FROG	**F**requency **R**esolved **O**ptical **G**ating
FWHM	**F**ull **W**idth at **H**alf **M**aximum
HTM	**H**eterodyne **T**ime **M**icroscope
IST	**I**nverse **S**cattering **T**ransform
KdV	**K**orteweg-de**V**ries
MI	**M**odulation **I**nstability
NLS	**N**on**l**inear **S**chrödinger
OPO	**O**ptical **P**arametric **O**scillator
OSA	**O**ptical **S**pectrum **A**nalysers
OS	**O**ptical **S**ampling
PBS	**P**olarization **B**eam **S**plitter
PDE	**P**artial **D**ifferential **E**quation
PDF	**P**robability **D**ensity **F**unction
PMF	**P**olarization **M**aintaining **F**iber
RMS	**R**oot **M**ean **S**quare
RW	**R**ogue **W**ave
sCMOS	**s**cientific **C**omplementary **M**etal-**O**xide-**S**emiconductor
SEA	**S**patial **E**ncoding **A**rrangement
SEAHORSE	**S**patial **E**ncoding **A**rrangement with **H**ologram **O**bservation for **R**ecording in **S**ingle-shot the **E**lectric field
SFG	**S**um **F**requency **G**eneration
SG	**S**ine-**G**ordon
SPIDER	**S**pectral **P**hase **I**nterferometry for **D**irect **E**lectric-field **R**econstruction
TM	**T**ime **M**icroscope
WSF	**W**hat (it) **S**tands **F**or
WS	**W**ave **S**haper
WT	**W**ave **T**urbulence
ZS	**Z**akharov-**S**habat

Chapter 1

Introduction

1.1 Integrable Turbulence

In this section, we will introduce the framework of our study. The integrable turbulence is a field of the classical physics initiated recently by V.E. Zakharov [1]. The integrable turbulence, rigorously saying, is not turbulence in its classical form [2]. Without loss of generality, it can be understood as studying of complex behaviour of random initial conditions, which can be found behind a dispersive nonlinear partial-differential equation integrable with the inverse scattering method [3, 4] [1].

One of remarkable features of this kind of equations is the localised particle-like solutions called *solitons*. They play a crucial role in understanding of the corresponding complex dynamics. We will describe some properties of the solitonic solution and show the difference with other solitary waves. Another remarkable feature is the existence of an infinite number of constant of motion. These equations can be integrated by the so called inverse scattering transform.

In general, this complex behaviour strongly depends on the initial state of a system. Therefore, at the end of this section, we will explain the particular choice of our random initial conditions and show its basic statistical properties.

1.1.1 Solitary waves and solitons

Solitons are isolated particle-like travelling waves which are solutions of certain partial differential equations. By its nature, soliton can be determined as a wave that preserves its structure during the propagation due to the interplay between dispersion (or diffraction in 2-D case) and nonlinearity of the system. The property which makes solitons similar to particles is elastic collision. Indeed, like particles, two solitons (asymptotically) restore their initial shapes after the collision, maybe besides some phase shift. Below, we will give a short review of the history of solitons and solitary waves and show some important equations which have solitonic solutions.

[1] The basics of this method will be explained later in Sec. 1.2.4.

1.1.1.1 Short history of solitons

Since the time when the first known soliton was observed by J. Scott Russell more than 180 years have passed. Riding a horse along a narrow barge channel, he noticed "a large solitary elevation, a rounded, smooth and well-defined heap of water, which continued its course along the channel apparently without change of form or diminuation of speed" [5]. After providing an experimental investigation of this phenomenon, he made several remarkable conclusions. Except the confirmation of the existence of the solitary water waves, he managed to find a ratio between the speed of the wave, its amplitude and the water depth. However, the theory developed at that moment didn't allow to predict such object and the works of Russell were a subject to criticism. Rehabilitation of the solitary wave came with works of Dutch scientists Diederik J. Korteweg and his student Gustav de Vries [6], who found in 1895 the equation most accurately describing the main effects observed by Russell. They derived a rather simple equation(known as KdV) for waves in shallow water and found its periodic wave solutions (expressed in terms of Jacobi elliptic functions) which in the asymptotic limit of large wavelengths give a solitary wave.

However, further progress in this field came only in 60 years this with the development of the computers. E. Fermi, J. Pasta and S. Ulam studied an anharmonic lattice with quadratic and cubic nonlinearities [7]. They expected a full thermalisation of the system, i.e. uniform redistribution of the energy along different modes. M. Tsingou provided for them a numerical experiment integrating one period of a simple cosine function with periodic boundary conditions. The results of the numerical study surprised researchers. Instead of expected thermalisation, they observed that energy was distributed among only few modes and didn't show any mixing. Moreover, the system demonstrated a tendency of periodical recurrence to the initial state. This phenomenon is known today as Fermi-Pasta-Ulam-Tsingou recurrence. In order to understand this effect, Kruskal and Zabusky studied a continuous analogue of this model. The corresponding equation was exactly the one derived by Korteweg and de Vries almost 70 years ago for shallow water waves! The periodic solutions and the solitary wave of KdV equation were well known at that time. However, Kruskal and Zabusky pointed out a very remarkable property of solitons, which was not known before. Namely, the fact that two solitons *collide elastically*, asymptotically recovering its initial shape. By analogy with particles, they coined the term *soliton*. We will use this property to draw a line between the solitons and other solitary waves. Thereby, we define the soliton as:

- Isolated, localized in space travelling wave
- Which preserves its shape in time
- And collides elastically with other solitons, except maybe a phase shift

To other localized travelling waves we will refer as solitary waves.

More detailed intoduction to the theory of solitons can be found in the book of M. Ablowitz and H. Segur [3], review of the solitons in [8].

1.1.1.2 Equations that have solitonic solutions

After the discovery, solitons (as well as solitary waves) were observed in many different systems [3, 9]. Soliton family can be divided in two big classes: conventional and *envelope* solitons. The solitons observed by Russell in the water channel (KdV equation) are of the first type. The fundamental envelope solitons can be seen as a localised group of waves moving together and preserving its envelope. The definition given above can be applied to the envelope solitons as well.

There are a lot of partial-differential equations modelling dispersive nonlinear media which have solutions in the form of the solitary wave. However, not all of them can be called solitons. As we mentioned before existence of solitonic solution is directly related to integrablility of the equations. In [10] reader can fined a (short) list of different kinds of integrable equations with solitonic solutions. This full list is still being replenished. Here we will consider three (relatively) simple and very general equations.

KdV equation. As we have seen the first soliton was observed in the media governed by the KdV equation, but it is not the only one historically important event associated with this equation. The method of integrating the nonlinear partial-differential equations known as Inverse Scattering Transform (IST) was shown on the example of KdV as well [11]. We will discuss this method later in Sec. 1.2.4. From the integration of the KdV equation, a new period of nonlinear physics has started.

The KdV equation can be written in the form:

$$u_t + 6uu_x + u_{xxx} = 0.$$

Which describes the evolution of a function u in time t. The second term represents nonlinear part and the third one - dispersion. Fundamental solitonic solution can be written as: $u = 2k^2\, sech^2 k(x - 4k^2 t - x_0)$, where k and x_0 are constants. This solution represents a bell shaped localised wave similar to one observed by Russell.

As we now, solitons can be observed in the shallow water, but KdV equation is universal. So the range of its applicability is much wider. As an example we can give ion-acoustic waves in plasma [12], liquid-gas bubble mixture [13], atmospheric Rossby waves [14], etc.

Remarkably, the 2-dimensional versions of the KdV called Kadomtsev-Petviashvili equations are also integrable and, hence, also has family of solitonic solutions [15, 16].

Sine-Gordon (SG) equation. Another historically important equation called Sine-Gordon was derived in the framework of differential geometry. It brought into the soliton theory a widely used Bäcklund transformation. Bäcklund derived it studying surfaces of constant Gaussian curvature in 1880. Knowing solution of one partial differential equation (PDE) we find solutions of another one if there is a corresponding Bäcklund transformation. Its variation called auto-Bäcklund transformation allows to recurrently reconstruct

the whole hierarchy of solitons. The SG equation can be expressed as follows:

$$u_{tt} - u_{xx} + \sin(u) = 0$$

Integrability of the SG equation was first proved by Ablowitz Kaup Newell and Segur [17]. For the list of applications of the SG equation we refer reader to review of Scott, Chu and McLaughlin [8].

Nonlinear Schrödinger (NLS) equation. This equation we will study in details in the present manuscript. We will discuss later in this chapter (see Sec. 1.2). This equation has maybe the widest range of applications among the equations discussed in the section. In the 1-dimensional case it is usually written as follows:

$$iu_t + u_{xx} + 2\sigma|u|^2 u = 0$$

where $\sigma = \pm 1$. The case when $\sigma = 1$ NLS equation called focusing (see Sec. 1.2.2), $\sigma = -1$ respectively defocusing (see Sec. 1.2.3).

NLS equation was integrated by V.E. Zakharov and A. B. Shabat [18]. This equation has an exact solution in the form of the envelope soliton.

NLS equation found its applications in deep-water wave dynamics [3, 19, 20], electro-magnetic waves in media with third order nonlinearity [21], magnetic spin waves [22], plasma physics [18], etc. Hasegawa and Tappert [23, 24] first derived the NLS equation in fiber optics. In the presented manuscript we will consider complex dynamics of light in optical fibers and demonstrate emergence of some particular envelope solitons.

Remarkably, also it's generalized version called Vector NLS which can be represented as a set of N coupled 1-D NLS equations:

$$iu_{jt} + u_{jxx} + 2\left(\sum_{n=1}^{N} \sigma_n |u_n|^2\right) u_j = 0$$

can be integrated in the case when N = 2 and $\sigma_1 = \sigma_2 = 1$. This system is known as Manakov model [25]. It can be applied to the fibers with constant birefringence [26].

1.1.2 Integrable turbulence is not turbulence

From the general point of view, "wave turbulence" names all the complex phenomena arising from the nonlinear propagation of random waves [27]. In this sense, integrable turbulence can be seen as a peculiar case of wave turbulence. However, in the standard form of the wave turbulence theory, the dynamics is dominated by the resonant interaction. On the contrary, as we'll see below, no resonant interaction exist in the integrable turbulence [28].

1.1.2.1 Wave turbulence

Wave turbulence (sometimes called weak turbulence) theory studies dynamics of weakly nonlinear and dispersive random waves [27, 29]. It is originated from the pioneering work of R. Peierls [30], where he describes the

kinetics (including the evolution of spectrum and probability density function of amplitude) of phonons in anharmonic crystals. Later, the approach of wave turbulence found its application in plasma physics [31, 32], hydrodynamics [33, 34], optics [35–37] and many different areas of physics.

Below, we cite a definition of the wave turbulence given in the book of S. Nazarenko [27]: "Wave turbulence (WT) can be generally defined as out-of-equilibrium statistical mechanics of random nonlinear waves". Also, further in this book we can find an important refinement: "Notably, the WT language, i.e. triad or quartic *resonant* wave interactions, is sometimes also used to qualitatively describe situations where waves are not so weak and when formally the WT theory is invalid." Presence of the resonant interactions is the key difference between the standard wave turbulence and integrable turbulence. Usually, in the WT approach, it is common to eliminate the nonresonant terms by providing a canonical transformation.

1.1.2.2 Integrable turbulence

Studying the complex evolution of random initial conditions in the integrable equations one has to take into the account nonresonant interaction terms [36]. Indeed, the linear dispersion relation[2] $k(\omega)$ doesn't have nontrivial resonances. As a consequence, we do not find direct or inverse energy cascades and related effects observed in the WT framework. However, the presence of the solitonic content, instabilities and gradient catastrophes leads to a variety of not trivial effects, which will be widely discussed in the present manuscript.

This problem was considered in the work of P.A.E.M. Janssen in the framework of the water waves [38]. He studied a narrowband limit of deterministic Zakharov equation [39] which describes the potential flow if the ideal fluid of infinite depth. This limit leads to the Nonlinear Schrödinger equation. The author describes the evolution of the spectrum as well as the fourth order moment of amplitude probability density functions. He proved an important statement that statistics deviates from Gaussian, which is not possible without taking into the account nonresonant terms.

Let's demonstrate the absence of the resonances in the quasi-linear case of 1-D NLS equation[3]. The linear dispersion relation can be expressed as $k = -\beta\omega^2$. Therefore, we obtain the set of equations describing the conservation of energy and momentum:

$$\begin{cases} \omega_1^2 + \omega_2^2 = \omega_3^2 + \omega_4^2 \\ \omega_1 + \omega_2 = \omega_3 + \omega_4 \end{cases} \tag{1.1}$$

[2]Reader has to take into the account that notations used in hydrodynamics (therefore in the wave turbulence) are different from ones used in optics. The dispersion relation in hydrodynamics is written as $\omega(k)$. The reason is the following change of variables: $t \to z$ and $x \to \tau$. z and τ variable are convenient for the description of the optical experiments, where z can be considered as fiber length and τ is the time.

[3]It is easy to show that for the higher dimension (or generalised one-dimension [40]) version of NLS equation the WT approach can be fully applied [37, 41]

Inverting this to

$$\begin{cases} (\omega_1 + \omega_3)(\omega_1 - \omega_3) = (\omega_4 + \omega_2)(\omega_4 - \omega_2) \\ \omega_1 - \omega_3 = \omega_4 - \omega_2 \end{cases} \tag{1.2}$$

Finally, we see that the system 1.1 has only trivial solutions:

$$\begin{cases} \omega_1 = \omega_3 \\ \omega_2 = \omega_4 \end{cases} \quad or \quad \begin{cases} \omega_1 = \omega_4 \\ \omega_2 = \omega_3 \end{cases} \tag{1.3}$$

However, the resonances could occur in this system due to the nonlinear effects. For example, exponential growth of a perturbation of a monochromatic wave known as modulation instability (see Sec. 1.2.2.2) can be considered as a consequence of nonlinear phase-matching [21].

1.1.3 Partially-coherent light

The choice of random initial conditions may significantly affect the behaviour of the system governed by dispersive nonlinear PDE. Here, we provide a short overview of widely used random initial conditions. For our studies, we have chosen a particular case of a partially-coherent wave with Gaussian statistics. These initial conditions are of particular importance in different physical systems. Finally, we present general statistical properties of partially-coherent waves, essential for understanding the results of the present work.

1.1.3.1 Different initial states often considered in the framework of integrable turbulence

The randomness of initial conditions naturally appears in majority of real experiments. Particularly in optics, one can encounter an optical noise of different origin: from slow thermal fluctuations to the shot noise, caused by the discrete nature of light. All these effects are stochastic and, hence, have to be studied with statistical methods. Generally, the random process can be considered as a certain superposition of random variables. The theory of the random processes knows many different examples, however, in the framework of the integrable turbulence, the process of paramount importance is the *complex Gaussian process* [42].

This importance is related to the fact that many physical processes can be considered as a supposition of large number of *independent* random variables. According to the central limit theorem (which we show in the next section) such superposition leads to the Gaussian statistics [42]. In such processes, real and imaginary parts of the random function have Gaussian distributions. Integrable turbulence studies the evolution of such random initial signal in the nonlinear dispersive media. As an example, we can give random superposition of water waves in the ocean or photons with random phases in the amplified spontaneous emission source propagated in an optical fiber.

The complex Gaussian process can be found in its different representations. We will discuss three of them, most widely considered in the framework of integrable turbulence.

Condensate with small noise. On the of the major numerical studies [43] in the context of integrable turbulence was provided with random initial conditions known as condensate. According to different sources the term condensate was coined in analogy with Bose-Einstein condensate or the dense superposition (condensate) of solitons. The initial conditions, in this case, can be written as follows:

$$\Psi(0,x) = 1 + \epsilon(x) \qquad |\epsilon| \ll 1$$

where ϵ is Gaussian distributed small complex variable[4]. In many integrable systems the constant solution (if such exist) of corresponding partial-differential equation is unstable [44]. A small perturbation of the constant solution will rapidly grow[5].

In the original work of V.E. Zakharov [1], where the framework of the integrable turbulence is defined, he pointed out two types of important initial conditions: with rapidly decaying zero boundary conditions and periodic (or quasi-periodic) boundary conditions. The importance of these initial conditions is directly connected to the method of integration of the nonlinear PDE. In this case the Finite Gap theory of the Inverse Scattering Transform has to be applied. This will be discussed in Sec. 1.2.4.

Gaussian process with zero boundary conditions. Initial state of the system which corresponds to this process can be seen as Gaussian distributed complex function multiplied by a rapidly decaying envelope. This initial conditions may appear in different contexts. For example, it was considered in the context of the Hanbury Brown Twiss interferometry with interacting photons [45, 46]. In this case, solitonic content separates from the dispersive waves after some propagation distance. Therefore, we can observe only transient dynamics in all its complexity. However, the presence of the rapidly decaying envelope significantly simplifies the statistical analysis.

Gaussian process with periodic boundary conditions. This type of random processes can be represented by a complex function with real and imaginary parts distributed by Gaussian and which has a certain periodicity defined by the size of the box. This can be seen as a Gaussian noise confined in a circle. So when radius of such circle goes to infinity we obtain the classical complex Gaussian noise. The case finite radius is often used for the numerical simulations and the analytical studies, while infinite case is natural for experimental investigations. Our study, presented in this manuscript will be dedicated mostly to these cases. We will choose the parameters of periodization in order to keep all the statistical properties of the classical Gaussian process.

[4] This also can be seen as a constant plus a weak random phasor.

[5] This phenomenon is known as modulation instability and will be defined more precisely in Sec. 1.2.2.2

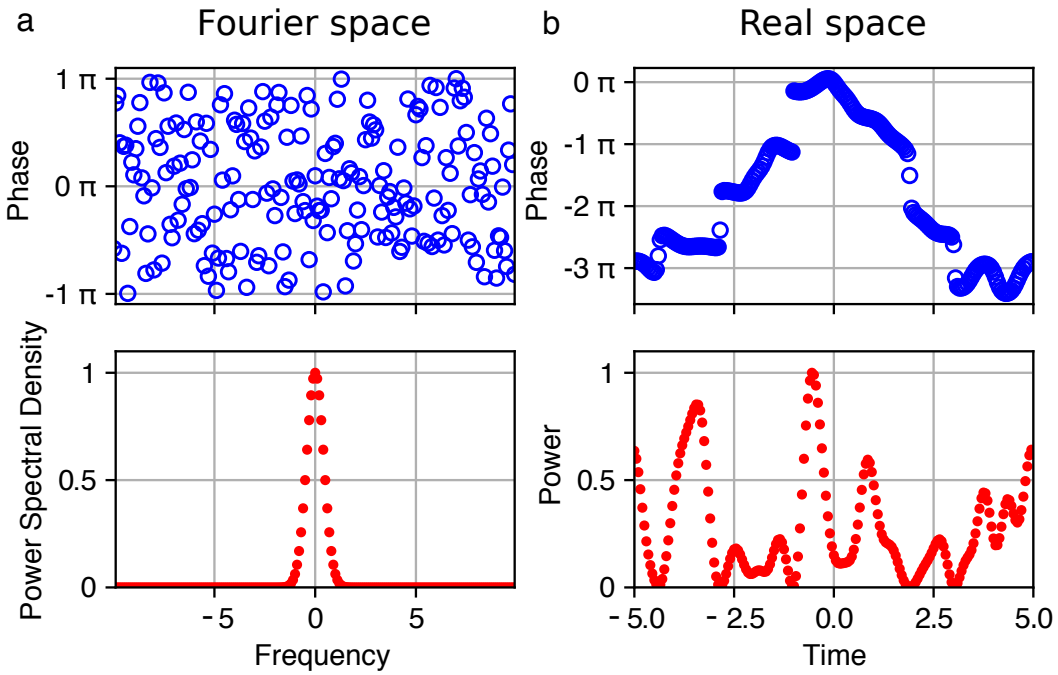

FIGURE 1.1: Example of partially-coherent initial condition with finite spectral width and periodic boundary conditions. (a) Representation in the Fourier space. Phase of each Fourier component is an uniformly distributed random variable varying from -π to π. Spectrum was chosen to be Gaussian. (b) Resulting representation in the real space. Creating the signal in the Fourier space we guaranteed periodicity in the real space. Phase experiences the π-jump in the points where power goes to zero.

Working in the framework of integrable turbulence we make the following important assumption: the contributing random variables have a finite spectral width. It is natural consideration from the physical point of view because any considered media will have some spectral transparency windows. Such random functions represent well certain random ocean states [47, 48] and speckle fields in optics [49] or, already mentioned, partially-coherent light produced by the amplified spontaneous emission source. Example of such periodical representation of the Gaussian random process with the finite spectral width is depicted in Fig. 1.1. Left part of the figure shows representation in the Fourier space, while the right one in the real space.

1.1.3.2 Central limit theorem

Now, let's define more explicitly the central limit theorem and essential conditions to guarantee its validity. We will call a set of *independent*[6] (not necessarily identically distributed) random variables as U_i, where $i = 1, ..., n$. Each of the random variables has its mean value μ_i and variances σ_i^2. We

[6]By independent we meant that the joint probability density function can be expressed as a multiplication of initial probability density functions.

define a new variable Z in the following way:

$$Z = \frac{1}{\sqrt{n}} \sum_{i=1}^{n} (U_i - \mu_i)$$

The central limit theorem states that if the number of the contributing random variable U_i tends to infinity ($n \to \infty$) the probability density function of Z converges to the Gaussian one:

$$\lim_{n\to\infty} P_Z(z) = \frac{1}{\sqrt{2\pi}} e^{-z^2/2}$$

1.1.3.3 Statistical properties of partially-coherent waves

In our studies, we investigate dynamics of initial conditions defined as a superposition of large (but finite) number of Fourier modes with uniformly distributed from $-\pi$ to π random phases:

$$\Psi = \sum_{i=1}^{n} X_i e^{in\Delta\omega t}$$

with $X_i = 1/\Delta T \int_0^{\Delta T} \Psi e^{-in\Delta\omega t}$ the Fourier modes ($\Delta\omega = 2\pi/\Delta T$). In order to satisfy the conditions of central limit theorem the Fourier modes have to be δ-correlated: $< X_n X_m >= n_{0n}\delta_{nm} = n_0(\omega_n)$. Therefore, the real and imaginary part of the complex function Ψ have zero-centred Gaussian distributions. Often, in the experiments and simulations we use Gaussian spectrum, but in general the shape of the spectrum doesn't affect the dynamics. To the distribution real part of Ψ we will refer as $\mathcal{R}$ and to imaginary part as $\mathcal{I}$. Using the rules of the transformation we can find a distribution of $|\Psi|$ and $|\Psi|^2$. This information is important because these variables are measurable in real experiments.

$\mathcal{R}$ and $\mathcal{I}$ are independent so the joint probability is just a multiplication of probabilities:

$$p_Z(\mathcal{R},\mathcal{I}) = p_Z(\mathcal{R})p_Z(\mathcal{I}) = \frac{1}{2\pi\sigma^2} e^{-\frac{\mathcal{R}^2+\mathcal{I}^2}{2\sigma^2}}$$

Let's introduce the following change of variables:

$$\mathcal{R} = A\cos(\phi) \qquad \mathcal{I} = A\sin(\phi)$$

So the Jacobian is:

$$J = \frac{\partial(\mathcal{R},\mathcal{I})}{\partial(A,\phi)} = \begin{pmatrix} \cos(\phi) & -A\sin(\phi) \\ \sin(\phi) & A\cos(\phi) \end{pmatrix}$$

The determinant of Jacobian equals to A. Therefore the joint distribution of A and ϕ:

$$p_Z(A,\phi) = p_Z(\mathcal{R},\mathcal{I})det(J) = \frac{A}{2\pi\sigma^2}e^{-\frac{A^2}{2\sigma^2}}$$

The variables A and ϕ are also independent, hence we can conclude that ϕ is uniformly distributed (see Fig. 1.2b):

$$p_Z(\phi) = 1/2\pi \qquad \int_{-\pi}^{\pi} p_z(\phi)d\phi$$

and A (and hence $|\Psi|$) according to the Rayleigh distribution (see Fig. 1.2c):

$$p_Z(A) = \frac{A}{\sigma^2}e^{-\frac{A^2}{2\sigma^2}} \qquad A \geq 0$$

Now let's perform the same procedure for $P = A^2/2$. Here P is the directly measurable intensity. The resulting probability density function for P is:

$$p_Z(P) = p_Z(A = \sqrt{2P})\left|\frac{\partial A}{\partial P}\right| = \frac{1}{< P >}e^{-\frac{P}{<P>}}$$

where $< P >= \sigma^2$. Therefore, the intensity of the field is distributed exponentially (see Fig. 1.2d).

1.1.4 Rogue Waves

One particular area of the application of statistical nonlinear physics is the study of the Rogue Wave phenomena. Rogue Waves are high amplitude waves which appearance is very unprobable according to the linear statistical theory. There are different explanations of this phenomena known today. One of them proposes to include weak nonlinearity into the consideration. A leading order nonlinear model describing the unidirectional deep-water wave (under some strong assumptions) is 1-D focusing NLS equation. Therefore, the problem of ocean Rogue Waves can be considered in the framework of the integrable turbulence.

1.1.4.1 Rogue Waves in ocean

Rogue Waves (RW) are giant deep-water waves observed in the open ocean that appear more frequently than it is predicted by the normal law [20, 47, 48, 50]. Indeed, the distribution of the wave elevation in the ocean assuming a linear superposition of the many independent waves with random phases is shown to be Gaussian [51] which follows directly from the the central limit theorem demonstrated previously. Surface elevation corresponds to the real part of the random complex function considered in Sec. 1.1.3.3. Therefore, the probability of giant waves observation rapidly goes down with the increasing wave amplitude.

However, such observations were reported and these waves caused a real damage to shipping boats [20]. One of the first accepted evidence of the

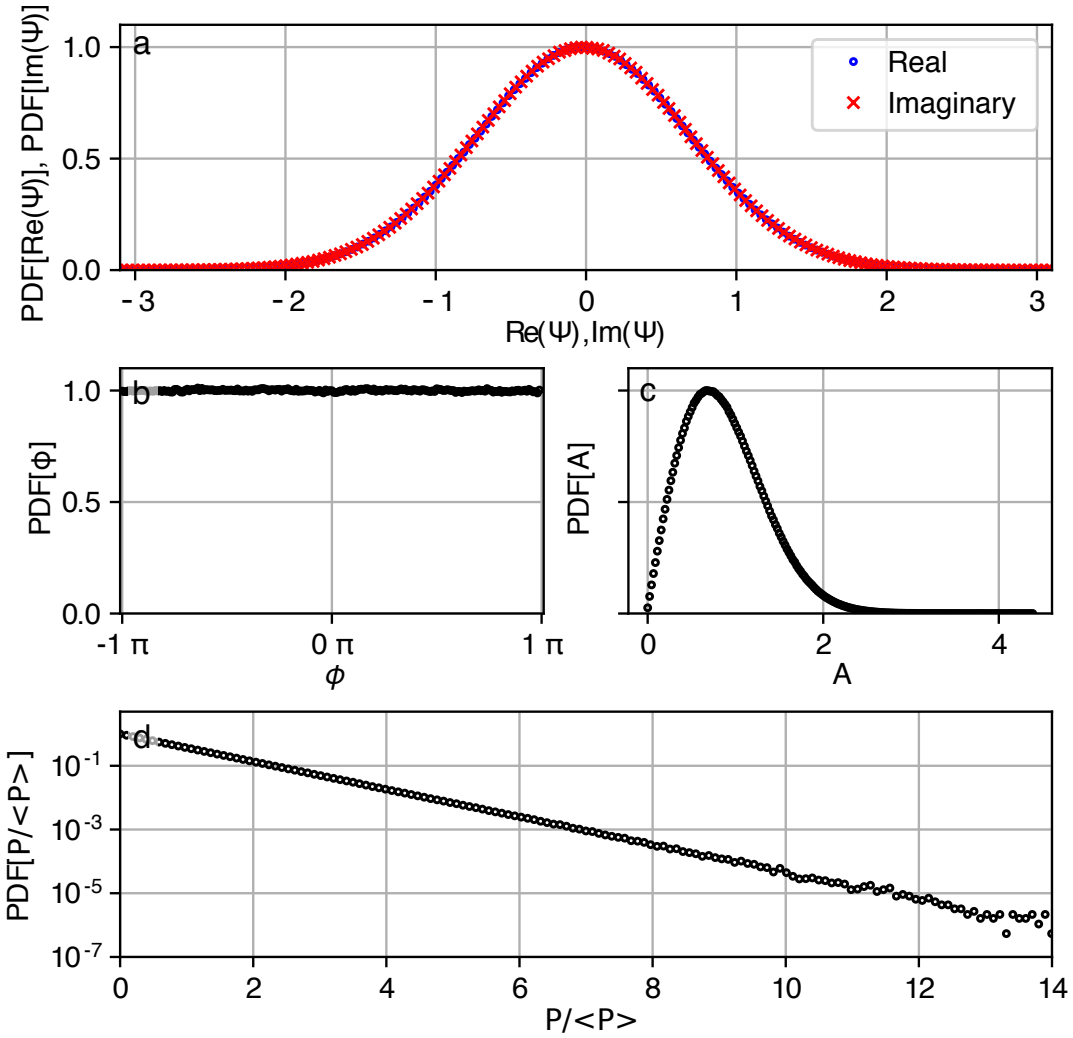

FIGURE 1.2: Numerically computed distributions of different physical variables following from the Gaussian distribution of the real and imaginary parts of the function describing a random process. (a) Distributions of the real and imaginary part. (b) Uniform distribution of the phase. (c) Rayleigh distribution of the amplitude. (d) Exponential distribution of the intensity.

RW existence was the "New Year wave" recorded on the Draupner platform in the North Sea on 1 January 1995. This wave had a wave height of 25.6 metres, while modern boats are designed only to withstand only 10-15 meter waves. Since this event is highly unprobable some other explanation has to be adopted.

Significant part of researchers proposes to take into the account the weak nonlinearity always presented in the ocean. Therefore, the RWs can be seen as a result of the nonlinear dynamics of some stochastic initial state. However, I would like to stress that until today there are ongoing debates about the nature of the RWs. Other possible explanation could be found in [20].

In order to define the Rogue wave, oceanographers often use the notion of the significant wave hight H_s. It equals to averaged over $1/3$ of the highest waves among all measured in the time series (a wave height is a distance between a crest and the adjacent trough). If statistics is Gaussian,H_s approximately corresponds to 4 times the standard deviation of the surface elevation. So it is possible to introduce a threshold $2.2H_s$ and consider all the waves higher than this threshold as RW. This definition is taken mostly due to the inability to control the experimental conditions in the ocean and, as a consequence, to record a sufficiently large data set with close external conditions.

Another way, applicable in the controlled (laboratory) conditions, is to compute Kurtosis, the normalized fourth order moment of a statistical distribution, which characterise its non-Gaussianity [52]. This approach allows to get additional information about the process and quantify how the nonlinearity affects the state.

1.1.4.2 Rogue Waves in optics

Under a strong assumption that the flow in the ocean is irrotational and the water is inviscid we can apply the NLS equation for the surface wave envelope in the narrow-band limit. NLS equation can describe dynamics of the ocean wave only at the leading order without taking into the account many important mechanisms such a wave breaking. However, making this link we are able to investigate the RW phenomena in the framework of the integrable turbulence assuming unidirectionality of the waves. Therefore, this gives a possibility to provide well controlled experiments in other physical systems[7] such as fiber optics [53].

After the pioneering paper of Solli et al. [54], there were hundreds of research articles only in the domain of optics on the subject of the RWs [55–57]. However, the term RW became a synonym of localised high amplitude structure and very often the connection to ocean waves is lost.

[7] More about applicability of NLS to the water waves and other physical system can be found in the Sec. 1.2.1.1

1.2 Nonlinear Schrödinger equation

Nonlinear Schrödinger equation (or NLS) is a dispersive nonlinear partial-differential equation which can be exactly solved. The NLS equation can describe at the leading order a large variety of real physical systems. It is one of the simplest equation which governs dynamics of waves in media with (second order) dispersion and cubic nonlinearity (four-wave mixing). Study of the NLS equation can be divided into two big parts: cases of focusing and defocusing nonlinearity.

The focusing NLS has a big family of bright solitonic solutions. Second order solitons (or solitons on the finite background) are the subject of particular interest because they were considered as prototypes of so-called Rogue Waves in the ocean. The defocusing NLS doesn't support the bright solitonic solutions, but instead, it has dark ones. This family of solutions can be seen as a localized dip on the finite background. A modulated (in deepness, background amplitude or separation distance) train of the dark solitons (also called dispersive shock wave) is one of the objects which naturally arise in the dynamics of random waves governed by defocusing NLS and, hence, can be found in many different circumstances.

The way to find different families of solutions of NLS is to use its integrability by the Inverse Scattering Transform (IST) method [3, 4]. This method can be considered as a nonlinear analogue of the Fourier transform, which is widely used in solving the linear partial differential equations. In the following sections, we will introduce the basics of IST and show some important examples.

1.2.1 Universality of NLS equation

NLS equation describes dynamics of quasi-monochromatic waves in media with non-zero second order dispersion and where four-wave mixing dominates other nonlinear interactions. This case is universal and widely presented in different physical systems. Here we present a short overview of the most significant real systems governed by the NLS equation at the leading order.

1.2.1.1 NLS in optics and other physical systems

In the field of nonlinear optics NLS equation follows directly from Maxwell equations [21]. It appears in the study of the electro-magnetics wave propagation in the transparent (far any from resonances) dielectric media with the third order nonlinearity when the slowly varying envelope approximation is valid. These conditions are very often satisfied in optical fibers. For wavelengths larger than critical[8] the optical fiber supports only one transverse mode. In this case the NLS equation can be reduced to its 1-D version.

[8]Parameter $V_c = a(n_0^2 - n_c^2)^{1/2} 2\pi/\lambda$, where a is the core radius, n_0 and n_c are the core and cladding refractive indexes and λ is the wavelength must be less than 2.405.

In fiber optics the 1-D NLS equation is widely used in the following form:

$$i\frac{\partial A}{\partial z} - \frac{\beta_2}{2}\frac{\partial^2 A}{\partial t^2} + \gamma|A|^2 A = 0 \tag{1.4}$$

In this form, the second term represent the group velocity dispersion and the third one the cubic nonlinearity. Dispersion coefficient is the result of the Taylor expansion of the mode-propagation constant $\beta_2 = \frac{1}{c}\left(2\frac{dn}{d\omega} + \omega\frac{d^2n}{d\omega^2}\right)$, where c is the speed of light, n - refractive index and ω is the frequency. Changing the sign of dispersion we pass from focusing ($\beta_2 < 0$) to defocusing ($\beta_2 > 0$) NLS. The coefficient that represents nonlinearity can be found as $\gamma = \frac{n_2\omega_0}{cA_{eff}}$, where n_2 is the nonlinear index coefficient, A_{eff} - effective core diameter, c - speed of light. The nonlinear index coefficient is connected with the third-order susceptibility as follows: $n_2 = \frac{3}{8n}Re(\chi^{(3)})$.

However, the fiber optics is not only one area of application of the NLS equation. In hydrodynamics focusing 1-D NLS is used as a leading order equation for describing unidirectional deep-water gravity waves propagation [19, 20, 58]. There were many possible derivations of the NLS equation in the context of the water waves. It naturally appears as a narrow band limit of the so-called Zakharov equation. In the case of the water waves the nonlinear coefficient can be expressed as $\chi^{(3)} = -k_0^3$ and dispersion one is $\beta_2 = 2/g$, with g the acceleration of gravity and k_0 the wave number of the carrier wave [59]. Water waves described by focusing 1-D NLS can be found in different contexts. For example, it is possible to obtain wavetrain whose dynamics can be governed by 1-D NLS in water tanks [47, 48, 59–61].

In this case, the wavetrain is created by a remotely controlled paddle (a wavemaker). In the open ocean, appropriate conditions are achievable in two cases [3]. First is an ocean storm in a restricted area which generates a wavetrain with a wide spectrum. Far from the storm area, in the absence of wind, the wave packet becomes nearly monochromatic with so-called JONSWAP spectrum [52, 62], so the NLS conditions could be satisfied. However, use of the 2-D NLS in this case is more appropriate. Another case requires the presence of the wind which acts over a long time and distance. The wind can generate almost monochromatic and one-dimensional wave packet.

The defocusing NLS can also describe water waves but in another context. The defocusing NLS has a connection with the KdV equation and can describe the dynamics of the slowly varying envelope of the shallow water waves [63]. It is shown that 1-D defocusing NLS can be applied when conditions $kh > 1.363$ is satisfied [64], where h is the water depth and k is the wave vector (note that k and ω are reversed in optics and hydrodynamics).

Also, the NLS equation is applicable for the description of nonlinear waves in plasma [65, 66] and Bose-Einstein condensate [67]. A review of applications of the NLS equation to these fields of physics can be found in [68].

1.2.2 Basic properties of the focusing 1-D NLS

Focusing (and defocusing) 1-D NLS equation has same non-trivial properties which we will discuss below. The principal difference between the defocusing and focusing NSL is that stationary solutions could be unstable under small perturbations in the focusing case. Also, the defocusing NLS doesn't have bright solitonic solutions (and hence all the family of the stationary solutions related to it), but has dark ones instead. Finally, we will discuss solitons on the finite background of the focusing NLS equation which are often considered as prototypes of the RWs in the ocean.

1.2.2.1 Stationary solutions

In the most general case, the stationary solutions of the 1-D NLS equation can be expressed in terms of elliptic Weierstrass function $\wp$ [69]. A general expression for the stationary wave as well as its stability analysis can be found in [69, 70]. The simplest solution of this kind is so-called cnoidal wave[9]. This solution is a (quasi-doubly) periodic wavetrain which profile doesn't change with time. In the limit of large periods, this solution can be approximated by a superposition of fundamental solitons. There are two branches of this solution dn and cn with respect to the Jacobi elliptic function which represents it. The exact expression of these solutions is the following:

$$u_{dn}(x,t) = e^{i\Omega t}\nu\, dn(\nu x, s^2) \tag{1.5}$$

$$u_{cn}(x,t) = e^{i\Omega t}s\nu\, cn(\nu x, s^2), \tag{1.6}$$

where Ω, s and ν are related to the periods of the elliptic function.

Figure 1.3 shows the profile of solutions from two branches of stationary solutions of the focusing NLS equation with different values of the parameter s, while all other parameters are fixed. We plotted the solution profiles at $t = 0$, when they are real on both branches. Fig. 1.3 (top) depicts the dn branch. Values of parameter s 0 (blue dotted line), 0.95 (black line), 1 (red dashed line). The case of small s solutions on the dn branch is close to the simple continuous wave solution with the small sinusoidal perturbation, when s equals to zero amplitude of perturbation goes to 0 and solution converges to the continuous wave. Values of s between 0 and 1 correspond to the periodically modulated solutions (case of $s = 0.95$ is shown in Fig. 1.3 (top) by black). In the limiting case, when the values of s are close to 1, solutions converge to the fundamental soliton, which can be expressed as follows:.

$$u_s(x,t) = n\, e^{in^2xt} sech(nx), \tag{1.7}$$

where n is a parameter related to one of the periods, $sech(x) = 1/\cosh(x)$.

[9] The word 'cnoidal' came from the name of cn Jacobi elliptic function which is closely related to $\wp$

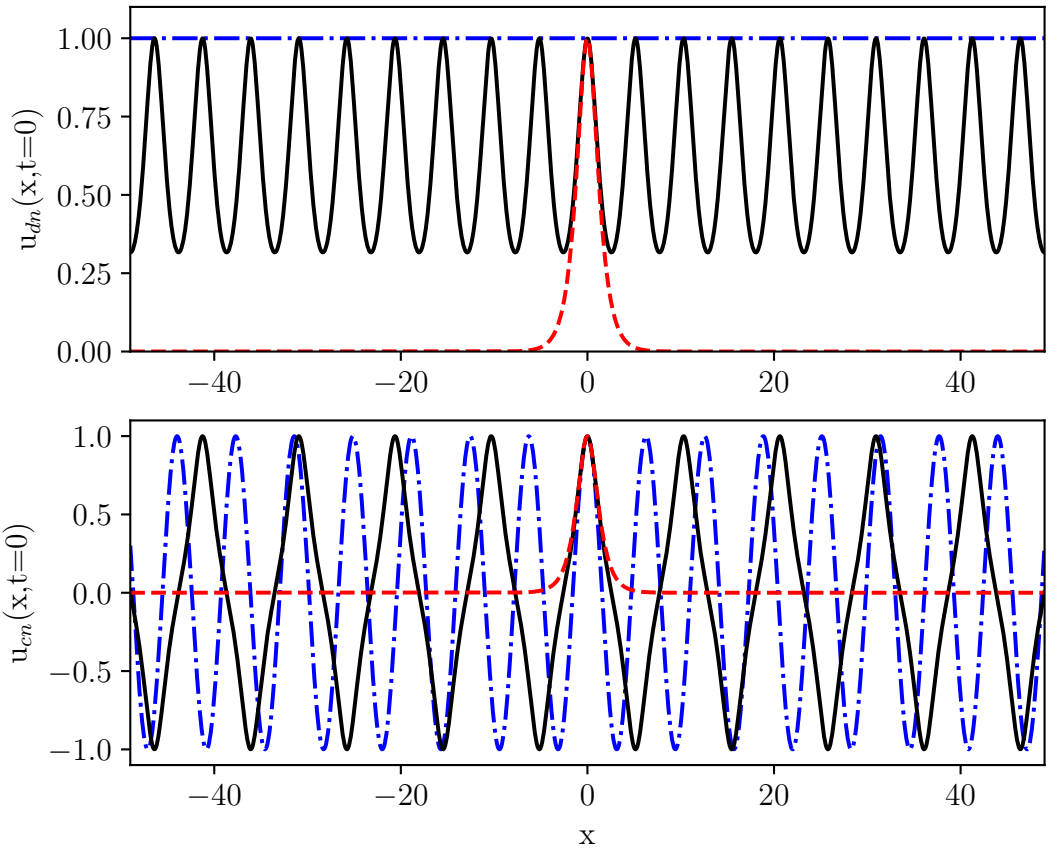

FIGURE 1.3: Two branches of stationary solutions of the focusing NLS equation. (top) The dn branch with values of s 0 (blue dotted line), 0.95 (black line), 1 (red dashed line). (bottom) The cn branch. Values of parameter s are the same.

Solutions on the cn branch with the small values of s are close to the simple cos(x) function and in the limiting case converges to it. In the intermediate interval of values of s we can see periodical function which phase alternates between 0 or π. Remarkably, the modulus of such periodical function coneverges to the one from another branch with the same (sufficiently large) value of s . And finally, when s tends to 1 we obtain exactly the same fundamental soliton as in the previous case.

However, presented solutions can be unstable under small perturbations because of presence of the modulation instability (MI) in the focusing NLS equation (it is also known as Benjamin-Feir or Bespalov-Talanov instability).

1.2.2.2 Modulation instability

Exponential growth of small perturbations can be often found in different physical systems. This phenomenon is known as modulation instability (MI). Almost simultaneously in 1960th modulation instability was discovered theoretically or experimentally by different independent groups in different fields of physics [71] such as optics [72–74], plasma physics [75] or hydrodynamics [76].

1- D focusing NLS equation is one of the simplest models demonstrating this behaviour. Single-mode fiber allows to study this phenomenon in the very well controlled experiments. In the context of single-mode fiber optics the MI can be seen as interaction of the narrow main band with small side bands or in other way: exponential grows of perturbation of the monochromatic or quasi-monochromatic wave (see Fig. 1.4). In this case it is common to provide a linear stability analysis and introduce the notion of the gain spectrum [21]. Indeed, modulation instability is a result of four-wave mixing which becomes efficient for some range of frequencies. The maximum gain for 1-D NLS equation in the form 1.4 has the spectral component which can be found as:

$$\Omega_{max} = \pm\sqrt{\frac{2\gamma P_0}{|\beta_2|}}, \tag{1.8}$$

where P_0 is the background level.

Pioneering experiments in fiber optics were provided by Tai, Hasegawa and Tomita in 1986 [77]. Since that time, modulation instability was widely studied in the context of fiber optics [78–83].

Modulation instability plays the key role in the evolution of the condensate and formation of the high amplitude structures out of small perturbation of a plane wave [43, 84–91].

Typical evolution of the condensate is depicted in Fig. 1.4. Left part of the figure shows the spatio-temporal dynamics diagram of the power. The cross-section of the diagram at three different positions plotted in the right-top part of the figure. In the right-bottom part the corresponding spectra are depicted. As one can see we start with a plane wave plus very small Gaussian shaped (in spectrum) noise. After some propagation (see the orange cross-section) modulation of power is slightly increased, while in spectrum we already distinctly see the emergence of the side bands. Finally, at the nonlinear stage of

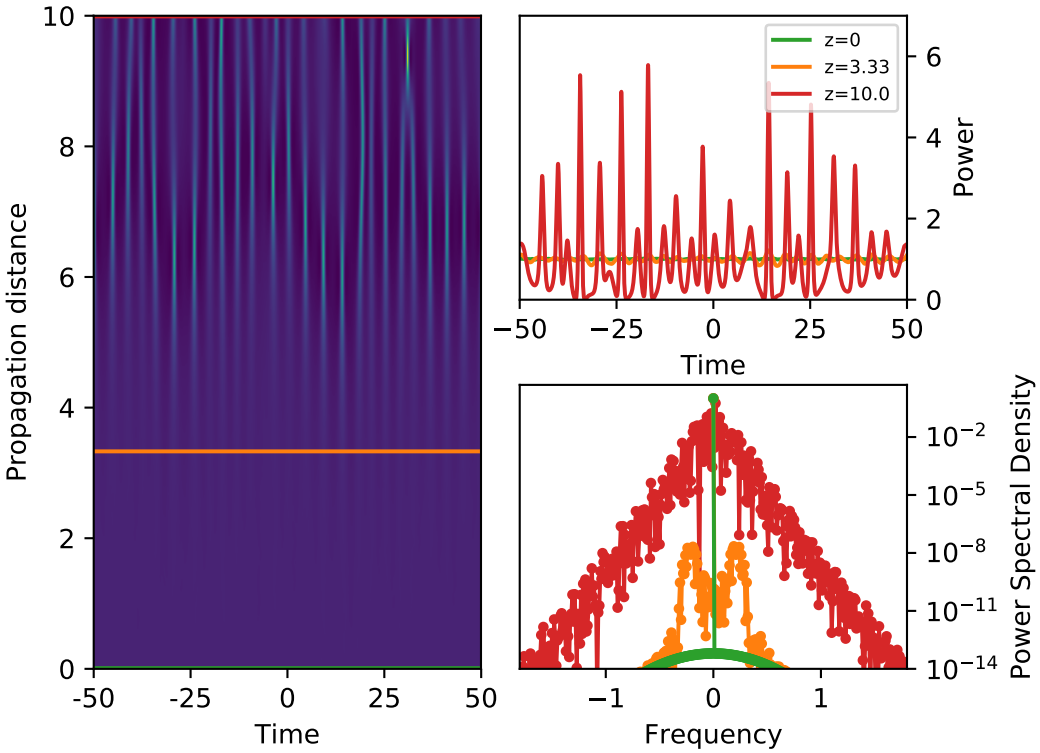

FIGURE 1.4: Numerical simulation of the evolution of a plane wave with small noisy perturbation. All units are dimensionless. Brighter colours correspond to higher power. (left) Spatio-temporal diagram showing the modulation instability acting on the quasi-monochromatic wave. (right-top) Power profiles at three different cuts of the diagram. Colours are preserved. (right-bottom) Corresponding spectra.

modulation instability (red cress-section) we observe emergence of the high amplitude structures. At this moment spectrum is spread around the central band and has exponentially decaying tails.

MI is often considered as the main driving mechanism of the generation of so-called Rogue waves (RW) known from the oceanography [20, 43, 61]. Therefore, exact solutions of the 1-D NLS that can be observed in the evolution of the condensate are considered as a prototypes of the RW. Such solutions are called solitons on the finite background. In the next section we will consider such solutions in details.

Finally, I would like to point out a new result obtained by Grinevich and Santini [92] using the in the finite gap theory of inverse scattering method (see Sec. 1.2.4.3). One of the supplementary results of their study allows to obtain IST spectrum for arbitrary perturbation of the condensate analytically. This possibility can significantly advance the study of integrable turbulence of NLS with the condensate as initial condition.

1.2.2.3 Solitons on the finite background and Rogue Waves

Another wide class of solutions of the focusing 1-D NLS equation which we will consider is solitons on the finite background. They can be seen as soliton of certain amplitude interacting with the plane wave (or background). Dynamics of such solution depends of the ratio of amplitudes of the soliton and the level of the background. There are three well known members of this class: Akhmediev breather [93], Peregrine soliton [94] and Kuznetsov-Ma soliton [95, 96]. These solutions were found using different methods including inverse scattering technique which will be considered later in this chapter. There is a generalised solution which unites all three solutions above. If 1-D NLS equation is written in the form:

$$iu_t + u_{xx} + 2|u|^2 u = 0$$

The generalised solution can be expressed as follows []:

$$u(x,t) = e^{i2t}\left[1 + \frac{2(1-2a)\cosh(2bt) + ib\sinh(2bt)}{\sqrt{2a}\cos(\omega x) - \cosh(2bt)}\right], \tag{1.9}$$

where a a control parameter which defines the properties of the solution, $b = \sqrt{8a(1-2a)}$ and $\omega = 2\sqrt{1-2a}$.

Akhmediev breather corresponds to the case when soliton amplitude is less than the background level. Formula 1.9 gives the Akhmediev breather solutionin the range of parameter $a \in (0, 0.5)$. Such solution splashes only ones along all the x scale and asymptotically converges to a plane wave (see Fig. 1.5 top-left). Changing the ratio of the soliton and backgrounding amplitude this solutions changes period between the spikes. When the amplitude of the soliton is higher than amplitude of the plane wave we observe a periodicity in time. This corresponds to Kuznetsov-Ma soliton (parameter $a \in (0.5, 1)$). Peregrine soliton is the limiting case of two other solutions

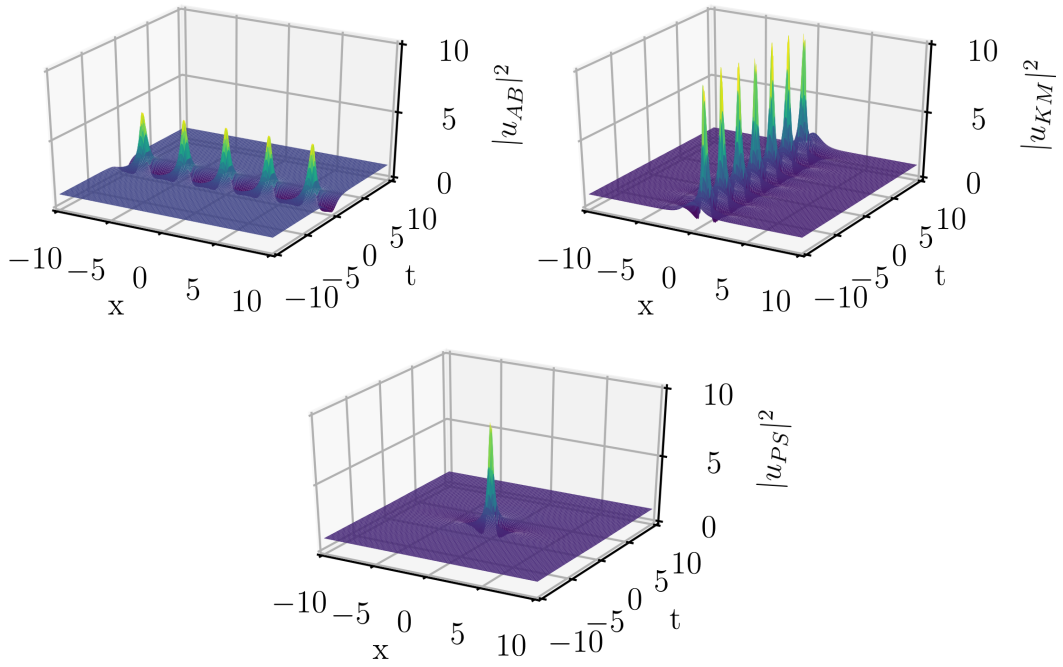

FIGURE 1.5: Solitons on the finite background plotted using the exact analytical expression. (top-left) Akhmediev breather. (top-right) Kuznetsov-Ma soliton. (bottom) Peregrine soliton

(see Fig. 1.5 bottom). It appears as a single high amplitude spike localised in space and time. Parameter a has to be set exactly to 0.5 in the formula 1.9.

As we discussed earlier, under some strong assumptions the integrable turbulence behind the 1-D focusing NLS equation can describe the evolution unidirectional ocean waves (see Sec. 1.1.4 and 1.2.1.1). Therefore, it is naturally to consider localized solutions of the 1-D NLS equation as prototypes of the RW [19, 97, 98]. Among all the localised solutions of the 1-D fNLS equation, solitons on the finite background are good candidates to this role. Taking into the account the fact that RW, according to observations [99], appears only once as a localised high amplitude structure, it is natural to consider the Peregrine soliton as a main candidate [100].

1.2.3 Basic properties of the defocusing 1-D NLS

Changing the sign before the nonlinear (or dispersive) term pass from focusing to defocusing NLS. Physics of defocusing NLS is drastically different, while the general properties, like integrability and infinite (and complete) set of integral of motion, remain present. In the present manuscript the integrable turbulence behind the 1-D defocusing NLS will investigated as well as for its focusing counterpart. Thus, we present here a short overview of some basic properties of the defocusing 1-D NLS. More detailed discussion will be provided in the chapter 4.

1.2.3.1 Dark solitons

Defocusing NLS also supports the solitonic solutions. However, unlike the focusing NLS, defocusing solitonic solutions have a form of a dip on the finite background (see Fig. 1.6). Dip width depends on dispersion and nonlinearity of the system as well as its deepness and background level. Solitons with the dip until zero level of intensity (black line in Fig. 1.6 (top)) are called black solitons. If the bottom of the dip has some finite non-zero value the soliton called gray (red dashed line in Fig. 1.6 (top)).

The corresponding IST problem was investigated right after the one for the focusing NLS also by V.E. Zakharov and A.B Shabat [101]. Numerical evidence of this phenomenon as well as more general formula which includes the grey solitons were presented in [24], the multiple soliton formula is shown in [102]. After several years dark solitons were observed in optical experiments [103–105]. A new wave of interest to the dark solitons came with their observation in the Bose-Einstein condensate [106] and other quantum systems (for example [107]).

For the dNLS written in the dimensionless form:

$$i\frac{\partial u}{\partial t} - \frac{1}{2}\frac{\partial^2 u}{\partial x^2} + |u|^2 u = 0 \tag{1.10}$$

The general formula for the dark soliton is following:

$$u(0,x) = \eta[Btanh(\xi) - i\sqrt{1-B^2}] \tag{1.11}$$

where $\xi = \eta B(x - x_0)$, parameter B is the deepness of the dip (B=1 gives the black soliton, B=0 - continuous wave), η defines the background amplitude, x_0 is the initial shift.

In contrast with the bright solitons, the phase of the dark one experiences the jump of the value $2sin^{-1}(B)$. Thus, the phase jump in the case of the black soliton (B=1) equals to π (see Fig. 1.6 (top)). Decreasing the value of B we will see more and more smooth phase change. This chirp brings to the grey solitons non-zero propagation velocity, while the black soliton preserves its initial position, i.e. its group velocity coincides with the one associated to the carrying wave.

1.2.3.2 Dispersive shock waves

The shock wave can be generated in a medium by inducing an abrupt change of some physical quantity. In viscous media, propagating shock wave demonstrates a fast (nearly discontinuous) change of physical parameters. While in dispersive media it is found to be an expanding modulated nonlinear wavetrain. In the framework of the integrable equations, it was first studied in the case of the KdV equation. This problem arises in the description of one-dimensional ion acoustic waves in a collisionless plasma with cold ions. Full characterisation of the problem was given by Gurevish and Pitaevsky [108] using Whitham averaging theory [109].

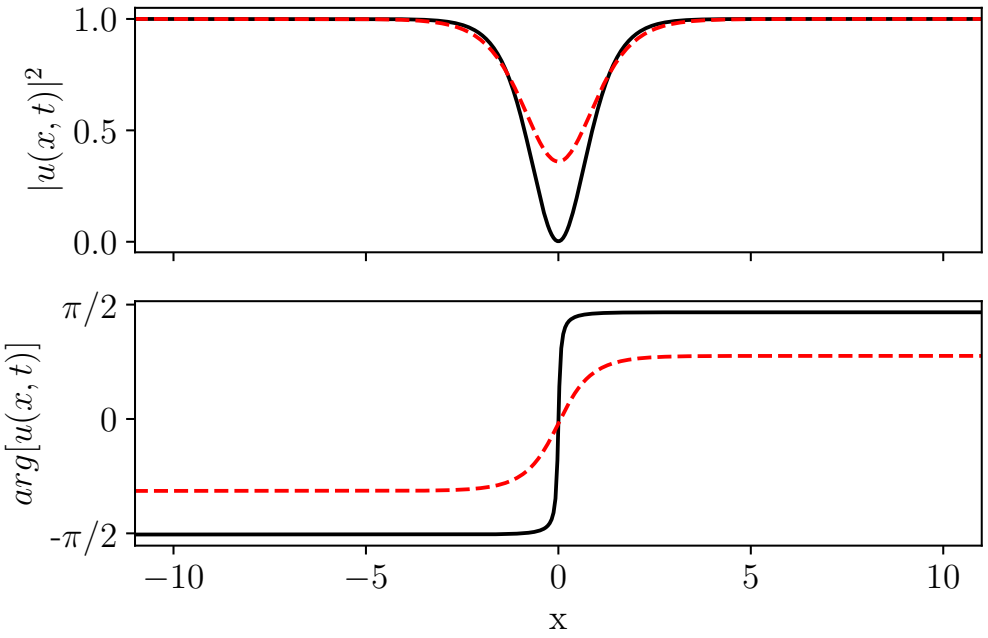

FIGURE 1.6: Two dark solitons of different deepness. Black line corresponds to the quasi-black soliton with the value of B close to 1, red dashed line to the gray soliton with B=0.8. (top) Amplitude modulus square. (bottom) Phase profile.

A dispersive shock wave (DSW) can be considered as a slowly modulated nonlinear wavetrain. It can be characterised by amplitude, frequency and mean value. Locally, all the fast oscillating components can be approximated by the basic solitonic solution of given nonlinear dispersive equation. Edges of DSW propagate with two different speeds different from the group velocity.

Whitham approach can be also used in the case of defocusing NLS equation where the initial discontinuity is regularised in a similar way [110]. First considered in [111] by Gurevich and Krylov, the problem of DSW generation in defocusing NLS was fully characterised by El et al. [112]. Important difference between the KdV and defocusing NLS is that in the latter case the DSWs are bi-directional.

This property can be seen in Fig. 1.7, where a double-side dam break problem is numerically integrated. Dam break (Riemann problem) is a classical problem of gas dynamics considering two initial constant states separated by a discontinuity. Recently, this problem was studied in optical experiments governed by 1-D defocusing NLS equation [113].

1.2.4 Inverse scattering transform

Integrability is a very significant and unique property of the partial differential equations like KdV and NLS. While linear PDEs can be solved using, for example, Fourier transform method, integrability of the nonlinear ones is rather an exception. The method of solving the 1-D NLS equation is called the Inverse Scattering Transform (IST). This powerful method was first shown in

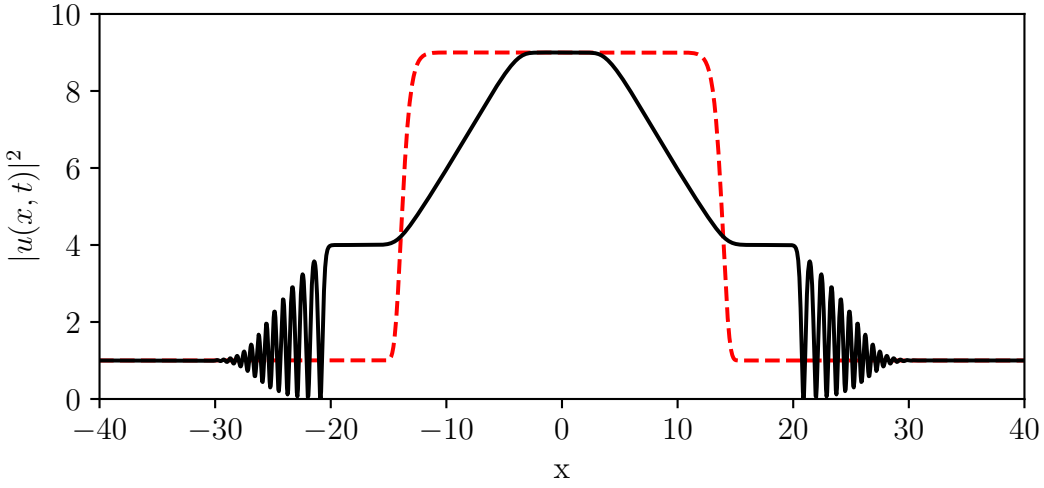

FIGURE 1.7: Dispersive shock waves in the double-side dam break problem of 1-D defocusing NLS equation.

the framework of the KdV equation (See Sec. 1.1.1.2), but shortly after was extended to other equations.

In this section, we will give a short historical overview of the IST method. Also, we will present essential calculations important for understanding the approach. In the given manuscript we will use the (quasi-)periodical version of the IST which will be also briefly discussed. In the end, we will give some examples of the IST spectra of some solutions presented earlier.

1.2.4.1 Historical background of inverse scattering transform

The IST method was presented by Gardner, Greene, Kruskal and Miura in 1968 for KdV equation [11]. It is started with an observation of Miura [114] that if v is a solution of so-called modified KdV equation $v_t - 6v^2v_x + v_{xxx} = 0$ then transformation

$$u = -(v^2 + v_x)$$

gives a solution of KdV equation. This fact was a basis of proof that KdV has infinite number of conserved quantities, but the most important consequence is that KdV has relation with Schrödinger equation known from quantum mechanics. Indeed, Miura transformation after substitution $v = \Psi_x/\Psi$ and generalization take the form:

$$\hat{L}\Psi - \lambda\Psi = \Psi_{xx} + (u - \lambda)\Psi = 0, \tag{1.12}$$

where λ does not depend on time.

We search an additional evolution equation in the form

$$\Psi_t = A\Psi + B, \tag{1.13}$$

where for the case of KdV $A = u_x$, $B = 4\xi - 2u$.

Equations 1.12 and 1.13 are chosen to give the KdV as their compatibility condition: $\Psi_{xxt} = \Psi_{txx}$. The time-independent eigenvalues λ often used for

characterisation of a solution. These equations define the scattering problem which is the basis of the Inverse Scattering Theory which will be discussed in the next section.

1.2.4.2 Inverse scattering transform of 1-D NLS: Zakharov-Shabat problem

Inverse scattering transform is a method of solving some nonlinear partial differential equations. It is powerful tool that is often referred as one of the most beautiful finding of mathematical physics of the XX century. It can be seen from different perspectives:

- Nonlinear equivalent of Fourier transform
- Canonical transformation of a Hamiltonian system
- Auto-Bäcklund transformation

Here we will consider the IST technique only from the first point of view. Let's first recall how the Fourier transform method can be used for solving linear partial differential equations. We consider a linear PDE: $u_t = \Lambda(u, \partial u/\partial x, \partial^2 u/\partial x^2, ...)$, where Λ represents a certain polynomial function. Then for initial conditions $u(0, x) = u_0(x)$ the solution at the time t_0 can be found by the following algorithm:

1. Provide a Fourier transform of the equation replacing $\partial_x \to ik$. In this case we obtain: $d\tilde{u}/dt = \sum_{n=1}^{N}(ik)^n\tilde{u}$, where $\tilde{u}$ is the spatial Fourier transform of u and N is the order of polynomial.
2. Solve ordinary differential equation in the Fourier space: $\tilde{u} = \tilde{u}_0 \exp(t_0 \sum_{n=1}^{N}(ik)^n)$, where $\tilde{u}_0$ is the Fourier transform of initial conditions.
3. Find the solution in real space providing inverse Fourier transform: $u(x, t_0) = 1/2\pi \int \tilde{u}_0 \exp(ikz - t_0 \sum_{n=1}^{N}(ik)^n)dk$

The IST approach to solving nonlinear PDE is similar. Instead of passing to the Fourier space, we will consider an associated *direct scattering* problem where scattering potential will evolve according to our nonlinear PDE. Equations describing the evolution of scattering data (reflection and transmission coefficients) are found to be rather trivial and exactly solvable. Knowing the scattering data at the needed moment of time, we can use a linear integrable equation known as Gel'fand-Levitan-Marchenko equation to solve the *inverse scattering* problem and reconstruct the potential which is the solution of the corresponding nonlinear PDE. The term nonlinear Fourier transform contains more than just similarity in the algorithm. In the limit of weak nonlinearity eigenvalues of the scattering operator are directly related to the Fourier spectrum of the solution. Later we will widely use these eigenvalues for identification of the solutions. The special case when the reflection coefficient equals to zero and eigenvalues are discrete corresponds to the fundamental solitonic solutions.

After the publication of the IST method for KdV equation [11], there were attempts to generalise it and apply to other nonlinear PDE. In the short period of time from 1971 to 1973 it was reported about the integration of 1-D NLS [18], modified KdV [115] and sine-Gordon [17], nonlinear equations with wide physical applications. Scattering problem for the NLS equations was found and solved by Zakharov and Shabat in 1972 [18]. It is expressed in the form of Dirac-type equations:

$$Y_x = \begin{bmatrix} -i\xi & u \\ -u^* & i\xi \end{bmatrix} Y \tag{1.14}$$

$$Y_t = \begin{bmatrix} -i2\xi^2 + i|u|^2 & iu_x + 2\xi u \\ iu_x^* - 2\xi u^* & i2\xi^2 - i|u|^2 \end{bmatrix} Y, \tag{1.15}$$

where Y is an n-dimensional eigenvector, ξ is the time independent eigenvalue.

There are two types of initial conditions exactly solvable with IST technique: rapidly decaying (with all derivatives) and (quasi-)periodic potentials. IST spectrum (spectrum of eigenvalues of the Eq. 1.14) for rapidly decaying potentials contains discrete value which corresponds to soliton and continuous one for dispersive radiation. The second case is significantly more complicated. In the framework of Integrable Turbulence it is unlikely to find rapidly decaying potentials, therefore we will consider the approach to periodical ones more detailed.

1.2.4.3 Finite-gap theory

The Inverse Scattering Transform for a (quasi-)periodical potential is more complicated task. Indeed, construction of this method required significantly refinement of existing scattering theory using advanced mathematical tools [116, 117].

It is convenient to start explanation of the finite-gap theory with the KdV equation since its associated scattering problem is related to the Schrödinger equation of quantum mechanics and hence direct physical analogies can be used. Indeed, the case of a particle scattering on a periodical potential is often studied in the framework of the solid state physics [118]. Since the inverse problem (reconstruction of the periodical potential) in periodical case requires knowledge of some advanced mathematics, we will discuss only direct problem which we will use in Chapters 3 and 4.

Let's consider the periodical potential u with the period T, so $u(x+T) = u(x)$ in the scattering problem defined by the Schrödinger equation 1.12. We will consider the eigenvalue problem for the operator $\hat{L} = -\partial^2/\partial x^2 + u(x)$ with such potential:

$$\hat{L}\Psi = \zeta\Psi \tag{1.16}$$

, eigenvalues ζ correspond the allowed energy state for a particle in periodic potential.

Let's define operator of translation $\hat{T}$ as: $\hat{T}\Psi(x) = \Psi(x+T)$. $\hat{T}$ is often called monodromy operator. It is chosen to satisfy the commutator relation with $\hat{L}$: $[\hat{L}, \hat{T}] = 0$. In our case the monodromy operator is represented by a 2X2 matrix:

$$\hat{T} = \begin{bmatrix} a & b \\ c & d \end{bmatrix}$$

If k is real, where $k^2 = \xi$, the basis of the solutions for Eq. 1.16 can be expressed as two complex conjugated functions ϕ and $\phi*$ and other solutions are linear combination of these two. We fix them in the way that:

$$\phi(x_0) = 1 \qquad \phi*(x_0) = 1$$

$$\phi_x(x_0) = ik \qquad \phi*_x(x_0) = -ik$$

So the Wronskian: $W(\phi, \phi*) = -2ik$ Therefore, the matrix $\hat{T}$:

$$\hat{T} = \begin{bmatrix} a & b \\ b* & a* \end{bmatrix}$$

Since the Wronskian is constant and doesn't depend on x, it is easy to show that $|a|^2 - |b|^2 = 1$, thus det($\hat{T}$) = 1.

Next, we can apply the Bloch's theorem from the solid state physics (which is a particular case of the Floquet's theorem) and define Bloch's functions as eigenfunctions of $\hat{T}$ and hence $\hat{L}$:

$$\hat{L}\Psi_\pm = \xi\Psi_\pm$$

also,

$$\hat{T}\Psi_\pm = \exp(\pm ipT)\Psi_\pm,$$

where p often called a quasi-impulse.

The trace of the monodromy matrix is an important characteristic in the Floquet analysis.

$$Tr(\hat{T}) = a + a* = 2a_R,$$

where a_R is the real part of coefficient a. Since the determinant of $\hat{T}$ equals to 1, we can express its eigenvalues as follows:

$$\exp(\pm ipT) = a_R \pm \sqrt{a_R^2 - 1}$$

$$2cos(pT) = Tr(\hat{T}) = 2a_R$$

From the solid state physics theory it is known that in order to have the Bloch function in the stable part of the spectrum corresponding quasi-impulse p must be real or in other words $|\exp(ipT)| = 1$. Thus, trace of the monodromy matrix will define the stable bands:

$$|Tr(\hat{T})| \leq 2$$

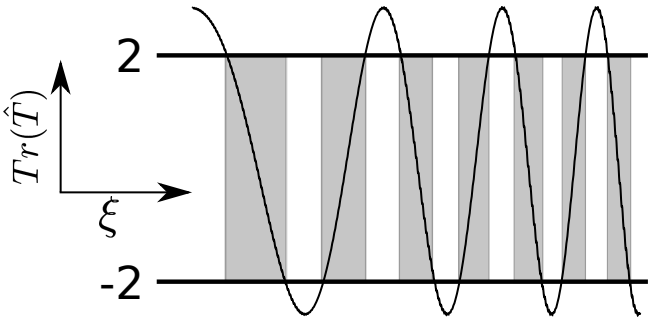

FIGURE 1.8: Example of the trace of the monodromy matrix as a function of the eigenvalue ξ. Gray rectangles depict the stable bands.

In Fig. (see 1.8) typical zone structure is depicted. We marked the stable bands (parts where $|Tr(\hat{T})| \leq 2$) by gray.

In analogy with the solid state physics we can see that instead of some discrete eigenvalues for the rapidly decaying potentials we have bands of a finite width separated by gaps. Inside the stable band we have an infinite number of eigenvalues, like infinite number of the states inside a zone of a solid. Further we will consider only the case when the number of the bands is finite, so some solutions can be explicitly constructed.

1.2.4.4 Examples of the IST spectra

Approach to the NLS equations is similar the one explained above. However, in the case of focusing NLS eigenvalues occupy all the complex plane. Meaning of the real and imaginary parts of the eigenvalues will be discussed later in Sec. 3.3 in the context of the Rogue Waves identification. In this section we will provide IST spectra of the periodical and rapidly decaying solutions shown previously in this chapter.

We start with dn branch of the cnoidal solutions of 1-D focusing NLS depicted in Fig. 1.3 (top). Let's investigate the behaviour of the trace of the monodromy matrix in this case. To simplify the task we will use an a priori knowledge that IST spectrum ξ of two limiting cases of dn branch, plane wave and soliton solutions, lie along the imaginary axis. it is natural to suppose that spectra of intermediate cases will also found there. So we will compute the trace of the monodromy matrix only for values of ξ which lie on the imaginary axis. Corresponding traces are plotted in Fig. 1.9 with the same colours as used in Fig. 1.3 (top). Trace of the dn(x,0), the plane wave, is plotted with blue line, the stable zone (where $|Tr(\hat{T})| \leq 2$) coloured with blue as well. As one can see the band lies from -i to i (it is also often called a branch-cut). The trace of the monodromy matrix in the intermediate case dn(x,0.95) is plotted with black. Stable bands are shaded by gray. The stable bands has a finite width and placed around the ξ 0.5i and -0.5i. In the cases of dn(x,1), the fundamental soliton, the size of the band is shrunk to zero. Hence, in this case as it was pointed out earlier we obtain two discrete points. Basing on this, we can finally construct the IST spectrum. It is shown in the Fig. 1.10. It is important to emphasize that the IST spectrum of the periodic problem also

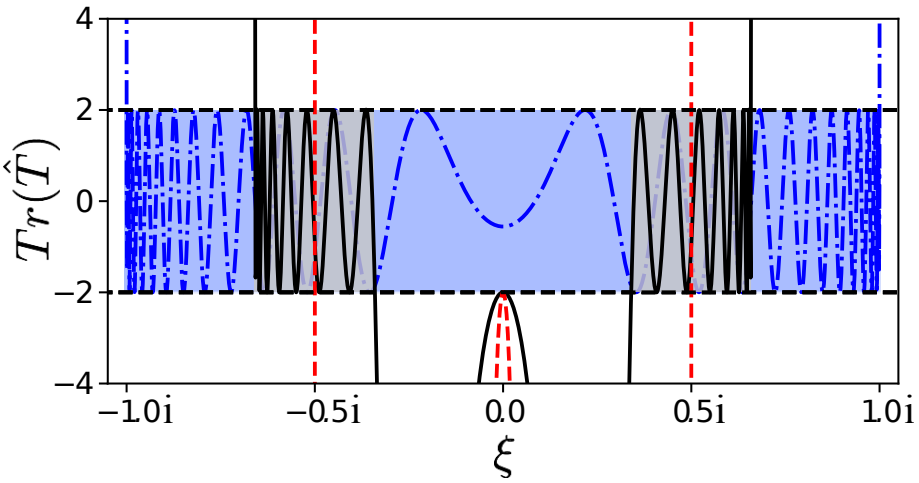

FIGURE 1.9: Trace of the monodromy matrix of the dn branch of cnoidal solution of the 1-D focusing NLS equation shown in Fig. 1.3 (top). All colours are preserved. Blue and gray areas show the stable band for the dn(x,0) and dn(x,0.95) respectively. The band of the solitonic solution dn(x,1) converges to the two discrete points -0.5i and 0.5i.

includes the real axis, this is not shown on the schematic figures. Method of numerical computation of the IST spectrum will be discussed later in Sec. 3.3.

Another kind of solutions discussed in this chapter are the solitons on the finite background plotted in Fig. 1.5. IST spectrum of such solutions (see Fig. 1.11), indeed, demonstrates the fact that they can be decomposed in two part: two complex conjugated discrete points that represent the solitons (red dots) and branchcut as a representation of the plane wave (blue line). Relative position of the complex conjugate points and the branchcut changes the dynamics of the solution. The branchcut is always found to be from -i to i if the amplitude of the plane wave is 1. In the case of the Akhmediev breather discrete point on the upper half of the complex plane (lower part is symmetrical) lies between 0 and i. When the discrete point reaches i, so it coincides with the upper limit of the branchcut, we obtain the Peregrine soliton. When the discrete point exceeds i, we have the Kuznetsov-Ma soliton.

In the framework of the finite-gap theory solutions of the NLS equation are often characterised by their *genus*. Genus can be calculated as N-1, where N is the number of bands in the spectral portrait. Physically, the genus characterizes the number oscillatory modes of a certain periodical solution [119]. From this point of view, the plane wave which has a single band (see Fig. 1.10) is therefore genus 0 solution. Cnoidal waves with parameter $s^2 \in (0, 1]$ (including solitonic solution) are represented by two separate bands, so they are genus 1 solutions. In the case of the solitons on the finite background we have branchcut and two discrete points (or two bands of infinitely small size), therefore they are genus 2 solutions.

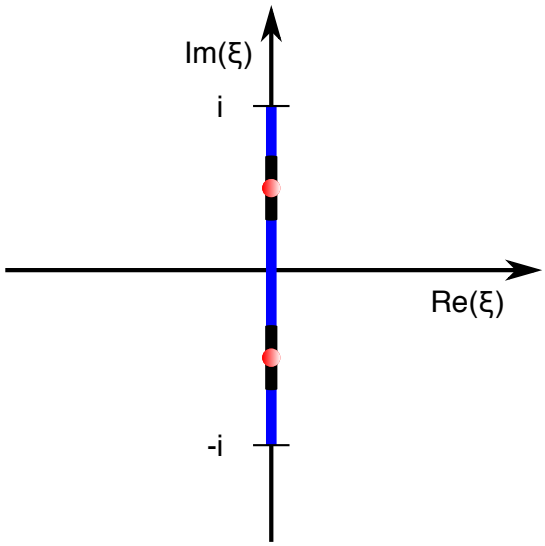

FIGURE 1.10: IST spectra for the dn branch of cnoidal solution of the 1-D focusing NLS equation shown in Fig. 1.3 (top). All colours are preserved. The bands which correspond to dn(x,0) are depicted by blue,for dn(x,0.95) by black and two discrete points of dn(x,1) are depicted by red.

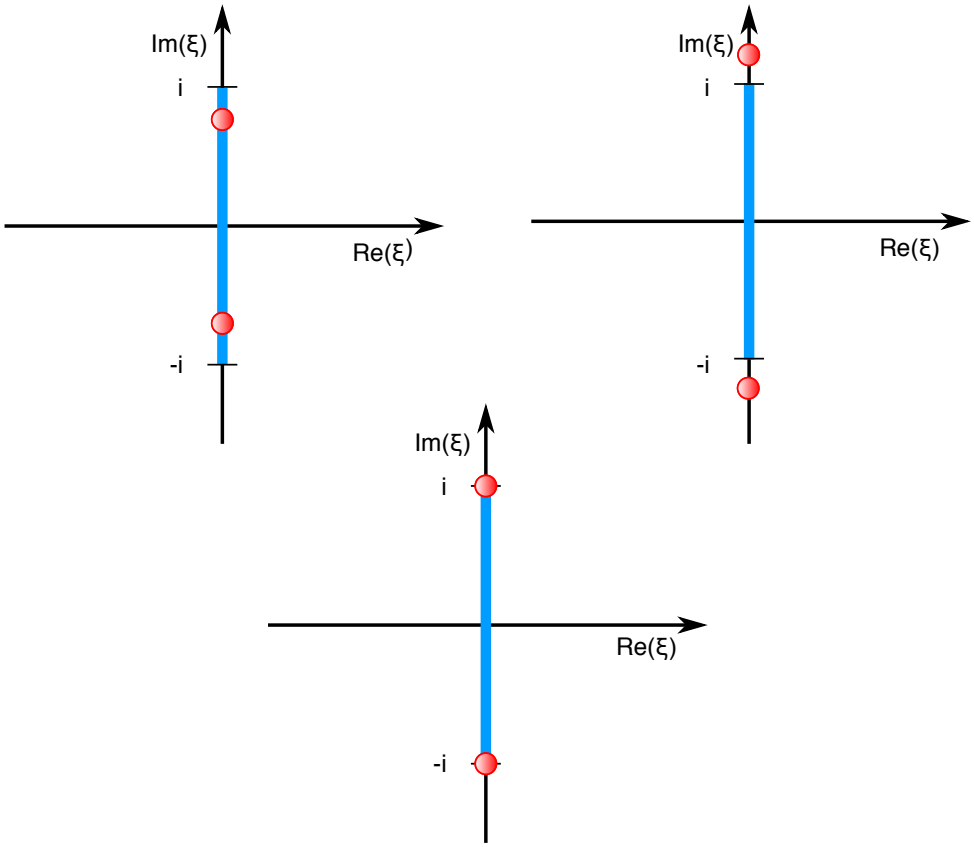

FIGURE 1.11: Schematic IST spectra of the solitons on the finite background of 1-D focusing NLS equation shown in Fig. 1.5. Arrangement of the figures is preserved. (top-left) Akhmediev breather. (top-right) Kuznetsov-Ma soliton. (bottom) Peregrine soliton.

1.3 Problematic of the study

Theoretical as well as experimental studies 1-D NLS integrable turbulence, known until now, do not cover some important aspects of this field. The origin of the 'heavy-tailed' probability density function in the case of the partially-coherent wave in focusing NLS system was not understood at the moment beginning of my work [53]. Experimental investigations of this question in optics requires a new ultrafast measurement tool, which is capable to measure power and phase profiles with resolution of few hundreds of femtoseconds in single-shot.

1.3.1 State of the art: Theory

The integrable turbulence originates from the article of Zakharov published in 2009 [1]. In this work, there are several fundamental problems posed for different kinds of integrable equation including NLSe. Among other questions, author considers a problem of the development of the condensate initial conditions in the framework of the 1-D focusing NLS equation. First, together with Gelash, they demonstrated the development of the condensate from a localised perturbation [88]. In the following work made with Agafontsev [43] they provided a numerical study of the noise-driven dynamics of condensate which gave an unexpected result: statistics of condensate initial condition at the stationary state is Gaussian. While in the defocusing case the condensate is stable. At the same time, it was shown by Walczak et al. [53] that evolution of the partially-coherent waves (which also have the Gaussian statistics, but at the beginning) leads to the 'heavy-tailed' probability density function in the focusing case and 'low-tailed' for the defocusing one. These two observations give an idea about the complexity of the integrable turbulence of the NLS equation.

Partially-coherent initial conditions evolution problem can be solved exactly by implanting the zero boundary conditions employing the infinite line IST [46]. However, consideration of the periodical problem is a much more complicated task. Soto-Crespo, Devine and Akhmediev considered a problem of transition from condensate to the partially-coherent initial condition using the (periodic) IST approach [120, 121]. They concluded that dynamics of the partially-coherent initial conditions is dictated by solitons with non-zero speed, while in the case of condensate by not moving breathers.

There are several developed approaches to the integrable turbulence problem in the framework of the NLS equation. One of the cases that brought some insights to the problems is the limit of weak nonlinearity. So the wave turbulence approach can be used [36–38]. In this case, taking into the account non-resonant terms, it is possible to derive kinetic equations for the evolution of the spectrum and hence fourth-order moment of the field.

Another case which gave significant result is the limit of small dispersion. When the dispersion is eliminated directly from the NLS equation, so-called zero dispersion limit, the problem of incoherent light dynamics can be solved exactly [122]. However, the presence of a small dispersion leads to entirely

new effects that couldn't be observed in the zero dispersion limit. Another approach to the small dispersion is called a semi-classical (or dispersionless limit). Instead of the NLS equation, an equivalent system of equations has to be considered. The dispersionless limit can be achieved by eliminating a term with a small parameter (which is proportional to the ratio of nonlinear and linear lengths) in such a system of equations. Working in this limit, Dubrovin, Grava and Klein [123] and later Bertola and Tovbis [124] derived a theory of gradient catastrophe[10] and its regularisation in the focusing NLS equation for some smooth rapidly decaying initial conditions. Bertola and Tovbis showed that the regularisation of the gradient catastrophe universally goes through the formation of the of the local Peregrine soliton which is often considered as a prototype of the Rogue Wave. However, until now the role of the regularisation of the gradient catastrophe in the integrable turbulence was not clear.

Defocusing case is often considered as trivial because of the absence of the modulation instability. However, dynamics of the random wave, in this case, reveals some non-trivial effects like dispersive shock waves formation [125]. It is important to mention that versatile theoretical and experimental studies of the gradient catastrophe and dispersive shock waves formation were provided [111, 112, 126–130].

1.3.2 State of the art: Experiment

Theoretical study of the random waves propagation, especially in the framework of IST, requires periodic boundary conditions[11]. While in experimental studies of the random waves, continuously ongoing random signal source is used. This is equivalent to an infinitely large window. One of the main experimental challenges is to deal with the non-periodical signal, keeping at the same high resolution and sufficiently large window of measurements.

Experimental investigation of the optical Rogue waves started with the work of Solli, Ropers, Koonath and Jalali in 2007 [54]. In this work, the authors provided measurements of statistics of the high amplitude events, but in the framework generalised NLS equation, including the Raman scattering. The scheme of the measurements is based on the spectral filtering of the optical signal in the area far from the central part of the spectrum. In this way, it was possible to separate high amplitude events that have a broad spectrum from others.

Experimental studies in the framework of 1-D NLS equation were provided mostly for some deterministic initial conditions. The important role in the experimental studies took the observation of the exact solutions of 1-D

[10] In the context of the focusing 1-D NLS equation, the gradient catastrophe is of different nature than the one occurring in the wave breaking phenomenon in defocusing 1-D NLS.

[11] Indeed, the theoretical study of partially coherent waves that present in the full time scale exhibit the problem of infinite energy (even the Fourier transform must be defined carefully). The solution is to use periodic boundary conditions and take the large box limit.

NLS. It started with observation of bright [131] and dark [105] solitons using auto- and cross-correlation. When the solitons on the finite background brought the attention of the community due to their possible connection with the Rogue waves, they were observed experimentally [84, 85, 91]. Kane and Trebino proposed the main tool[12] for these experiments called FROG (Frequency-Resolved Optical Gating) in 1993 [133, 134]. This tool allows one to measure power and phase profiles of a periodic signal. Meanwhile, the experiments with partially-coherent waves require single-shot measurements since we work with a nonperiodic signal. FROG technique has a single-shot modification called PG XFROG [135]. However, it doesn't provide a sufficient window of measurements.

Another tool which allows measuring intensity and phase at single-shot is the streak camera. However, it does not provide sufficient dynamic range together with resolution needed for the study of fast fluctuating random fields. Indeed, due to the electron beam repulsion, there is a trade-off between resolution and dynamic range. For the experiments with random light propagating in nonlinear media, it is important to have high values for both characteristics because of the emergence of high amplitude structures.

1.3.3 Motivation and objectives

The short overview presented above shows that there are several important open questions to answer:

- What is the mechanism of generation of the high amplitude structures in the integrable turbulence of 1-D focusing NLS equation?
- How to connect local behaviour with the evolution of statistical parameters?
- What is the origin of the 'heavy-tailed' and 'low-tailed' statistics in the case of partially-coherent initial conditions?
- Can the theoretical results obtained in the dispersionless limit of NLS equation be applied in the general case?
- How to describe the change in the behaviour of the system passing from partially-coherent initial conditions to condensate?

Basing on this, we can formulate the objectives of the current manuscript. They can be divided into two major parts:

1. Development of an optical measurement tool working in single-shot with resolution of hundreds of femtoseconds and window of measurements of tens of picoseconds, which is able to measure power and phase profiles with a high dynamic range.

[12] There are several alternative techniques. For example, if only the power profile is needed, Optical Sampling technique [132] can be used (see Sec. 3.1.2). However, FROG remains the most popular tool.

2. Application of this tool to direct measurements of coherent structures that emerge in fiber optics investigations of the 1-D NLS integrable turbulence. Combination of experimentally obtained results together with numerical simulations and theory in order to get new insights into the integrable turbulence in focusing and defocusing regimes.

Chapter 2

Ultrafast measurements of non-periodic optical waves using the Time Microscopy technique

Ultrafast measurements in optics have almost 60 years-long history of development. This field emerged simultaneously with pulsed lasers and hence necessity of its characterisation. Despite significant progress, during these years all existing measurement techniques have their limitations, especially if we speak about simultaneous intensity and phase measurement of non-periodic (random) signals. In this chapter, a new ultrafast measurement technique appropriate for this purpose is presented. We discuss here its advantages and disadvantages in comparison with other techniques, show a detailed scheme of its experimental realisation, analyse possible measurement errors.

2.1 Ultrafast measurements in optics

After development of the first laser by Theodore H. Maiman in the year 1960 [136] this field experienced a very fast growth [137]. As a result, just after one-year of investigations pulsed radiation from the ruby laser was obtained using Q-switching technique [138]. After several years of development, researchers broke the picosecond limit of light impulse duration using the mode-locking technique [139, 140]. After implementation of Ti:sapphire lasers [141] one can easily obtain few tens of femtoseconds pulses in laboratory conditions. Since the light pulses became shorter and shorter, very fast a problem of their characterisation [142] has arisen. Indeed, almost immediately laser pulses overcame the bandwidth of photodiodes available at that time. Besides the direct measurements, a sampling technique could be used, but for the sampling a shorter event than the pulse itself is required.

The idea of using the pulse itself to characterise its width has naturally appeared. This technique is called *autocorrelation* [143]. The idea is relatively simple: split the pulse under investigation into two parts, introduce a delay for one of them and provide measurements changing the delay (see Fig. 2.1). If the two parts are simply superimposed on the detector this called the *field* autocorrelation. The measured quantity is related with the Fourier spectrum

via the Wiener-Khinchin theorem. The simplest implementation which allows one to estimate the duration of the ultrafast signal is the *intensity* autocorrelation. In this case, the two parts of the signal superimposed inside a nonlinear crystal. Therefore, measured quantity is:

$$C(\tau) = \int_{-\infty}^{+\infty} P(t)P(t+\tau)dt$$

Where the optical power is $P(t) = E(t)E^*(t)$, with $E(t)$ the actual electric field.

This approach is the 'grandfather' of all modern pulse measurement technique. Since that time it was significantly improved: instead of simple delay line a Michelson interferometer with a variable arm length difference could be used which makes the autocorrelation sensitive to the pulse chirp (*interferometric* autocorrelation), using two-photon absorption to significantly increase the bandwidth of measurements [144] and finally measurements of higher-order autocorrelation can be provided [145]. However, as it was mentioned by R. Trebino in the article [146]:

> "Autocorrelation...yielded only a blurry black-and-white image of the pulse."

Indeed, this approach, even its advanced variation, suffers from the presence of so-called 'coherent artefacts' and induce an ambiguity in measurements of complex fields [147].

One of the most spread and efficient approaches to characterisation of ultrafast signals is a *spectrogram* measurements. Originated from the work of Treacy [148]. It requires the recording of time-frequency distribution. Significant breakthrough has happened in 1991 when J. Chilla and O. Martinez extended this approach by using a nonlinear wave mixing in a crystal [149–151]. This method known today as *sonogram* measurement. It can be seen as a superposition of a spectrally filtered signal with itself inside a nonlinear crystal. In the original article authors used a single slit mask in a grating compressor. This made possible to measure the phase and intensity of femtosecond chirped pulses.

In 1993 when D.J. Kane and R. Trebino introduced a technique known as FROG (Frequency-Resolved Optical Gating) [133]. The basic FROG configuration is depicted in the Fig. 2.1. From the first look, FROG is very similar to the autocorrelation, but FROG instead of the intensity requires spectrum measurements as a function of delay. This difference is fundamental, because now we have a 2-D phase-retrieval problem, instead of 1-D. The 2-D phase-retrieval problem has a unique solution and contains only trivial ambiguities [134]. However, this technique has certain disadvantages. First of all, FROG requires quite sophisticated recovery algorithm based on the method of generalized projections for the phase reconstruction [152]. Recently, several more advanced, but not less sophisticated algorithms were proposed. For example, a novel algorithm based on ptychography technique was proposed in [153]. Improvements allow reconstructing a full signal information even from a spectrally incomplete FROG traces. Also, FROG has benefited

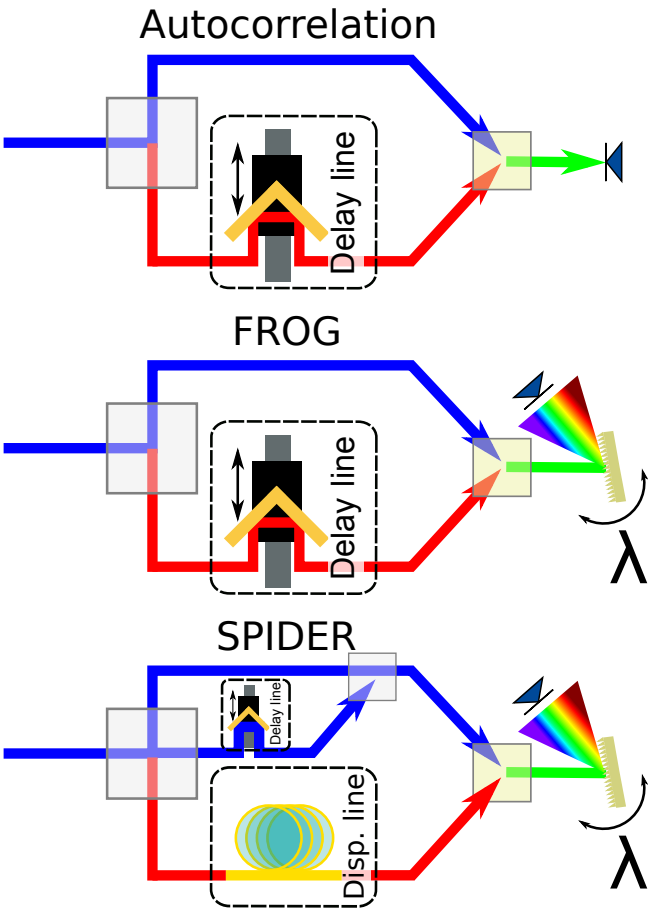

FIGURE 2.1: Schemes of the fast optical signal characterization methods. (Top) autocorrelation. A signal divided into two parts. One of them experiences a controllable temporal delay. Two parts are superimposed directly on the photodiode (field autocorrelation) or in a nonlinear crystal (intensity autocorrelation). (Middle) FROG. Similar to the intensity autocorrelation, but instead of the photodiode detection, the spectrum measurements are provided. The resulting FROG trace is a 2-D image of spectrum as a function of delay. (Bottom) SPIDER. A chirped replica of a signal is superimposed with its two copies. The spectrum of the resulting pattern allows to extract the phase and intensity.

from a novel wave of improvements with a deep-learning approach, which helped to increase the robustness of the signal reconstruction with a low signal-to-noise ratio [154]. Now the technique has many variations which make it flexible and adaptable to different needs [134, 155]. Today it can be considered as a most widely-spread technique of ultra-short pulse measurements.

Another large family of ultra-short pulse measurement technique is SPIDER (Spectral phase interferometry for direct electric-field reconstruction) [156]. The principal scheme is depicted in the Fig. 2.1. In this scheme, the signal, doubled using a delay line, interacts with its chirped replica. Strong sides of this method are following: it doesn't require an external reference and any moving parts (delay is constant). Also, the data retrieval process is relatively simple. Hoverer, there is a strong weakness of this method. In the presence of a jitter or phase oscillations, satellite pulses can be invisible. This fact is extensively discussed in the article [157]. Finally, it is not appropriate for the single-shot measurements in its classical arrangement.

However, further development revealed possibilities of rearrangements of presented techniques in order to achieve the single-shot operation. Indeed, in [135] a polarization-gating arrangement combined with cross-correlation frequency-resolved optical gating (PG XFROG) is presented. It is capable to provide required measurements, but over a very limited time window $\sim 4\,ps$. The single-shot extension of the SPIDER is also possible [158], however It requires a high signal power. Evolution of the spectral interferometry techniques unavoidably led to two-dimensional spatial arrangement setups. Spatially encoded arrangement for spectral phase interferometry for direct electric field reconstruction (or SEA-SPIDER) was presented in 2005 [159, 160] . This tool satisfy all the criteria to be adopted for the partially-coherent waves measurements, but like the XFROG doesn't provide sufficient window of measurement.

Another ultrahigh-speed detector is the Streak Camera. The operating principle of the Streak Camera is based on the imaging with the electron tube [161]. Early development of the Streak Camera showed possibilities to detect light with picosecond resolution [162]. In 2002 attosecond arrangement was demosntrated [163]. The main disadvantage of the Streak Camera is the interplay between the dynamic range and resolution [164]. It is related to physical repelling of electrons inside the bunch emitted from the cathode by a light impulse.

Along with the development of the autocorrelation measurements was developed a theory of *temporal imaging*. This theory is based on the mathematical space-time analogy under certain conditions and allows one to slow down the temporal evolution of signal. We will discuss it extensively in the next section of this chapter. Here I would like to mention that it was developed and ready for the effective measurements of the optical intensity profile at the beginning of 70th. However, it was unnoticed in the optical community until the work of Brian H. Kolner and colleges in 1989 [165]. However, this technique doesn't provide the phase measurement without some significant extensions.

Recently, temporal imaging approach was extended by using a dispersive Fourier transform (DFT) [166] to measure intensity and phase in single-shot [167, 168]. This technique is based on the analogy between angular Fourier transform in Fraunhofer diffraction scheme and temporal Fourier transform (for example after a linear propagation in an optical fiber). So it makes possible to record the power spectrum of the signal in single-shot simultaneously with the power profile. The phase reconstruction is made using the Gerchberg–Saxton algorithm or its generalisations [169]. This information is enough for the phase reconstruction without ambiguity. Further development of the DFT method reveals the possibility to provide an amplification and even resolve particular parts of the spectrum with a better resolution [170].

Comparison of the measurement techniques (including resent ones such as STARFISH [171] and SEA-TADPOLE [160]) is given in Tab. 2.1. However, reader has to take into the account that parameters of a technique can vary significantly from one implementation to another. In the table we provided typical values found for basic implementations of the measurement techniques.

TABLE 2.1: Comparison of the existing ultra-short pulse measurements techniques. In the column Disadvantages we discuss reasons why this technique could not be applied to the partially-coherent waves measurements. For the primary sources of information see [134, 142, 146, 168, 172].

	Phase measurements	Single-shot operation	Resolution	Time window	Disadvantages
Direct photodetection	No	Yes	∼20 ps	Inf	Low resolution
Streak Camera	No	Yes	0.1-10 ps	0.01-1 ns	Choice between dynamics and resolution
Autocorrelation	No	No	∼1 fs	∼1 ns	No single-shot operation
Sonogram	Yes	No	∼10 fs	∼ 1 ps	No single-shot operation
FROG	Yes	No (the basic version)	∼1 fs	∼1 ns	No single-shot operation
XFROG	Yes	Yes	∼10 fs	∼10 ps	Short window of measurements
SPIDER	Yes	No (the basic version)	∼1 fs	∼100 fs	Some pulses could be invisible [157]
SEA-SPIDER	Yes	Yes	∼10 fs	∼10 ps	Short window of measurements
Time lens	No	Yes	∼200 fs	∼100 ps	No phase information
SEA-TEADPOLE	Yes	No	∼1 fs	∼ 10 fs	No single-shot operation
STARFISH	Yes	Yes	∼10 fs	∼ 1 ps	Short window of measurements

2.2 Basics of the Time Microscopy

In this section, we will discuss in details the time-space analogy used in the temporal imaging technique. Application of this approach to the creation of a Time Lens played an important role in the ultrafast measurements. After some years of development, quite naturally, ideas of extension of the Time Lens to a Time Microscope have appeared.

Further, we will show a precise scheme of experimental realization of the Time Microscope. This arrangement provides a straightforward intensity profile retrieval and requires relatively simple adjustment and calibration. We will propose a time calibration (conversion of the camera pixel to time) and resolution determination methods. We will discuss the appearance of aberrations due to the presence of the higher-order dispersion in the compressors. We will show how it affects the resolution value estimates. In order to investigate the aberration problem, we provide extended numerical simulations of the Time Microscope. This reveals a complexity of resolution determination and hence the time calibration (the time calibration is not possible without the precise compressor tuning).

Next, we will present an experimental realisation of the Heterodyne Time Microscope arrangement which enables to solve the problem of single-shot simultaneous phase and intensity measurements over a large temporal window. Finally, we propose a rearrangement called SEAHORSE which removes the problem signal's aberrations completely.

2.2.1 Principles of temporal imaging

The term Time Microscope came from the direct analogy with conventional spatial optical beam evolution in a simple double-lens microscope [173–176]. This time-space analogy has a pure mathematical nature. It makes a link between the equation of the paraxially propagating beam's evolution in the transverse direction and second-order chromatic dispersion in time under the slowly varying approximation, on one hand. On the other hand, it connects quadratic phase inducing by a thin lens and nonlinear interaction with a chirped pulse or the electro-optical modulation (see Fig. 2.2). These analogies gave a born to a rapidly-growing sub-domain of ultrafast optics: temporal imaging.

First time this analogy was pointed out by Akhmanov and his colleagues in the late 60th [177, 178]. Since that time the possibility to provide the temporal imaging in optics in order to manipulate the waveforms was extensively discussed. However, the first experimental realization of this idea is performed for a purely electrical signal by Caputi in the article [179], where he mentioned possibilities to realize a similar scheme for detection of optical and acoustical signals. However, only after a significant delay, the Time Lens was adopted for detection of optical signals [165, 180].

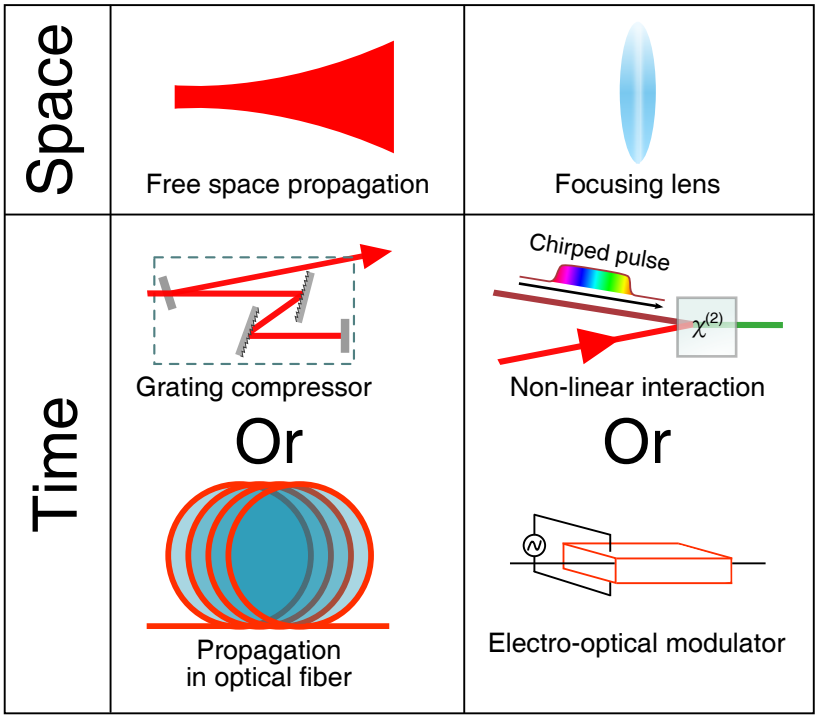

FIGURE 2.2: Scheme of possible space-time duality realisations. Analogies between paraxial diffraction depicted as cross-section of a free space propagated beam and second-order dispersion in time represented as light beam propagated through a grating compressor or equally in optical fiber in linear regime. Effect of quadratic phase induced by conventional thin lens juxtaposed with nonlinear interaction of a chirped pulse with the studied signal. Also, a possibility of electro-optical phase modulation could be considered as an alternative approach.

2.2.1.1 Diffraction - dispersion analogy

The discussed time-space similarity is surprisingly profound. Let's look at this analogy closer. Our starting point is the system of Maxwell equations [181]. We will consider only its form in the case of absence of free charges and non-magnetized media which is almost always valid in optics. Also, the media will be considered as linear, isotropic and without losses. Further, we combine, as usual, Maxwell's equations by applying the rotor operation to the Maxwell-Faraday equation. Obtained field evolution equation will be approximated in two different way: monochromatic field bounded to the propagation axis for the description of paraxial diffraction and narrowband plane wave for dispersion. The full derivation is explained in several monographs [173, 174] and here only the steps necessary for understanding will be given.

Maxwell's equations in the discussed conditions take form:

$$\begin{aligned} &\textit{Coulombs's Law} && \nabla \cdot \mathbf{D} = 0 \\ &\textit{Absence of free magnetic poles} && \nabla \cdot \mathbf{B} = 0 \\ &\textit{Faraday's Law} && \nabla \times \mathbf{E} = -\frac{\partial \mathbf{B}}{\partial t} \\ &\textit{Ampere's Law} && \nabla \times \mathbf{H} = \frac{\partial \mathbf{D}}{\partial t} \end{aligned}$$

Classical transformations assuming the harmonic time dependence lead to the Helmholtz equations in the Fourier space [181]:

$$(\nabla^2 + \mu\epsilon\omega^2) \begin{bmatrix} \mathbf{E} \\ \mathbf{B} \end{bmatrix} = 0 \tag{2.1}$$

As usual, we will concentrate out attention on the part describing the electric field evolution.

In order to describe the *paraxial diffraction* we can consider the wave as monochromatic at the frequency ω_0. According to the shift theorem of the Fourier transform:

$$\mathcal{F}[\mathbf{E}] = \mathbf{E_0}(x, y, z)\delta(\omega - \omega_0)$$

Paraxial limit leads to the phase evolution mostly along z axis

$$\mathbf{E_0}(x, y, z) = E(x, y, z)e^{-ikz}$$

where

$$k^2 = \mu\epsilon\omega_0^2$$

Taking into the account that diffractive spreading contributes the most to the field envelope curvature, the associated Helmholtz equation can be rewritten in a simpler form:

$$\boxed{\frac{\partial E}{\partial z} = -\frac{i}{2k}\left(\frac{\partial^2 E}{\partial x^2} + \frac{\partial^2 E}{\partial y^2}\right)} \tag{2.2}$$

The narrow-band dispersion could be described with a similar parabolic differential equation as 2.2. Indeed, lets consider a plane electro-magnetic wave propagation in the media with dispersion. Since the wave is plane, we completely neglect its evolution in the transverse direction. Presence of dispersion implies the frequency dependent propagation constant $\beta(\omega)$. Hence the total electric field could be expressed as follows:

$$\mathbf{E}(x, y, z, t) = \mathbf{A}(z, t)e^{i(\omega_0 t - \beta(\omega_0)z)}$$

Therefore

$$\mathcal{F}[\mathbf{E}] = \mathcal{A}(z, \omega - \omega_0)e^{-i\beta z}$$

Narrow-band approximation makes it reasonable to provide the Taylor expansion of the propagation constant around the central frequency ω_0:

$$\beta(\omega) = n(\omega)\frac{\omega}{c} = \beta_0 + \beta_1(\omega - \omega_0) + \frac{1}{2}\beta_2(\omega - \omega_0)^2 + \dots$$

Where $\beta_i = \frac{d^i\beta(\omega)}{d\omega^i}$ for $\omega = \omega_0$.

In this way the equation 2.1 takes the form:

$$\frac{\partial\mathcal{A}(z,\omega-\omega_0)}{\partial z} = -i\left[(\omega-\omega_0)\beta_1 + \frac{(\omega-\omega_0)^2}{2}\beta_2\right]\mathcal{A}(z,\omega-\omega_0)$$

After a common (especially in fiber optics) change of variables $\tau = t - \frac{z}{v_g}$ and $\xi = z$, we obtain:

$$\boxed{\frac{\partial\mathcal{A}(\xi,\tau)}{\partial\xi} = i\frac{\beta_2}{2}\frac{\partial^2\mathcal{A}(\xi,\tau)}{\partial\tau^2}} \tag{2.3}$$

Parabolic equations 2.2 and 2.3 apparently similar and can be written in an unified form of diffusion equation [174]:

$$\frac{\partial u}{\partial t} = c\nabla^2 u$$

with a well-known solution

$$u(x,y,t) = \frac{1}{(2\pi)^2}\int\int_{\infty}^{\infty}\mathcal{F}[u(x,y,0)]e^{-c(k_x^2+k_y^2)}e^{i(k_x x+k_y y)}dk_x dk_y \tag{2.4}$$

Appropriate change of variables in the expression 2.4 immediately gives the general solution for the equations 2.2 and 2.3.

2.2.1.2 Thin lens - time lens analogy

Another irreplaceable component of temporal imaging is the *Time Lens*. The main principle is to impose the quadratic phase in time on the dispersed signal under investigation, which is similar to what is happening with light beam in transverse spatial direction after passing a lens [182]. Indeed, it is easy to show that the phase transformation in transverse direction induced by a thin spherical lens under the paraxial approximation is:

$$E'(x,y) = E(x,y)exp[-i\frac{k}{2f}(x^2+y^2)] \tag{2.5}$$

where f is the focal length, n - refractive index and k is the wave number.

As it is depicted in the Fig. 2.2 as a temporal analogue of a thin lens could be a nonlinear interaction (usually via three or four-wave mixing) with a chirped pulse. The appropriate chirp can be induced using a dispersive element like compressor or linear propagation inside a fiber in the presence

of second-order dispersion, which gives the temporal quadratic phase. In the time domain, an expression for the quadratic phase can be written as follows [165]:

$$A'(\tau) = A(\tau)exp[-i\tau^2/2\phi_2^f] \tag{2.6}$$

where ϕ_2^f proportional to the chirp of the pump.

Indeed, the result of nonlinear interaction is a multiplication of complex field envelopes or its conjugated versions, so the phase term of the pump will be 'transmitted' to the resulting signal. For example, let's consider the sum frequency generation (SFG) precess. Further, we assume that signal has the frequency ω_1, the pump - ω_2 and the result of SFG $\omega_3 = \omega_1 + \omega_2$. We assume that the pump in this case is undepleted. The equations for the field envelopes evolution (along z axis inside the crystal) can be written as follows [183]:

$$\frac{dA_1}{dz} = K_1 A_3 e^{-i\Delta kz} \tag{2.7}$$

$$\frac{dA_3}{dz} = K_3 A_1 e^{+i\Delta kz} \tag{2.8}$$

where Δk is the wave vector mismatch and coefficients

$$K_1 = \frac{2i\omega_1^2 d_{deff}}{k_1 c^2} A_2^*,\ K_3 = \frac{2i\omega_3^2 d_{deff}}{k_3 c^2} A_2$$

here d_{eff} denotes the nonlinear coefficient of the crystal.

Assuming that the wave vector mismatch equals to zero and no signal at the frequency ω_3 was injected in the beginning, we immediately get the solution of the amplitude A_3:

$$A_3(z) = iA_1(0)e^{i\psi_2} R \sin(\kappa z) \tag{2.9}$$

where R is a coefficient depended from $\omega_{1,3}$, $\kappa^2 = -K_1 K_3$ and ψ_2 is the *phase* of the pump. Thus the quadratic phase of the pump will be induced on the resulting signal.

Thereby, a nonlinear interaction (such as SFG) of the signal with a linearly chirped pump can serve as a temporal analogue of the lens.

2.2.1.3 Spatial and temporal imaging with a lens

Using this direct analogy and basic knowledge of geometrical optics one can easily compress or stretch a signal under investigation, i.e. provide *temporal imaging*. The simplest way to provide imaging is to use a lens. The analogy is direct (see Fig. 2.3) and the obtained magnification can be computed simply by laws of geometrical optics.

Let's recall some results of geometrical optics. For a thin lens (like one depicted in the Fig. 2.4) the following imaging equation is valid:

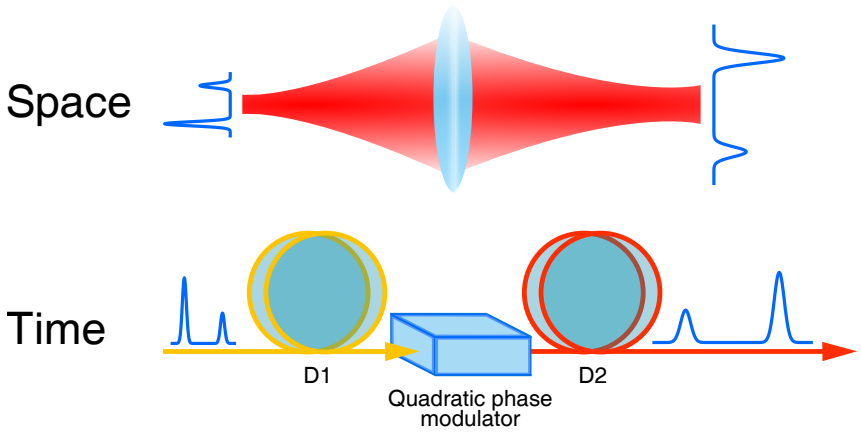

FIGURE 2.3: Image formation with space and time lenses. D1 and D2 are dispersions of different values and signs.

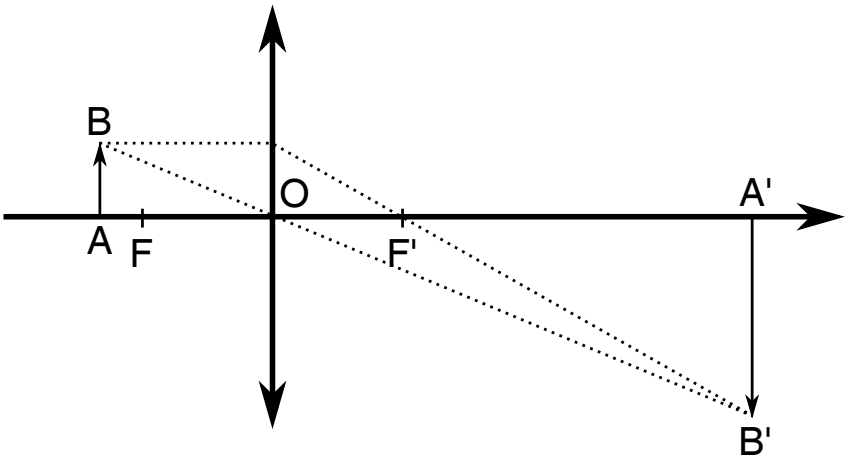

FIGURE 2.4: Image formation with a thin lens. The case of magnification.

$$\frac{1}{\overline{\overline{OA'}}} - \frac{1}{\overline{\overline{OA}}} = \frac{1}{\overline{\overline{f}}} \tag{2.10}$$

The fulfilment of this equation guaranties observation of a sharp image.

The ration of distance from object to lens and from image to lens gives *magnification*:

$$M = \frac{\overline{A'B'}}{\overline{AB}} = \frac{-\overline{OA'}}{\overline{OA}} \tag{2.11}$$

By analogy we can construct a *magnifying temporal lens*. The equivalent temporal domain equation is [174]:

$$\frac{1}{\phi_2^{in}} + \frac{1}{\phi_2^{out}} = \frac{1}{\phi_2^{f}} \tag{2.12}$$

Here ϕ_2^{in}, ϕ_2^{out} are the input and output group delay dispersions. $\phi_2 = \beta_2 \xi_d$, were ξ_d is analogue of propagation distance in the free space and β_2 is the second order dispersion coefficient. Therefore, ξ_d^{in} is smaller than ξ_d^{out} to obtain magnification).

The ratio between distances from object to lens and from image to lens gives *magnification*:

$$M = -\frac{\phi_2^{out}}{\phi_2^{in}} \tag{2.13}$$

2.2.1.4 Time Lens

A tool, based on this duality, is called Time Lens. The Time Lens today is a widely-spread optical device for ultrafast measurements. After the first demonstration [165] this method experienced significant technical improvements. Indeed, an experimental realisation of the Time Lens presented in [173] had 300 fs resolution with 103 magnification factor and 5.7 ps temporal window. After few years of development, this tool was significantly improved and simplified. It was found that silicon chip can be used as an efficient nonlinear medium for the broadband four-wave mixing process [184–187]. Also, a possibility of simple external triggering was proposed [188].

All these improvements led to the efficient commercialisation of the Time Lens. Today it is as simple-to-use equipment with a pigtailed input and output. In order to stay fibered, the 4-wave mixing is used for the nonlinear interaction. Commercial Time Lens provides 0.3-1 ps temporal resolution and magnification factor 40-500 depending on the chosen temporal window (30 - 500 ps) [189].

The Time Lens was used for investigation of different physical problems. For example in [90] a Time Lens having a resolution $\sim 300fs$ was used for real-time measurements of ultrafast coherent structures at the nonlinear stage of modulation instability.

2.2.1.5 Spatial and temporal imaging with a microscope

Scheme of imaging with a microscope is shown in the Fig. 2.5. As one can see, here the modern version which requires observation with a camera is depicted. The main difference between imaging with this microscope and the classical one is that the output beam is not collimated, therefore cannot be observed with the eye. This configuration implies that the object has to be placed exactly in the focal plane of the first lens (objective) and the image will be formed in the focus of the second (tube) lens.

The temporal analogue of the microscope can be realized in different ways. Very often the term Time Microscope is used as a reference to a Time Lens [173]. However, it is possible to construct a very efficient temporal analogue of a real spatial microscope.

As well as the spatial microscope, temporal one is made of two (temporal) lenses. Equivalent of the tube lens is the conventional Time Lens presented in the previous section. However, in this case, the input group delay dispersion of the signal (equivalent to the free space propagation object-lens) must have exactly the same absolute value but opposite sign as the one of the pump. This means that the object is in the 'focal plane' of the Time Lens. This operation can be also considered as time-to-frequency conversion.

Role of the tube lens in the Time Microscope plays a single-shot spectrometer. Indeed, the single-shot spectrometer provides the Fourier transformation of initial signal. As it is known, spatial Fourier transform of the object can be observed in the focal plane of a focusing lens [182]. Let's consider a collimated monochromatic wave with a transverse profile $E(x,y)$. As it was mentioned before (Eq. 2.5), after passing a lens the transverse profile obtains the quadratic phase $E'(x,y) = E(x,y)exp[-i\frac{k}{2f}(x^2+y^2)]$. Next ,we apply the Fresnel diffraction formula in order to find the amplitude distribution in the focal plane ($z = f$). Assuming that the amplitude equals zero everywhere except the lens area, we obtain:

$$E'_f(x,y) = \frac{exp\left[i\frac{k}{2f}(x^2+y^2)\right]}{i\lambda f} \times \iint_{-\infty}^{+\infty} E(u,v)exp\left[-i\frac{2\pi}{\lambda f}(ux+vy)\right] \mathrm{d}u\mathrm{d}v \tag{2.14}$$

here k is the wave vector and λ - wavelength.

One can immediately see that this is exactly the 2-D Fourier transform of the initial profile of the field amplitude $E(x,y)$ [1]. Therefore the spectrum resolving devises like the diffraction grating can be used in order to represent the temporal analogue of the tube lens.

In this way, the spectrally encoded time is resolved in space or in time depending on the type of spectrometer.

[1] Remarkably, the expression 2.14 can be also considered as a Fraunhofer diffraction pattern of the initial signal.

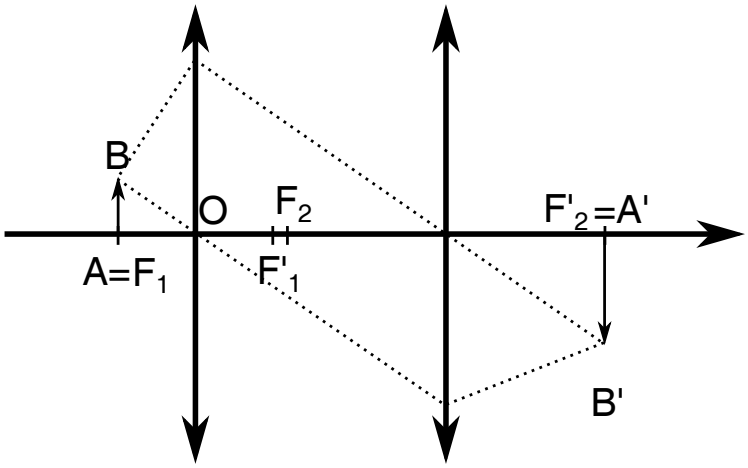

FIGURE 2.5: Image formation with a microscope.

Like it will be shown later, Time Microscope enables one to record in single-shot random optical signals with a window of the order of 40 ps, resolution of two hundreds of fs and the dynamical range up to 40 dB.

2.2.2 Experimental realization of the Time Microscope

The Time-Microscope (TM) setup (see Fig. 2.6 for the detailed scheme) explained in this section was used in [190] to provide direct observations of a partially-coherent waves dynamics in an optical fiber. The TM provided 1-D temporal snapshots of the signal's power profile at the output of the fiber with resolution[2] $\approx 250\ fs$, over the window of $\sim 30\ ps$. Possible dynamical range is up to 40 dB. As explained in the previous part, the Time Microscope consists of two parts: Time Lens and system similar to a single-shot spectrometer. The operating principle can be also understood from another point of view: after passing the Time Lens temporal power profile is encoded in a frequency profile, then the frequency profile is resolved with a diffraction grating, which corresponds to frequency to angle conversion, and finally spatially resolved profile is recorded with a camera.

Since this configuration of the TM (Fig. 2.6) maps temporal dynamics of a signal into space, it is not reasonable to speak about magnifications factor.

2.2.2.1 Pump laser

The 800 nm pump pulses are emitted by an amplified Titanium-Sapphire laser (Spectra Physics Spitfire, 2 mJ, 40 fs, a spectral bandwidth of 25 nm), operated at 500 Hz. The pulse amplification technology is close to the one proposed in the article [191]. Only 100 nJ are typically used here. For inducing (normal) dispersion on the 800 nm pulses we simply adjusted the amplifier's output compressor. It is possible due to the fact, that before the amplification, pump is highly stretched with some normal dispersion. In order to induce the required quadratic phase chirp for the TM, it is just not

[2]The problematic of the resolution determination will be explained in the section 2.2.6.

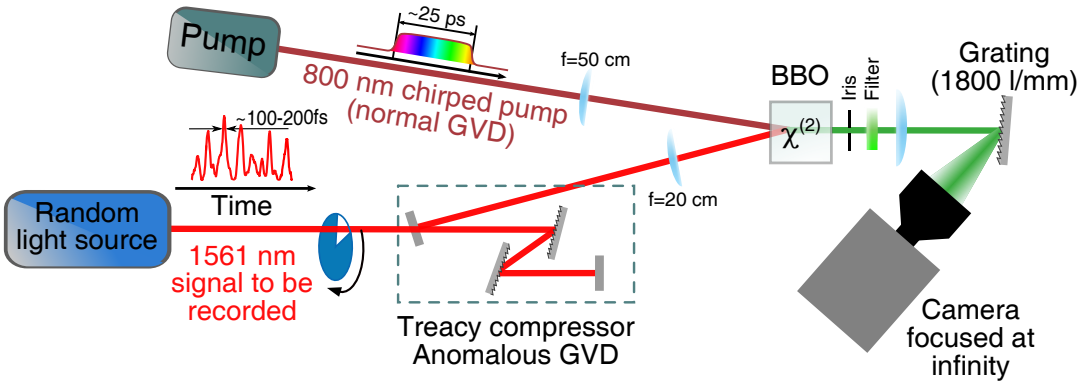

FIGURE 2.6: Scheme of the Time Microscope.

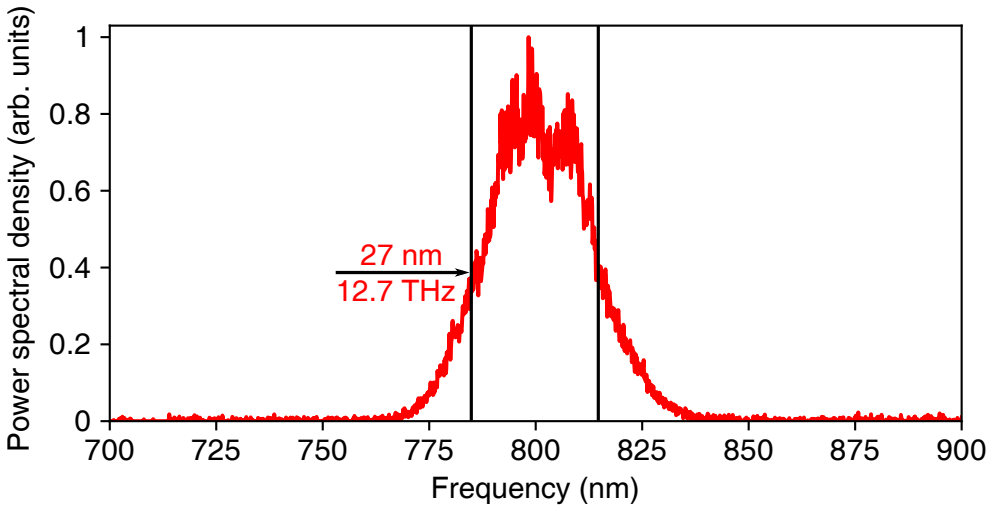

FIGURE 2.7: Spectrum of the pump laser after amplification.

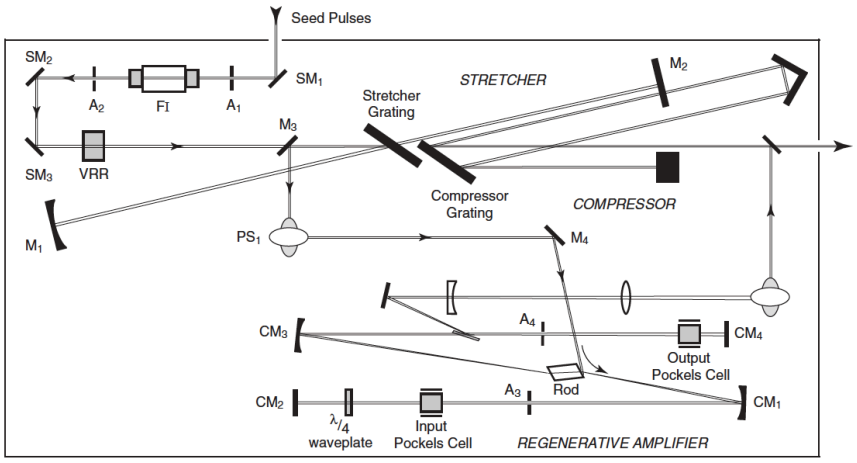

FIGURE 2.8: Schematic illustration of the short pulse amplifier. Picture is taken from the user manual of the Spectra Physics Spitfire amplifier.

fully compensated. This is done by moving the roof mirror in the compressor (right top of the schema Fig. 2.8) The dispersion was fixed to 0.23 ps^2, leading to chirped pulses duration about 20 ps. The beam at the output of the amplifier has $\approx$ 90% of ellipticity and 9 mm diameter (by the $1/e^2$ definition) according to the laser specifications. Finally, the spectral width is 12.7 THz as can be seen in the Fig. 2.7 [3].

2.2.2.2 Home-made femtosecond fiber laser

The Time Lens resolution was estimated using a home-made all-fiber femtosecond laser [4] (see Fig. 2.9). The laser emits $\sim$ 70 fs pulses at 1560 nm central wavelength with the 35,9 MHz repetition rate. The laser's loop resonator is passively mode-locked employing the effect of nonlinear polarization rotation (similar to the one explained in the article [193]). Spectral width 24.9 nm. At this stage, we didn't achieve synchronization, so resolution (section 2.2.4) estimates require additional step of searching for the frames which contain the information.

2.2.2.3 Beam geometry

In order to provide efficient nonlinear interaction, both 800 nm and 1550 nm beams should have the highest possible intensity (limited by a crystal damage threshold) inside the nonlinear crystal, as well as Rayleigh lengths

[3] Precise measurements of the pump spectrum helped us to detect and solve a common problem of the double pulse emission

[4] The laser is made by prof. Serge Bielawski and M.S. Mickael Cavagna as a project for masters thesis [192]

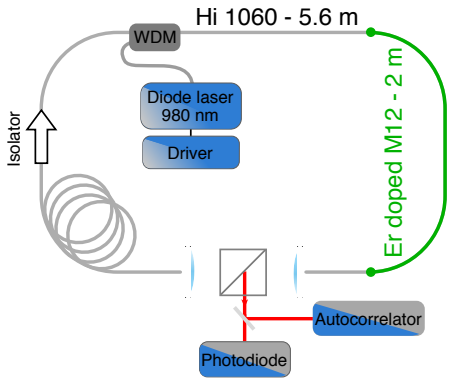

FIGURE 2.9: Scheme of the home-made fiber femtosecond laser.

have to be of the order of the crystal length [183]. Beams overlapping distance inside the crystal have to be larger than the thickness of the crystal. In the presented case this distance is estimated as $0.7\,mm$. Also, beam size has to be optimised in order to be less sensitive to the aberrations of the system. Moreover, the focal distance of the focusing lenses before crystal cannot be too small, because the angle between signal and pump beams is around 12.5^o. Finally, vertical 528 nm signal size on the sCMOS (scientific complementary metal–oxide–semiconductor) camera have to be of the order of one pixel, which will increase the signal-to-noise ratio. The optimal beam waist diameter $D = 2w_0$ have to be found in the region defined by all the limitations presented above.

According to the ray transfer matrix analysis for the Gaussian beam complex parameter $\frac{1}{q} = \frac{1}{R} - \frac{i\lambda_0}{\pi w^2}$:

$$\begin{pmatrix} q_2 \\ 1 \end{pmatrix} = k \begin{pmatrix} A & B \\ C & D \end{pmatrix} \begin{pmatrix} q_1 \\ 1 \end{pmatrix} \Rightarrow q_2 = \frac{Aq_1 + B}{Cq_1 + D}$$

where the ABCD matrix for a thin lens and free space propagation is given by

$$\begin{pmatrix} A & B \\ C & D \end{pmatrix} = \begin{pmatrix} 1 & d \\ 0 & 1 \end{pmatrix} \begin{pmatrix} 1 & 0 \\ -\frac{1}{f} & 1 \end{pmatrix} = \begin{pmatrix} 1 - \frac{d}{f} & d \\ -\frac{1}{f} & 1 \end{pmatrix}$$

This gives after all necessary transformations expression for the minimum of the waist:

$$w_{min} \approx \frac{f\lambda}{\pi w_0} \tag{2.15}$$

Here w_0 is an initial waist, f - focal distance and λ - light wavelength.

Using the formula 2.15 we can estimate the 1550 nm beam diameter after the collimation part. As it was mentioned before, we used a molded aspheric lens with maximal available focal distance (f=11 mm) having numerical aperture larger than the one of the fiber (0.25-0.3). Hence, the beam diameter after collimation is approximately 2.6 mm. In order to decrease the waist size inside the crystal, beam was first magnified 4 times with a telescope made by a plano-concave f=-25 mm and a plano-convex f=100 mm lenses. The focal distance of the lens before the nonlinear crystal is chosen to be 200 mm

(see Fig. 2.6). This provides the comfortable alignment without blocking the pump beam. Therefore, the resulting 1550 nm beam diameter inside the nonlinear crystal was 38 μm.

The output 800 nm beam diameter coming out of the amplifier is estimated as 9 mm. Beam diameter inside the crystal has to be of the same order that one of the 1550 nm beam. Hence, no magnification is needed for the pump beam, as it is shown in the Fig. 2.6. The beam focused with f=50 cm lens had a waist diameter $w_{min} = 56\,\mu m$. This could be reduced by choosing a lens with shorter focal distance, however, since we used less than one percent of available pump power the decision was made in favour of larger waist for two reasons: comfortable alignment and larger overlapping area inside the crystal.

2.2.2.4 Treacy compressor

Theory of double grating compressor is well developed and here we will not derive it from the first principles, but rather use results that can be found in the works of E. B. Treacy [194, 195] or in many books (e.g. [21]).

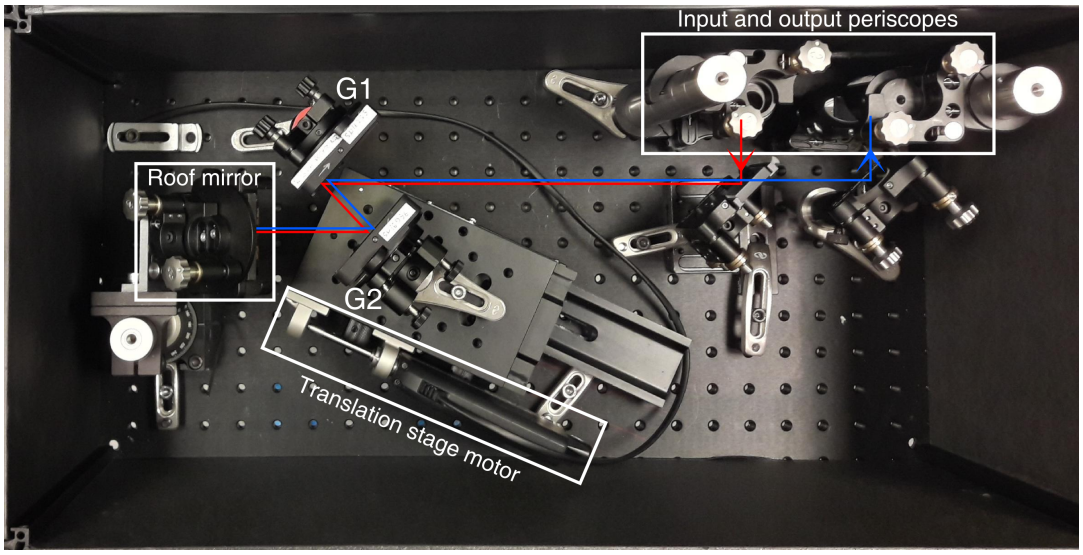

FIGURE 2.10: Photography of the Treacy compressor. Input beam is depicted by red, output by blue. Beam (red) enters the compressor and reaches necessary hight by the first periscope. After passing through the grating pair (G1 and G2) beam changes its hight on the roof mirror. Reflected beam (blue) path back the grating pair and leaves the compressor by another periscope. Dispersion is controlled by adjusting the distance between the compressor with the high precision motorized translation stage.

In our case the configuration is following (on the photo Fig. 2.10): beam entering the compressor (red line) is dispersed at order one of a blazed diffraction grating Thorlabs GR50-0616 [5] (G1, G2) with 600 grooves per millimeter. The angle between the incident beam and the first grating is 40°. After the

[5]Further, these gratings will be replaced by ones less sensitive to the thermal effects. For details see appendix A

second grating (G2, the same parameters as G1), which is strictly parallel to the first one, therefore the beam is collimated. Distance between gratings is fixed to 42 mm. The induced second-order dispersion grows linearly with the distance (see equation 2.16) It can be changed using a high precision motorized translation stage equipped with Newport CONEX- LTA-HS DC servo motor and SMC100 Single Axis Motion Controller. Detailed explanation of the distance adjustment will be given in the section 2.2.4. Beam, reflected by the roof mirror has the same angle, but different height (depicted by blue). It is done to separate the initial signal and the chirped one. Then beam passes all the way back and leaves the compressor by another periscope.

The light polarization has to be perpendicular to the grating grooves The compressor is designed in such a way that light polarization (our case horizontal) is perpendicular to the diffraction grating grooves which corresponds to the maximum efficiency according to the grating's specifications. Polarization of the light before the compressor is horizontal (due to the PBS cube), grooves are vertical to the table. Hence, periscopes have to be designed in the way to not change the light polarization.

Another important experimental aspect is the possibility to have thermal lensing effect on the diffraction gratings inherent to use of the high power signals (this is necessary to keep optimal signal-to-noise ratio). Illustration of this could be found in the A. In order to reduce the effect of thermal lensing, we have installed a rotating chopper, synchronized with the Pockels cell inside the resonator of pump amplifier (bottom part of the Fig. 2.8). More detailed explanation of the synchronization of laser, camera and chopper will be done further in this section.

The setup shown in the Fig. 2.11 introduces a different delay for different frequencies of the signal. The value of the second order phase delay is given by [6]:

$$\phi_2 = \frac{-8\pi^2 c d_0}{\omega_0^3 \Lambda^2 \cos^3(\theta_{r0})} \approx -0.23 ps^2 \tag{2.16}$$

Here θ_{r0} is the angle angle between reflected beam and normal to the grating surface (Fig. 2.11) for the central frequency $\omega_0 = 2\pi c/\lambda_0$, where λ_0 is the central wavelength and c is the speed of light. Relation between $\theta_r(\lambda)$ and θ_i can be found using the simple grating equation $\sin(\theta_i) - \sin(\theta_r) = m\lambda_0/\Lambda$. As it was mentioned before $\theta_i = 40^\circ$. d_0 is the distance between gratings and Λ - grooves' period.

2.2.2.5 Sum frequency generation

Quadratic temporal phase is provided to the signal by noncolinear sum frequency generation (SFG) in a $\chi^{(2)}$ beta barium borate (BBO) crystal. The BBO crystal has 8 mm length and is cut for noncollinear type-I SFG ($\theta = 24.2^\circ$,

[6] The value of ϕ_2 below is given for the configuration of TM presented in the article [190]. Also, I would like to point out that the value of dispersion of the 1550 nm signal is exactly opposite to one of the 800 nm pump pulse as it is required.

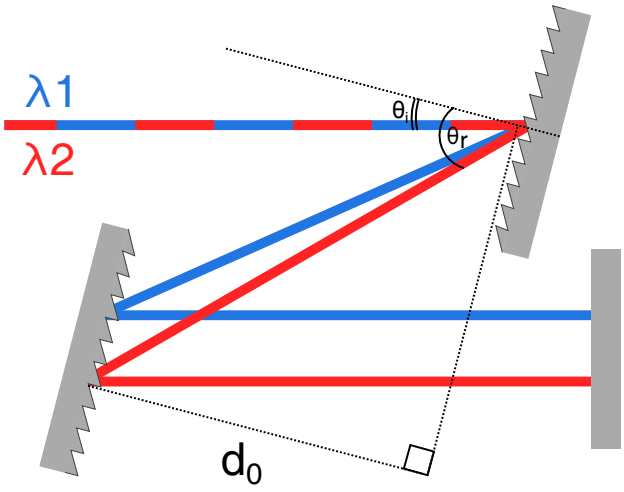

FIGURE 2.11: Scheme of two different monochromatic beams passing through the double-path grating compressor. The beams have close wavelengths λ_1 and λ_2. Here θ_i is initial angle 40°, $\theta_r(\lambda)$ - angle between reflected beam and normal to the grating surface.

$\phi = 90°$, external angle between pump and signal = 12.5°). The BBO is a negative crystal [196] and hence the type I phase-matching scheme is ordinary-ordinary-extraordinary beams' polarizations (ooe) [197]. The crystal's main plain is perpendicular to the optical table, hence the 800 *nm* and 1550 *nm* beams were horizontally polarized, the resulting 528 *nm* beam is vertically polarized. The effective interaction distance corresponding to the spatial walk-off of the 528 *nm* signal (since the 800 *nm* pump and 1550 *nm* signal are polarized along the ordinary axis the Poynting vector coincides with wave vector *k*) is estimated to 0.9 *mm*, with overlapping length 0.7 *mm*. The temperature is maintained at $\approx 23°C$. The crystal was mounted on a rotatable support, which allows to correct a posteriori the possible alignment mismatch.

2.2.2.6 Single-shot spectrometer

The second "lens" of the TM is formed by the collimating lens (f=20 *cm*) after the nonlinear crystal, diffraction grating and sCMOS camera focused at infinity. This arrangement plays a role of a single shot spectrometer, which helps to convert frequency into space (time is encoded into the frequency in the previous step). The camera is a sCMOS Hamamatsu Orca flash 4.0 V2 (C11440-22CU), equipped with a 60 *mm* lens (Nikkor Micro 60*mm* f/2.8 AF-D). Blazed diffraction grating Thorlabs GR50-1850 has 1800 grooves/mm and operates at the first order. In order to block the 1550 *nm* and 800 *nm* beams iris pinhole and 40-*nm* bandpass filter around 531 *nm* (FF01 531/40-25 from Semrock) were installed right after the crystal.

Unfortunately, in the arrangement presented in the article [190] we didn't take into the account that the 528 *nm* beam is polarized vertically, along with

the grating's grooves. This decreases the grating efficiency by 30%. In future realizations it is going to be improved.

2.2.2.7 Camera specifications, settings and triggering

Digital sCMOS camera we worked with accepts an external triggering. The trigger (exactly the same as one for the chopper) has the same origin as one applied to the output Pockels cell inside the amplifier of the pump laser (see the 2.8). Electrical signals trigging the camera have to satisfy certain conditions: 3.3 V for voltage complementary metal-oxide-semiconductor level, electrical pulse duration > 1 μs (500 μs is used). In order to fulfil the conditions, trigger was regenerated by Stanford DS345 arbitrary waveform generator. In order to simplify triggering we have set a generator delay almost equal to the time between two pulses, hence the emission of a pulse triggers camera to take a snapshot of the next one.

Camera setting allows one to take shots continuously defining the exposure time by external trigger. This corresponds to so-called synchronous readout mode of the camera operating. At the shortest exposure time (2 ms) it reaches the highest possible performance [7]. The 528 nm signal was aligned at the center of the camera for two reasons: to decrease aberrations and to be able to decrease the vertical image size to 8 pixels (while horizontal is 2024 pixels). In this operating mode camera reads pixels information from center to edges and hence camera performance strongly depends on the vertical image size. Exposure time is 2 ms, which is exactly the time between two pump pulses, quantum efficiency is 80% at the 528 nm, RMS dark noise is ≈ 2 electrons while the saturation value is 30,000 electrons, leading to a ≈ 40 dB dynamical range. Image output is 16-bit shade of gray depth saved in a binary format.

All the optical elements are coated for an appropriate wavelength.

2.2.3 Power profile reconstruction and typical window of measurements

Power profile reconstruction is a straightforward procedure in this configuration of the TM. However, output profile is multiplied by a Gaussian-like transfer function and, therefore, must be retrieved. This implies calculation of the averaged signal envelope for the full profile reconstruction.

Here we would like to demonstrate the power profile reconstruction taking as a example a signal of amplified spontaneous emission (ASE) source. The signal of ASE is stochastic and non-periodic, therefore it is appropriate for demonstration of the single-shot regime. The broad spectrum of ASE source was shrieked to 0.5 THz Gaussian-like shape using a programmable

[7] Here performance should be understood as number of shots per second with minimal exposure time and delay between two shots.

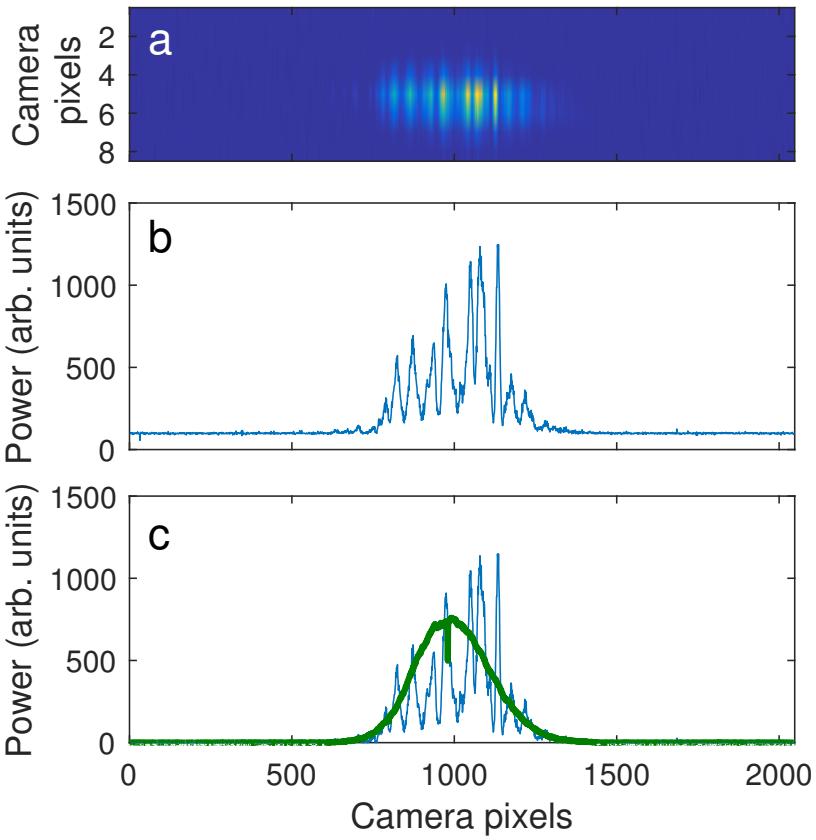

FIGURE 2.12: Power profile reconstruction of the ASE signal. (a) A typical snapshot obtained with a Time Microscope. (b) Line with a maximum overall power (the 5^{th} line in the picture a). (c) Average TM response envelope of a corresponding set (green) and the maximum overall power line with subtracted background.

optical filter. [8] We provided filtering in order to keep duration of the power fluctuations above the resolution of the TM (resolution estimates will be presented in the section 2.2.4).

The power profile is reconstructed by taking one horizontal line with maximum average power from each of recorded snapshot. In the case shown in the Fig. 2.12, it is the 5^{th} horizontal line Fig. 2.12a. The line is plotted in the Fig. 2.12b. Usually the position of the maximum average power line stays unchanged within one set of data.

The sCMOS camera has a non-zero background level which has to be subtracted (for example, it is visible on the Fig. 2.12b). In order to do this, we average the first 200 pixels (of 2048 pixels) of each snapshot over all the set (see Fig. 2.12). In this area the effect of the signal is negligible and, hence, we can evaluate the background level. Typically, the background value is 100 counts (one count corresponds to 0.46 electrons). Next, we compute a mean signal envelope which corresponds to Time Microscope response, by averaging the lines over a big set of snapshots, usually around 50,000. The envelope which corresponds to the chosen set of data is plotted by green in the Fig. 2.12c. It is visible that camera has a one-pixel defect around 1000^{th} pixel which systematically influences the recorded data. This defect will be corrected in further investigations. The background level has to be subtracted from the response envelope as well as each line separately (Fig. 2.12b). The real power profile (Fig. 2.12c) is the result of division of each line by the envelope and multiplication by an experimentally measured power 2.13a,b.

2.2.3.1 The window of measurements

The window of measurements has to be chosen according to an allowable signal-to-noise ratio in every particular case sine there are many independent factors affecting it: signal shot noise, noise of the amplifier, mechanical vibrations, camera readout noise etc. In our case, the window borders could be chosen as the full width at the $1/e^2$ of the maximum of the envelope (this rule is obtained empirically). In fact, this corresponds to the value $\approx$ 472 pixels (34 ps) [9], but the value was rounded to 423 (30 ps) window (see Fig. 2.13a,b).

2.2.4 Optimal resolution and compressor tuning

Overall Time Lens resolution depends on the accuracy of the relative second-order dispersion of the pump and the signal. Following the time-space analogy, it is equivalent to the precise object placing in the focal plane of the objective in order to obtain a sharp image.

Let's fix, for example, the dispersion of pump to $0.23ps^2$ (normal dispersion). This value leads to a window of measurements $\gtrsim$ 30 ps for the pump pulses of 40 fs at 800 nm central wavelength. Then, by changing distance between the two gratings in the Treacy compressor we adjust the dispersion

[8] More detailed information about the source and the filtering method can be found in the section 3.2.1 of the next chapter.

[9] The procedure of time calibration is explained further in the section 2.2.5.

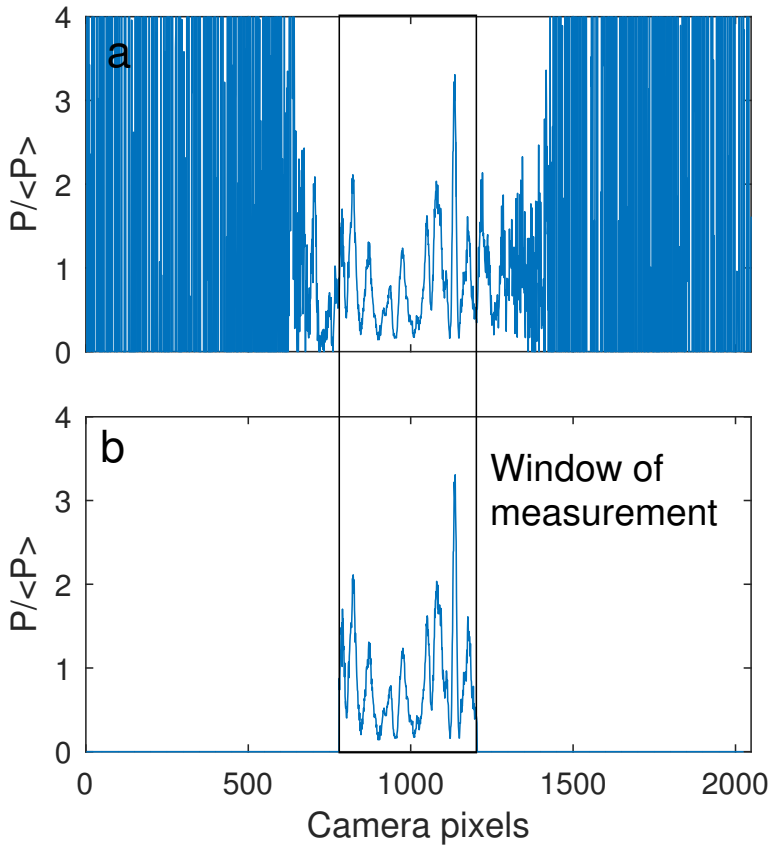

FIGURE 2.13: Window of measurements. (a) Result of division of the signal by the envelope the Fig. 2.12c. (b) Retrieved signal shrieked to the window of measurement. The window is chosen symmetrically from the maximum of the envelope.

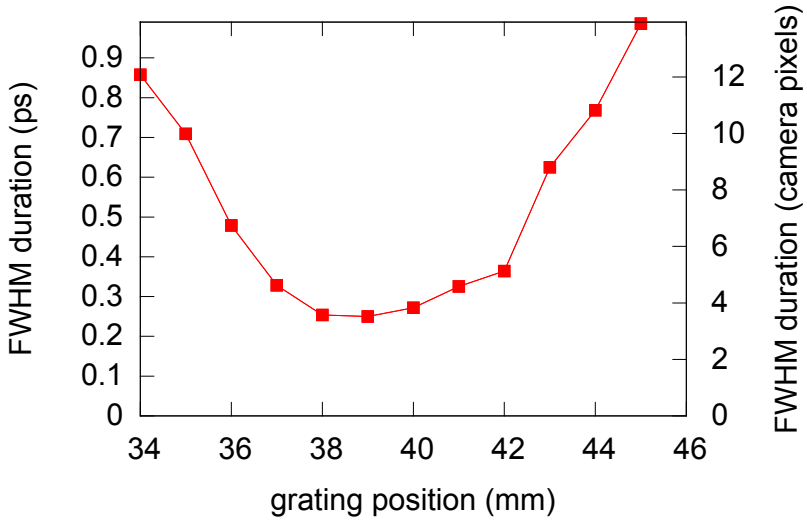

FIGURE 2.14: Resolution curve. Dependence of pulse durations measured with the TM as a functions of distance between grating in the 1560 nm Treacy compressor. Input pulses are produced home-made femtosecond laser presented in the section 2.2.2.2. Each value has been determined by fitting with a Gaussian-like function. The minimum value corresponds to 250 fs for FWHM.

added to the signal under investigation (a single 70 fs pulse in this case). Measuring the pulse width at the center of the frame [10] as a function of the distance between the gratings we can find the optimum (see Fig. 2.14). In the configuration presented in [190] the optimal distance between the compressor gratings was 39 mm. We will consider the narrowest pulse width measured at the optimal distance as the value of resolution.

All further calibrations and measurements are made with this distance fixed. Later in this chapter we will discuss more precisely how the presence of aberrations affects the estimates of the Time Microscope resolution.

The narrowest measured pulse at the optimal position will be considered as the resolution of the Time Microscope. One of the shortest pulses found in the experimental data is depicted on the Fig. 2.15. We used the home-made femtosecond fiber laser described in the section 2.2.2.2 as a source. The full width of this pulse at the half-maximum is approximately 250 fs. This value is taken as the resolution of the presented configuration of the Time Microscope.

2.2.5 Time calibration

Before starting any measurements the Time Microscope has to be calibrated. In order to complete the intensity profile retrieval, we have to calibrate the horizontal axis of the snapshots as time in picoseconds. This requires measurements of a signal with well-separated parts and a known time delay between them.

[10] It is important to provide pulse width measurements at the center, otherwise higher order dispersion terms can crucially affect the width.

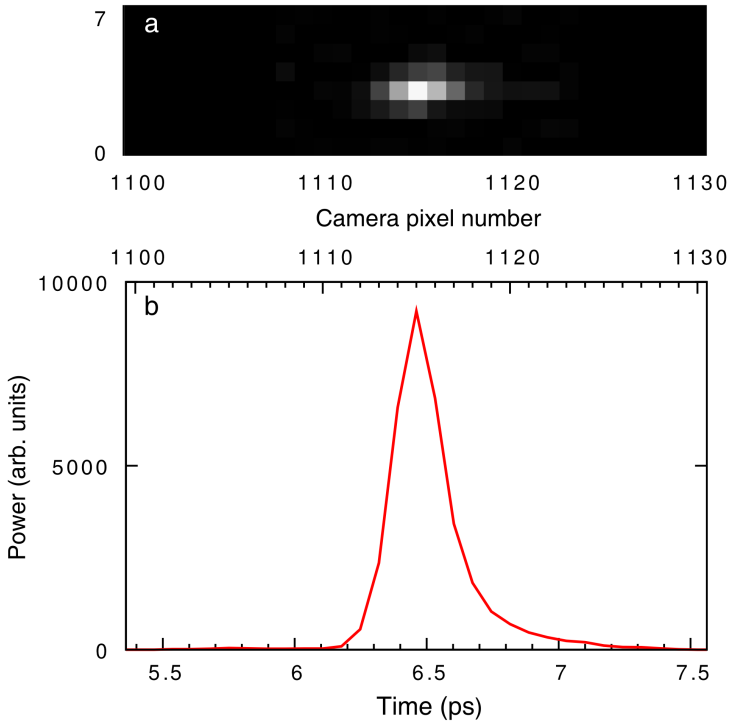

FIGURE 2.15: Experimental measurements of $\approx 70\ fs$ pulse with the TM. (a) Raw image recorded with the TM. (b) Pulse profile obtained making a cross-section of the image above.

In the experiment, we took a double pulse signal as a measure. We produced a series of two pulses by injecting a linearly polarized 700 fs pulse (tunable picosecond laser from Pritel) in a polarization maintaining fiber with the polarization direction of the pulse at 45 degrees with respect to the birefringent axes. Separation takes place because of the difference in refractive indexes of fiber's axis, and hence the group velocities. This means that the separation time will linearly increase with the length of a fiber. By placing a polarizer at the output of the fiber (also at 45 degrees with respect to the fiber's axes), we obtain two identically polarized pulses that are separated in time (see Fig. 2.16a). We measured independently the pulse delay (5.6 ps) by taking corresponding spectrum Fig. 2.16b and extracting the spectral distance between oscillations. Inverse of the distance equals to the delay:

$$|\mathcal{F}[S(t) + S(t - t_0)]|^2 = |\tilde{S}(\omega) + \tilde{S}(\omega)e^{-it_0\omega}|^2 = 2\tilde{S}^2(\omega)[1 + \cos(\omega t_0)]$$

Where $\mathcal{F}$ is the Fourier transform, $S(t)$ is a single pulse, $\tilde{S}(\omega)$ its Fourier domain representation and t_0 - the delay between two pulses.

Distance between 5 central peaks is 0.895 THz (depicted in Fig. 2.16b). This gives 0.179 THz per oscillation, consequently 5.59 ps of delay between pulses. Then we easily obtain the correspondence between pixel spacing and time. In the presented Time Microscope arrangement the scaling was 71 fs/pixel. It is applied to all results presented in the article [190].

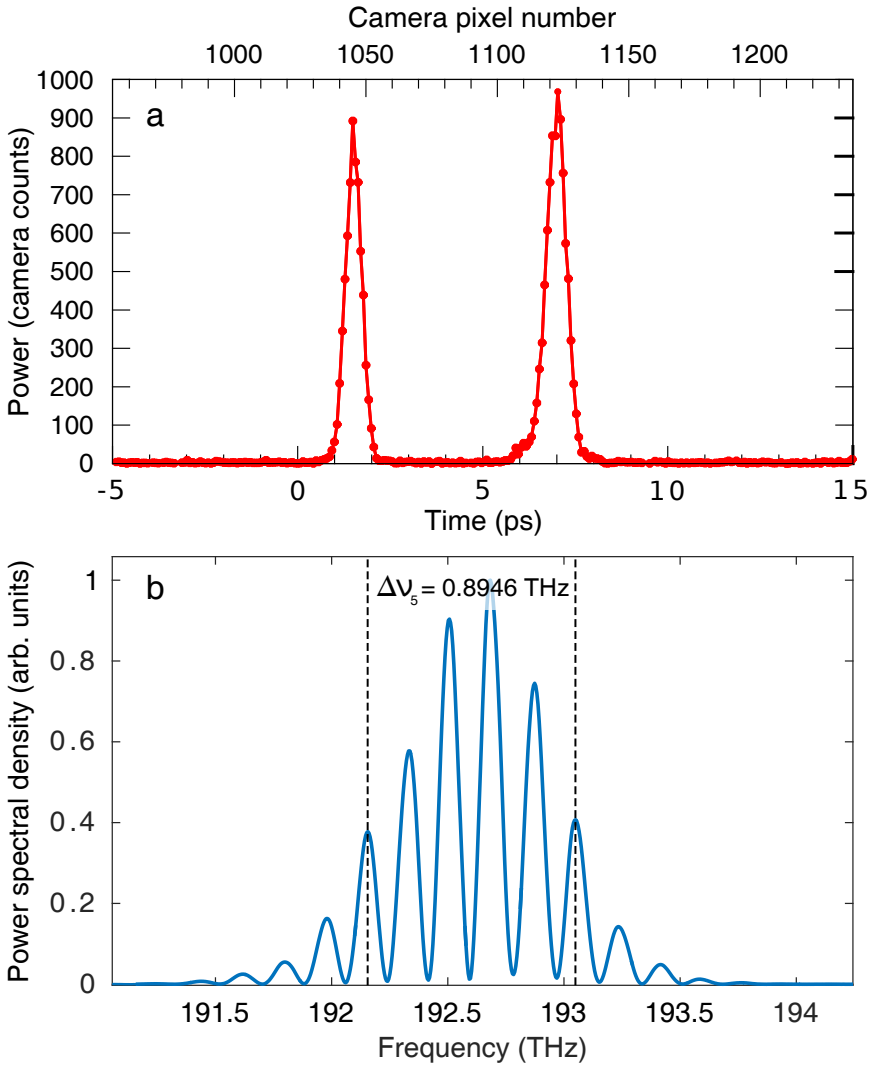

FIGURE 2.16: (a)Time microscope response to a series of two pulses (700 fs long) with known spacing. This gives the correspondence between pixel spacing and time: 71 $fs/pixel$. Note that the lower scale has been defined after this calibration has been made. (b) Corresponding spectrum. The spectral width between 5 peaks is 0.89 THz, which gives the spacing 5.6 ps

2.2.5.1 Numerical estimates of time-to-frequency conversion

We can confirm the time calibration result having time-to-frequency conversion formula. Indeed, knowing the exact configurations of the TM setup we can estimate distance in camera pixels between couple of pulses shown above. Analytical approach allows one to estimate the correspondence between time scale of initial signal and resulting frequency scale after passing through the first lens of the Time Microscope. This conversion ratio can be found as follows: let's consider first the ideal case when there is no 3^{rd} order dispersion. Hence, the effect of the ideal time microscope on the signal S(t) we express as follows:

$$\widehat{TM}[S(t),P(t)] = \mathcal{F}\left[\mathcal{F}^{-1}\left[\mathcal{F}[S(t)]e^{i\phi_2\omega^2}\right]\cdot\mathcal{F}^{-1}\left[\mathcal{F}[P(t)]e^{-i\phi_2\omega^2}\right]\right] \quad (2.17)$$

Where $S(t), P(t)$ it is the signal and pump amplitudes, $\mathcal{F}$ and $\mathcal{F}^{-1}$ are direct and inverse Fourier transformations. The equation 2.17 can be easily understood following the setup 2.6. The first Fourier transform operation corresponds to the diffraction grating before the camera which provides the angular FT. Then there is a multiplication of two terms of the form $\mathcal{F}^{-1}\left[\mathcal{F}[X(t)]e^{i\pm\phi_2\omega^2}\right]$ where X(t) is the signal or the pump function: S(t) or P(t). This is a representation of the sum frequency generation process with the linearly chirped signal of pump. The chirp has the same absolute value - ϕ_2, but of different signs. This is the result of the Treacy compressors tuning.

Applying the convolution theorem we immediately obtain:

$$\widehat{TM}[S(t),P(t)] = \sqrt{2\pi}\mathcal{F}[S(t)]e^{i\phi_2\omega^2/2} * \mathcal{F}[P(t)]e^{-i\phi_2\omega^2}$$

$$= \sqrt{2\pi}\int_{-\infty}^{\infty}\mathcal{F}[S(t)](\omega-\tau)e^{i\phi_2(\omega-\tau)^2}\mathcal{F}[P(t)](\tau)e^{-i\phi_2\tau^2/2}d\tau$$

For simplicity of the calculations, let's now assume a shifted Dirac delta function $\delta(t-t_0)$ as a signal. Hence, the Fourier transform of the signal according to the shift theorem is $\frac{1}{\sqrt{2\pi}}e^{-i\omega t_0}$

After necessary transformations:

$$\int_{-\infty}^{\infty} e^{-i(\omega-\tau)t_0}e^{i\phi_2(\omega-\tau)^2/2}\mathcal{F}[P(t)](\tau)e^{-i\phi_2\tau^2/2}d\tau$$

$$= e^{i\phi_2\omega^2/2-i\omega t_0}\int_{-\infty}^{\infty}\mathcal{F}[P(t)](\tau)e^{i(t_0+\phi_2\omega)\tau}d\tau$$

As one can notice this exactly corresponds to the inverse Fourier transform of the $\mathcal{F}[P(t)](\tau)$ with respect to $t_0+\phi_2\omega$. Hence, the final result doesn't depend on the pump profile and just equals to:

$$\widehat{TM}[\delta(t-t_0),P(t)] = e^{i\phi_2\omega^2/2-i\omega t_0}P(t_0+\phi_2\omega)$$

Hence, the wanted time to frequency conversion coefficient is just

$$\frac{\nu}{t_0} = \frac{1}{2\pi\phi_2} \approx 0.7\,THz/ps \tag{2.18}$$

As one can notice, assumption of the delta-like signal leads to the result which doesn't require any particular assumption of pump function P, except maybe its representability by a Fourier integral.

2.2.6 Aberrations analysis

Despite of the wide range of arbitrary signals that could be measured by presented Time Microscope arrangement, it has its natural limitation. For

example, the finite width of the pump laser spectrum, as well as SFG bandwidth, limits the resolution and window of measuring. The low (typically 1%) efficiency of the SFG process limits the minimal measurable power [11].

Another significant limitation is the presence of the 3^{rd} order dispersion in the grating stretchers and compressors. This effect leads to deviation of the phase profile from an ideal quadratic form. Following the space-time analogy, this can be considered as aberrations of a Time Lens [173, 175, 176, 198]. Higher order dispersion induces asymmetry to measured pulses and significantly stretches them temporally [199], while for the pump it imposes a distortion similar to the one in classical optics. That is why point spread function of the TM will start to increase after some optimum, while test pulses will be shorter and shorter. This makes measurements of pulses shorter than $\approx 150 - 200\ fs$ impossible with the presented setup.

Indeed, the effect of the compressor can be expressed [21]:

$$A_{out}(t) = \int_{-\infty}^{\infty} \mathcal{F}[A_{in}](\omega-\omega_0) exp\left[\frac{i}{2}\phi_2(\omega-\omega_0)^2 + \frac{i}{6}\phi_3(\omega-\omega_0)^3 + i\omega t\right] d\omega \tag{2.19}$$

Where $\mathcal{F}$ corresponds to the Fourier transformation, ϕ_2 is given in the section 2.2.2.4 and ϕ_3 is:

$$\phi_3 = \frac{24\pi^2 c d_0[1+\sin(\theta_{ro})\sin(\theta_i)]}{\omega_0^4 \Lambda^2 \cos^5(\theta_{ro})} \tag{2.20}$$

Here I use the same notations as in equation 2.16. In the presented configuration of Treacy compressor the value of ϕ_3 is $\sim 5 - 7\,10^{-4} ps^3$

It is possible to construct a simplified model of the TM, assuming the output signal is simply the multiplication of chirped signal and pump. To verify the effect of the higher order dispersion let's provide a numerical experiment assuming hyperbolic secant shapes for the amplitudes of the signal and pump pulses. As an initial condition, we take 7 pulses of 70 fs each separated by 5 ps (marked by blue in the Fig. 2.17a) and one 30 fs pulse for the pump (depicted by orange Fig. 2.17a - zoom). Next by adding the corresponding chirp both to signal (- 0.23 ps^2) and pump (+0.23 ps^2) we obtain in the direct space what is depicted on the Fig. 2.17b (colors are preserved). The last step is multiplication of pump and signal and providing the Fourier transformation of this (see Fig. 2.18a,e for the result). The effects shown in the Fig. 2.18(a-h) could be found also analytically assuming a Gaussian-like profiles of the pump and signal, it is going to be a subject of further investigations.

The ideal case, is depicted in the Fig. 2.18a,e. Here we used the value of 2^{nd} order dispersion -0.23 ps^2 for the signal and +0.23 ps^2 for the pump. This corresponds exactly to the value of dispersion induced by compressor in the article [190]. Picture Fig. 2.18a reveals the nature of signal's envelope, which

[11] One of the perspective directions of the Temporal Microscopy development is the replacement of sum frequency generation by difference frequency generation. This will allow one to provide ultrafast measurements and amplify the signal at the same time.

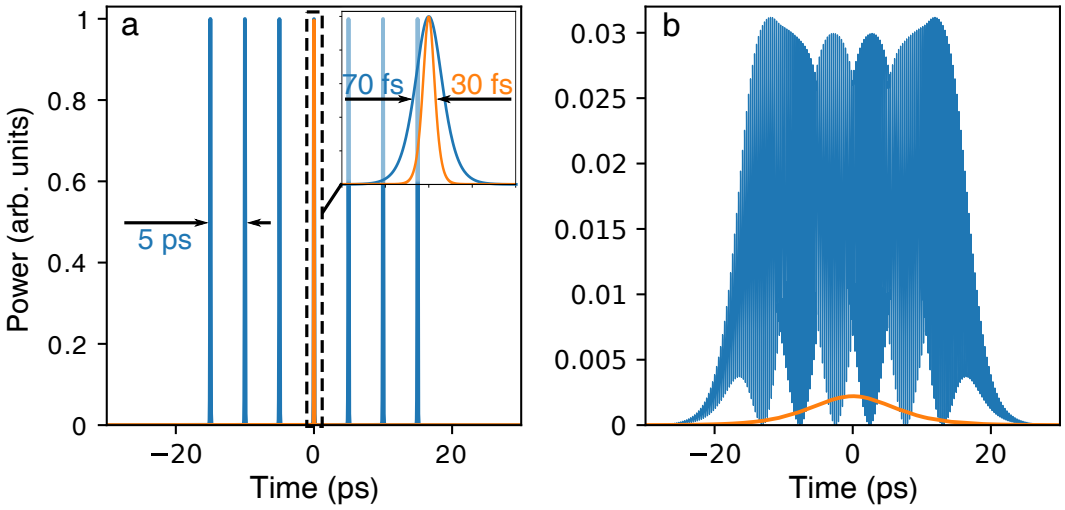

FIGURE 2.17: Simulation of the Time Microscope. (a) blue pulses of 70 fs are taken as initial signal. Orange pulse of 30 fs is the pump. (b) the same signals experienced dispersion: 0.23 ps^2 for the pump and the same but negative for the signal. Usage of these parameters simulates experiments described in the articles [190, 200]

TABLE 2.2: Details of numerical simulations for the Fig. 2.18

Picture on the plot 2.18	ϕ_2 signal, ps^2	ϕ_2 pump, ps^2	ϕ_3 signal, ps^3	ϕ_3 pump, ps^3
a	-0.23	0.23	0	0
b	-0.23	0.23	5.14×10^{-4}	0
c	-0.23	0.23	0	5.14×10^{-4}
d	-0.23	0.23	5.14×10^{-4}	5.14×10^{-4}

we extract during the power profile reconstruction. Summary of all values used in the simulation are presented in the Tab. 2.2.

I would like to stress here, that *the horizontal axis of all the plots presented in Fig 2.18 has the meaning of time*, since the time is encoded into the frequency in the presented TM arrangement.

Then we can understand the role of 3^{rd} order dispersion adding it systematically to the signal (Fig. 2.18b,f), pump (Fig. 2.18c,g) and both (Fig. 2.18d,h). The value of the 3^{rd} order dispersion is always the same 5.14×10^{-4} ps^3. It is computed with the formula 2.20 using the real experimental parameters. In the case when 3^{rd} order dispersion is added only to the signal we observe the classical picture of pulse broadening and presence of the oscillating tail, which approximately can be fitted by Airy function in the limit of large higher-order dispersion [21, 199]. Adding the 3^{rd} order dispersion to the pump only (Fig. 2.18c,g) we see that it contributes in similar way as in the previous case. However, the oscillations appear on the other side of the pulse (while the 3^{rd} dispersion has the same sign and absolute value as before) and have lower amplitude, also the pulse width is not the same in

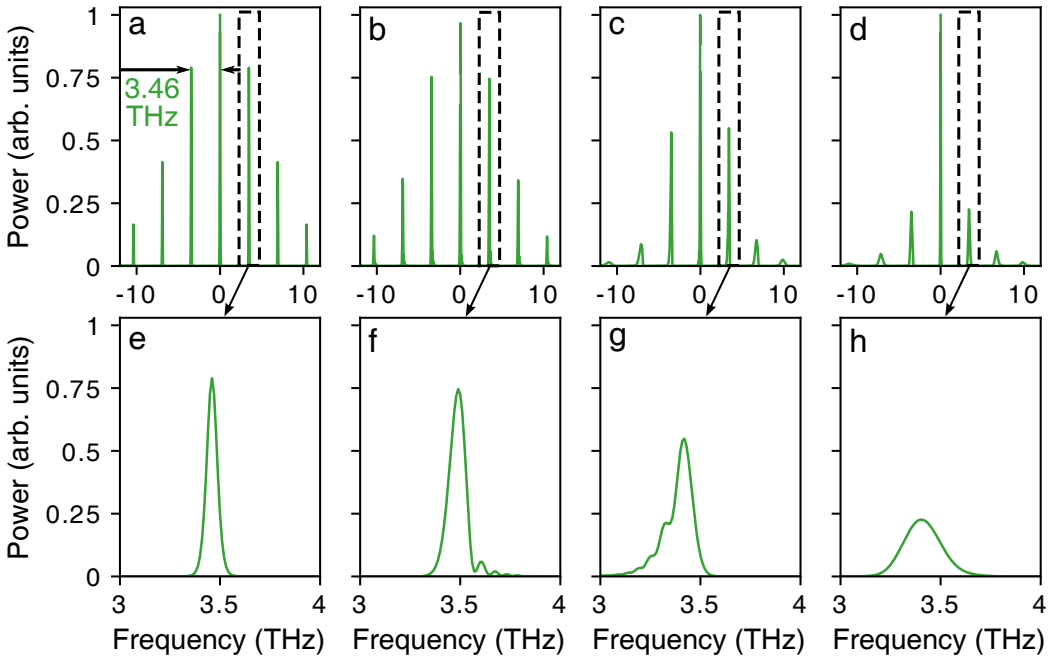

FIGURE 2.18: Simulation of the Time Microscope. Effect of the 3^{rd} order dispersion on the signal detection. (a,e) the ideal case, no higher order dispersion therm is added. (b,f) 3^{rd} order dispersion is added to the initial signal depicted by blue in the Fig. 2.17. (c,g) Show the effect when higher order dispersion term is added to the pump onlt. (d,h) depicts the case when 3^{rd} order dispersion is added to the signal and pump together. The value of the 3^{rd} order dispersion is always the same $5.14 \times 10^{-4}\ ps^3$. This value is computed with the formula 2.20.

different positions of the frame. This effect can be interpreted as an inhomogeneity in the time scale (time is slower in the edges of the frame than in the center). As a result, the pulses now are shifted from initial position, also they are significantly broader than before. In the case when the 3^{rd} order dispersion of the same sign and value is added to the signal and pump we observe no oscillations, but the broadening and shifting (temporal inhomogeneity) appear even more distinctly (Fig. 2.18d,h)

It is rather not trivial to estimate the effect of the 3^{rd} order dispersion on the pump pulses, because of the presence of a regenerative amplifier between stretcher and compressor, but in general we will suppose that the higher order dispersion is completely compensated when the pulse is fully compressed. Hence, the 3rd order dispersion of the chirped pulse can be estimated knowing the characteristics of the output compressor. Also, according to the Fig. 2.15 b from the section 2.2.4, where the TM snapshot of a 70 fs pulse is depicted, there is a direct similarity with the Fig. 2.18h.

The distance in the spectral lines according to the Fig. 2.18a is about 3.46 THz for 5 ps Fig. 2.17a, which gives $\approx 0.7\ THz/ps$ for the conversion ratio for the given Time Microscope configuration. This is consistent with the result of analytical estimations 2.18.

It is also verified that the role of the 4^{th} order dispersion is negligible.

2.2.6.1 Influence of aberrations on the resolution estimates

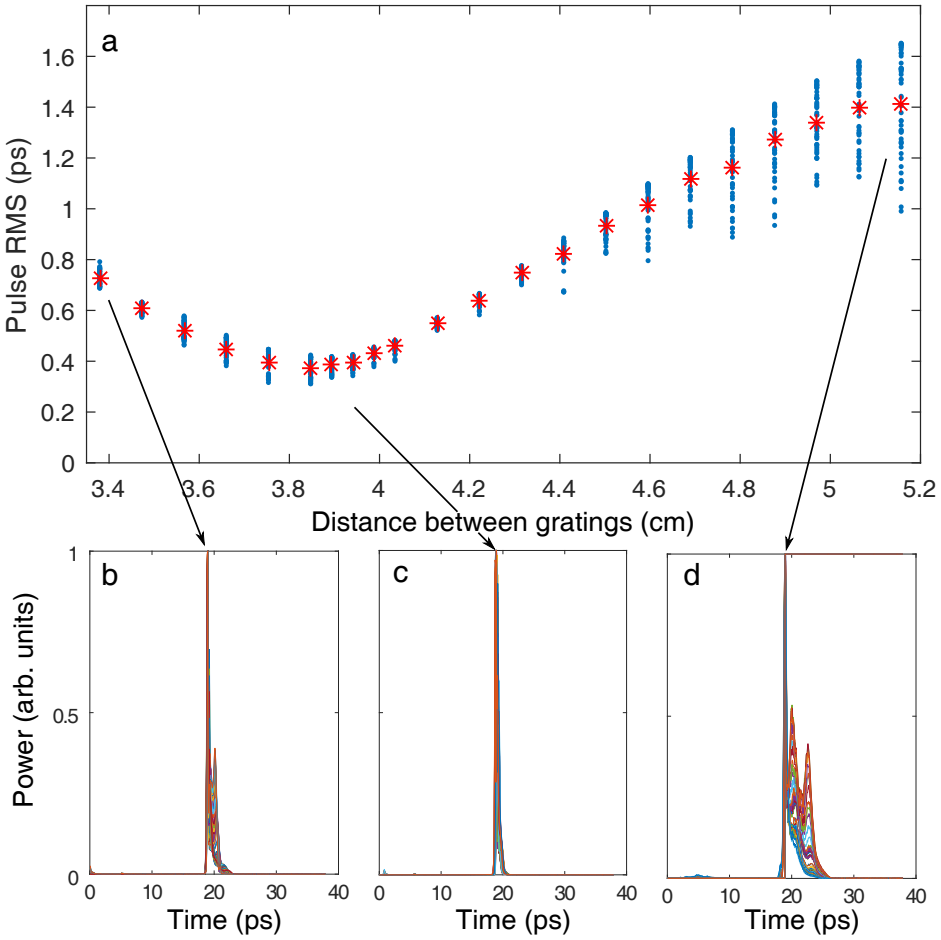

FIGURE 2.19: (a)Root mean square of the pulses measured with the Time Microscope [200], versus distance between grating planes in the 1560 nm compressor. Input pulses are produced by a 70 fs Erbium doped fiber-laser. The minimum value corresponds to $\sim$250 fs at the full with at the half maximum. Blue dots show every RMS value taken into the account, (b-d) show the superposition of several pulses measured at the given grating distance (b-3.4 cm, c-3.85 cm, d-5.2 cm).

The effect explained above influences directly the resolution of the Time Microscope. Therefore, the procedure presented in the section 2.2.4 has to to be verified taking into account the aberrations. Here we will provide numerical simulations similar to those presented before. Formulas 2.16, 2.20 allows to estimate dispersion of 2^{nd} and 3^{rd} orders at any distance between gratings. Hence, we are able to simulate numerically the compressor tuning and confirm estimates of the optimal distance between gratings. Results of this numerical experiment can be compared with real experimental data.

First, let's look more precisely on the data obtained experimentally. Taking the fixed area around the center of pulse, we can estimate the root mean square (RMS) value. It is not correct to fit such complex pulses with the Gaussian function, therefore our criterion is base on the RMS estimates. We

TABLE 2.3: Details of numerical simulations depicted in the Fig. 2.20. Parameters match exactly the configuration of the TM presented in [200].

Picture on the plot 2.20	ϕ_2 signal, ps^2	ϕ_2 pump, ps^2	ϕ_3 signal, ps^3	ϕ_3 pump, ps^3
a	-0.176	0.21	3.92×10^{-4}	5.14×10^{-4}
b	-0.189	0.21	4.2×10^{-4}	5.14×10^{-4}
c	-0.202	0.21	4.5×10^{-4}	5.14×10^{-4}
d	-0.215	0.21	4.79×10^{-4}	5.14×10^{-4}
e	-0.228	0.21	5.08×10^{-4}	5.14×10^{-4}
f	-0.241	0.21	5.37×10^{-4}	5.14×10^{-4}
g	-0.254	0.21	5.66×10^{-4}	5.14×10^{-4}
h	-0.267	0.21	5.95×10^{-4}	5.14×10^{-4}
i	-0.28	0.21	6.24×10^{-4}	5.14×10^{-4}

need to fix the computation window because of presence of the small satellite pulses, which can crucially increase the RMS value. The window was fixed from -10 to +80 pixels from the position of maximum, because of visible asymmetry. As one can notice, measured pulse width at the optimal distance between the compressor gratings (3.85 cm; pulses shapes displayed in Fig. 2.19b) is much larger than we expect ($\sim$ 130-140 fs instead of 70 fs). This is exactly the influence of the effects explained in the beginning of this section. Indeed, we see here that the aberrations play a crucial role being the first limitation for measurements of the ultra-short pulses with the Time Microscope.

Blue dots in the Fig. 2.19a represent the RMS of fifty highest amplitude pulses at a given distance between the compressor grating, red stars show the averaged value. We would like to point out the spreading of RMS values of a certain pulses far from the optimal grating distance. In order to understand this effect, we can provide the numerical simulations of the compressor tuning with the approach explained before. Also, the extracted pulse profiles are displayed in the Fig. 2.19b,c,d. The discussed effect is visible by eye, especially for the point far from optimum Fig. 2.19d.

Figure 2.20 shows the simulation of the compressor tuning presented in the Fig. 2.19a. For the simulations, we took the same signal and pump width as in the section 2.2.6: 30 fs for the pump and 70 fs for the signal. Signal contains 5 pulses separated by 5 ps. Simulations show how the recorded frames change with changing distance between gratings. By the dashed green line ideal case is depicted. The black line shows the same but with the presence of 3^{rd} order dispersion. Exact values if the 2^{nd} and 3^{rd} order dispersion coefficients are presented in the Tab. 2.3. It is visible that the higher order dispersion significantly changes the signal inducing inhomogeneity. Remarkably the 3^{rd} order dispersion makes it possible to observe a sharper pulse even if the distance between gratings is not optimal.

The simulations predict that the inhomogeneity in time within the fame is going to be change with changing compressor distance. In order to verify this prediction,we also plot the dependence of the fifty highest amplitude

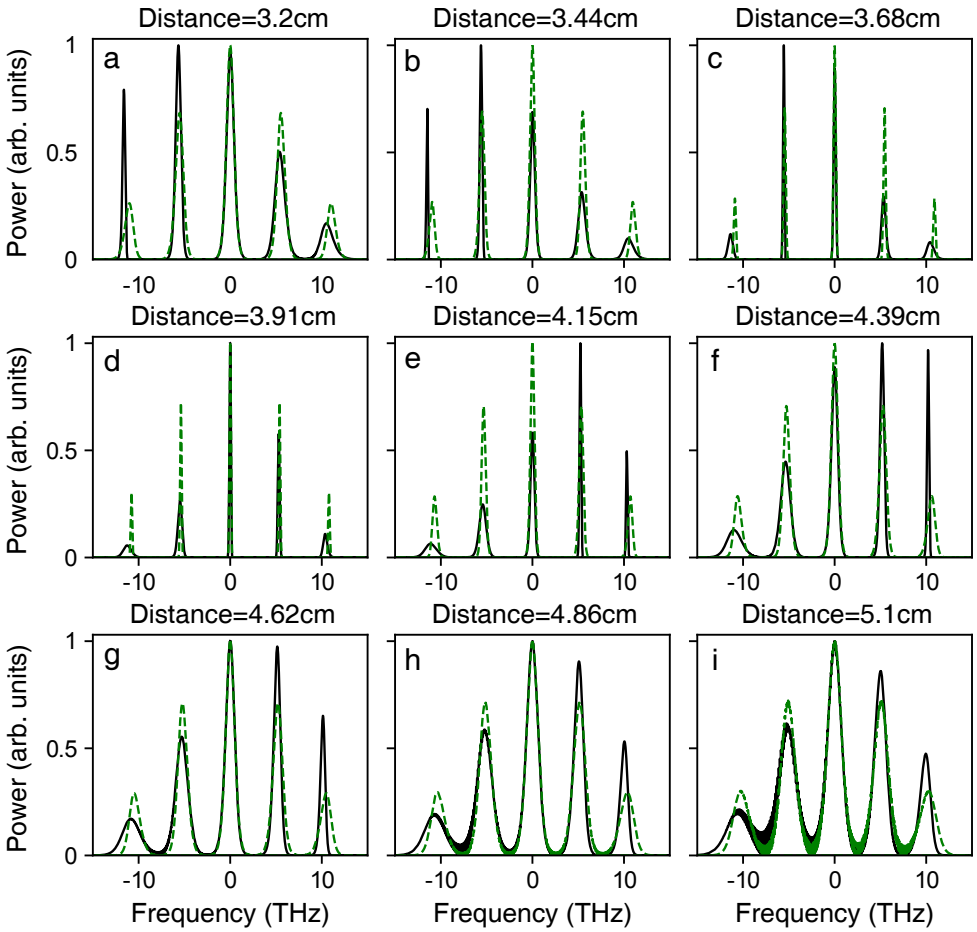

FIGURE 2.20: Simulation of the compressor tuning. (a-i) show the signal measured with a simulated Time Microscope with the different distance between gratings of the signal compressor, while the pump compressors stay untouched. Green dashed lines represent the ideal case when only the 2^{nd} order dispersion is added, black lines show the same, but with the presence of the 3^{rd} order dispersion. 3^{rd} order dispersion of the pump is fixed, while the dispersion coefficients of the signal were recomputed according to the formulas 2.16 and 2.20.

pulse RMS as a function of the maximum position within the frame Fig. 2.21. We, indeed, observe the predicted inhomogeneity and the fact that the 3^{rd} order dispersion can lead to a sharper picture on the edges of the frame. For example, it can be well seen for the distance 5.15 *cm* (dark blue dots) on the Fig. 2.21.

Finally, provided simulation Fig. 2.20 and the right data representation Fig. 2.21 confirm that measurements of the resolution must be done at the center of the frame. Also, it shaded some light on the reason why RMS value on the Fig. 2.19 becomes spread for the large compressor distances.

2.3 Heterodyne Time Microscope

In this section, we propose a scheme of spatial heterodyning extension of the Time Microscope for single-shot measurements of the power and phase

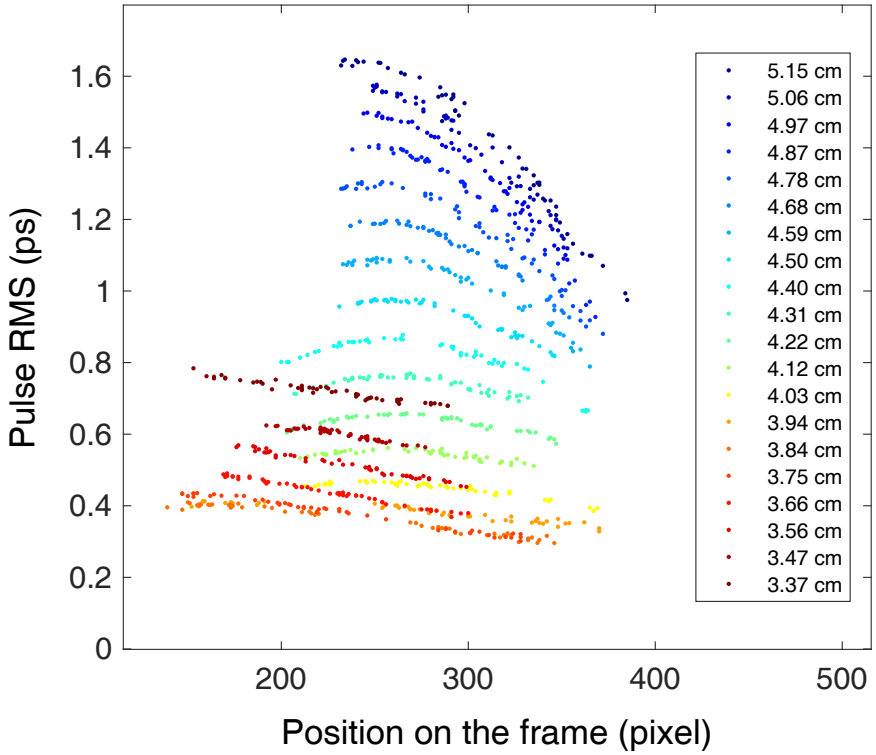

FIGURE 2.21: Experimentally measured dependence of the fifty highest amplitude pulses root mean square on its position on the recorded frame. Distance between the grating was varied from 3.37 cm to 5.15 cm. Optimal distance is 3.85 cm. Data correspond to one depicted in the Fig. 2.19a. The frame center is at 256^{th} pixel.

profiles. The phase measurement is always challenging task in optics, especially for the ultrafast signal. Information about the phase opens a wide range of possibilities for studying light dynamics. It is particularly important to measure the phase in single-shot for investigations of optical turbulence. Our spatial arrangement has certain advantages in comparison with the temporal [201] realisation. This allows to provide the efficient study of optical turbulence which will be presented in the next chapters.

2.3.1 Extension of the Time Microscope for the heterodyne phase measurement

Investigation of optical turbulence and for formation of Rogue Waves requires following characteristics of the measurement tool: possibility to measure the phase and power simultaneously and in single-shot, large window of measurements (tens of ps), high resolutions ($\leq 250\,fs$), high dynamic of recording (40 dB), and a broad bandwidth (f) On the moment of beginning of our research, there was no tool (to the best of our knowledge) which could fulfil these requirements. From other hand the Time Microscope demonstrated a good potential to become an optimal tool for these needs, apart from

the fact that it didn't provide the phase measurements. Also we took into the account that the only one dimension of the sCMOS camera was used. The camera was a strong point in the presented TM, so we decided that the phase has to me encoded into the second dimension of the camera. Therefore the optimal to way to extend the Time Microscope for the phase measurements is so called spatial encoding arrangement (SEA) [159].

2.3.1.1 Spatial encoding arrangement

The spatial encoding arrangement is extensively used in ultrafast measurements. Usually this method of encoding is applied to a spectral interferometry technique and, hence, the frequency is encoded into the horizontal axis. Remarkable realisations of this scheme are SEA-SPIDER [159, 160] or relatively simple realozation Spatial Encoded Arrangement for Temporal Analysis by Dispersing a Pair of Light E-fields (SEA TADPOLE) [202]. Typical snapshot obtained with method is presented in the Fig. 2.22. It is very common to retrieve information from such kind of frame using a Fourier transform-based method. Indeed, the vertical axis contains visible fringes, therefore the Fourier transform will give a picture with one main band and two side bands. The argument of the side band can be considered as a relative phase, while the position of the band will give the frequency of the fringes. The vertical axis can contain information about the phase directly or some information leading to the its retrieval. Into the horizontal axis can be encoded time or for example frequency. Also, more advanced holographic methods such as Spatially and Temporally Resolved Intensity and Phase Evaluation Device: Full Information from a Single Hologram (STRIPED FISH) can be used [203].

This is the general view on the spatial encoding arrangement. Our technique called Heterodyne Time Microscope can be considered as a SEA. Particularly, in our case the horizontal axis will contain time evolution while vertical will show directly the signal's phase. The possibility of direct observation of the signal is one of strong sides of our tool.

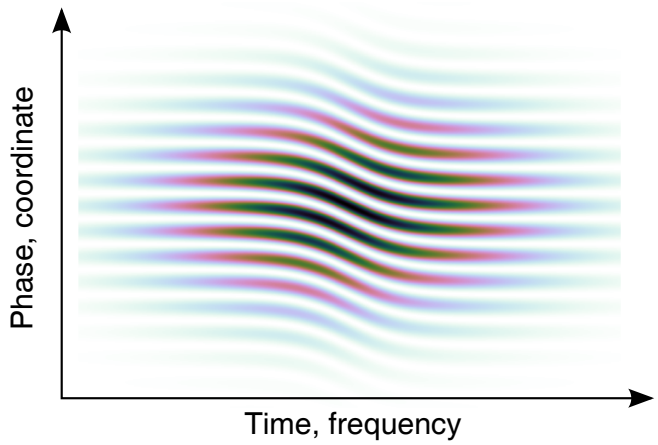

FIGURE 2.22: Typical snapshot obtained with a spatial encoding arrangement setup. Picture is generated numerically.

2.3.1.2 Setup

The setup described in preveause section 2.2 can be extended in order to provide simultaneous single-shot intensity and phase measurements without trade-off on the resolution and the size of the window of recording [200]. The general approach is to combine the demonstrated temporal microscopy technique and heterodyne measurements of the signal. In order to achieve this, the beams geometry is turned to be elliptical with the long axis $\sim 0.5\ mm$ (perpendicular to the table) and short axis $\sim 25\ \mu$m for the waist inside the BBO crystal. Heterodyning requires a stable monochromatic reference, that is why we added the third optical path (as it is depicted in the Fig. 2.23a) with a tunable single-mode laser operating in the range of wavelengths around the central wavelength of the signal. Reference beam is shaped to have similar elliptic geometry. The reference and the signal under investigation are focused together in the nonlinear crystal with a small vertical angle (see Fig. 2.23b). Resulting interference fringes move vertically in time depending on the relative phase difference between the signal and the reference beams. The phase of the reference considered as a constant within a duration of the window of measurements. This was tested experimentally by using the CW source as a signal (this will be shown later in Fig. 2.26). Resulting image contains the phase information on the vertical axis and the intensity information on the horizontal (plot in the Fig. 2.23b).

The basis of the HTM presented in the article [200] is the Time Microscope of the previous section 2.2.2 under some modifications. *Signal generation* part remains the same, as well as the *pump*. However, now much more significant part of the provided power will be used due to the diagrammatically increased vertical beam's size. The pump pulse energy raised from 100 nJ to 20 μJ. We also changed the gratings in the *Treacy compressor* to increase the thermal stability: 600 lines/mm Spectrogon PC 0600 NIR gratings, operated at an angle of incidence of 49 degrees, and separation distance 38.5 mm. This corresponds to the value of $\phi_2 \approx -0.21\ ps^2$. The optimal separation distance between the grating surfaces was found by using the same technique as one explained in the previous section 2.2.4, but the *home-made laser* is replaced by its more stable commercial analogue: femtosecond Erbium Laser (ELMO, from Menlo Systems GmbH). The femtosecond laser spectral width is now $\sim 15\ THz$, the pulse duration is $< 80\ fs$. *Time axis* calibration procedure didn't change (see section 2.2.5), new conversion ratio is 78.7 $fs/pixel$. *The BBO crystal* is changed from 2 mm instead of 4, it is cut with the same angle. *Camera performance* is significantly improved by using the Camera Link data transfer system together with a fast computer hard drive. This allows us to increase the pump pulse repetition to 1 kHz, without any problem of triggering or synchronization, thus decrease twice the recording time.

2.3.1.3 Beam geometry

The signal beam has the same optical path in the beginning: it is collimated at the output of the fiber by f= 11 mm aspherical lens and then magnified by the factor 4 using the telescope made of a plano-concave f=-25 mm

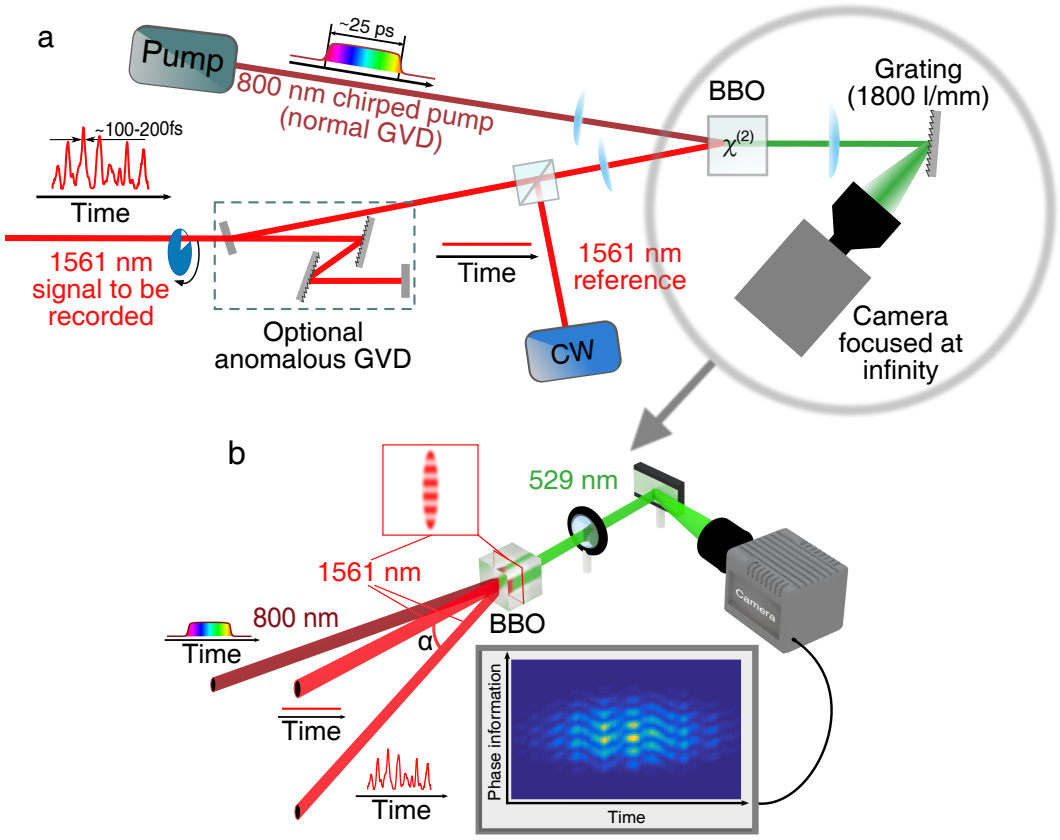

FIGURE 2.23: Experimental setup of Heterodyne Time Microscope arrangement for amplitude and phase measurement of arbitrary signals. (a) Complete setup. (b) Detailed 3-D view of the setup.

and a plano-convex f=100 *mm* lenses, so the beam's diameter is 10.5 *mm*. To obtain the required elliptical profile we shape the beam along the vertical and horizontal axis separately. For the vertical axis, another telescope of two plano-convex cylindrical lenses with focal distances 400 and 50 *mm* is constructed. After passing the telescope beam keeps the same horizontal size but its vertical diameter is decreased by a factor of 8. Now beam size is 1.313 by 10.5 *mm* in diameter. Horizontal axis is sufficiently small for the efficient sum frequency generation and at the same time sufficiently large to provide a necessary number of resolvable interference patterns necessary for the phase measurements. Vertically beam has the same size as in the TM arrangement presented before, so we focus it inside the BBO crystal with a f=200 *mm* plano-convex lens. Finally, the beam diameters at the waist are 1.313 *mm* and 36 μm.

The pump beam is shaped in a similar way. As in the previous case, the beam diameter at the output of the regenerative amplifier is $\sim$ 9 *mm*. For the reshaping to elliptical form, we used a telescope made of two cylindrical lenses with 400 *mm* and -100 *mm* focal distances. Resulting vertical beam side decreased to 2.25 *mm* while the horizontal was the same. We focused the pump beam horizontally inside the BBO crystal with a 20 *mm* cylindrical lens, consequently the resulting beam diameters are 2.25 *mm* and 23 μm.

The reference generated by the monochromatic laser and amplified is

transferred to the Time Microscope by a PM single-mode optical fiber connected directly to the amplifier. In order to make sufficiently large initial diameter we used a long focus collimator (ThorLabs F810APC-1550, NA = 0.24, f = 37.13 mm). The elliptical beam profile is achieved as always with a cylindrical lenses telescope employing two lenses of 250 and -50 mm, so the vertical and horizontal beam diameters were 1.4 and 0.03 mm. It is added to the optical path of the signal with a non-polarizing beam splitter cube before the last focusing f=20 cm cylindrical lens (in the Fig. 2.23a) approximately 2-3 mm above the signal beam. The distance to the minimal horizontal waist inside the BBO crystal is $\sim$25 cm, which gives the angle between the beams $\alpha \approx 10\,mrad$. This angle with the given vertical beam diameter will lead to $n = \frac{\sin(\alpha)d}{\lambda} \approx 9$ visible patterns. Here λ is the wavelength, d - vertical diameter of the beam inside the crystal. Taking into the account the size of one camera pixel (6.5 μm) we can estimate that each pattern after a collimation with a 20 cm lens will occupy $\approx$ 15 pixels which is enough to be resolved if the interference patterns are delivered sharp to the camera pixels. [12]

TABLE 2.4: Summary of the estimated vertical and horizontal diameter of the pump, signal and reference beams inside the optical crystal.

	Pump	Signal	Reference
λ, nm	800	1561	1561
Vertical beam diameter, mm	2.25	1.313	1.418
Horizontal beam diameter, mm	0.023	0.036	0.029

2.3.1.4 CW source

The source of the monochromatic signal used in the experiment is APEX AP3350A. The spectral width is estimated to be 300 kHz, hence the coherence time scale of the source is $\sim 3\,\mu s$. Since the time window in the HTM is much less (40 ps), the phase of the reference can be considered as a constant over the observation window. In order to achieve sufficient power (typically several watts), the reference is amplified using an Erbium-doped fiber amplifier (Keopsys). In order to achieve a minimum noise level we used maximum possible [13] value of the power of the CW source as well as amplifier's diode current. Wavelength tuning accuracy is 6 pm according to the manual.

[12] The distortion of the interference patterns in the vertical direction could be caused by several factors the most important are: vertical mismatch between the signal and reference beams and non-zero spatial walk-off angle of the 528 nm signal inside the BBO crystal. All this leads to the loose of pattern visibility and hence higher phase retrieval mistake. However, experiments show that with appropriate alignment the phase is sufficiently accurate (See section 2.3.4 for the verification).

[13] The upper limit for the injected power to the amplifier is 0 dBm. We used -2 dBm for the sake of safety even if the CW source could supply more.

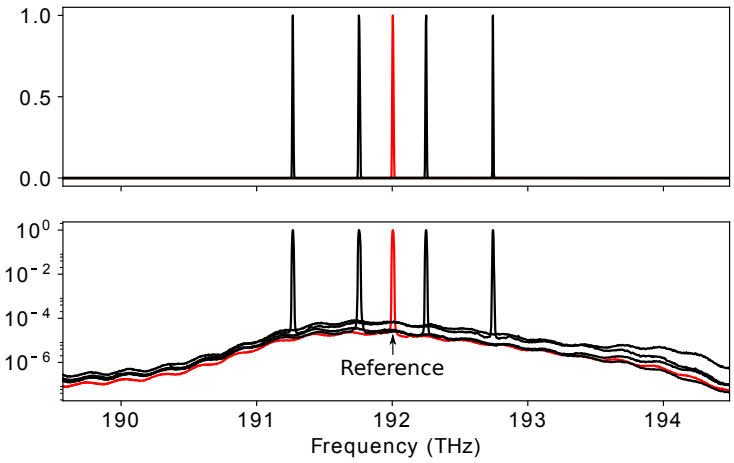

FIGURE 2.24: Recorded spectra of the amplified continuous wave reference. The central wavelength is chosen at the maximum of amplified spontaneous emission noise.

2.3.2 Heterodyne Time Microscope tuning

2.3.2.1 What is the same in tuning

The window of measurements in the presented HTM arrangement is extended in comparison with the one in [190]. Now we consider a window of $\sim$ 40 *ps* as a region of trust. Indeed, further investigations described in the chapter 3 show that despite the increased level of noise at the edge of the power profile, numerical nonlinear holography allows one to reconstruct a picture of spatiotemporal dynamics.

All the conclusions about *aberrations* described earlier are valid for the horizontal axis of a 2-D snapshot. The presence of the 3^{rd} order dispersion in the stretcher and compressor for the pump and signal will always lead to distortion of a real signal. A possibility to significantly decrease the aberrations is presented further in the section 2.4.

The procedure of the *Treacy compressor adjustment* didn't change. However, with the more stable fs-laser, we can observe directly the role of the aberration while tuning the compressor. Indeed, the resulting aberrations are the interplay between the 3^{rd} order dispersion of pump and signal. Since the 2^{nd} and 3^{rd} order dispersions are proportional to the distance between compressor's grating (see formulas 2.16, 2.20), changing the distance we can induce the controllable change to the dispersion of the signal while keeping the same dispersion of the pump. This can significantly extend our understanding of the aberrations in the Time Microscope.

Moreover, this can give an incontrovertible evidence of the crucial role of the higher order dispersion terms of the pump. Indeed, for the distance between the gratings fixed far from optimum we distinctly see that the asymmetry of recorded single pulses strictly depends on its horizontal position within the window.

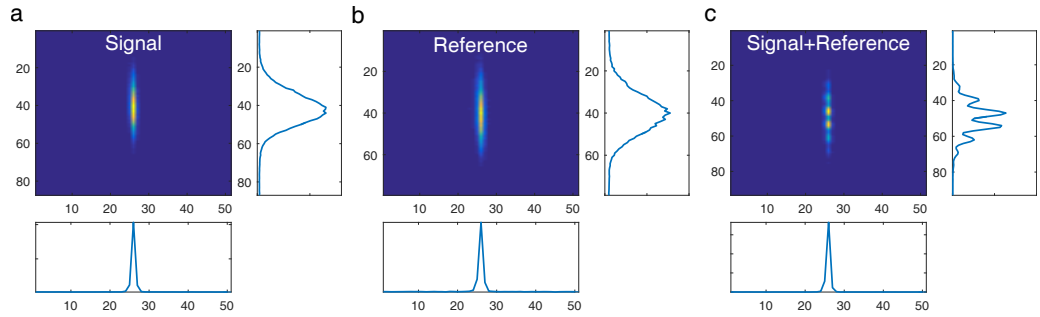

FIGURE 2.25: Snapshots recorded at the zero order of the diffraction grating with the time microscope. (a) Line corresponding to the signal alone, (b) reference alone, (c) signal and reference together. The optimal tuning corresponds to symmetric line of the width close to 1 pixel.

Method of the *horizontal axis calibration to time units* remained the exactly the same as explained before.

2.3.2.2 Tuning at the 0^{th} order of diffraction grating

Due to the specific beam geometry, the final right ellipticity check has to be provided. This can be done using the zero order of the diffraction grating placed right before the sCMOS camera. In the case of blazed gratings, the reflection at the 0^{th} order is analogous to a specular reflection from a flat surface and hence such configuration can be considered simply as a recording with a diffusive mirror. The resulting 2-D snapshot obtained at the 0^{th} order have to contain a single 1-pixel-width vertical line in the case of separate recording of signal and reference and a vertical line with sinusoid-like oscillations of the same width in the case when signal and reference are recorded together. See the picture in the Fig. 2.25. Observation of asymmetry or significant line broadening is a signature of possible misalignment.

2.3.2.3 Phase calibration. Importance of the right frequency choice

Phase retrieval algorithm, which will be presented later, requires the accordance between the frequencies of the signal and reference. In other words, snapshot of a signal with a constant phase, which central wavelength equals to the one of reference, has to contain only horizontal lines like in the Fig. 2.26c. This is directly related to the fact that interference patterns don't move inside the crystal within the time equal to the temporal width of the pump.

In order to provide this calibration, we plugged the second output of the CW laser source to the signal input of the time microscope. Keeping the central wavelength of the reference we changed the wavelength of the signal from 1555.37 to 1567.37 nm. It is natural to guess that the phase evolution, in this case, is going to be linear with a leading coefficient proportional to the difference between the central frequencies of the signal and reference. Indeed, this conjecture is well proved by the presented experimental results in the Fig. 2.26a-e. Our setup provides a relatively wide range of possible

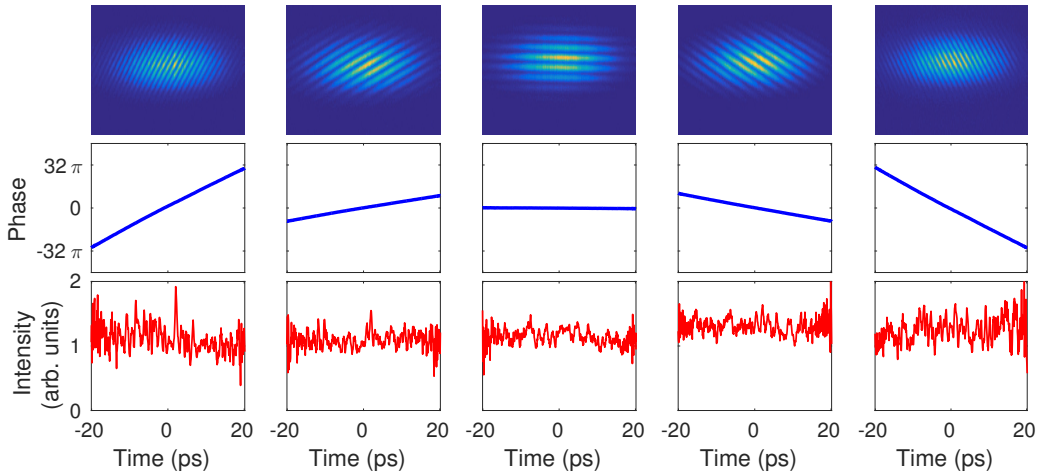

FIGURE 2.26: Monochromatic wave phase measurements. Raw images (top) and retrieved phase evolutions (middle) obtained when the signal comes from a monochromatic laser source with various wavelengths, from left to right: λ_S = 1555.37 nm, λ_S = 1559.37 nm, λ_S = 1561.37 nm, λ_S = 1563.37 nm and λ_S = 1567.37 nm .In all cases the wavelength of the reference is fixed to λ_R = 1561.37 nm. Bottom layer shows the recovered intensity profile. The noise related to the interference of the spontaneous emission of amplifier and monochromatic signal. Corresponding spectra are depicted in the Fig. 2.24.

measurements with detuned frequencies (we retrieved to phase of the signal detuned by $\pm$ 6 nm or $\pm$ 0.75 THz) [14].

Besides the CW reference, the amplifier also produces some spontaneous emission noise (see Fig. 2.24 bottom picture in log scale). In many cases, the interference between the noise and reference can be neglected [15], but the experiments with the Heterodyne Time Microscope (especially ones where the reference was recorded separately) show that detuning from the central wavelength of the spontaneous emission noise leads to appearance of noise on the retrieved power profile. It can be well seen in Fig. 2.26 where the third row represents the intensity profile.

From another side, the limiting factor is that central wavelengths of the signal and reference should coincide, otherwise the interference fringes will always move with the time (for example see the Fig. 2.26) and, hence, corrections have to be added to the phase retrieval algorithm. The choice of the signal's central wavelength depends on availability of tunable experimental equipment.

For retrieved signal the sign of the phase has to be also determined. Indeed, it is possible to use both: reconstructed complex field envelope and its conjugated. Here we take an agreement that the positive slope of the phase

[14] In further investigations this degree of freedom will allow us to observe the effect of Raman scattering [21] directly. This effect is followed by transfer of energy from the center of a spectrum to the lower energy part (Stokes component). The effect was observed due to a characteristic sharp phase inclination, which is the evidence of the change of frequency. This will be shown in the next chapter 3.2

[15] For example, if ϵ is the small power of the noise at a frequency ω_i, the visibility of interferences with the single frequency wave at ω_0 (P_0) is $4\sqrt{\epsilon/P_0}$

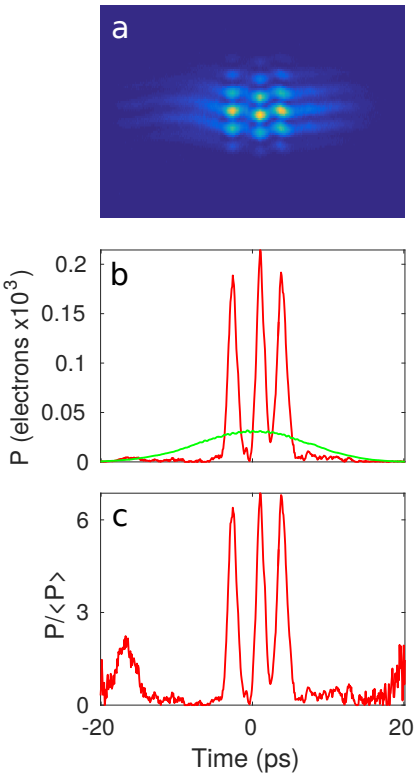

FIGURE 2.27: Intensity reconstruction. (a) 2-D snapshot obtained with the HTM. (b) Power profile before division by the envelope (red) and envelope (green). (c) Reconstructed power profile after division by envelope.

corresponds to the sign plus. This implies that the time axis is directed from left to right. This fact will be proved later in Sec. 2.4.2.

2.3.3 2-D snapshot processing for phase and power reconstruction

2-D snapshots (see for example Fig. 2.27a or 2.28a - a non-periodic signal that will be under investigation in the next chapter) recorded with the HTM contain full information about phase and intensity of a signal under investigation. However, if the phase evolution is connected to relative positions of interference patterns maxima and visible directly, in order to extract the real value of intensity additional information about reference (CW) is required. To fulfil this gap we also recorded snapshots of the reference alone for each set of snapshots for signal and reference together.

Intensity along one vertical line is given by interference between signal and reference which creates oscillating vertical patterns on the frame (see Fig. 2.28a,b). Position of maxima depends on the relative phase between the signal and reference $\Delta\phi_0(x)$. We suppose that that the reference intensity (I_r) is a constant in the time of the frame. Therefore, the intensity distribution over the whole frame recorded with the sCMOS camera could be presented

in the form:

$$\begin{aligned} I(x,y) =& I_r * E_r(x,y) + I_s(x) * E_s(x,y) + \\ & 2\sqrt{I_r * E_r(x,y) * I_s(x) * E_s(x,y)}V\cos(k_y y + cy^2 + \Delta\phi_0(x)) \end{aligned} \tag{2.21}$$

Where I_r and $I_s(x)$ are the reference and signal intensities, $E_r(x,y)$ and $E_s(x,y)$ are their envelopes, $k_y = 2\pi/d$ where d is the spacing between interference patterns, c is a possible chirp, V is the fringes viability which depends mainly on system alignment, the relative phase between signal and reference is $\Delta\phi_0(x)$. In the presented analysis we neglect the chirp c. Horizontal envelope in given by spectral width of the 531 nm signal which means it depends on both spectral widths of signal and pump as well as phase-matching bandwidth. Vertical size of envelope is the minimal (between signal and pump) vertical diameter of the beam inside the crystal, multiplied by the magnification factor of the imaging system after the crystal.

Our goal is to retrieve the signal's intensity profile $I_s(x)$ and the phase $\Delta\phi_0(x)$.

2.3.3.1 Intensity reconstruction

Intensity of the signal in a given point x_i of a frame is the difference between averaged data along the corresponding vertical line (for example green line in the Fig. 2.28a) and the value of the 1-D envelope of the reference $\int I_r E_r(x_i,y)dy$. We provide vertical averaging of the signal in order to get rid of cosine part of the Eq. 2.21 [16]

$$\int_0^{y_{max}} 2\sqrt{I_r * E_r(x_i,y) * I_s(x_i) * E_s(x_i,y)}V\cos(k_y y + \Delta\phi_0(x_i)dy \backsimeq 0$$

The expression above is valid only if the number of interference fringes is sufficiently large. We estimated the number of visible fringes as $n = \frac{\sin(\alpha)d}{\lambda}$. Therefore, it is always possible to increase this value if it is needed. However, there is a limit at witch fringes loose the viability, so the optical value of has to be found.

The last step is to divide the signal by its 1-D envelope $\int E_s(x,y)dy$ (see Fig. 2.27b - green line). The 2-D envelope $E_s(x,y)$ is found by averaging over all the frames, as it was done for the reference. All negative values of the signal under investigation (if such exist) are set to zero [17]. In order to get rid of edge effects and provide the normalization to the average power, each profile is divided by the envelope of the signal as it is depicted in Fig. 2.27c.

The real power profile can be reconstructed by measuring the average power with a powermeter. First, we can plot $P(x)/ < P >$. Here, the $< P >$

[16] The approach of taking only one line with the maximum of intensity (as it is done for the simple TM 2.2.3) is not valid any more because of presence of vertical interference fringes.

[17] Setting to zero the negative intensity points bias the statistical analysis of the recorded signal. However, this is can be done in the case when the signal-to-noise ratio is sufficiently good and the bias is very small.

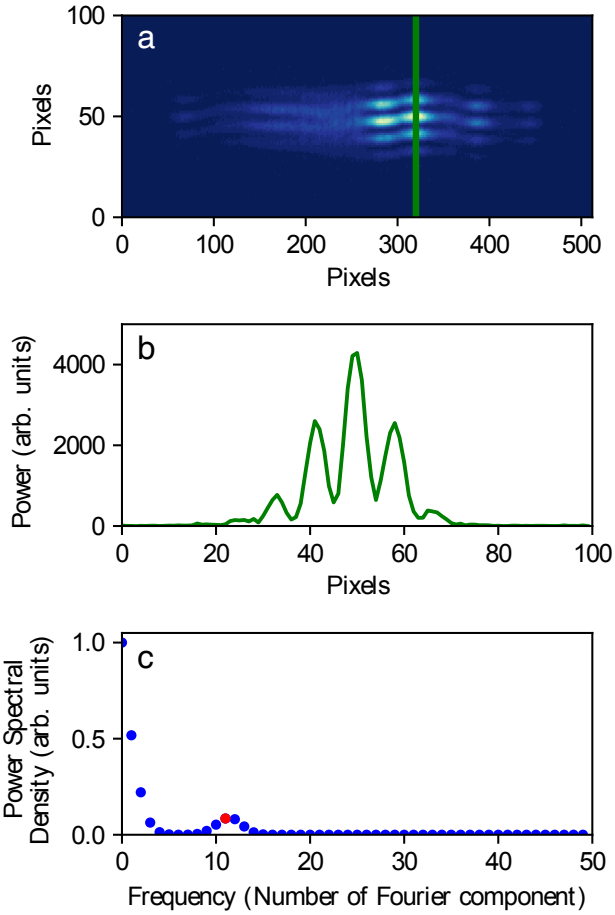

FIGURE 2.28: Phase reconstruction. (a) A 2D snapshot of a non-periodic signal. (b) Intensity profile along the green vertical line depicted above. (c) Corresponding Fourier spectra of the intensity profile. By the red dot highlighted the Fourier mode, argument of which is extracted.

can be considered as a maximum value of the envelope. Then multiplying by the real averaged power measured experimentally, we can plot the required profile $P_{exp} \times P(x)/ < P >$.

2.3.3.2 Phase reconstruction

Typical spectrum of a function like (2.21) contains one main band and two symmetrical side bands. The phase reconstruction is provided by extracting the argument of the second maximum (side band) in Fourier spectrum of each vertical line (red dot in Fig. 2.28c). Argument of the side band gives the relative phase $\Delta\phi_0$ in the cos term. Position of the sought peak in the spectrum is fixed from one vertical line to another. It is determined from averaged spectrum over all the spectra corresponding to each vertical line in the frame. We suppose that the phase of the reference is a constant in the considered period of time (40 ps) hence the term $\Delta\phi_0$ represents the phase of the signal under investigation.

2.3.4 Verification of the retrieval algorithm by reproducing the mean optical spectrum

The reported resolution of simultaneous power and phase measurement allows us to provide versatile tests of the recording quality and repeatability. One of the most illustrative tests is the retrieval of the mean optical spectrum. Indeed, having access to the complex envelope of the signal's electric field we are able to reconstruct the mean optical spectrum. This test is especially relevant because direct measurement of the optical spectrum is the everyday routine of many optical experiments including our.

The procedure of the spectra reconstruction is trivial: we take the square root of the retrieved power profile $P(t)$ and multiply it by a super-Gaussian function (to avoid the Fourier transform artefacts making the signal fully periodic) with the power factor n=15. Further, we take the exponent of the complex one and the retrieved phase profile $\psi(t)$. After multiplication of all the elements, we finally take a Fourier transform (see Eq. 2.22). Choice of the *positive* phase sign (because there is an ambiguity) will be fully justified later in the subsection 2.4.2.

$$S(\omega) = \mathcal{F}\left[\sqrt{P(t)}e^{-[(t/2t_0)^2]^n}e^{i\psi(t)}\right] \tag{2.22}$$

In order to obtain a realistic spectrum, this operation has to be repeated over at least 10,000 different snapshots of a single recorded with the same experimental conditions. Since optical spectrum analysers (OSA) provide the information about the power spectral density [18], we take modulus square of each of 10,000 spectra and average them $< |S(\omega)|^2 >$. In order to compare two spectra we shift them in the 'center of mass' and normalize by maxima. The center of mass is defined as:

$$\omega_{cm} = \int < |S(\omega)|^2 > \times \omega d\omega / \int < |S(\omega)|^2 > d\omega$$

As a test signal, we used an amplified spontaneous emission source, due to the complexity of its output signal. We were able to control the spectral width of ASE by using a programmable optical filter. Finally, the averaged power of the signal was increased with an erbium amplifier. This set of tools exactly repeats the one presented before in the Sec. 2.2.3. The result of the comparison of OSA recorded spectrum and reconstructed is depicted in the Fig. 2.29. In the plots a,c,e typical signal of 0.1 THz (FWHM) is displayed. Pictures c and e show its phase and power respectively. The reconstructed spectrum is depicted in Fig. 2.29g. The spectrum is symmetric and well fitted with the HTM recorded data. When we increase the spectral width of the ASE signal we immediately observe more fluctuations in the given window of measurements (Fg. 2.29 b,d,f). The width of the structures decreases from $\sim 10ps$ to $\sim 1.5ps$. Increasing the spectral width we can observe deviation

[18] The spectral analyser used in the experiment is Yokogawa AQ6370B. We used it in the high sensitivity mode with resolution 0.02 nm.

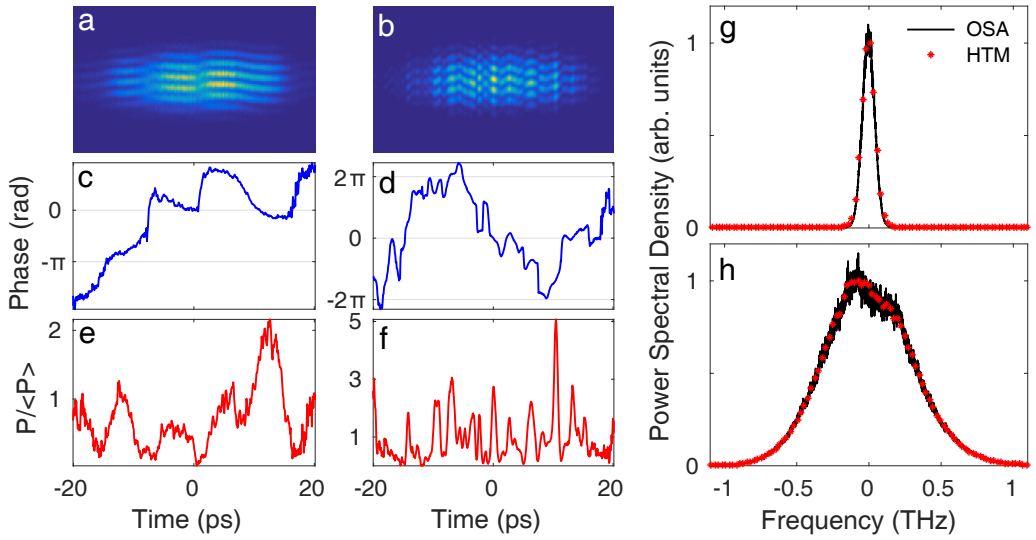

FIGURE 2.29: Phase, amplitude and spectrum of partially coherent waves (ASE). a–f, The width $\Delta\nu$ of the (average) optical spectrum of the partially coherent light waves emitted by an ASE source is adjusted by using a programmable filter. Results correspond to $\Delta\nu$ = 0.1 THz (a,c,e,g) and $\Delta\nu$= 0.7 THz (b,d,f,h). a,b, Typical raw images recorded by the sCMOS camera of the HTM for ASE light with a spectral width $\Delta\nu$ = 0.1 THz (a) and $\Delta\nu$ = 0.7 THz (b). c,d, Phase retrieved from the interference pattern. e,f, Optical power normalized to the average power. In contrast to the raw signal in a and b, the signal in e and f is divided by the average power($P(t)/ < P >$). g,h, Optical spectra corresponding to $\Delta\nu$ = 0.1 THz and $\Delta\nu$ = 0.7 THz, respectively. Red stars represent the spectrum computed from the averaged Fourier transform of the envelope of the electric field recorded with the HTM. The spectrum recorded by the OSA is plotted with black lines for comparison.

of the spectrum from the Gaussian. It is the consequence of the inhomogeneity of the initial ASE spectrum. Remarkably, we are able to match not only the correct spectral width, but also the details of asymmetry of the spectrum recorded by using the OSA.

This test does not provide the proof that the focus of the HTM is correctly tuned, because $< |S(\omega)|^2 >$ is not sensitive to the additional phase adjustment. However, it demonstrates that the combination of the phase and amplitude measurements is acceptable for further investigations.

2.4 Removing aberrations. Spatial Encoding Arrangement with Hologram Observation for Recording in Single-shot the Electric field (SEAHORSE).

The Heterodyne Time Microscope arrangement suffers from the presence of the aberrations. Here we propose a completely new setup which doesn't require the compressor for the signal. Recording the full complex amplitude of the signal, opens a possibility to add the dispersion numerically during

the ex post analysis. Therefore, we remove completely the one of two major aberration sources.

2.4.1 Setup

As it is mentioned above (Sec. 2.2.6) the main source of the aberrations is the third order dispersion effects. However, since we measure the amplitude and the phase simultaneously, it is possible to skip the Treacy compressor and reconstruct the sharp image numerically, with a technique similar to the so-called *digital holography* in spatial imaging [204–206]. The corresponding scheme can be found in Fig. 2.30a.

Holography was invented by D. Gabor in 1948 [207] even before the appearance of the lasers. After, it was significantly improved by introducing the off-axis reference [208]. The digital reconstruction of the holographic images was first shown by J. Goodman and R. Lawrence in 1967 [209]. With appearance of sensitive detectors such as Charged Coupled Devices (CCD) or Complementary Metal-Oxide Semiconductor (CMOS), digital holography overcame possibilities of conventional holography. For example, possibility to provide Digital Holographic Microscopy [210] which allows to change numerically the position of the focus and reconstruct a sharp image different layers of a material under investigation. More detailed overview of the digital holography reader can find in [206]. From this point of view, our ultrafast measurement technique can be considered as a temporal analogue of the off-axis digital holography.

The exact value of the second order dispersion to be added can be found precisely from the compressor parameters or estimated numerically by gradually increasing the applied dispersion to the blurred image of a pulse until we obtain maximum sharpness ((Fig. 2.30e)). More explicitly, we combine reconstructed [19] power and phase into the complex field envelope. Then, employing the fast Fourier transform algorithm, we pass to the spectral domain. Next, spectral density of the signal is multiplied by the exponent with corresponding second order dispersion term. Finally, we use the inverse fast Fourier transform algorithm to return in the temporal domain. In terms of variables introduced before it can be written as follows:

$$S(t) = \mathcal{F}^{-1}\left[\mathcal{F}\left[\sqrt{P(t)}e^{i\psi(t)}\right]e^{i\frac{\phi_2\omega^2}{2}}\right]$$

where $S(t)$ is the reconstructed signal, $P(t)$ and $\psi(t)$ are the power and the phase retrieved from the 2-D hologram, ϕ_2 - second order dispersion coefficient.

Further, we will demonstrate the benefits of numerical reconstruction showing a double-plus signal measurement. This powerful technique is applicable not only to the pulse-like signals (Fig. 2.30a), but also for the study of partially-coherent wave dynamics. However, the role of the higher order dispersion effects on the pump are also presented.

[19] The procedure of the initial power and phase reconstruction from the hologram is exactly the same as for the HTM.

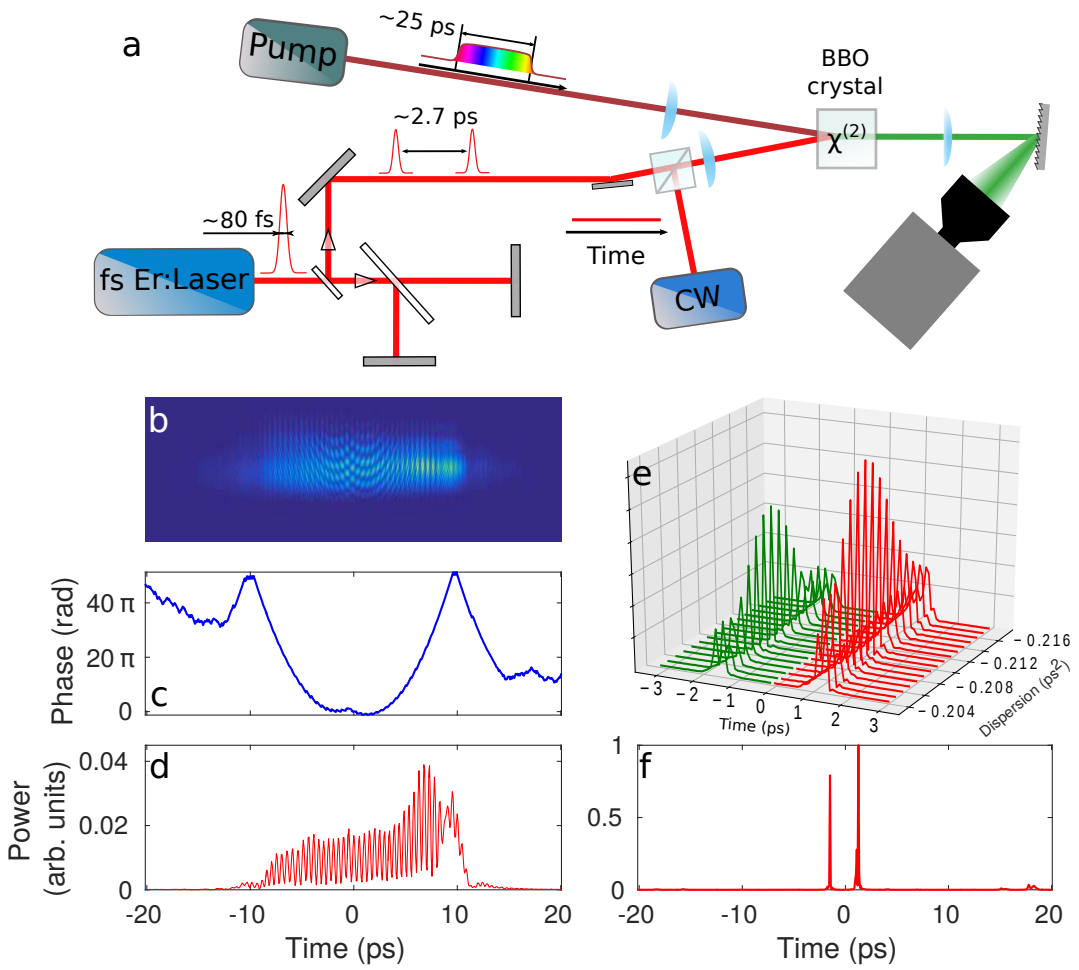

FIGURE 2.30: Spatial Encoding Arrangement with Hologram Observation for Recording in Single shot the Electric field (SEAHORSE). (a) scheme of experimental setup adapted for the double pulse measurements. (b,c,d) Corresponding 2-D snapshot with the temporal hologram, retried phase and power. (e) The image reconstruction by adjusting the second order dispersion coefficient. (f) Reconstructed sharp image of the double-pulse signal.

2.4.2 Phase sign and direction of time axis

Provided Heterodyne Time Microscope measurements contain an ambiguity in a sign of the phase. In other words it possible to consider both the complex field envelope and its conjugated. In order to restrict it let's consider the monochromatic reference and signal (see Fig. 2.26). In this case, the slope of the phase depends on the difference between the signal and reference frequencies ($\delta\omega = \omega_s - \omega_r$, where ω_r - frequency of the reference and ω_s - of the signal). We settled the definition in the way that positive slope should correspond to the positive phase. The sine of the slope depends on the direction of the time axes (horizontal axes of the frame).

In order to determine this direction, we employ an experimental approach. In the Fig. 2.30 the reconstruction of the double pulse signal recorded with digital holography time microscope is depicted. One can notice that in our

configuration of the Michelson interferometer the pulse which has longer optical path cross a beam splitter twice while the other one doesn't traverse it. Since the beam splitter is made of fused silica, it induces anomalous dispersion for the considered range of wavelengths. Hence, the pulse which arrives first to the camera needs more dispersion during the reconstruction. Indeed, in the Fig. 2.30e the maximum compression point for the pulse depicted by green is $\sim 0.001 ps^2$ after the one depicted by red. Hence, we can conclude that the time axis is oriented from left to right.

Taking into the account all of the above we conclude that for the case when $\delta\omega > 0$ the phase is positive.

2.4.3 Comparison between HTM and SEAHORSE

In order to provide the comparison between the SEAHORSE and HTM, we recorded a single 70 fs pulse using both instruments. The result of measurements is depicted in Fig. 2.31. Striking difference in the wide spectrum pulse measurement is observed. The role of the higher order dispersion is now unquestionable. However, even the SEAHORSE shows some deviation from the real pulse duration. A possible reasons for the presence of 3^{rd} order dispersion in the pump pulse. Another explanation is that the width of the pulse is actually shorter than the time corresponding to the distance between two points in time. This is significant and fundamental limitation of all Time Microscope measurements.

The pulse measured with the HTM method has width ≥ 250 fs, while one measured with the SEAHORSE has $\sim$80 fs [20], which is almost exactly the time which corresponds to the time between two points of discretization (79 fs for the arrangement presented in [200]). Indeed, the main part of the pulse recovered with the SEAHORSE consists of 1 point (black line in Fig. 2.31).

There is a visible possibility to increase discretization by adding zeros to the high frequency part of the spectrum of the signal before reconstruction. This method of interpolation is the most relevant because we don't add any additional information about the complex field envelope. The result of such interpolation is depicted in Fig. 2.32. The black line in the Fig. 2.32 is exactly the one plotted in Fig. 2.31. Blue dots represent the case when there are 1024 zeros added to the Fourier spectrum (spectral zero padding). One can see that we obtain 5 points inside the pulse instead of one. We immediately observe that signal became narrower, but we obtain some additional oscillation on the lift side of the pulse. If we add more zeros, like in depicted by green dots in the Fig. 2.32, we simply better resolve the the main part of the pulse as well as oscillation tail.

How it was mentioned before, another source of errors is the power profile noise induced by the phase measurements noise. However, it is barely visible, because for the case of the one pulse almost all the power concentrated in one pixel.

[20] For the pulse reconstruction process reader can proceed to the section of supplimentary video of the article [200].

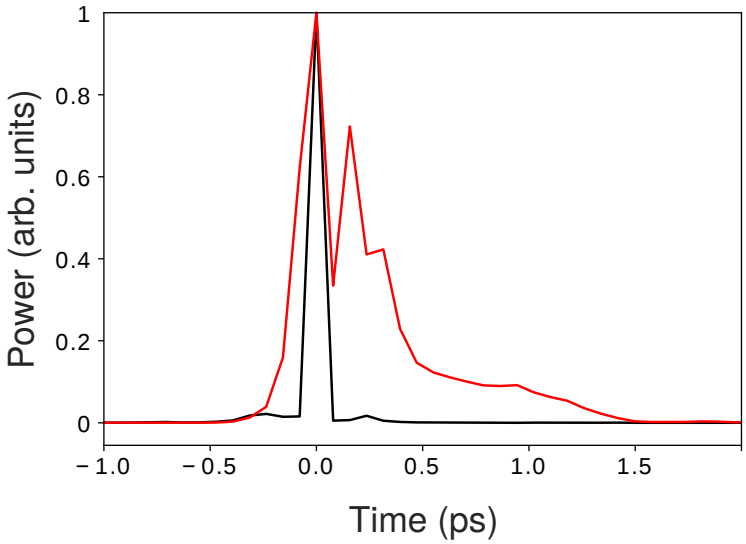

FIGURE 2.31: Comparison between HTM and SEAHORSE. Single 70 fs pulse obtained with HTM (red) and SEAHORSE after reconstruction (black).

While for the broad spectral width the difference is visible immediately, for the width < 1 THz almost no difference is observed. This will be demonstrated in the next chapter on the example of a stochastic signal.

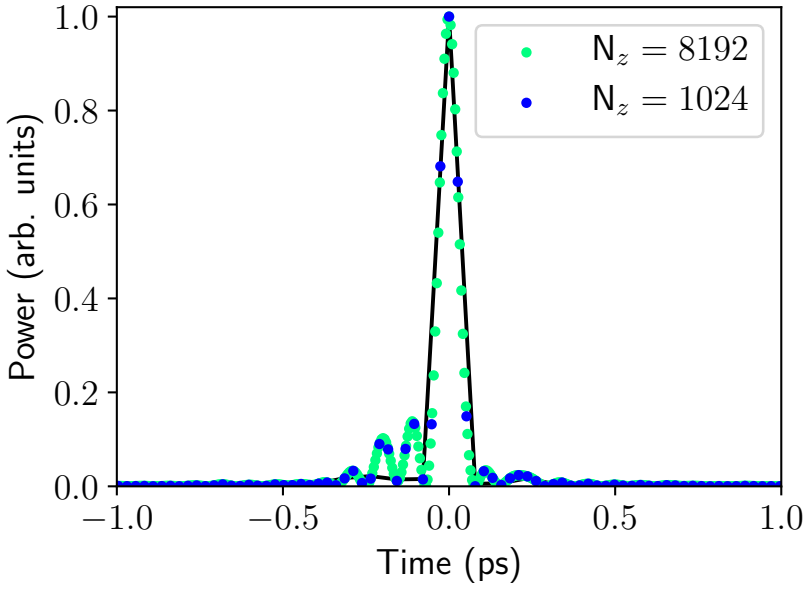

FIGURE 2.32: Interpolation of the SEAHORSE hologram. A 70 fs pulse recorded with the SEAHORSE. (Black line) pulse reconstructed directly from the hologram, the same as one depicted in Fig. 2.31. (Blue dots) 1024 points zero padding in the Fourier space. (Green dots) the same but with 8192 points.

Chapter 3

Peregrine soliton as a prototype of rogue waves in the integrable turbulence

Recently, a rigorous mathematical result was obtained by A. Tovbis and M. Bertola for the semi-classical limit of NLS equation [124]. This result shows that the Peregrine soliton (exact solution of NLS) appears locally as a regularization of a gradient catastrophe[1] during a focusing dynamics in the case of zero boundary conditions. This process is universal and takes place even in the case of completely solitonless initial conditions.

The theorem of Tovbis and Bertola allows looking at the problem of rogue wave formation from completely another angle. Indeed, Peregrine soliton was widely considered as a prototype of RW, but this solution has a pure asymptotic behaviour and requires careful choice of initial conditions in order to be observed in the real experiment. However, it is localized version has all the chances to be registered.

In this chapter, we will discuss the semi-classical limit of NLS. Also, we will show empirical evidence of the theorem validity in optical experiments with both deterministic and random initial conditions. And finally, we will demonstrate the crucial role of the localized Peregrine soliton in the process of formation of high amplitude events in the integrable turbulence employing local and statistical approaches.

3.1 Gradient catastrophe in the focusing NLS and its regularisation. Tovbis-Bertola theorem.

In this section, we will discuss the semi-classical limit of focusing NLS and the mechanism of regularization of the gradient catastrophe in this case. Also, we will demonstrate some important properties that could be extracted from the semi-classical theory. Finally, we will provide the experimental evidence of the fact that a structure similar to Peregrine soliton [2] can be observed

[1] The term gradient catastrophe in the case of focusing NLS has to be distinguished from the one adopted to explain the wave breaking in defocusing NLS.

[2] More precisely we can say that all family of structures which appears as a regularisation of gradient catastrophe caused by self-focusing dynamics has the same *genus* as the Peregrine soliton. The definition of the term genus will be given later in this chapter.

even in the regime far from semi-classical approximation.

3.1.1 Semi-classical limit of the focusing NLS

Theory of the weakly nonlinear limit of NLS can be resolved exactly with a standard for this case tool called weak (or wave) turbulence in the context of random wave [36]. This approach gives an exact kinetic equation for the NLS equation. However, this theory doesn't provide the full explanation of the complex phenomena behind the NLS equation. When the nonlinearity becomes dominant in the evolution, some other approach should be developed. This brings us to the widely used approximation of the semi-classical limit which approaches this problem from the other side. In this approximation, the dispersion term has a smaller impact in comparison with the term corresponding to the cubic nonlinearity. However, setting the dispersion term directly to zero in the NLS equation leads to some trivial results in which the intensity profile doesn't evolve with the time [122]. Therefore, some other approach with expanded dispersion term has to be used. The appropriate form of the equation could be obtained with so-called Madelung transformation [110].

Let us start with a classical form of focusing NLS widely used in fiber optics community:

$$i\frac{\partial A}{\partial z} + \frac{|\beta_2|}{2}\frac{\partial^2 A}{\partial t^2} + \gamma|A|^2 A = 0 \tag{3.1}$$

Where β_2 and γ are the standard designations in fiber optics for second order dispersion and nonlinear coefficient respectively.

In the semi-classical limit nonlinearity dominates dispersion, so the dispersion length $L_D = T_0^2/\beta_2$ is much larger than the nonlinear length $L_{NL} = 1/\gamma P_0$ and actually tends to infinity. It is natural to introduce the small parameter ϵ for this system. In our case it can be a ratio: $\epsilon = \sqrt{L_{NL}/L_D} = \sqrt{|\beta_2|/\gamma P_0 T_0^2}$. With the change of variables to dimensionless $\xi/ = z\sqrt{L_{NL}L_D}$, $\psi = A/\sqrt{P_0}$ and $\tau = t/T_0$ (T_0 here is the typical time scale of initial conditions) classical focusing NLS 3.1 can be transformed into[3]:

$$i\epsilon\frac{\partial \psi}{\partial \xi} + \frac{\epsilon^2}{2}\frac{\partial^2 \psi}{\partial \tau^2} + |\psi|^2\psi = 0 \tag{3.2}$$

Madelung transformation was invented at the birth time of quantum mechanics when the attempts to rewrite the Schrödinger equation in terms of hydrodynamical variables were made [211]. However, this approach is applicable to the NLS system as well. It can be expressed as follows:

$$\psi(\xi,\tau) = \sqrt{\rho_m(\xi,\tau)}e^{i\phi(\xi,\tau)},\ u(\xi,\tau) = \phi_\tau(\xi,\tau) \tag{3.3}$$

[3]For the overview of the used change of variable in this chapter see appendix C.

where $\sqrt{\rho}$ is the wave amplitude and u - the instantaneous frequency. NLS can be expressed as system of equations by separation of real and imaginary parts:

$$\rho_\xi + (\rho u)_\tau = 0 \tag{3.4}$$

$$u_\xi + u u_\tau - \rho_\tau + \frac{\epsilon^2}{4}\left[\frac{\rho_\tau^2}{2\rho^2} - \frac{\rho_{\tau\tau}}{\rho}\right]_\tau = 0 \tag{3.5}$$

In this form, the meaning of the Madelung transformation can be easily understood. Indeed, the first equation is simply continuity equation, with ρ - fluid density and u - flow velocity field. The second is analogue of Euler equation for dispersive hydrodynamics but with a negative pressure $p = -\rho^2/2$.

Lets now consider the simplified system where the term proportional to ϵ^2 (by analogy called quantum pressure) is neglected. After taking the dispersionless limit (neglecting the term with ϵ^2), Eq. 3.4 and 3.5 take a form of focusing nonlinear geometrical optics equations:

$$\rho_\xi + (\rho u)_\tau = 0 \tag{3.6}$$

$$u_\xi + u u_\tau - \rho_\tau = 0 \tag{3.7}$$

Dynamics of the system before appearance of any singularity can be described by Eq. 3.6 and 3.6 [110, 212].

Let us take a smooth bell-like shaped function as an initial condition, for example $\rho(0,\tau) = \rho_0(\tau) = sech^2(\tau)$ with no chirp $u(0,\tau) = 0$ [4]. Tendencies of behaviour of such function can be clearly seen by considering a short distance evolution $\xi \ll 1$. In this case ρ and u can be represented as a Taylor expansion by ξ. Let's consider only first two terms in expansion $\rho(\xi,\tau) = \rho_0 + \rho_0'\xi$. Hence, the equation 3.6 leas directly to $u \simeq \rho_0'\xi$. Substituting to the equation 3.7 we get the system [213]

$$u \simeq \rho_0'\xi$$

$$\rho \simeq \rho_0 - \frac{\xi^2}{4}\left[\rho_0^2\right]''$$

The short distance limit reveals the tendency of dynamics. According to the formula above, the intensity is going to change (at least at the very beginning of propagation) proportionality to the term $\left[\rho_0^2\right]''$. This means that in the area where this term has a negative sign, the solution tends towards higher amplitude. As reader can see in Fig. 3.1 the second derivative of the sech^2 function is negative almost everywhere. At the point $\tau = 0$ it has its minimum, which implies that the function is going to grow fast around the center and hence further propagation will lead to the *self compression*.

[4] More strictly, the function taken as initial condition should be from the Schwartz space, *i.e.* that function is rapidly decreasing with all its derivatives, this condition is important for the inverse scattering theory in the case of zero boundary conditions.

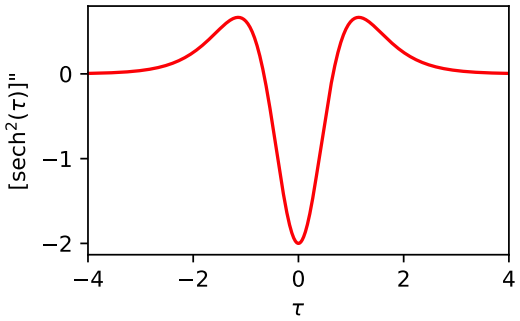

FIGURE 3.1: Second derivative of the sech^2 function.

Numerical study of the dynamics [5] of the full system of equations 3.6 and 3.7 shows that the initial shape of the function, indeed, is going to focus around the point of maximum (See Fig. 3.2). At the same time, the instantaneous frequency $u(\xi, \tau)$ grows from one side and decreases from another, passing by zero at the maximum point.

At a certain critical value of ξ (ξ = 0.5 in Fig. 3.2) derivative of ρ and u tends to infinity. This point is called the point of *gradient catastrophe*. In general, this effect occurs even if the derivative of ρ or u tends to infinity independently from each other. For the given example the position of the point can be found explicitly [214, 215].

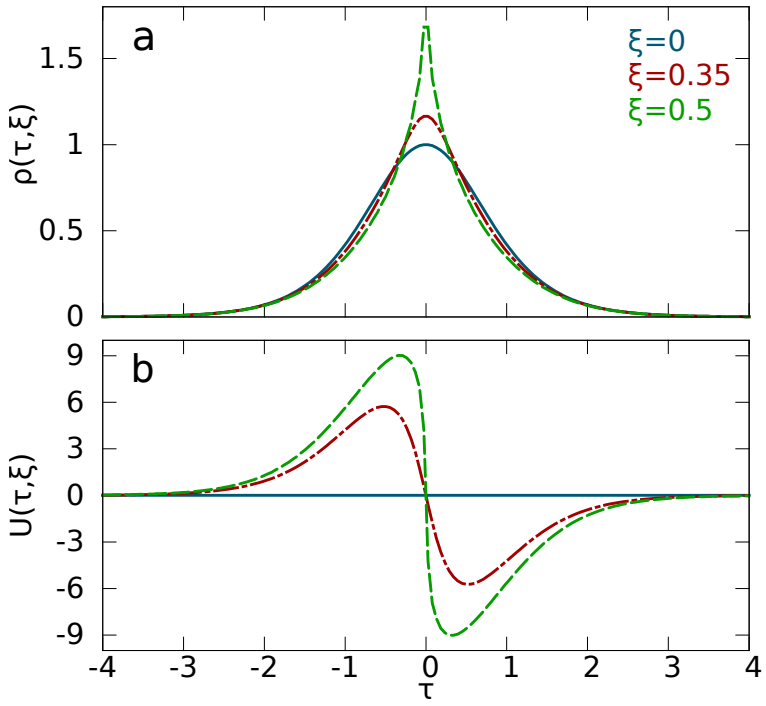

FIGURE 3.2: Dynamics of the bell-like shaped initial condition in the NLS system under the dispersionless limit. ρ and u profiles are displayed for ξ = 0, 0.35 and 0.5. Original figure can be found in [216].

[5] The system 3.6- 3.7 can be reduced to a linear form by a hodograph transformation and solved explicitly [212].

Remarkably, a similar analysis was provided by S. A. Akhmanov, A. P. Sukhorukov, and R. V. Khokhlov in 1966 for a two-dimensional laser beam propagating in nonlinear media [214]. Authors predicted self-focusing up to a singularity point (point of the gradient catastrophe). Authors figured out that the approach employing the nonlinear geometrical optics approximation fail at the point of singularity and further investigations are not possible.

Indeed, subsequent steps of analysis around the gradient catastrophe point require knowledge of theorems that are topics ongoing development of modern mathematics [123, 217]. Here we will make an attempt to describe the general approach and make an overview of main results without immersing into technical details.

Emerged singularity has to be regularized which is not possible in the reduced model (Eq. 3.6 and 3.7). Hence, consideration of the full system of equations 3.4 and 3.5 is needed to resolve the problem. In [124] A. Tovbis and M. Bertola rigorously proved that the behaviour of the system around the point of gradient catastrophe has a *universal* character. Indeed, error correction approach employed by authors enables to find shape and amplitude at the maximum compression point of a structure which appears as regularisation of this singularity up to some order of precision. Surprisingly, up to $\mathcal{O}(\epsilon^{1/5})$ [6] corrected solution *locally* (in the neighbourhood of the position of the maximum compression) fits the exact rational solution of the 1-D focusing NLS called Peregrine soliton. The Peregrine soliton can be seen as a breather-like solution on the finite background localised in space and time [61, 94, 218]. The Peregrine soliton is depicted in Fig. 3.3. It has the finite background everywhere besides the area around the zero point (Fig 3.3a). For the background equals to 1 amplitude of the breather at the maximum compression point is 3 (see Fig. 3.3b). Remarkable feature of the Peregrine soliton is the typical π-phase jump depicted in Fig. 3.3c, which is a signature of the fact that the amplitude reaches zero value (at $\xi = 0$).

More explicitly, error corrections discussed above give at the leading order:

$$\begin{aligned}
&\textit{For the position} && \xi_m = \xi_c + \mathcal{O}(\epsilon^{4/5}) \\
&\textit{Shape} && |\psi(\tau, \xi_m)| = a_0 \left(1 - \frac{4}{1 + 4a_0^2(\tau/\epsilon)^2}\right)[1 + O(\epsilon^{1/5})] \\
&\textit{Amplitude} && a_0 = \sqrt{\rho(0, \xi_c)} + \mathcal{O}(\epsilon^{1/5})
\end{aligned}$$

where ξ_m is the position of maximum temporal localization (explicit formula of which will be given in Sec. 3.2.2), ξ_c is the catastrophe point.

Above, term a_0 plays the role of the (finite) background level at the leading order. Hence, according to the formula, maximum amplitude is $\sim 3a_0$ up the rate of precision. Theory predicts that for the maximum amplitude will converge to the value $3\sqrt{2}$ with $\epsilon \to 0$.

[6] Symbol $\mathcal{O}$ (*Landau's symbol*) is used to show the asymptotic behaviour of functions (errors in our case). For example we can write $e^x = 1 + x + x^2/2 + \mathcal{O}(x^3)$.

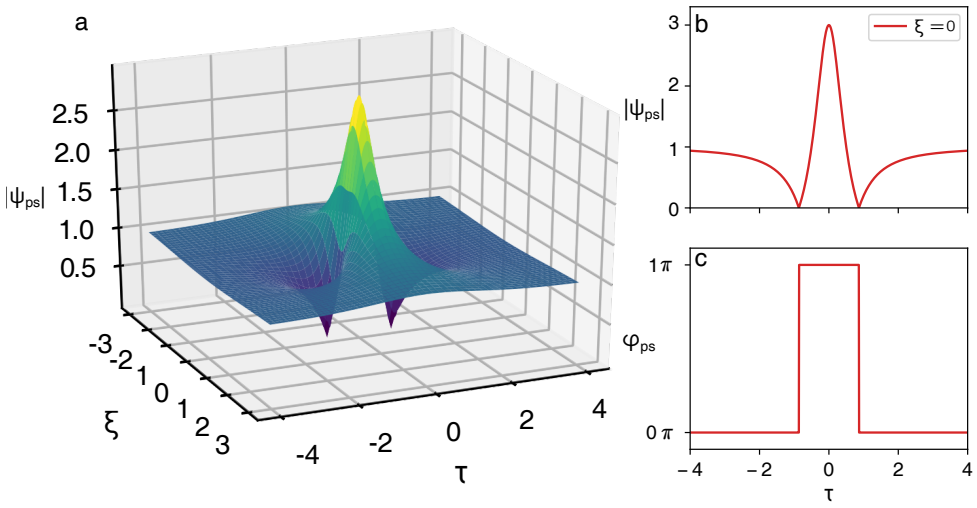

FIGURE 3.3: Analytical formula of the Peregrine soliton. (a) Spatio-temporal diagram. (b-c) Cross-section of amplitude and phase profile at the maximum compression point ($\xi = 0$).

Here it is important to stress that the mechanism of formation of the Peregrine soliton as regularisation of the gradient catastrophe is *completely different* from one connected to modulation instability [76, 90]. Indeed, as it was mentioned before the case of gradient catastrophe is universal, therefore it is present for the all variety of initial conditions that satisfy the requirements of the theorem, whereas emergence of the Peregrine-line breather from modulation instability requires very well defined initial conditions [218, 219]. Also, the regularisation has a local nature, so the above corrections to the shape of the singularity are valid only around the compression point.

Now, let's provide simulations of the full NLS equation in order to verify the results presented above. We start with the initial condition defined by $\sqrt{\rho} = sech(\tau)$ with no chirp $u = 0$; $\phi = 0$. The numerical solver is based on the step-adaptive finite-difference method including Runge-Kutta approach to solving a system of ordinary differential equations (for discussion of different integration methods see [21, 220, 221]). For the simulations, the form 3.2 of NLS equation with coefficient $\epsilon = 1/20$ was used. It is not possible to solve numerically cases with very low values of ϵ, due to the amplification of the numerical noise by modulational instability. Grid parameters are 2000 points from -4 to 4 for τ and 1500 points from 0 to 2 for ξ. Absolute tolerance of the ordinary equation solver is 10^{-10}. In Fig. 3.4a reader can find the resulting spatio-temporal diagram. For small values of ϵ (1/20 here) or high solitonic content [7] one can observe a cone of coherent structures (see Fig. 3.4a) after the gradient catastrophe point (for which the theory above is developed). Number of coherent structures is increasing with time. The whole dynamics can be separated into stages, at each stage number of coherent structures in increasing by one. The number of observed stages is directly proportional to

[7] For the considered initial conditions integer part of $1/\epsilon$ is equal to the exact number of solitons, while the fractional part describes the dispersive radiation content.[ASK ref!! michke]

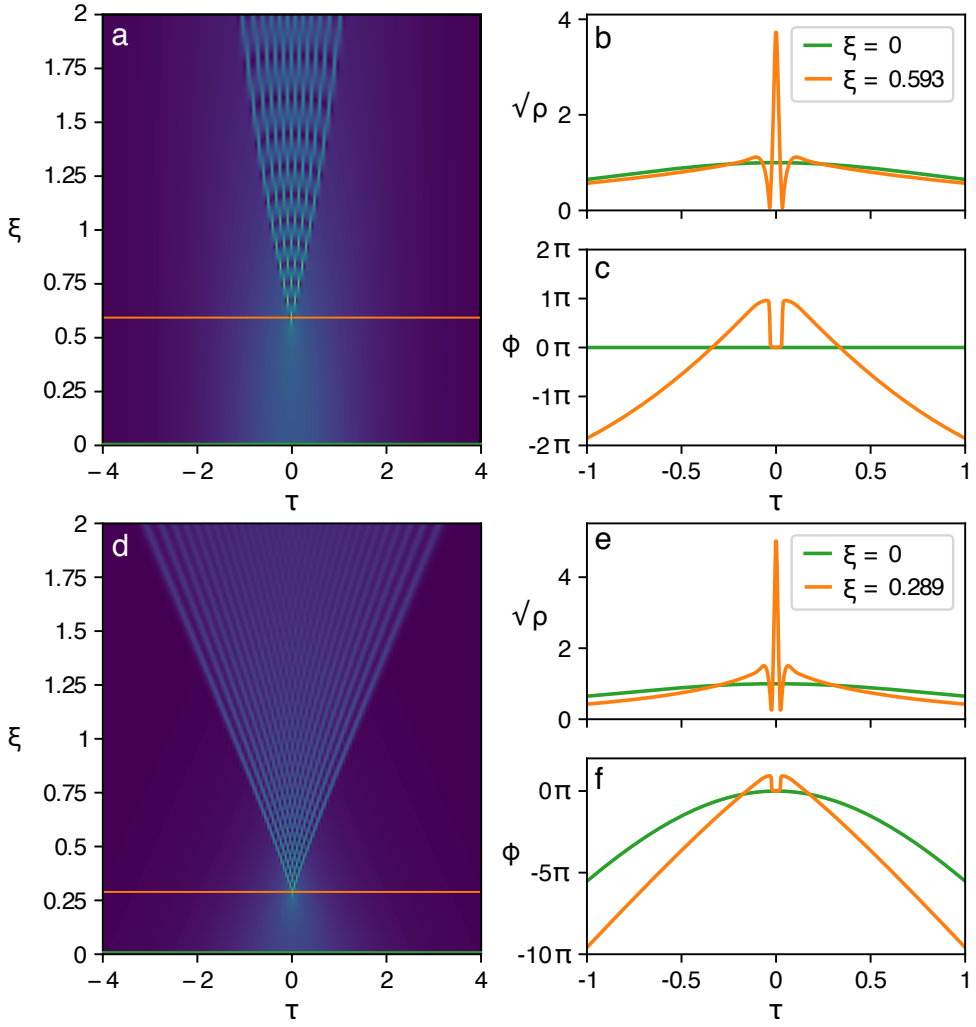

FIGURE 3.4: Numerical simulation of the focusing NLS equation. Behaviour at the gradient catastrophe point. Parameter ϵ in the simulation is equal to $1/20$. (a,b,c) Spatio-temporal diagram, amplitude and phase cross-section at the maximum compression point. $20sech(\tau)$ function is taken as initial condition. (d,e,f) the same but for the solitonless potential. $20sech(\tau)\exp[-i\mu\log(\cosh(\tau))]$, here $\mu = 2$.

the value of $1/\epsilon$. All further breather-like singularities inside the cone shown in the Fig. 3.4a are of the same genus [8] as the first one. After some point (not depicted on the picture) the order of the solutions is increasing. In literature it is known as *bifurcation point* [110]. In Fig. 3.4b-c the cross-section of the spatio-temporal plane showing the amplitude and phase close to the point of gradient catastrophe is depicted. Figure 3.4b demonstrates the amplitude ($\sqrt{\rho}$) profile at the beginning of simulations ($\xi = 0$) and the first maximum compression point. One can immediately find similarities with the Fig. 3.3b. The characteristic π-phase jump is also present in Fig. 3.4b, but due to the 2π periodicity it is turned upside-down.

It was mentioned before that the appearance of the PS is a local event

[8] The genus (or simply order) of solution connected to the Riemann theta-functions will be discussed later in the chapter dedicated to the inverse scattering transform 3.3.

and in general *doesn't depend on solitonic content* of initial conditions [217] (presence of the discrete values in the Zakharov-Sabbat spectrum). Here, I would like to illustrate this statement by taking exactly the same initial conditions and integration parameters as before, with the only one change: a special chirp $u = -\mu \tanh(\tau)$ or for the phase $\phi = -\mu \log(\cosh(\tau))$, where $\mu \geq 2$ is added to the initial *sech* profile. The initial conditions are depicted in Fig. 3.4e-f with green line. This particular chirp makes the initial condition completely solitonless [9]. This means that taking this special chirped Nsech profile we will obtain only dispersive radiation at the stationary state. In Fig. 3.4d the spatio-temporal diagram for the solitonless initial conditions is shown. The difference in dynamics is visible immediately. First of all, the gradient catastrophe happens much earlier $\xi_c \approx 0.29$ instead of 0.6. Second, the boundary of the cone is close to being straight. The angle of the cone is much wider. Third, the dynamics is scaled. Indeed, the width of the Peregrine soliton is narrower and the distance between different peaks is shorter in the case of the solitonless potential. Nevertheless, all the features of the gradient catastrophe are preserved: local Peregrine soliton shape, as well as π-phase jumps, are presented in Fig. 3.4e-f at the point of the gradient catastrophe.

3.1.2 Experimental evidence of the local Peregrine soliton emergence from deterministic initial conditions

In this section, we will demonstrate two results showing the applicability of the Tovbis-Bertola theorem to real experimental conditions. Both of them are made with simple Gaussian-like initial conditions. One of the experiments is done with the frequency-resolved optical gating technique (FROG), described in the section 2.1 of the previous chapter. Since a periodically pulsed signal can be used, the phase and power profiles are measured simultaneously, while the cut-back technique has been used to partially reconstruct spatial (ξ coordinate) dynamics. The second experiment employs an optical sampling (OS) oscilloscope. It was necessary to investigate all range of parameters, in order to verify the Tovbis-Bertola theorem at the limits of its applicability. OS technique demonstrated a good flexibility in terms of measurable power. Thus, it was employed even despite its inability to retrieve the phase information. The two experiments were realized in different laboratories. Here we will focus on the last one (using OS oscilloscope) that I have made in laboratory PhLAM, Lille, presenting only the most significant results obtained by our colleges. This investigation is published in the article [222].

The principal scheme of the experiment is depicted in Fig. 3.5. Laser pulse emitted by a Titanium Sapphire laser (equipped with an optical parametric oscillator) is spectrally filtered in order to achieve the desired values of ϵ. Then, the filtered pulse is injected into $400m$-long single-mode polarisation

[9] Corresponding Zakharov-Sabbat spectrum will be shown at the end of the chapter (Sec. 3.3.

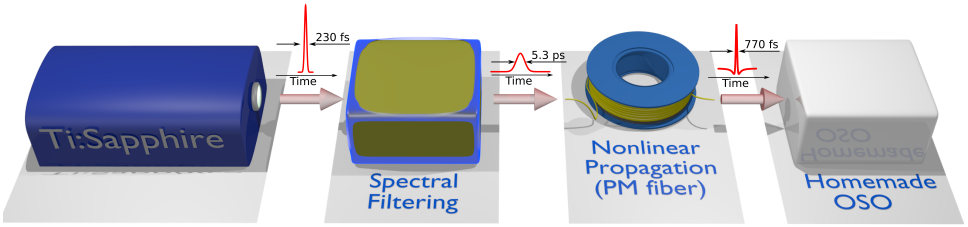

FIGURE 3.5: Principal scheme of the experiment implying optical sampling oscilloscope.

maintaining fiber, which is used as a nonlinear dispersive medium. Resulting intensity profile is studied with a homemade OS oscilloscope.

The detailed scheme of OS oscilloscope is shown in the picture 3.6. The OS oscilloscope is based on the mode-locked Ti:Sapphire laser (Coherent) emitting with 80 MHz repetition rate $\sim$140 fs-pulses at a central wavelength λ_p = 807 nm. A part of the pulse is used to pump optical parametric oscillator (OPO) (Coherent Chameleon Ultra II). Orientation of nonlinear crystal inside the OPO is chosen to obtain the output wavelength changed to 1525 nm, the wavelength suitable for experiments with telecommunication fibers. The choice of the fiber is reasoned by the wish to be fully described by the 1-D NLS. Indeed, nonlinear rotation of polarization [21] or interaction between different modes requires more complex models like vector NLS [223] or 2-D Gross-Pitaevskii equation [224, 225]. The first beam at 807nm is used as a pump for the OS, while the second one was a signal under investigation injected into the fiber. These two pulses are synchronized, which means that using a long (of the order of distance between two neighbour pulses) delay line it is possible to superimpose them inside a second-order nonlinear crystal.

However, it is not possible to provide optical sampling measurements of a narrow pulse using a wider one. Indeed, the Peregrine soliton which appears during the nonlinear propagation inside the fiber is much narrower than the initial pulse (see Fig. 3.4). Since the duration of 1525 nm and 807 nm pulses is approximately the same, we have to broaden the signal pulse at 1550 nm by applying a spectral filter. Also, it is important to keep the balance between the achievable power, spectral width and available fiber length, because the gradient catastrophe occurs at the certain point which is a function of the listed parameters. We estimated the necessary spectral width as 0.1 THz. Trying many techniques we have selected spatial filtering using a diffraction grating (GR50-0616 Thorlabs) and injection stage, as it is depicted in Fig. 3.6. The input beam diffracted by the grating has angular distribution of frequencies, therefore the injection losses naturally filter side frequencies. It has to be taken into the account that presented technique can induce a chirp of the signal, but during the experiment, significant effect wasn't observed. In Fig 3.7 experimentally measured spectra are depicted. The blue line corresponds to initial spectra at the output of OPO, the green line shows the filtered spectrum and the red line- spectrum after nonlinear propagation in 400m fiber, at the gradient catastrophe point. Using the filtering technique we shrank the

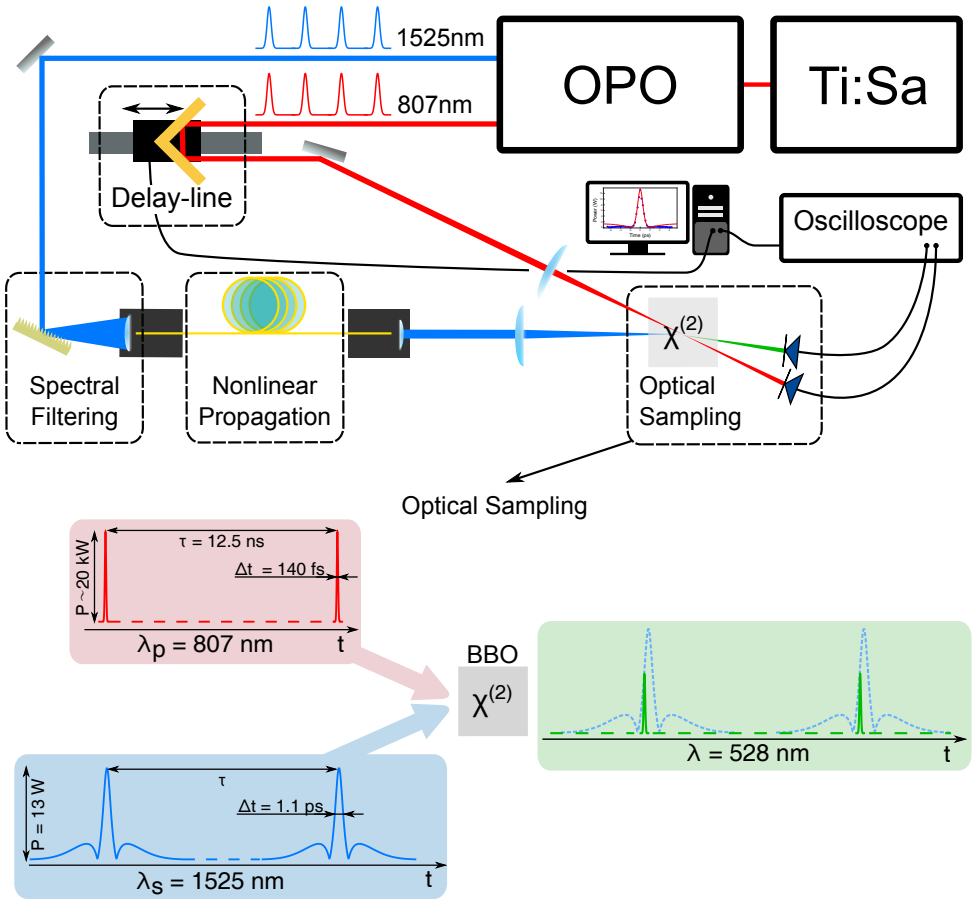

FIGURE 3.6: Detailed scheme of optical sampling oscilloscope (top). Signal sampling via sum frequency generation (bottom).

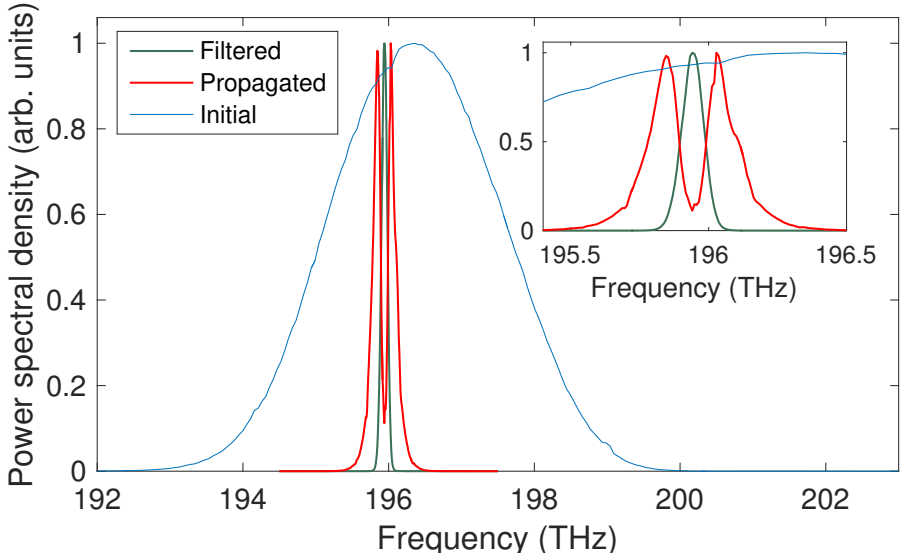

FIGURE 3.7: Spectral filtering and propagated pulse spectrum.

spectral width from 2.8 to 0.1 THz.

In Fig. 3.5 (bottom) the optical sampling process is depicted. After filtering and nonlinear propagation inside the optical fiber signal is directed to the $\chi^{(2)}$ crystal. After passing the delay line, the pump beam also enters the crystal (see Fig. 3.5 (top)). Typical duration of a coherent structure (conceivably a Peregrine soliton) is of the order of 1 ps, while the pump pulse has a 140 fs width at the half maximum. Period of the pump pulses (denoted as τ on the bottom picture) is the same as signal pulses, therefore moving the delay line it is possible to superimpose a pump pulse with a particular part of the signal in a periodic manner inside the BBO crystal. Here we use the same sum frequency generation process as explained in the section 2.2.2: type I phase-matching in BBO crystal. Phase-matching angle is 12.5^o. The efficiency of this process is relatively low, so the power of the pump pulses was set to $\sim 20kW$ to enable detection of the 13 W (peak value) signal pulses. The output signal at 528 nm is detected with a highly sensitive photodiode (MenloSystem FPD310-FV) having a gain of 10^4 and a rise time of 0.7 ns. Parasite light is filtered out with a short band-pass filter (FF01-770/SP-25 Semrock). It is important to point out that experimental results will change if the photodiode bandwidth is not appropriate. This point is widely discussed in the supplementary materials of the article [53]. The residual pump is registered with a simple p-i-n photodiode as a reference for automatic data treatment. Both signals are acquired with a fast oscilloscope (Lecroy WaveRunner 104MXi-A, bandwidth 1 GHz, 10 GS/s).

We have designed a special software which allows automatizing all the process of signal's intensity profile measurements. Here we provide exact steps of data acquisition process, including the treatment algorithm.

First of all, we align manually the delay line in order to see maximum visible SFG signal. The delay line is equipped with a high precision motorised 1-D translation stage similar to the one used in the compressor of the Time

Microscope. Using the delay line we choose the beginning of the measurement window (position where the signal is no longer visible on the oscilloscope). Further, the software requires input data: initial motor position (mm), size of the window (mm), step (mm), the temporal window of the oscilloscope (sec) and a number of averaging. The accuracy of the motor is of μm for the distances of the order of mm. For example, the data presented in Fig. 3.8 (green) is recorded with parameters: 7.6 mm position, 2 mm window, 40 μm step, 1 μsec of oscilloscope recording and 2 times averaging. Initial motor position depends on manual tuning. Here the signal is averaged only two times, because of the presence of jitter and power fluctuations, so the recording time has to be as short as possible. However, recording of the initial pulse is much less sensitive to the power fluctuations, so data was averaged 5 times, with the step 0.01 mm. During the experiment several configurations of parameters were tried, parameters presented above are chosen as optimal.

Then the acquisitions were provided according to the following algorithm: (i) delay between signal and pump has to be found before recording. In order to increase the precision, the motor position which corresponds to the maximum of the signal must be chosen. The program searches for the maxima of the pump and the signal and then automatically determines the delay. A shift is present because of the optical path and cable length differences. We assume that this shift doesn't change during experiments. (ii) The program begins recording from the starting point set before. It reads data from oscilloscope over the window set before as well (1 μs typically). This corresponds to 80 recorded signal pulses. At the next step script averages all the 80 values. The resulting value is taken as the signal power of at the given delay length. (iii) Program repeats the same measurements over the whole window. This gives 50 points for propagated signal and 160 for initial. (iv) all the recording procedure is repeated 10 times in order to check stability and provide additional averaging. At this step, additional corrections are made to get rid of slow temperature fluctuation effects. More explicitly, we shifted the data in time to superimpose maxima, because temperature fluctuations lead to a change of the fiber length.

Before recording, we have provided detailed estimation of the resolution of our homemade device. For this purpose, we recorded a cross-correlation trace. It is easy to do in the presented configuration just by overcoming the filtering part.The FWHM of the cross-correlation function is around 440 fs. We suppose that emitted pulse has a hyperbolic secant shape with a width of 200 fs (datasheet). We also assume the Gaussian impulse response of filtering tool $h(t) = e^{-(t/\tau)^2}$, therefore the appropriate value of τ is 125 fs. Hence, the temporal resolution of our OS oscilloscope is 250 fs.

Results of recording are shown in Fig. 3.8. Green stars represent experimentally recorded propagated pulse, blue circles - initial pulse. The delay distance was recalculated to the picoseconds using a double-pulse reference with a known separation time as it was done in the previous chapter. Power

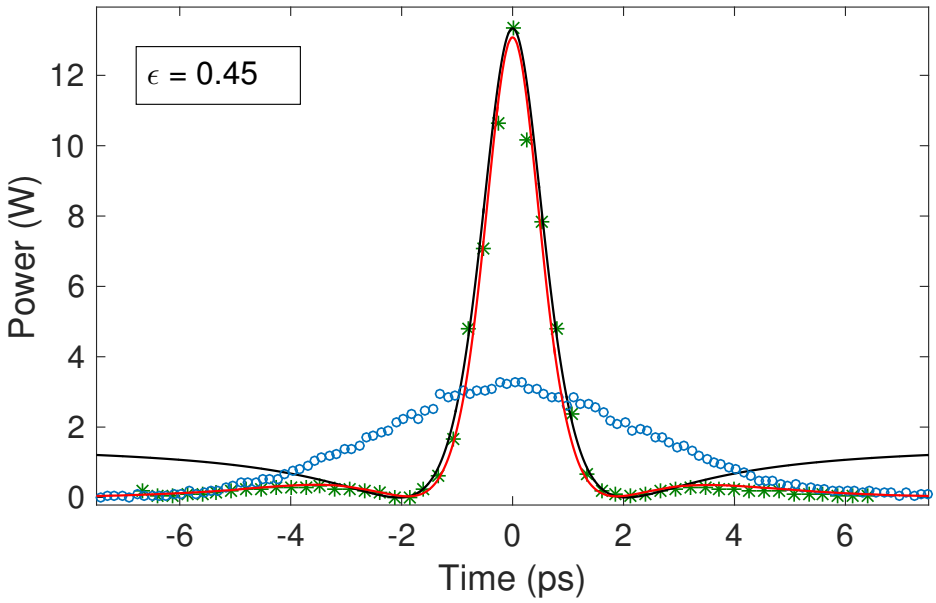

FIGURE 3.8: Results of experimental measurement of a pulse profile at the point of the gradient catastrophe with the optical sampling oscilloscope. Blue circles and green stars show the measured data before propagation in the fiber and at the gradient catastrophe point, the black line is analytical Peregrine soliton formula applied without a fit, red line corresponds to numerical simulations of the experimental data taken as initial conditions while assuming a constant phase.

scale was retrieved by measuring average power of the signal under investigation and applying the formula:

$$P(t) = \frac{P_m(t) * P_{avg}}{\nu_r \int_{t_b}^{t_e} P_m(t)dt}$$

where P_m is voltage measured with the oscilloscope, t_b and t_e it is the beginning and the end of the window of measurements, ν_r is the repetition rate. Red line represents numerical simulation of the NLS equation in the form $iA_z + \frac{|\beta_2|}{2}A_{tt} + \gamma|A|^2A = 0$. As initial conditions for the NLS solver we used Gaussian fit of the pulse recorded before propagation in the fiber (blue circles). In this case we employed the symmetrized split-step Fourier method [226] of integration of NLS described for example in [21]. Following parameters were used: integration distance is 396 m with a step 10^{-4} m, real fiber parameters β_2 = -16 ps^2/km and γ = 2.4 $W^{-1}km^{-1}$. Black line is the analytical formula of the Peregrine soliton in experimental variables:

$$A_{PS}(z,t) = \sqrt{P_0}\left[1 - \frac{4(1+2iz/L_{NL})}{1+4(z/L_{NL})^2+4(\omega_{mod}t)^2}\right]e^{iz/L_{NL}} \tag{3.8}$$

where P_0 is the power at the gradient catastrophe point, $L_{NL} = 1/\gamma P_0$ and $\omega_{mod} = \sqrt{\gamma P_0/|\beta_2|}$. P_0 is taken at the maximum of initial pulse. For this arrangement value of ϵ is equal to 0.45 which is far from the limit considered in

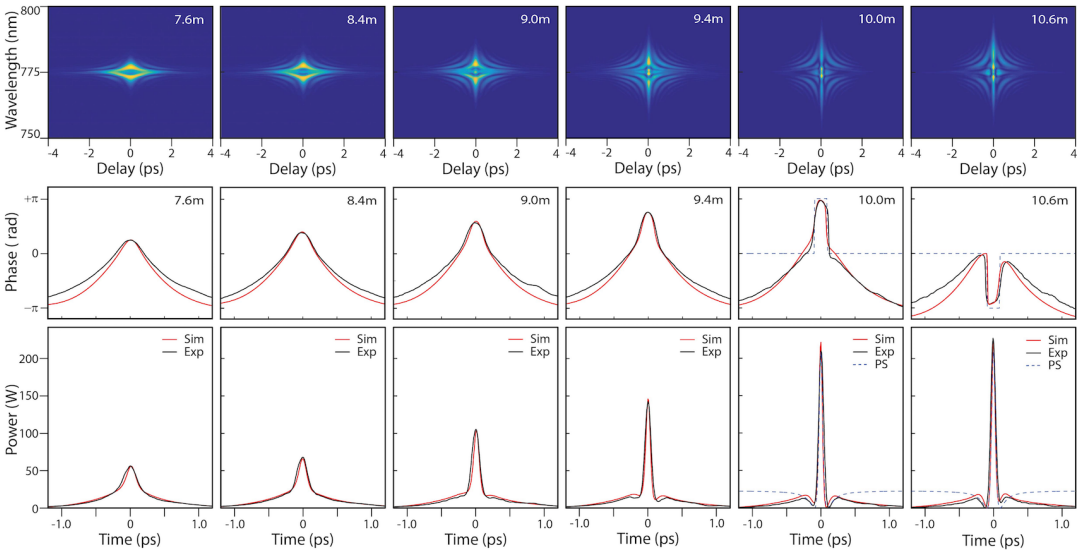

FIGURE 3.9: Measurements of a single pulse power and phase profiles in an optical fiber with the frequency-resolved optical gating technique. (top) FROG traces measured at different propagation distances using the cut-back technique. (middle and bottom) corresponding power and phase profiles. Measurements are provided in Institut FEMTO-ST, CNRS Université Bourgogne-Franche-Comté, Besançon, France.

the Tovbis-Bertola theorem. Remarkably, this effect with close experimental parameters including the value of ϵ was observed in 1-D watertank [227] but was not considered in the framework of the theorem of Tovbis and Bertola. Applicability of the word Peregrine soliton to the detected structure will be discussed later in this chapter.

Experimental results obtained with the FROG (made in institute FEMTO ST, Besançon) setup are depicted in Fig. 3.9. In this case, Ge-doped highly nonlinear fiber is used. Fiber parameters are β_2 = -5.23 ps^2/km and γ = 18.4 $W^{-1}km^{-1}$. In Fig. 3.9 (middle) power profiles of a pulse having (initially) 1.1 ps duration at different propagation lengths are shown. At the maximum compression point recorded coherent structure is fitted with the analytical formula of Peregrine soliton (dashed line). Phase profile experiences the π-phase jump. This dynamics is, indeed, very similar to one explained in the previous section. Initial pulse has the value of $\epsilon \sim 0.17$, which corresponds to approximately to 6 solitons in the initial hump.

Concluding, I would like to point out that this behaviour of the NLS system (shown in Fig. 3.9) is known in fiber optics community since many years [131, 228, 229], but was never considered form this perspective. Remarkably, it is included in the classical books on nonlinear fiber optics and known as 'high-order soliton pulse compression'. Many attempts were made to get rid of the 'pedestal' of the coherent structure [230]. Tovbis-Bertola theorem reveals fundamental nature of this phenomenon and provides new insights.

Figs. 3.8 and 3.9 clearly show the reported universality of the regularization of the gradient catastrophe is observed during the experiments described well by 1-D NLS equation. Coherent structure well fitted by the Peregrine soliton appears over a wide range of experimentally available initial conditions. The result described by the Tovbis-Bertola theorem is robust and works even far from the semi-classical limit.

3.2 Role of Tovbis-Bertola scenario in dynamics of the partially-coherent waves

Focusing NLS model demonstrates a wide range of applicability in different physical systems. Remarkably, it plays a role of a connection point between such distant areas as hydrodynamics and nonlinear optics [59]. Unidirectional deep-water gravity waves could be described at the leading order by the focusing NLS. Hence, this connection could be employed in order to provide fully-controlled table-top optical experiments for investigation of the rogue wave phenomena observed in 1-D waves propagation in the water tank.

Integrable turbulence framework requires stochastic initial conditions. Since the signal is non-periodic, more advanced techniques of single-shot ultrafast optical measurements are needed, for example HTM or SEAHORSE.

In this section, results of the experimental investigation for partially-coherent light dynamics in an optical fiber are presented. We provide extensive numerical simulations of this dynamics using real experimental parameters. Employing numerically obtained as well as experimental data we show the crucial contribution of the Tovbis-Bertola mechanism to the formation of the Rogue Waves in the context of integrable turbulence.

3.2.1 Nonlinear propagation of the partially-coherent waves in optical fibre: ultrafast measurements with the HTM and SEAHORSE

In order to understand the role of the Tovbis-Bertola scenario in the rogue waves (RW) formation process, we performed extensive experimental investigation using the HTM and SEAHORSE. Recording the phase and power profiles of the random signal simultaneously we were able to instigate the RW formation mechanisms by comparison with numerical simulations of the 1-D NLS equation.

High precision and the wide window of phase and power profiles measurements allow us to prove the nonlinear holography: recorded complex envelope of the signal at the output of an optical fiber can be backpropagated numerically to the initial state. Therefore, we can reconstruct the full spatio-temporal diagram of the *experimentally recorded* stochastic signal.

3.2.1.1 Numerical simulation of 1-D NLS with partially-coherent waves

It was shown [53] that statistical properties of partially-coherent light are changing after nonlinear propagation in a single mode optical fiber. Indeed, as it was explained in the Introduction 1.1.3.3, starting probability density distribution is exponential for the $|\psi|^2$. After the propagation of the light in focusing nonlinear dispersive media probability density function becomes 'heavy-tailed', i.e. probability of the high amplitude event to appear is increasing. This fact becomes intuitively clear from the spatio-temporal diagram depicted in Fig. 3.10a.

The diagram shows the partially-coherent wave having the average power P_0 = 2.6 W and the spectral width $\Delta\nu$ = 0.1 THz which propagates in a single-mode fiber with parameters β_2 = -20 ps^2/km and γ = 2.4 $W^{-1}km^{-1}$. We take the 1-D NLS equation in the form widely used experimental optics (Eq. 3.1). As one can see, high amplitude coherent structures (such as one depicted in Fig. 3.10b,c by orange) appear from completely smooth initial condition (green in the same figures) after $\sim$ 200 m of nonlinear propagation. Presence of these high amplitude structures have a crucial contribution to the statistical distribution, leading to the 'heavy-tailness'. We underline that this high amplitude coherent structure (Fig. 3.10b,c) locally matches with the Peregrine soliton formula. In order to plot the red line in Fig. 3.10b,c we simply substitute the fiber parameters and initial conditions (green line) peak amplitude to the Peregrine soliton formula.

The numerical model of the initial random field with Gaussian statistics is constructed by a classical random phase scheme [36, 53, 231] we produce a Gaussian spectrum and add a uniformly distributed [-π, π] random phase to each Fourier component. In this way, we obtain a complex function which is similar to a signal produced by the ASE source. The step-adaptive NLS equation solver is similar to one explained in the previous section.

Numerical simulation is a very important preliminary step before the start of an experiment. It allows one to carefully choose the investigated range of parameter and anticipate some important results. All the numerical simulations of partially-coherent light dynamics presented in this chapter are provided in the way described above.

3.2.1.2 Adaptation of the HTM and SEAHORSE to the partially-coherent light measurements

Partially-coherent light source. Experiments with the TM were provided in order to investigate the dynamics of partially-coherent waves in an optical fiber. Experimentally, partially-coherent initial conditions are obtained with an amplified spontaneous emission (ASE) source from Highwave Optical Technologies operating around the central wavelength 1550 nm and at output power $\approx$ 7 dBm and corresponding diode current 1.5 mA. During the experiment, we were able to control the spectral width of the partially-coherent wave. It has a paramount importance since the spectral width defines the temporal coherence and contributes to the characteristic dispersion length ($L_D = \frac{1}{\beta_2 \Delta\omega^2}$). The tool we used is a fully programmable optical filter

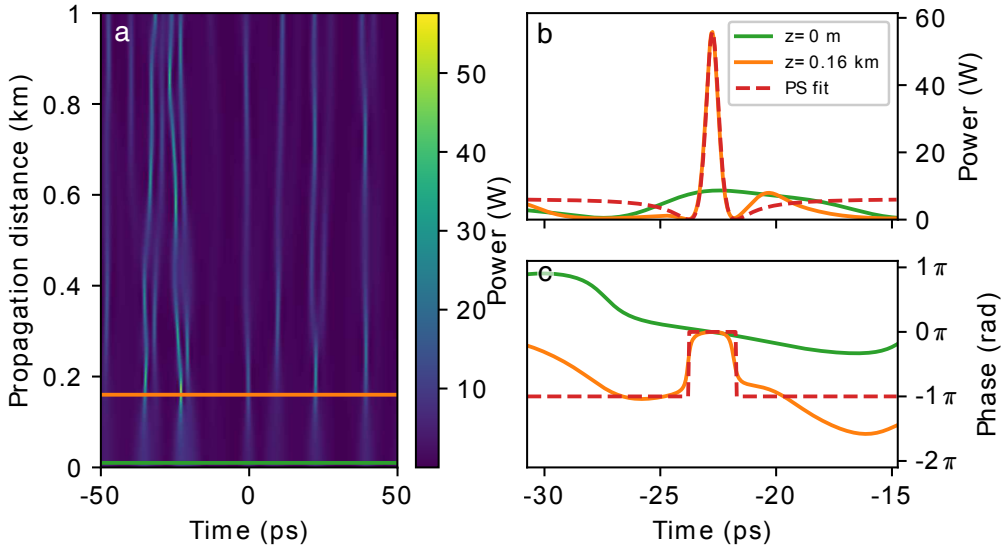

FIGURE 3.10: Simulations of the random wave propagation in the focusing NLS system. Simulation parameters are close to the experimental: β_2 = -20 ps^2/km and γ = 2.4 $W^{-1}km^{-1}$, average power $P_0 = 2.6\ W$ and spectral width $\Delta\nu = 0.1\ THz$. (a) Spatio-temporal diagram. Green and orange lines correspond to 0 and 160 m respectively. Orange line shows the distance at which the first localised structure is appearing (-23 ps). (b) Power profile around the maximum of the first localised structure and initial conditions at the same time. Colours are conserved. An application of the Peregrine soliton formula is depicted with red lines. (c) The same (as b) for the phase profile.

based on high resolution Liquid Crystal on Silicon technology (Waveshaper 1000S, Finisar) operating in the range 1527.4 nm to 1567.5 nm with 8 pm resolution (central wavelength was set to be 1562 nm - which corresponds to one of the maxima of the ASE spectrum). The output signal is amplified by an Erbium-doped fibre amplifier (Keopsys) the photo-diode current was set to 3.462 A which gives the output power 39.2 dBm (8.3 W). Power which contributes to the nonlinear length ($L_{NL} = \frac{1}{\gamma P_0}$) is controlled before the injection into the optical fiber with a $\lambda/2$ plate and a polarization beam splitter cube (PBS). The ratio L_D/L_{NL} defines the dynamics of the partially-coherent light in the nonlinear media in the 1-D NLS model. All the elements constituting the light source are fiber connected. ASE and programmable optical filter are connected directly with single mode PM fiber with FC/APC connector, filter and amplifier with two similar optical fibers (amplifier's input and output are pigtailed) through APC-APC connector.

Injection and optical fiber. The output of the amplifier is pigtailed by a single mode polarization maintaining fiber (PMF) with FC/APC connector (in order to prevent any back-reflection). Injection into the long fiber was provided with two 3-axis micro-precision translation stages equipped with the f=4.5 mm aspherical lenses. As it was explained before, $\lambda/2$ plate, PBS cube and another $\lambda/2$ plate are installed between the translation stages to control the injected signal's power and it is polarisation. The polarization control is important because the fiber we used as a nonlinear medium is also PM, hence

the light must be injected along one of the fiber's birefringent axes. Otherwise, the experiment is no longer governed by 1-D NLS, but rather coupled pair of NLS equations [21]. The fiber used as the nonlinear medium is 500 m-long PMF Fibercore HB-1550T with dispersion parameter $\beta_2 \approx -22\, ps^2 km^{-1}$ (experimentally measured see the Fig. B.3 in Appendix B), the nonlinearity coefficient estimated as $\gamma = 2.4\, W^{-1} km^{-1}$ (measured relatively and proved by numerical simulations. See Appendix B), numerical aperture 0.14 - 0.18 and Mode Field Diameter 7.0 - 9.2 μm. Light power and polarization transmitted to the TM were regulated by another $\lambda/2$ plate and PBS cube. It is collimated with another high precision translation stage equipped with a f = 11 mm aspherical lens.

In order to be able to increase the spectral width of the signal to 1 THz, we have to move the center of the signal's spectrum to 1561 nm. This value doesn't correspond exactly to the maximum of amplified spontaneous emission of the erbium amplifier, but close enough to minimize the noise. The CW source is tunable with a good accuracy $\pm 6\, pm$ and the central wavelength of the continuous wave source was fixed 1561.37 nm (see the Fig. 2.26c).

3.2.1.3 Partially-coherent light measurements with the HTM

After passing all the calibration and tuning procedures described in details in Ch. 2, we are able to record the signal corresponding to the partially-coherent wave dynamics with resolution $\sim$ 250 fs using the HTM and $\sim$ 80 fs with the SEAHORSE. The window of measurements was chosen to be 40 ps. Some results shown in this section are published in [200].

Initial conditions. We start with the recording of the initial conditions: light emitted by the ASE source, filtered and amplified. We already presented some typical snapshots of the initial conditions used for the numerical spectrum reconstruction (see Fig. 2.29e-f). Figure 3.11a,b shows the power spectral density plot of the random light at the input of the HTM and original ASE spectrum (blue line). The Gaussian spectrum shaped with the programmable optical filter had the widths 0.05, 0.1, 0.5, 0.7 THz. For the broad spectrum (0.7 THz) we can observe a sharp jump in power density around the 191.2 THz (see the log-scale plot Fig. 3.11b). This is the signature that we are out of operating frequency range of the programmable filter. It was always possible to shift the central frequency to some higher value, but I would like to recall about the presence of interplay between operating range of the filter, tunable CW source and spontaneous emission in the amplifier. Our criterion was the lowest possible noise on the recorded signal. Since the interference of the signal with the noise of the amplifier contributes the most, we kept the central frequency of the signal at the value which is the closest possible to the maximum power of the noise. However, this minor detail doesn't affect the accuracy of the experiment.

The snapshots of the ASE emitted signal recorded with HTM are depicted in Fig. 3.12. As one can see the ASE signal contains random power oscillations. The characteristic duration of the structures is proportional to $1/\Delta\nu$, where $\Delta\nu$ is the spectral width of the ASE light. Indeed, the signal of smallest

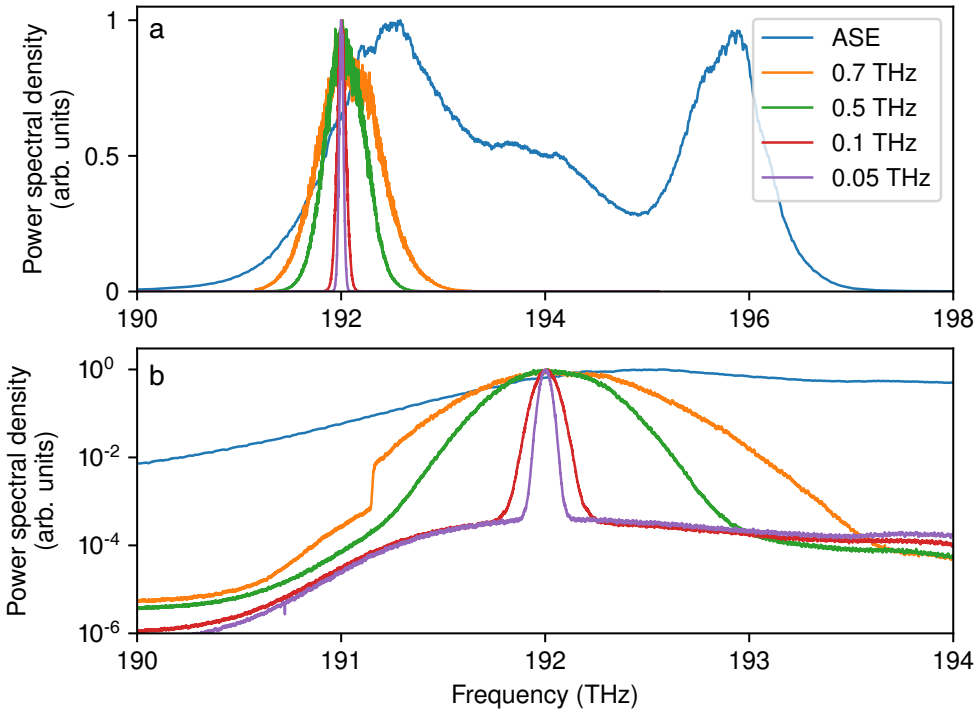

FIGURE 3.11: Experimentally measured spectra. (a) Original spectrum of ASE light source (blue) and power spectral density of signals after filtering and amplification. (b) the same in the log-scale and zoomed around the 192 THz.

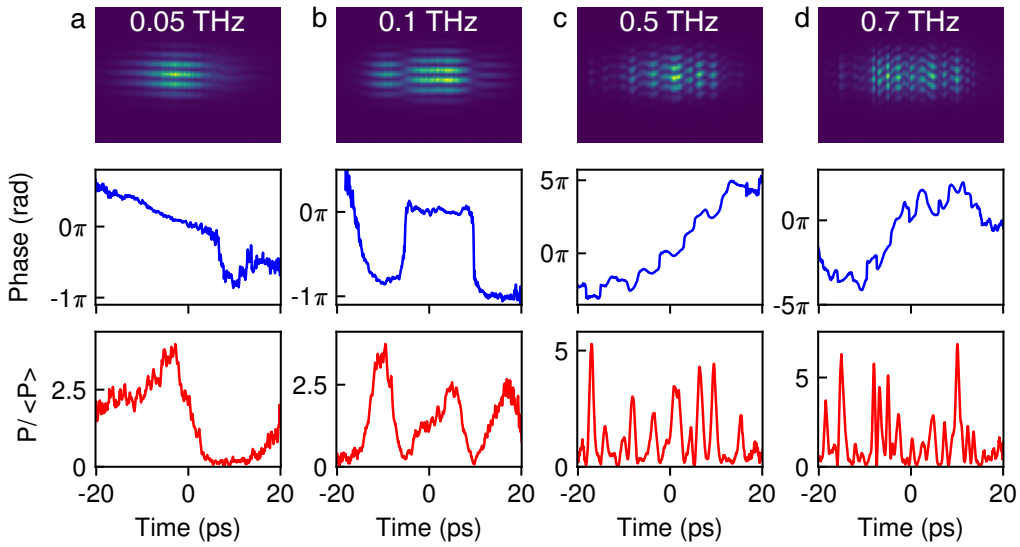

FIGURE 3.12: Recording of ASE emitted signal with the HTM. (a-d) Demonstrate the typical snapshots of the ASE signal and corresponding phase and power profiles. The spectral widths of the recorded signal were 0.05, 0.1, 0.5, 0.7 THz (depicted from left to right).

measured spectral width (0.05 THz) contains only one structure, 0.1 THz signal contains three, 0.5 THz - around nine, 0.7 THz - more than twelve. The phase profiles contain several π-phase jumps in the moments when power tends to zero. It is also important to underline that very often the phase is quasilinear inside a given structure (see Fig. 3.12 a and b (the structure in the middle of the frame)).

Nonlinear dynamics of partially-coherent [10] can be determined by the ratio of the typical initial condition duration and the duration of the fundamental soliton $\sqrt{\beta_2/\gamma P_0}$. Therefore, we have to investigate a wide range of parameters in order to observe all variety of possible scenarios. Indeed, in order to choose the most illustrative range of parameters we recorded all the combination of signals at the output of 400 m PM fibers with spectral width 0.05, 0.1, 0.5, 0.7 THz and average powers 0.5, 1, 2.6, 4 W. Here we will present only some of them.

Role of the average power. Let's fix the spectral width to the value 0.1 THz and change only the average power. Experimentally the power was controlled by combination of $\lambda/2$ plate and PBS cube. Figure 3.13 shows how the spectral width changes at the output of the PM fiber. We observe a significant spectral broadening that increases with the power. Observed spectra are the result of the interplay between two effects: non-resonant four-wave mixing and group velocity dispersion [125, 233]. This effect in the zero dispersion limit [11] was described by J. Manassah [122]. Also, due to the initial asymmetry and Raman effect, the spectrum evolves in slightly asymmetric was. This is remarkably visible in the log-scale plot (Fig. 3.13b).

Tovbis-Bertola scenario. In order to observe the scenario of regularisation of the gradient catastrophe discussed in the beginning of this chapter, we have to choose the range of parameters in the way that the first step of formation of the local Peregrine soliton will be likely at the output of the fiber. For the 400 m fiber we set the spectral width to 0.05 THz and average power to 0.5 W. Looking at the initial stage of the nonlinear dynamics we are able to distinguish the evolution of each coherent structure separately, before the moment when they start to interact.

Another criterion is that the typical size of the initial structures has to be larger than the size of fundamental soliton $\sqrt{|\beta_2|/\gamma P_0}$. This will move us closer to the semi-classical limit considered by A. Tovbis and M. Bertola. Indeed, the coefficient $\epsilon = \sqrt{L_{NL}/L_D} = \sqrt{|\beta_2|/\gamma P_0 T_0^2}$ has to be as small as possible (in the theorem it tends to zero). T_0 is proportional to $1/\Delta\nu$ (the spectral width). ϵ decreases with power as $1/\sqrt{P_0}$ and with spectral width as $\Delta\nu$. Therefore, it is much more efficient to decrease the spectral width.

[10] Due to the spontaneous emission, phases of distinct Fourier components are uncorrelated, therefore according to the Central limit theorem this leads to the Gaussian statistics of the real and imaginary part of the signal [232].

[11] Here, it is important to distinguish dispersionless and zero dispersion limits. The first limit was used in the beginning of the chapter when we neglected the quantum pressure term in the expanded system of equations 3.4 and 3.5, while the second simply implies that the dispersion term in the NLS equation is set to zero.

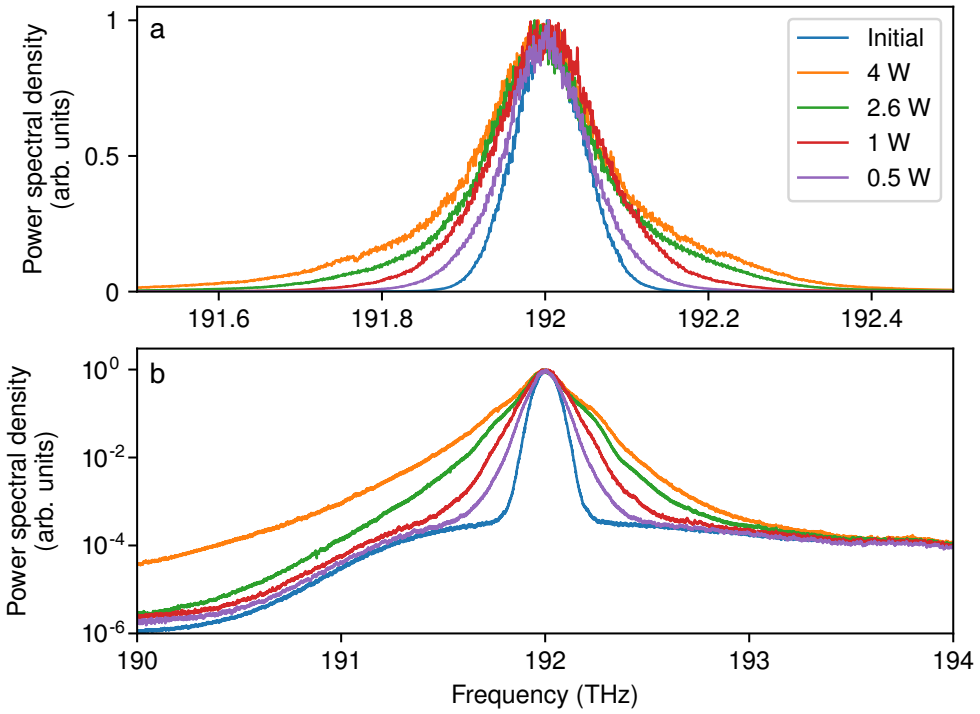

FIGURE 3.13: Experimentally measured spectra of the partially-coherent signal having the initial width 0.1 THz after propagation in the 400 m PM fiber. (a) Spectra of the output signal with different average powers (0.5, 1, 2.6 and 4 W) (b) same as in a, in log-scale.

Thus, we have chosen initial parameters of the partially-coherent light as follows: 0.05 THz - spectral width and 0.5 W of average power. Snapshots recorded at the output of the 400 m PM fiber are depicted in Fig. 3.14. Here we can clearly observe the process of regularisation of the gradient catastrophe. Snapshot are ordered from left to right according to the stages observed previously in Fig. 3.9.

I would like to stress that here we did not reconstruct the dynamics of certain initial hump [12] like it is done in Fig. 3.9. Here, we are able to observe such pictures because of the presence of similar initial humps with slightly different peak powers, so the gradient catastrophe happens at different positions.

3.2.1.4 Comparison with the numerical simulations

An important step of recording is the comparison with the numerical simulations. In one of the following sections (Sec. 3.2.1.7) we will provide a statistical analysis of the experimentally recorded incoherent light and compare it with numerics. Here, I would like to demonstrate similarities in the local dynamics and shapes of coherent structures which emerge during the nonlinear propagation. In order to provide the comparison we have chosen the

[12] We will provide the full dynamics reconstruction using the Nonlinear Digital Holography in one of the next sections (Sec. 3.2.1.6)

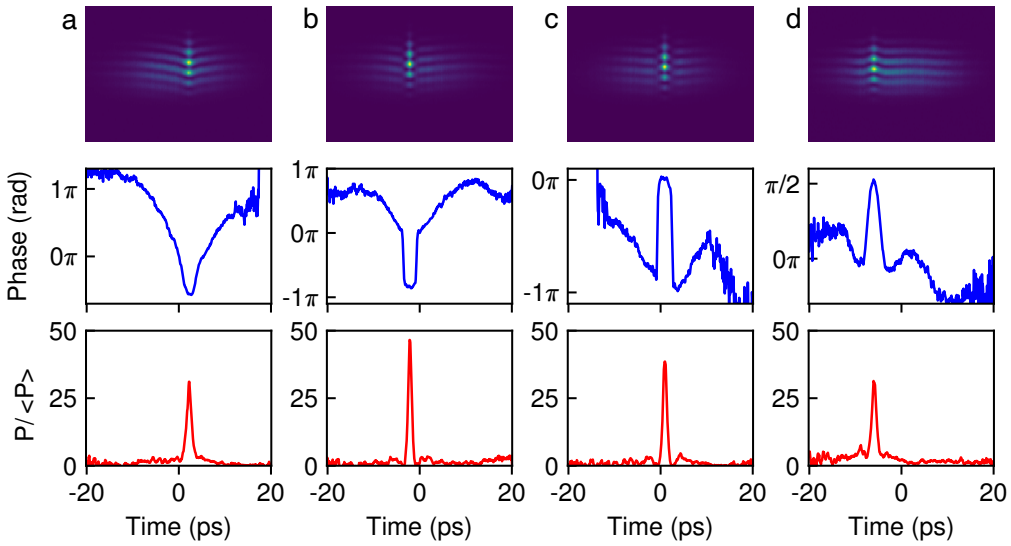

FIGURE 3.14: Observation of the different stages of formation of the localized Peregrine soliton with HTM. Initial partially-coherent light has 0.05 THz spectral width and 0.5 W average power. Snapshots are recorded at the output of the 400 m PM fiber.

most illustrative initial parameters of the signal: 0.1 THz of spectra width and 2.6 W average power. Looking through thousands of recorded snapshots, we extracted four of the most interesting.

Chosen snapshots depicted in Fig. 3.15b-e. The reconstructed phase and power profiles are plotted below with blue and red lines respectively. Snapshots b and c were chosen because of the complex structures that contain multiple (3 in b and 4 in c) connected peaks. They resemble stages of multisoliton initial conditions evolution. Also, snapshots b and c are interesting because of the opposite phase profile curvature. The snapshot d has the maximum peak power among all snapshots from the analysed set. The peak power is ∼40 times greater than the average power of the injected light, i.e. more than 100 W. I would like to attract the attention of reader to the phase of this high amplitude coherent structure. The phase is linear with a visible inclination. According to the phase calibration curve (see Fig. 2.26) this means that there is a frequency downshift. It is known that for high amplitude pulses propagating in optical fiber the intrapulse stimulated Raman scattering effect can lead to the frequency downshift [21, 234]. Finally, the snapshot e shows a Peregrine soliton-like structure similar to one obtained from deterministic initial conditions (Sec. 3.1.2). It has all the signatures of the Peregrine soliton which emerges as a regularization of the gradient catastrophe, including the π-phase jump.

The numerical simulations of the partially-coherent light propagation in the optical fiber are provided in the way described at the beginning of the section (Sec. 3.2.1.1). We used the NLS equation in the form 3.1 with experimentally estimated fiber parameters (Sec. 3.2.1.2, Appendix B): β_2 = -22 ps^2/km and γ = 2.4 $W^{-1}km^{-1}$. Phase and power profiles found in numerical simulations are depicted in Fig. 3.15f-i. As reader can see we managed to find

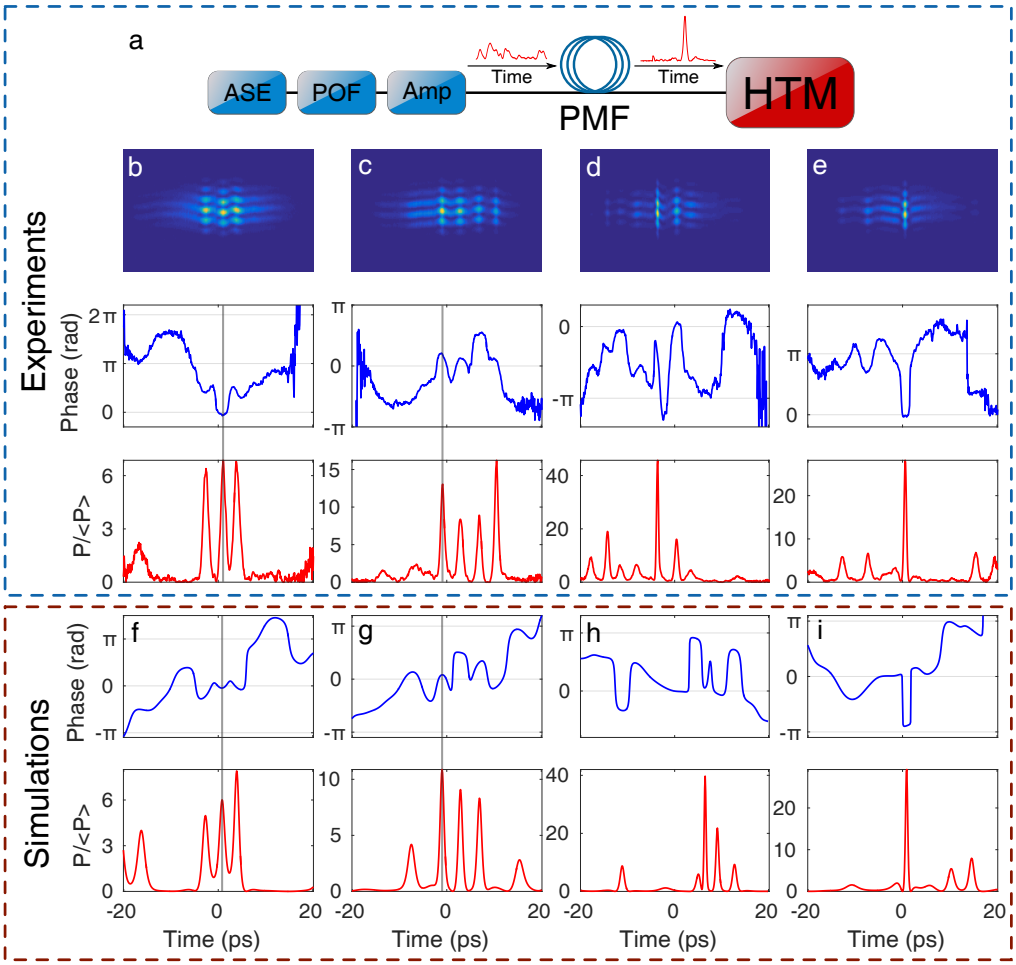

FIGURE 3.15: Nonlinear random waves measured with the HTM setup. (a) Scheme of experiment. Partially-coherent light filtered and amplified is injected into the PM fiber and detected with the HTM. (b-e) Snapshots of the random waves recorded with the HTM, recovered phase (blue) and amplitude (red) profiles. (f-i) Corresponding numerical simulations demonstrating the same power and phase profiles.

the exact analogue of coherent structures measured with HTM including the temporal width and particular phase behaviour. However, the absence of the Raman scattering term in the propagation equitation doesn't allow us to find the analogue of Fig. 3.15d in numerical simulations. Nevertheless, we present the numerical simulation where potentially similar structures can be observed. The same initial conditions as in Fig. 3.15h numerically propagated with Raman scattering term can be found in Appendix D.

3.2.1.5 Partially-coherent light measurements with the SEAHORSE

In the previous section, we demonstrated that HTM is the appropriate tool for the measurements of nonlinear dispersive waves in optical fibers. Temporal resolution of the HTM (250 fs) is smaller than the typical width of the measured structures. This means that it is also possible to provide the

same kind of measurements using the SEAHORSE setup, which provides even higher resolution (80 fs) and is free of the signal's aberrations.

Figure 3.16 shows the partially random wave recorded with the SEAHORSE. In order to provide the comparison we used exactly the same experimental parameters: 400 m PM fiber with β_2 = -22 ps^2/km and $\gamma = 2.4\ W^{-1}km^{-1}$, ASE emitted light with 0.1 THz spectral width and 2.6 W average power. The first row in Fig. 3.16 shows the 'temporal holograms' of random waves recorded with the SEAHORSE setup. The second and third rows show the extracted phase and amplitude profiles. However, on this stage, it is just a 'blurred' replica of the signal. Further, we numerically adjust the 'focus' of the Time Microscope and obtain the real image of the random waves (depicted in the fourth and fifth rows of the Fig. 3.16). We used the value of the second-order dispersion that corresponds to the one found numerically reconstructing a single pulse as well as estimations with the compressor parameters (see formula 2.16). This value was -0.21 ps^2. Division by the averaged envelope was provided after the tuning of the digital 'focus'. Thus, the third row is shown without division by the envelope, while the fifth with.

I would like to highlight the fact that we managed to find again exactly the same set of structures as ones shown in Fig. 3.15. Indeed, pictures a and b in the Fig. 3.16 contain the similar multipeak structures as ones depicted in Fig. 3.15b,c,f,g with remarkable resemblance in the phase and power profiles. Fig. 3.16c shows the high-amplitude structure affected by the stimulated Raman scattering (similar to Fig. 3.15d). The peak power is again 40 times greater than average. As in the previous case the structure like one depicted in the Fig. 3.16c (or 3.15d) is one over the whole set of 50,000 frames, so the experiment is still very well described by pure 1-D NLS equation. The last 'temporal hologram' show the structure similar to the local Peregrine soliton.

The change of the profiles before and after the adjustment of the digital 'focus' seems to be not significant. The reason for this is the narrow spectral width. However, I would like to point out that after the adjustment some very important properties are taking their place. First of all, we immediately see the linear inclined phase for the high-amplitude structure Fig. 3.16c and the right asymmetry in the power profile. Indeed, the intrapulse stimulated Raman scattering affected pulses has a well-defined asymmetry [235]. Second, it is the Peregrine soliton signature. The π-phase jump became sharp with the well-recognized shape. The 'wings' part the coherent structure profile touch zero level in the power profile.

Thereby the SEAHORSE technique can be fully used for the ultrafast partially coherent light recording.

3.2.1.6 Nonlinear Digital Holography

Precise measurements of the power and phase give a unique possibility to reconstruct the light dynamics in the optical fiber. Indeed, we can integrate directly the 1-D NLS equation knowing all necessary parameters (dispersion coefficient β_2, nonlinear coefficient γ). We will call this approach 'Nonlinear

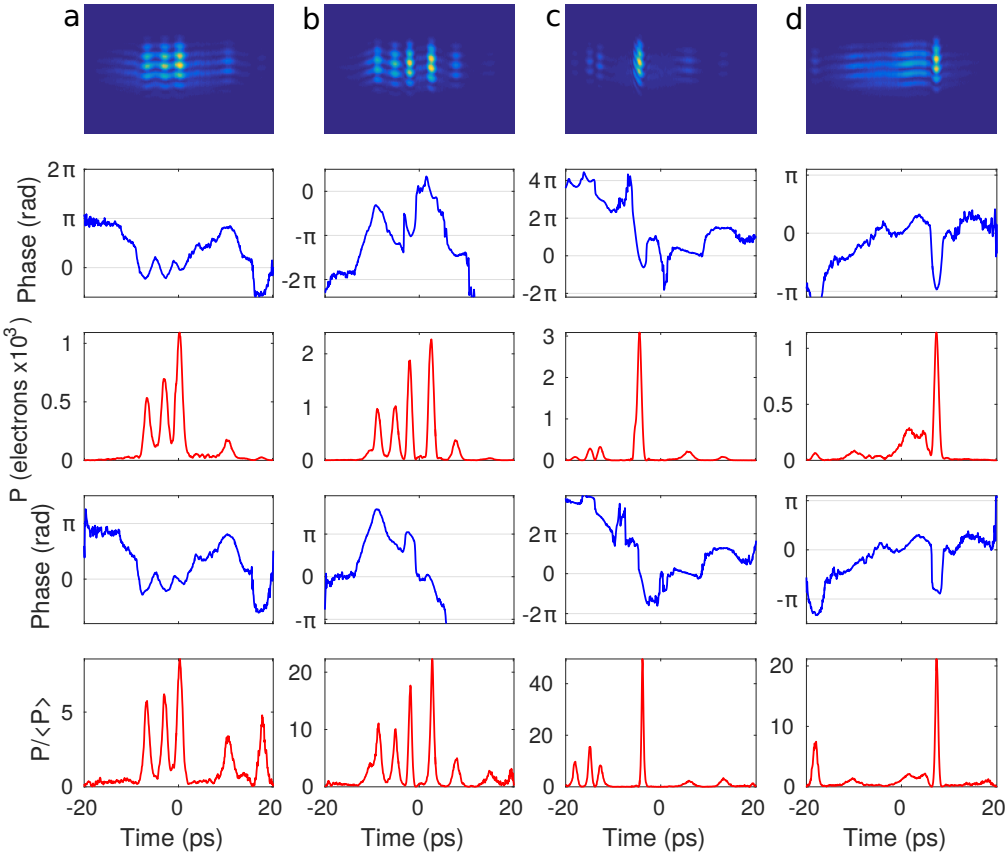

FIGURE 3.16: Partially-coherent light measurement with the SEAHORSE technique. The partially-coherent light after propagation in 400 m PM fiber having the same initial conditions as one depicted in the Fig. 3.15. The first row: 'temporal holograms' of random waves, recorded using the SEAHORSE. The second and third rows: extracted phase and intensity profiles without postprocessing. The power unit is here the number of electrons detected by sCMOS sensor. The fourth and fifth rows: numerically retrieved phase and intensity profiles by using the digital holography algorithm.

Digital Holography'. First, this technique was shown for the reconstruction of an optical path for a short chirped pulse propagated in optical fiber [236] and later for 2-D laser beam evolution in photorefractive crystals in defocusing and focusing cases [237, 238]. These experiments were provided for deterministic signals and, therefore, the phase and intensity can be reconstructed by simple FROG setup [13] (for the single pulse) or a homodyne detection scheme (for the 2-D paten reconstruction). As it was mentioned by authors in [236]:

> "It must be stressed that the reverse propagation method is not limited to near-soliton conditions but can be applied to any fiber in both dispersion regimes."

Indeed, using this approach we can reconstruct the full spatio-temporal dynamics of partially-coherent light during its nonlinear propagation in the optical fiber. In order to do this, we have to use some more advanced measurement techniques like HTM or SEAHORSE.

Reconstruction of the spatio-temporal focusing dynamics in optical fiber requires a wide window of measurements. The needed size of the window increase with the considered propagation distance. It is directly related to the presence of interactions between neighbour humps in the random signal. We would like to provide the Nonlinear Digital Holography for stage where it is possible to separate the dynamics of neighbour structures one from another. Another important factor for the reconstruction of the initial condition from measured signal at the output of a fiber is that estimated initial hump has to be much smaller than the window of measurement. In order to satisfy all these criteria, we made a decision to provide the Nonlinear Digital Holography for the 0.1 THz spectral width and 2.6 W of average power signal measured at the output of 100 m PM fiber.

Results are presented in Fig. 3.17. First of all, we provide the reconstruction of the light dynamics (pictures a-b) measured at the output of the 100 m fiber (pictures c-d). We will numerically propagate measured light back towards the input (pictures e-f) and forth to the double of real distance (200 m). As reader can notice we have chosen the structure similar to the local Peregrine soliton for the Nonlinear Digital Holography. Indeed, for the taken initial conditions the majority of the recorded frames contain the similar images. As an evidence, we provide here the comparison with the analytical formula of the Peregrine soliton without any parameter adjustment (black dashed line in Fig. 3.17c,d in the way similar to the one used for the Fig. 3.10. The spatio-temporal diagram shows the typical evolution of a single initial hump before the interaction with neighbours, the picture is similar to the one depicted in Fig. 3.10. We observe the hump self-compression which inevitably leads to the gradient catastrophe and hence to its regularisation accompanying emergence of the Peregrine soliton. At the next step we clearly see the double-peak coherent structure which can be seen as the first step of development of the cone (like one depicted in Fig. 3.4a). However, the value of ϵ approximately 0.2. So we can see only the first steps of this dynamics.

[13] For the discussion of the FROG technique see Sec. 2.1.

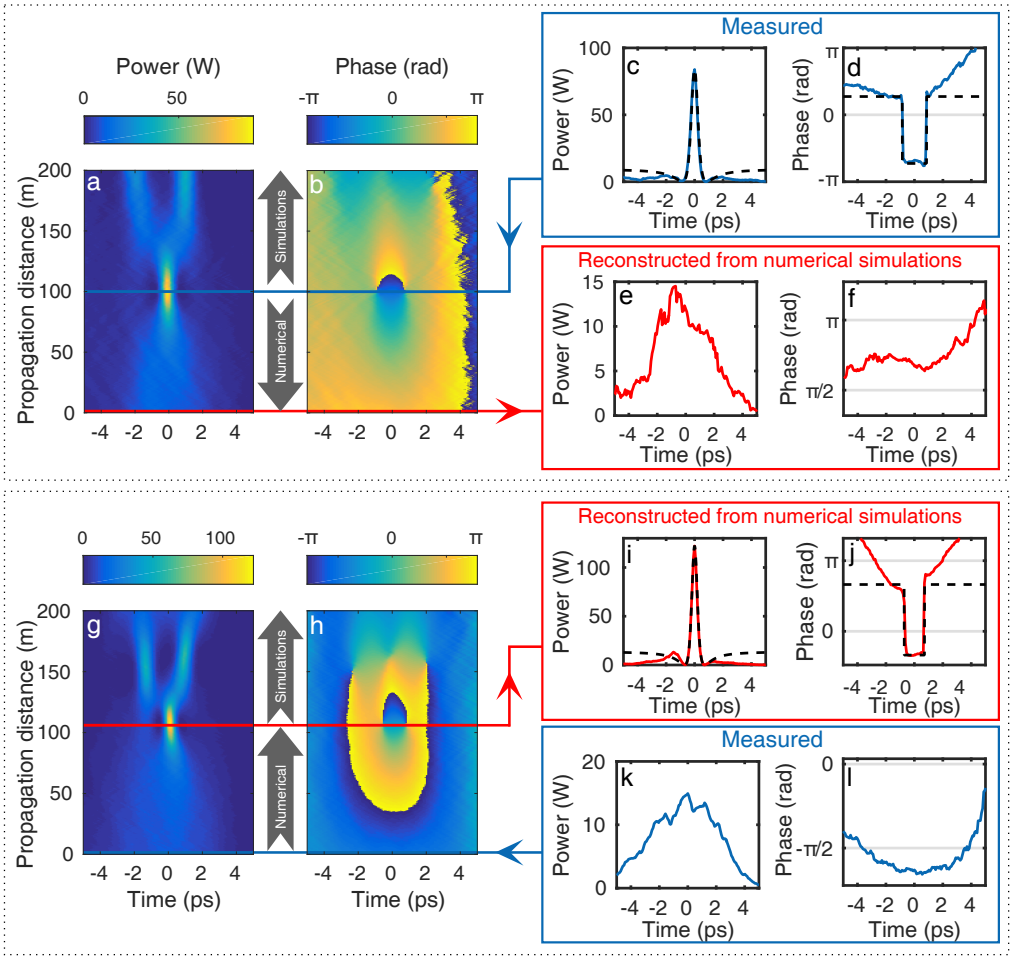

FIGURE 3.17: Nonlinear Digital Holography. Spatio-temporal diagram reconstruction using the experimentally recorded data with the HTM at the output of the 100 *m* PM fiber (a-f) and at the input (g-l).

At the next step, we provide the Nonlinear Digital Holography starting from the recorded initial conditions (Fig. 3.17g-l). We have chosen the frame which contains a hump (pictures k-l) similar to the numerically reconstructed one (e-f). The Nonlinear Digital Holography provides spatio-temporal diagram similar the one plotted above. Indeed, one can recognise all the stages of the formation of the local Peregrine soliton towards to the double-peak structure.

3.2.1.7 Comparison of statistical parameters

One of the rigorous ways to justify our measurements is to provide a statistical analysis of the recorded data and compare results with the numerical simulations. A close verification was shown before in Sec. 2.3.4, where we reconstructed the power spectral density. However, the phase adjustment for the for the SEAHORSE recorded 'temporal holograms' doesn't affect the shape of the power spectral density. It is also important to show that our experiment is governed by 1-D NLS equation.

How it was mentioned in the introduction 1.3.1 a remarkable characteristic of the partially-coherent light propagated in the optical fiber is the 'heavy' tailed probability density function (PDF) [53]. We can employ this fact and compute the PDF of the data recorded with the HTM, SEAHORSE and computed numerically for the same initial parameters. The PDF is a unique signature which will reveal possible mistakes in data reconstruction and parameters estimation.

We've chosen one set of parameters for the initial conditions: ASE emitted light with 0.1 THz spectral width and 2.6 W average power propagated in 400 m PM fiber with β_2 = -22 ps^2/km and γ = 2.4 $W^{-1}km^{-1}$.

The result of the comparison is plotted in Fig. 3.18. PDF computed using the HTM recorded data shown by green, with the SEAHORSE by red and with numerical simulations by blue. PDFs are indeed 'heavy' tail in comparison with an exponent (black line). As reader can see, all three lines coincide with remarkable accuracy. Thereby, presented above results can be considered as reliable.

3.2.2 Connection between local dynamics and statistics in focusing NLS

The Peregrine soliton-like structures very often can be found at the first steps of nonlinear dispersive propagation of the partially-coherent light in the optical fiber. It is related to the fact that partially-coherent initial conditions can be often considered as a set of independent humps governed by focusing dynamics [14] at the beginning of nonlinear propagation. Focusing dynamics of a hump inevitably leads to the gradient catastrophe and its

[14] In the defocusing case, this approach is not valid because the interaction between the humps happens shortly after the beginning of propagation. In the next chapter, it will be shown that this interaction is a one of the main driving mechanism of the defocusing integrable turbulence.

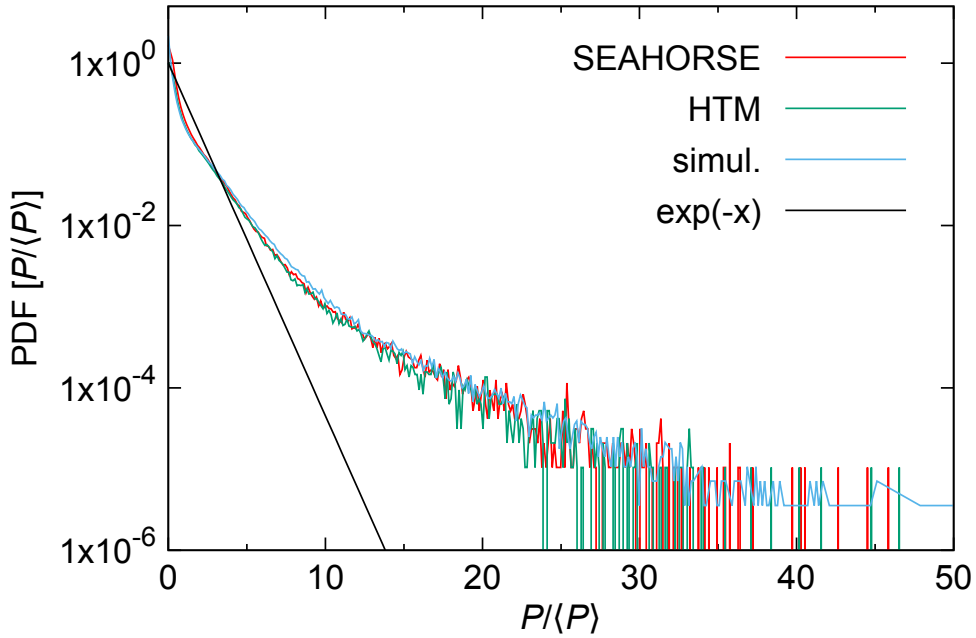

FIGURE 3.18: Comparison of the probability density function computed for the partially-coherent light of 0.1 THz spectral width and 2.6 W average power.

regularisation. There are statistically more probable parameters like peak power and duration of the hump (and therefore value ϵ) that can be found in the initial conditions. Indeed, the peak power distribution for the partially-coherent initial conditions follows the Rayleigh function, hence there is a well defined most probable peak power P_0. Also, as reader could see in the Fig. 3.12 there is a typical duration T_0 proportional to $1/\Delta\nu$ (the spectral width). Therefore, probability density function of finding certain value of $\epsilon = \sqrt{L_{NL}/L_D} = \sqrt{|\beta_2|/\gamma P_0 T_0^2}$ has a *well defined maximum*.

The theory developed by Dubrovin, Grava and Klein [123] and later by Tovbis and Bertola [124] predicts that the position of the gradient catastrophe depends on the value of ϵ. More explicitly, it gives the estimate:

$$\xi_{PS} = \xi_c + C\epsilon^{4/5} \tag{3.9}$$

where ξ_{PS} is the point of Peregrine soliton formation, $\xi_c = 1/2$ position of the gradient catastrophe, $C = 0.955262458...$ is a universal constant.

Hence, the statistical distribution of the positions of the emergence of the Peregrine soliton-like structure from different hump of the partially-coherent initial conditions can *be predicted knowing the distribution of* ϵ. The rigorous mathematical theory is developed for the semi-classical limit of NLS, however, as it was shown in the Sec. 3.1.2 we observe the described dynamics for the values of $\epsilon \sim 0.5$. Thereby, we can make the following statement:

> *Presence of the gradient catastrophe regularisation as a dominating mechanism in the system evolution implies the existence the statistically most*

probable position of the emergence of the local Peregrine soliton-like structures.

This conjecture can shed some light to the famous problem of the Rogue Wave description in the NLS framework. Indeed, the conjecture that the Peregrine soliton is a suitable candidate to the role of the Rogue wave is widely discussed in the community [56, 61, 100, 239, 240]. Indeed, the Peregrine soliton perfectly fits the famous description of the Rogue Waves: 'waves that appear from nowhere and disappear without a trace' [239]. However, before the Tovbis-Bertola theorem, Peregrine soliton was observed at the nonlinear stage of a noise-driven modulation instability of the continuous wave (or condensate). While in the case of partially-coherent initial conditions, gradient catastrophe dominates the modulation instability for the wide range of parameters. Here, we will not consider the competition between these two mechanisms, taking into account only the cases when gradient catastrophe dominates.

We start the demonstration of the stated conjecture by highlighting a remarkable fact. Kurtosis evolution of the partially-coherent wave propagated in the media governed by focusing 1-D NLS has a *local maxima*, which is not present in defocusing case [125, 241]. Kurtosis is the fourth order moment of the probability density function defined as follows:

$$K_4[X] = E\left[\left(\frac{X-\mu}{\sigma}\right)^4\right] = \frac{\mu_4}{\sigma^4} = \frac{E[(X-\mu)^4]}{(E[(X-\mu)^2])^2}$$

Where μ_4 is the fourth central moment and σ is the standard deviation, $E[...]$ is the expected value.

However, in experimental science it very common to use its modified version [59]:

$$M_4[X] = \frac{E[(X)^4]}{(E[(X)^2])^2}$$

This redefinition is related to the problems of reconstruction of the complex envelope for calculation of the expected value μ, but it well suitable for the description of the PDF. Further, we will refer to the M_4 as kurtosis.

Kurtosis is widely used as a measure of how 'heavy-tailed' is the PDF. Indeed, for the partially-coherent initial conditions having Gaussian distribution the kurtosis of $|\Psi|$ the equals to 2. Then after the nonlinear propagation, the PDF becomes 'heavy-tailed' and the value of kurtosis increases. It reaches a local maximum and then decreases until a certain value which corresponds to the stationary state. Saying in other words: *there is a certain propagation distance at which the probability density function is the most 'heavy-tailed' and, therefore, the probability to find a high-amplitude structure is the highest.* Thus, understanding of the origin of the kurtosis local maxima can give a clue about the origin of the Rouge Waves in the integrable turbulence in the framework of the focusing 1-D NLS equation.

The fact of the presence of the position with the highest probability of emergence of the high-amplitude wave is in a good agreement with the stated

conjecture. In order to verify possible relation between these two facts, we will provide two numerical experiments.

3.2.2.1 Numerical estimation of ϵ distribution

In order to estimate the distribution of ϵ (hence the distribution of the local Peregrine soliton-like structure appearance position) we create a set of partially-coherent initial conditions using the random phase approach (see Sec. 3.2.1.1). We create in the Fourier domain the Gaussian spectrum of certain FWHM and add the uniformly distributed [-π, π] random phase to each component. In the real domain, we obtain a periodical signal similar to one depicted in Fig 3.19(blue line). For the study, we created three sets of 100 realisations each. The sets correspond to the real experimental parameters: 0.05, 0.1 and 0.2 THz spectral widths with 2.6 W of average power. In order to pass from the Eq. 3.2 for which all the analytical results are obtained to the Eq. 3.1 the appropriate change of variables is required. Particularly for the distance: $z = \xi\sqrt{L_D L_{NL}} = \xi\sqrt{T_0^2/(P_0\gamma\beta_2)}$

In order to compute the ϵ distribution, first of all, an algorithm searches for all local maxima in the power profile by detecting the change of sign of the derivative. Next, it selects the peaks of the amplitude above a threshold (green line in Fig. 3.19). Parameters of the threshold are chosen empirically. For the threshold, we took the value 2.5 times the average power. This corresponds to the value of ϵ less than 0.3 for all considered parameters. It is done to separate the contribution of the high-amplitude peaks from small-amplitude peaks. Also, it is important to find the multi-peak structures, because their contribution (at the first stages) will be similar to the single-peak ones. In order to distinguish them, we have chosen a minimum duration between peaks in the way that all peaks within this interval are considered as one having the maximum amplitude found among them. In the presented case the threshold was 10 ps. For example, the chosen the peaks are depicted in Fig. 3.19 by magenta dots [15]. Then, the algorithm computes the FWHM for each of the chosen structures. The left and right sides of each chosen structure at the level of FWHM are shown by red and green dots in Fig. 3.19.

Finally, algorithm estimates the ϵ and computes the position at which the Peregrine soliton-like structure will appear as a regularisation of the gradient catastrophe (see Eq. 3.9) for each structure separately.

3.2.2.2 Calculation of the fourth moment of the PDF

Computation of the fourth order moment of a probability density function is rather straightforward. First, we take the initial conditions produced for the calculation of the ϵ distribution and run Monte Carlo simulations (see Sec. 3.2.1.1). We numerically propagate the partially-coherent initial conditions to the 1 km distance. The parameters of the fiber are taken as usual:

[15] In order to avoid the application of the artificial thresholds, criteria related to the amplitude at the maximum compression point has to be found. This will be made in further investigations.

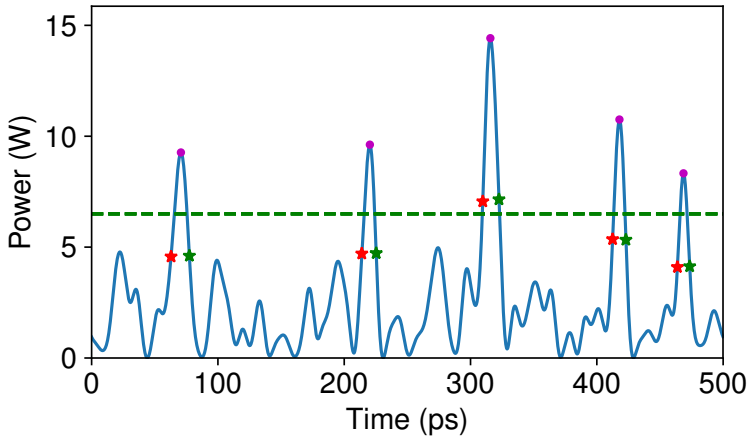

FIGURE 3.19: Example of the initial conditions processing. 500 ps -long window of 0.05 THz spectral width and 2.6 W power. (Blue line) is the power profile of the partially-coherent wave. (Magenta dots) are detected maxima above the threshold (green dashed line). (Red and green stars) show the left and ring side of the structure at the level of FWHM.

β_2 = -22 ps^2/km and γ = 2.4 $W^{-1}km^{-1}$. The dynamics is resolved with 100 points in z and 5,000 points in t. For each of 101 outputs we compute the M_4 and average over the whole set of 100 initial conditions. As it was mentioned above, we provided the numerical experiment for the three different initial conditions 0.05, 0.1 and 0.2 THz having 2.6 W average power.

3.2.2.3 Results of comparison

Here we investigate correlations between the maximum compression point of the Peregrine soliton-like structures and the kurtosis at the different propagation distances. We provided the comparison for the different sets of data: 0.05 THz (Fig. 3.20), 0.1 THz (Fig. 3.21) and 0.2 THz (Fig. 3.22). The average power of the initial conditions was the same 2.6 W. We use the twin-axes for the most spectacular illustration. First (blue) axis represent the dependence of the kurtosis M_4 of $|\Psi|$ on the propagation distance in km. The second (red) axis shows the dependence of the Peregrine soliton-like structures maximum compression point probability density on the same propagation distance. Axes are scaled in order to superimpose the two data.

As reader can see, in all the three cases (Fig. 3.20, 3.21, 3.22) the maximum of the kurtosis coincides with the maximum of the compression point probability density with a good accuracy. Moreover, the width of the maximum of the compression distribution coincides with the width of the 'overshoot' of the kurtosis as well. This tendency becomes more pronounced with increasing spectral width. This can be connected to the increasing number of taken into the account peaks inside the window of the fixed width (500 ps).

Therefore, we can conclude that the mechanism of the gradient catastrophe regularisation through the formation of the Peregrine soliton-like structures can play a crucial role in the formation of the high-amplitude structures

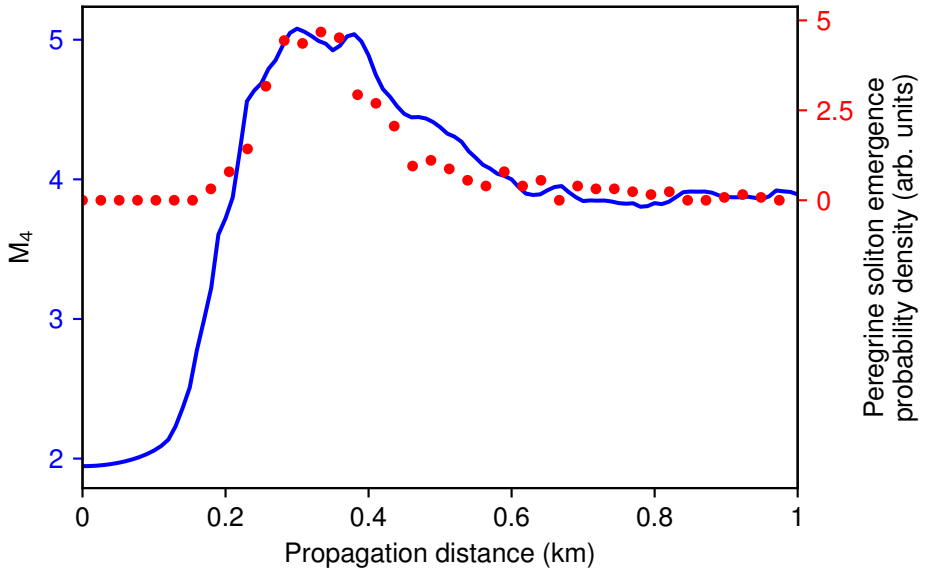

FIGURE 3.20: Comparison of the Peregrine-soliton-like structure maximum compression point distribution and the M_4 moment at different propagation distances. Partially-coherent initial conditions 0.05 THz and 2.6 W.

in the integrable turbulence of the focusing 1-D NLS equation. This mechanism leads to the statistically probable appearance of the Peregrine soliton-like structure at a certain distance of propagation. This process can be considered as a possible explanation of the Rogue Wave formation problem, of course only at the leading order. For example, the Tovbis-Bertola scenario could be well-recognised on the spatio-temporal diagrams recorded in a water tank (see [242], even for artificially created initial conditions). However, applicability of this approach to the non-integrable system has to be thoughtfully analysed which is far beyond the scope of this manuscript.

3.3 IST analysis of the experimentally measured PS emerged from the integrable turbulence

In this section, we will explicitly define the term Peregrine soliton-like structure employing the inverse scattering transform (IST) approach [16]. More precisely, we characterise the coherent structures by its Zakharov-Shabat (ZS) spectrum on the so-called λ plane obtained in the framework of the finite gap theory. Also, we will show the difference between global and local approaches to reconstruction of the IST spectra. Finally, we will provide the identification of the structures recorded experimentally with the HTM.

[16] Technically, we will use only the direct scattering part of the IST procedure, however we will refer to the obtained portraits as IST or Zakharov-Shabat spectra.

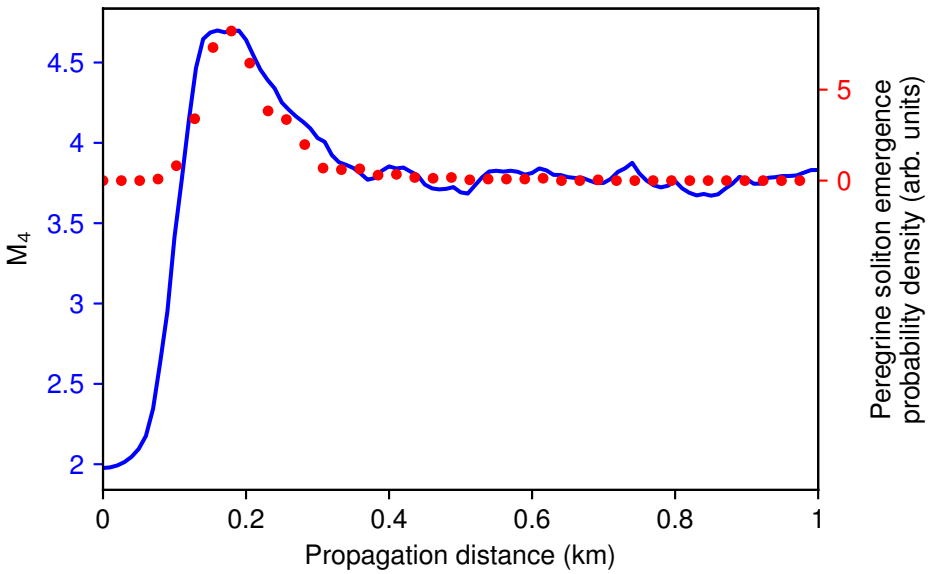

FIGURE 3.21: Comparison of the Peregrine-soliton-like structure maximum compression point distribution and the M_4 moment at different propagation distances. Partially-coherent initial conditions 0.1 THz and 2.6 W.

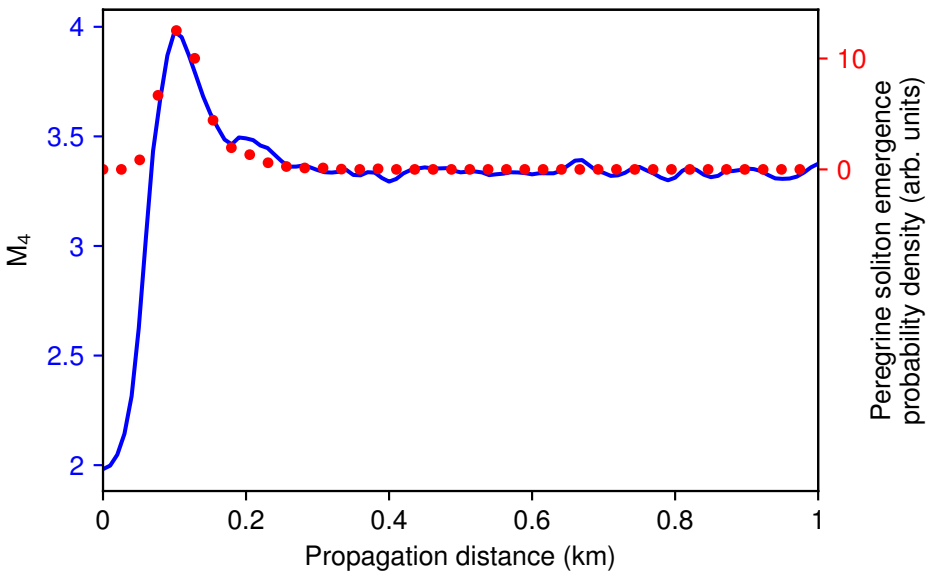

FIGURE 3.22: Comparison of the Peregrine-soliton-like structure maximum compression point distribution and the M_4 moment at different propagation distances. Partially-coherent initial conditions 0.2 THz and 2.6 W.

3.3.1 Fourier collocation method

The introduction to IST and integrability of the 1-D NLS equation is given in Sec. 1.2.4. As it is known for certain initial condition the ZS spectrum can be obtained analytically. For example, Satsuma and Yajima explicitly solved the ZS problem for solitonic initial conditions [243]. However, ZS spectrum can be found explicitly just for some of the deterministic initial condition. For other cases, numerical methods can be employed.

Here we will consider the focusing NLS equation in the form widely used in applied mathematics community:

$$i\frac{\partial u}{\partial t} + \frac{\partial^2 u}{\partial x^2} + 2|u|^2 u = 0 \tag{3.10}$$

It can be obtained from the Eq. 3.1 by the following change of variables:

$$u = A/\sqrt{P_0}; \quad t = z/2L_{NL} = zP_0\gamma/2; \quad x = t/T_0 = t/\sqrt{\beta_2/\gamma P_0}$$

where P_0 is a typical power.

We can define a so-called Lax pair for the fNLS found by Zakharov and Shabat [18]. We repeat here result presented in the introduction 1.2.4.

$$Y_x = \begin{bmatrix} -i\xi & u \\ -u^* & i\xi \end{bmatrix} Y \tag{3.11}$$

$$Y_t = \begin{bmatrix} -i2\xi^2 + i|u|^2 & iu_x + 2\xi u \\ iu_x^* - 2\xi u^* & i2\xi^2 - i|u|^2 \end{bmatrix} Y \tag{3.12}$$

where ξ is the spectral parameter and Y is a vector or matrix function. The equation 3.10 is a compatibility condition for the equations 3.12 and 3.11 (guaranties the equality of Y_{tx} and Y_{xt}).

Equation 3.11 can be inverted to show the spectral problem in more explicit way:

$$\begin{bmatrix} -\partial_x & u \\ u^* & \partial_x \end{bmatrix} Y = i\xi Y \tag{3.13}$$

The approach we employ for the computation of the ZS spectrum is called Fourier collocation method [244]. The idea of this method is to turn the ZS problem Eq. 3.13 into the matrix eigenvalue problem by expanding the eigenfunction Y and potential function (field complex envelope) u into the Fourier series:

$$Y = \begin{bmatrix} y_1(x) \\ y_2(x) \end{bmatrix} = \begin{bmatrix} \sum_{x=-N}^{N} a_{1,n} e^{ink_0 x} \\ \sum_{x=-N}^{N} a_{2,n} e^{ink_0 x} \end{bmatrix} \quad u(o,x) = \sum_{x=-N}^{N} c_n e^{ink_0 x}$$

where k_0 is $2\pi/Ł$, L is the length of the considered interval $x \in [L/2, L/2]$.

Hence, the term ∂_x can be expressed in the Fourier space as $\mathcal{B}_1 = ik_0 diag(-N, -N+1, ..., N)$ and multiplication by u(x,0) is replaced by the convolution matrix:

$$\mathcal{B}_2 = \begin{bmatrix} c_0 & c_{-1} & \cdots & c_{-N} & & & \\ c_1 & c_0 & c_{-1} & \ddots & \ddots & & \\ \vdots & c_1 & c_0 & \ddots & \ddots & \ddots & \\ c_N & \vdots & \ddots & \ddots & \ddots & \ddots & c_{-N} \\ & c_N & \ddots & \ddots & \ddots & \ddots & \vdots \\ & & \ddots & \ddots & \ddots & \ddots & c_{-1} \\ & & & c_N & \cdots & c_1 & c_0 \end{bmatrix}$$

Thereby, we can we can rewrite the equation 3.13 in the Fourier domain form:

$$M \begin{bmatrix} A_1 \\ A_2 \end{bmatrix} = \begin{bmatrix} -\mathcal{B}_1 & \mathcal{B}_2 \\ \mathcal{B}_2^{\dagger} & \mathcal{B}_1 \end{bmatrix} \begin{bmatrix} A_1 \\ A_2 \end{bmatrix} = i\xi \begin{bmatrix} A_1 \\ A_2 \end{bmatrix} \tag{3.14}$$

here $A_i = (a_{i,-N}, a_{i,-N+1}, .., a_{i,N})^T$

The last step is to solve the eigenvalue problem for the matrix $-iM$. We used a standard routine integrated into the SciPy package of Python.

There are different methods of computation of the ZS spectrum [19, 245], but they will be not considered in this manuscript.

3.3.2 Global and local approaches to the IST

Recently, a study of the RW phenomena was provided employing the *global* IST (ZS) spectra computation [120, 121] over a large size box. Starting with a perturbed plane wave (condensate), authors, by increasing the amplitude of perturbation, ended up with random wave close to the partially-coherent one. Thereby, they managed to shed some light to the problem of visible change of dynamics passing from one type of initial condition to another. One of the major conclusions of these works is that the solitons which form the initial conditions have much less velocity in the case of condensate. However, no information about *local* features can be extracted from the *global* IST spectra.

However, the IST approach is widely considered as a tool for identification and classifiaction of the RW [19]. It is shown in [119] that *local* IST analysis can be successfully used in order to identify coherent structures that emerge at the transient stage of the nonlinear dispersive waves propagation. The local approach requires treatment of the IST data in the framework of the finite-gap theory (periodic IST) [19]. The local IST analysis has a potential to reveal the nature of the RW. It is possible to estimate the proximity of RW under investigation to a certain exact solution of NLS by its local the ZS spectrum [219]. Therefore, it can help to better understanding the underlying mechanism of formation of the RW.

3.3.2.1 Global IST with zero boundary conditions

Here we will demonstrate the global IST pictures of the purely solitonic and purely solitonless initial condition. For the integration of the focusing NLS equation we use the approach explained in Sec. 3.1.1 to obtain similar spatio-temporal diagrams and Fourier collocation method to compute IST spectra.

We start with a simple two-soliton solution of NLS $u = Nsech(x)$ with $N = 2$ and its purely solitonless counterpart $u = Nsech(x)exp(-iN\mu \log(\cosh(x)))$ with N = 2 and $\mu \geq 2$. Corresponding spatio-temporal diagram is depicted in the in Fig. 3.23(solitonics - top, solitonless - bottom, simulations are done using the normalization of Eq. 3.2). As reader can see both of the considered initial conditions pass through the stage when the high-amplitude wave emerges. Let's now look at the IST portrait of these two potentials (Fig. 3.24). We see the expected two discrete points if the case of two-soliton potential (green) and no discrete points in the case of solitonless (red). I would like to point out that *the global IST spectrum does not change during the propagation*. Therefore, in the case of solitonless potential there is no signature in the global IST spectrum that the high-amplitude structure will appear.

It is even more visible in the case of ten solitons. We prepare the similar purely solitonic and solitonless potential, but close to the conditions Tovbis-Bertola theorem. The corresponding spatio-temporal diagram is shown in Fig. 3.25. We see that in the case of solitonless initial conditions the coherent structure which emerges is 20 times larger that the initial hump (Fig. 3.25(bottom-right)). However the IST portrait doesn't represent the fact that there is a well seen gradient catastrophe in the system which is regularised by the Peregrine soliton-like structure.

3.3.2.2 Interpretation of the Finite-gap spectrum

In the previous section we demonstrated that global IST spectral portraits do not reveal the transient local dynamic including the appearance of the high-amplitude structures. Indeed, the fact that the completely solitonless initial condition (which does not have any discrete point in the ZS spectrum) experiences the gradient catastrophe and, therefore, its regularisation with a Peregrine soliton-like structure, is the direct demonstration that another strategy has to be chosen for the nonlinear spectral analysis.

It was recently shown, that the local IST analysis in a window around the structure under investigation can be used for its identification [119]. However, the local analysis implies that the function will be truncated, thus zero boundary approach is no longer valid. At this point we enter the domain which called finite-gap theory. This theory works with periodical of quasi-periodical solutions of the NLS. The structure under consideration has to be truncated at the certain position and periodized. Peroidization populates bands of a finite width in the IST spectrum. More detailed explanation of the effect of periodization can be found in Sec. 3.3.2.4. The complex solutions are represented by several bands (like shown in Fig. 3.27). Number of bands,

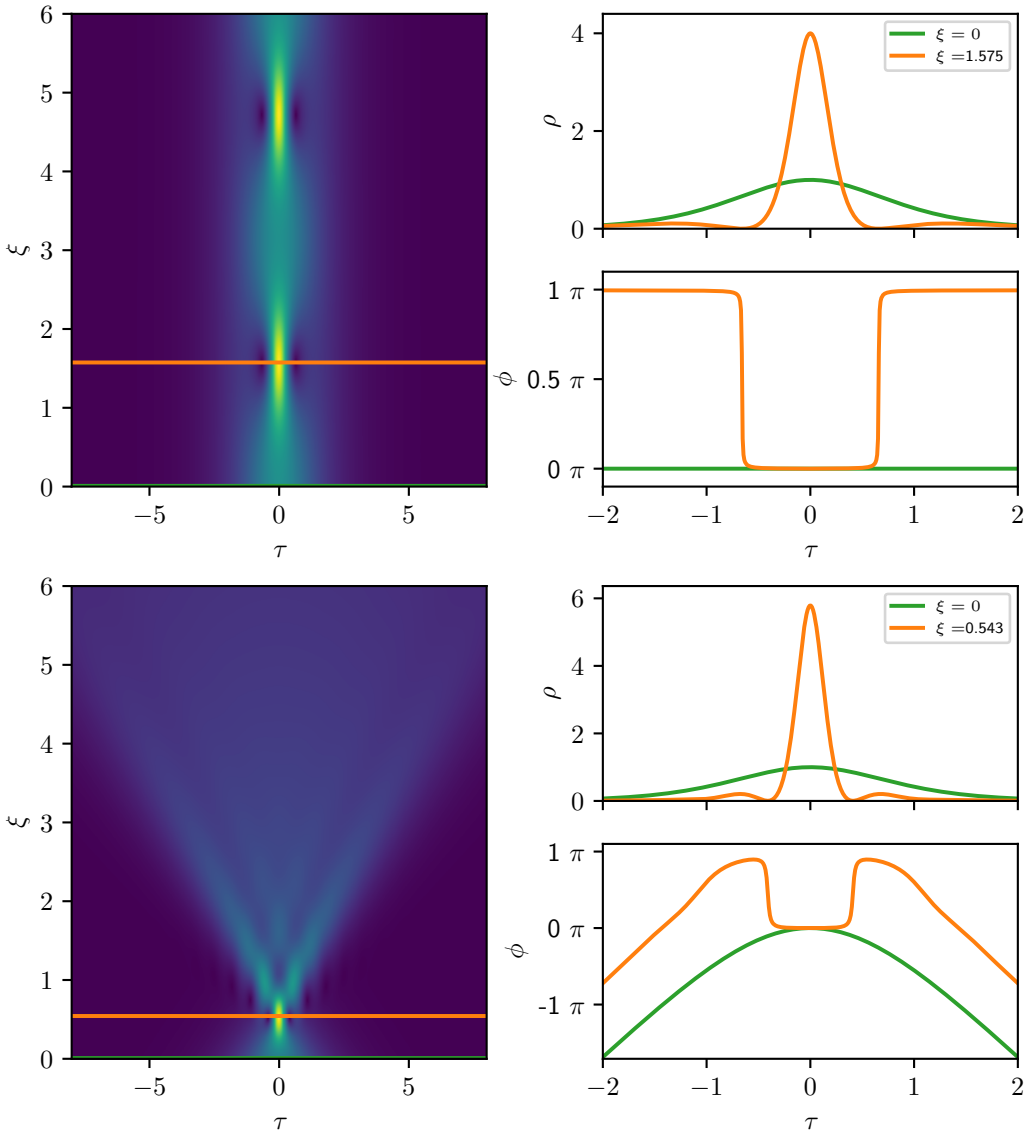

FIGURE 3.23: Spatio-temporal diagram of two-soliton $u = 2sech(x)$ (top) and solitonless $u = 2sech(x)exp(-i2\mu \log(\cosh(x)))$ with $\mu = 2$ solutions of NLS. (Right) The cross-section of the spatio-temporal diagram for the power and phase. (green) initial conditions, (orange) maximum compression point. Simulations are presented using the normalization of Eq. 3.2.

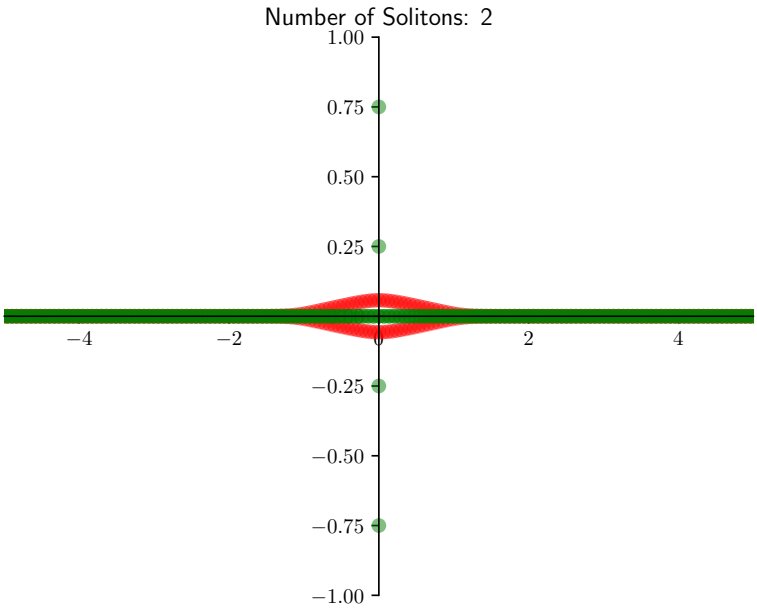

FIGURE 3.24: ZS spectra of the two-soliton (green) and corresponding solitonless (red) potentials. The vertical axis corresponds to the imaginary part of ξ, while horizontal to its real part.

its position and size are important parameters for the structures identification. In the framework of the finite-gap theory number of bands is connected with the *genus* of Riemann Theta functions. The genus of the certain solution can be found as $g = N - 1$, where N is the number of bands. Therefore, of the plane wave the genus is 0 , for soliton is 1 , for the Akhmediev breather, Kuzntsov-Ma and Peregrine solitons the genus is 2. Thereby, we can classify the coherent structures according to their genus.

Physical interpretation of the periodic IST spectrum *according to A. Osborn* [19] can be summarised as follows:

- Single band consists of two points connected by a spine.
- If the band crosses the real axis it is considered as *stable* stokes modes. For example, in the case of almost linear initial condition, IST portrait will contain only stable bands. Each band will simply represent the conventional Fourier mode. Similar picture of stable bands is shown in the Fig. 3.27 (left). By the blue line we depicted the band corresponding to the central Fourier mode, therefore, carrying wave (or finite-background).
- According to A. Osborne, the band which doesn't cross the real axis considered as *unstable* (see Fig. 3.27 (left)). Unstable bands often can be a signature of the presents of the high-amplitude event in the transient regime. For example, IST spectrum of the Peregrine soliton turns to

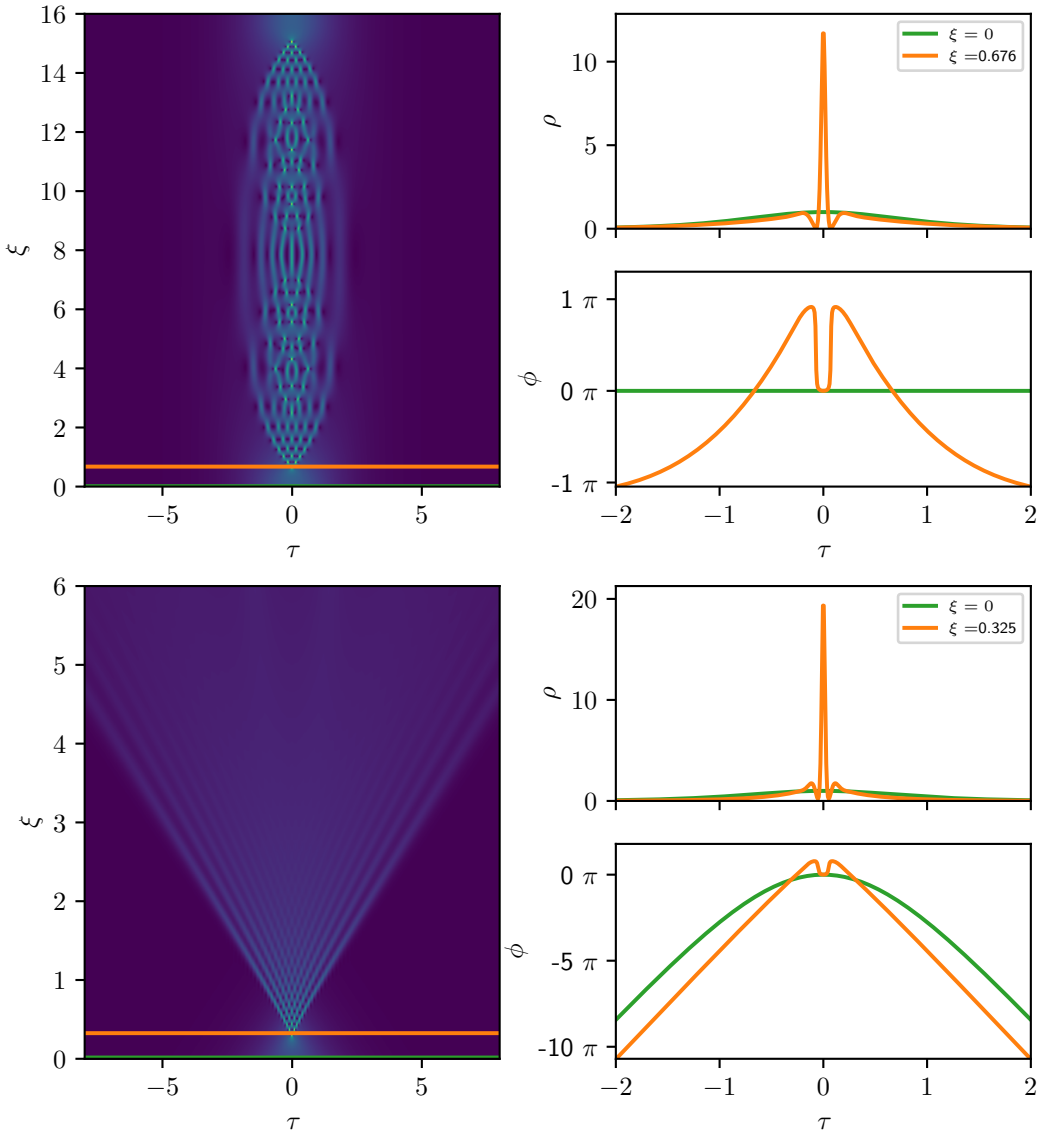

FIGURE 3.25: Spatio-temporal diagram of ten-soliton $u = 10sech(x)$ (top) and solitonless $u = 10sech(x)exp(-i10\mu \log(\cosh(x)))$ with $\mu = 2$ solutions of NLS. (Right) The cross-section of the spatio-temporal diagram for the power and phase. (green) initial conditions, (orange) maximum compression point. Simulations are presented using the normalization of Eq. 3.2.

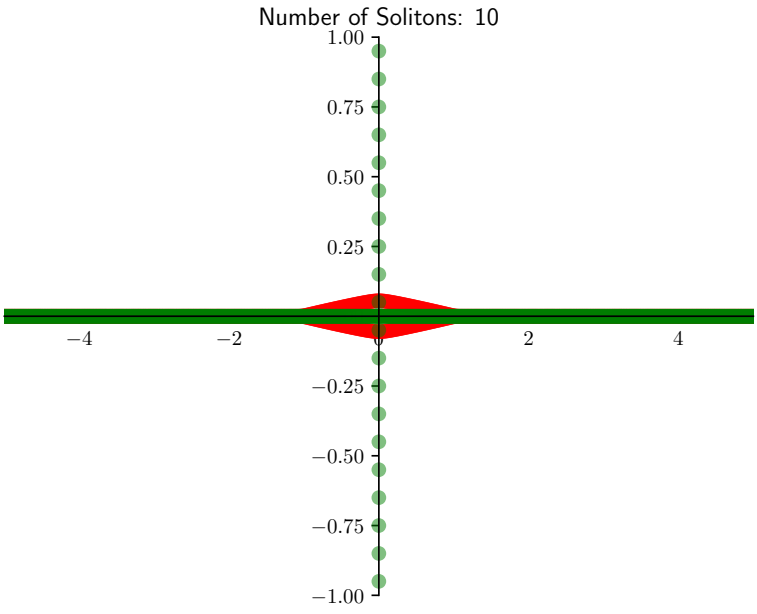

FIGURE 3.26: ZS spectra of the two-soliton (green) and corresponding solitonless (red) potentials. The vertical axis corresponds to the imaginary part of ξ, while horizontal to its real part.

the three bands shown in Fig. 3.27 (right). The is consistent with our statement about the genus of the solution.

- The position of the band along the imaginary axis represents the maximum amplitude which can be found eventually during the nonlinear propagation. Thus, maximum possible amplitude of the KM soliton in general is higher than PS which is in its turn higher than amplitude of AB with the same background level.
- The position of the band along the real axis corresponds to the velocity of the nonlinear structure in the x-t plane. Therefore, the coherent structure behind the spectrum depicted in Fig. 3.27 (left) will have non-zero velocity, in contrast to the Peregrine soliton which has bands along the imaginary axis.

3.3.2.3 Role of the window size

There are several parameters crucial for the correct numerical computation of the IST spectrum [219]. First of all we have to choose the correct window. The choice of the window is rather an empirical procedure. The correct window has to capture the structure under investigation itself as well as its close neighbourhood. This is illustrated in Fig. 3.28. The figure shows IST portraits of the Peregrine soliton truncated at the different positions ([-2,2]-blue dots, [-5,5]-green stars, [-10,10]-red crosses). As one can see, in the

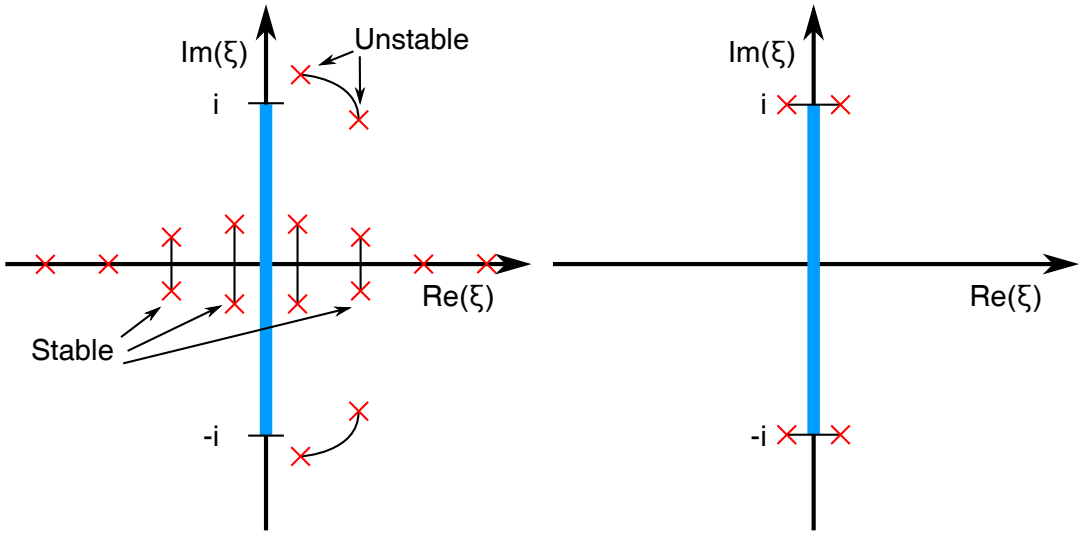

FIGURE 3.27: Artificially created IST spectra of the a complex solution of NLS (left) and the Peregrine soliton (right).

case of the Peregrine soliton, the choice of optimal window is straightforward. The considered solution of the NLS has a finite background which is well represented in the IST spectrum by the stable band crossing the real (horizontal) axis at the zero point. The background level is 1, so the band is disposed from $-i$ to i Therefore, the chosen window has to cut the soliton at the point where it has amplitude value close to the background level. Therefore, when the window doesn't contain the correct information about background level, the IST portrait becomes significantly distorted. Indeed, as one can see, the unstable band which corresponds to the window [-2,2] has a visible curvature and crosses the real axis lower than others. Reader could also noticed that larger windows lead to smaller bands.

It is also known that change of the sampling rate doesn't change the IST spectrum until certain point. In this sense, it is similar to the Fourier spectrum and conditions of Kotelnikov-Shannon theorem.

3.3.2.4 Role periodization in the local IST

The number of periodizations of the truncated function is one of the key parameters of the numerical IST spectra computing in the framework of the finite-gap theory with the Fourier collocation method [119]. Here we demonstrate the role of this parameter on the example of the Peregrine soliton. We have chosen an optimal window (as it is explained in the previous section) and computed the ZS spectrum changing the number periodizations. Figure 3.28 shows the corresponding spectra. The blue dots represent the IST spectrum without any preiodization, green stars correspond to 5 periodizations and red crosses to 10. Reader can immediately see that in the case when truncated signal is not periodized, we do not see the band crossing the imaginary axis. However, even after five periodizations we can observe a contour of the band. Increasing the periodization number we can see the band more

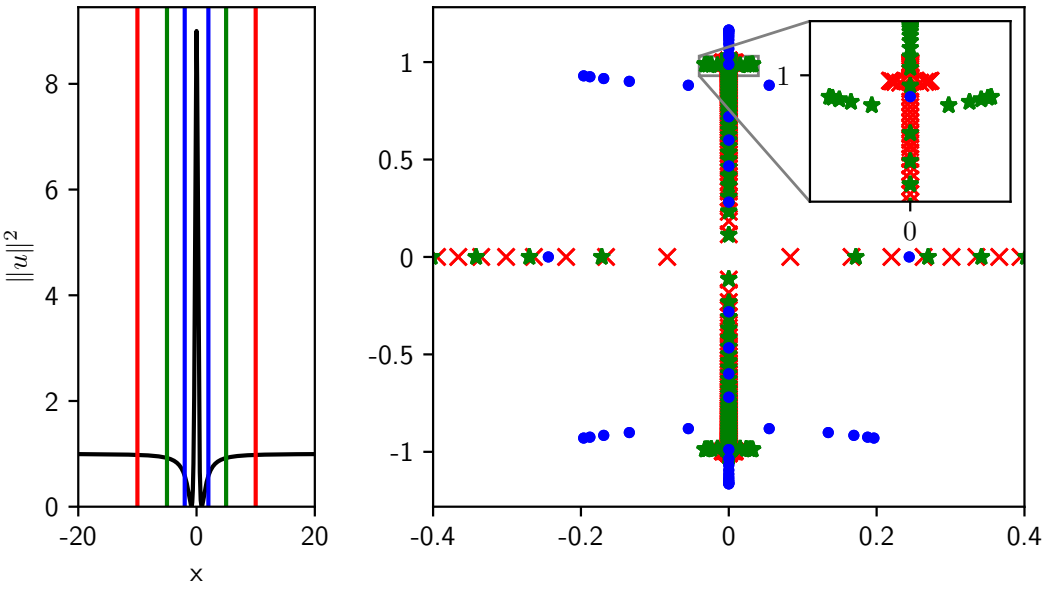

FIGURE 3.28: Effect of the window size on the IST spectra. (left)The Peregrine soliton truncated to the windows [-2,2] blue, [-5,5] green, [-10,10] red. (right) Corresponding IST spectra, the colour is preserved. The chosen window was periodized 30 times. The vertical axis corresponds to the imaginary part of ξ, while horizontal to its real part.

and more distinctly. Usually, in order to completely populate the band, it is needed approximately fifty periodizations.

3.3.3 IST Analysis of Tovbis-Bertola scenario

The local IST approach presented above is a powerful tool for identification of the complex structures emerged in the integrable optical turbulence. In this section we will employ this method in order to answer the following question: what kind of structures do we observe as a regularisation of the gradient catastrophe being far from the considered limit of the Tovbis-Bertola theorem? We can characterize them by the genus of the solution and closeness to the Peregrine soliton (position of the band crossing the imaginary axis). Comparison of the numerically generated structures from deterministic initial conditions and ones measured using HTM of SEAHORSE from the partially-coherent initial conditions can add an additional argument for the validity of the conjecture presented in the Sec. 3.2.2.

First of all, we would like to emphasise that the word 'local' doesn't mean only that the function has to be truncated, but also implies the careful choice of the value of the evolution variable. Indeed, Fig. 3.30 shows the change of the local IST portrait for the $\psi(0,\tau) = sech(\tau) and\, \epsilon = 0.02$ with the evolution coordinate [17]. Window and periodization are fixed. We can see that only

[17]It is always important to remember that the solutions of the NLS equation in the forms 3.1 and 3.2 must be renormalized to the dimensionless form 3.10. However, we present the data itself in the most appropriate form, while IST spectra are always computed for the dimensionless one.

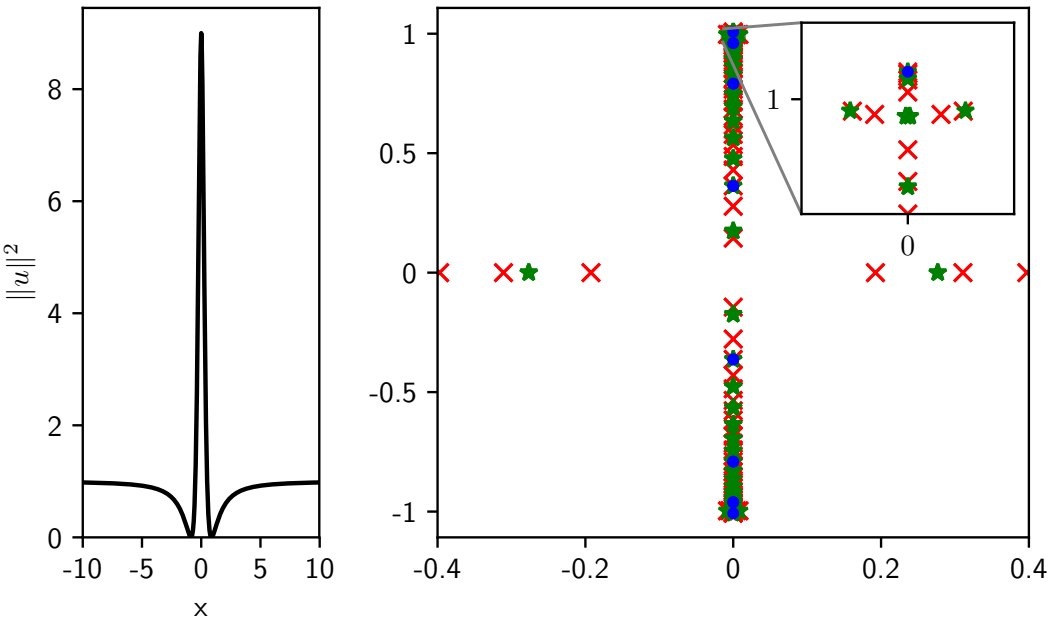

FIGURE 3.29: Effect of the periodization on the IST spectra. (left)The Peregrine soliton truncated to the window [-10,10]. (right) IST spectra of the signal. (blue dots) without periodization, (green stars) periodized 5 times and (red crosses) 10 times. The vertical axis corresponds to the imaginary part of ξ, while horizontal to its real part

one band is visible before the regularisation of the gradient catastrophe ($\xi = 0.42$) . Closer to the maximum compression point ($\xi = 0.53$) all three bands become visible, thus the genus of the solution becomes 2 instead of 0. Finally, the whole band can be seen exactly at the point of maximum compression ($\xi = 0.543$).

Also, we would like to show the the conservation of global IST spectrum. Fig. 3.31 shows the spatio-temporal diagram (left), intensity profiles of the initial condition (green) and the function at the maximum compression point (orange) depicted in the right-top and corresponding IST portrait (colours are preserved). We can see that global spectrum (right-bottom) of initial conditons (green dots) repeats with a good accuracy the spectrum at the maximum compression point (orange crosses). However, if we will choose a window around the Peregrine-like structure at the compression point, we immediately see all the signatures of the genus 2 solution: central band crossing the real axis (background) and the unstable band crossing the imaginary axis at the position. The solution is truncated at the positions shown in the intensity plot by red.

Finally, we will provide systematic calculations of the IST spectra of the local high-amplitude structure which emerges as a regularisation of the gradient catastrophe. We will take the $\psi(0,\tau) = sech(\tau)$ initial conditions and vary ϵ. In terms of the number of solitons $N = 1/\epsilon$, we will provide studies for N = 3,5,7...,17. We will propagate the initial functions with a numerical solver until the maximum compression point, truncate them at the maximum of the pedestal (see Fig. 3.31 right-top) and compute the IST spectrum. The

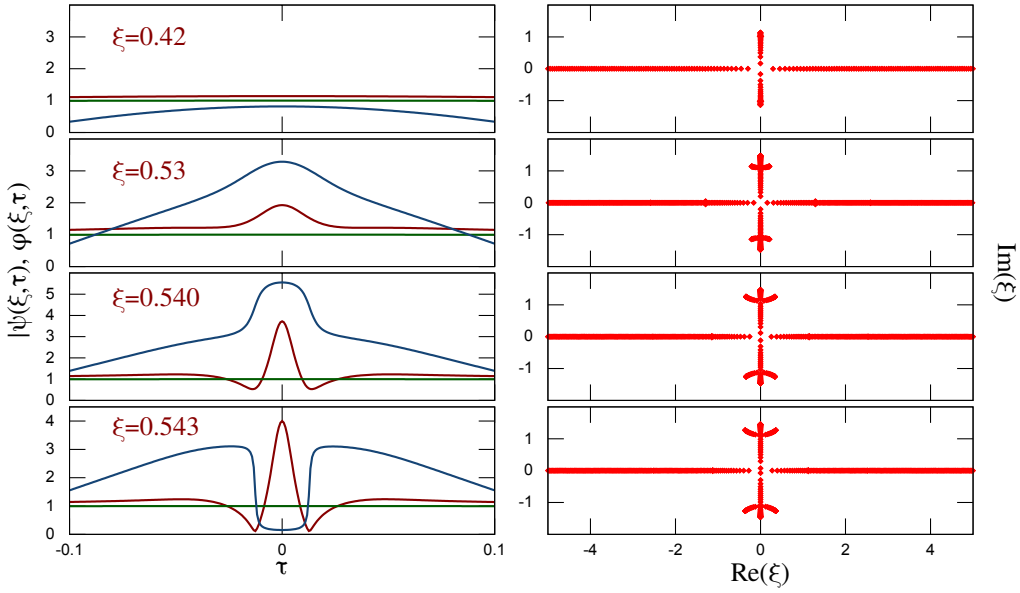

FIGURE 3.30: Change of the IST spectrum with the evolution coordinate. (left) Initial amplitude profile $\psi(0,\tau) = sech(\tau)$ with $\epsilon = 0.02$-blue, amplitude profiles at different propagation points $\xi = 0.42, 0.53, 0.54, 0.543$-red and corresponding phase profile -blue. (left) IST analysis with at different positions with fixed window size and periodization number. Similar figure is presented in the book [216].

result of this study is shown in Fig. 3.32. The left plot shows the whole IST spectrum of the solutions with the number of solitons from 3 to 17 depicted by colours from blue to red respectively. The IST spectra are normalized by the maximum of the imaginary part in order to provide the comparison. The left part shows a zoom of the area around the unstable bands.

According to the plot we can explicitly define the term Peregrine soliton-like structure. All the solutions have one central band which represents the background and two unstable bands crossing the imaginary axis. Increasing the number of solitons, therefore, getting closer to the conditions of the Tovbis-Bertola theorem, we immediately see that the unstable band moves towards the direction of the maximum of the central band (in the lower part of the complex plane the situations is symmetrically inverse). Also, the curvature of the unstable band visibly decreases. Hence, we can conclude that being far the limit $\epsilon \to 0$ we are able to exactly fit the emerged structure by the Peregrine soliton *only in the limited region*. This affects the local IST portrait, making it similar to the exact Peregrine soliton spectrum with inappropriately truncated window (see the blue dots on the Fig. 3.28). However, the local solution asymptomatically converges to the local Peregrine soliton, while decreasing ϵ value and, therefore, increasing the area of exact overlapping.

Even taking into the account the above statement, the Peregrine soliton stays the best fit for the locally emerged structures due to the focusing dynamics. I would like to recall here that for the fitting, no free variable was used. We simply substituted the parameters of the experiment (simulation)

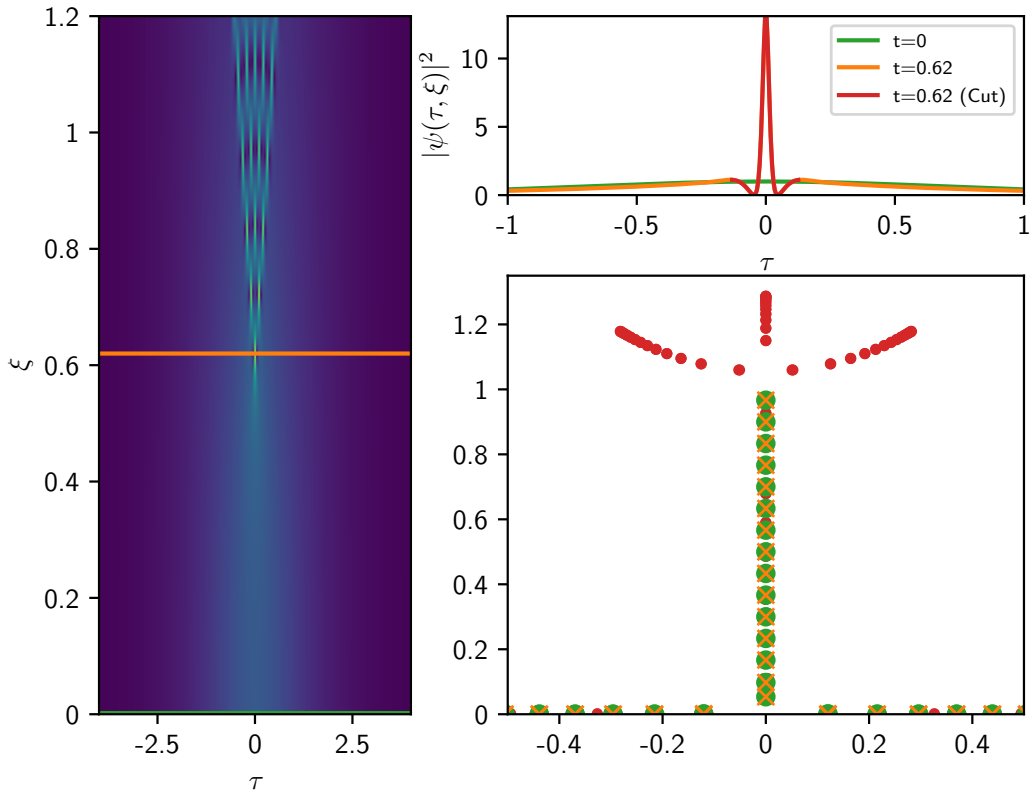

FIGURE 3.31: Conservation of global IST. (left) spatio-temporal diagram for $\psi(0,\tau) = sech(\tau)$ with $\epsilon = 1/15$. (right-top) intensity profile of the initial condition (green) , at the maximum compression point (orange), truncated for the IST computation (red). (right-bottom) global (green, orange) and local (red) IST spectra. The vertical axis corresponds to the imaginary part of ξ, while horizontal to its real part. Colours are preserved.

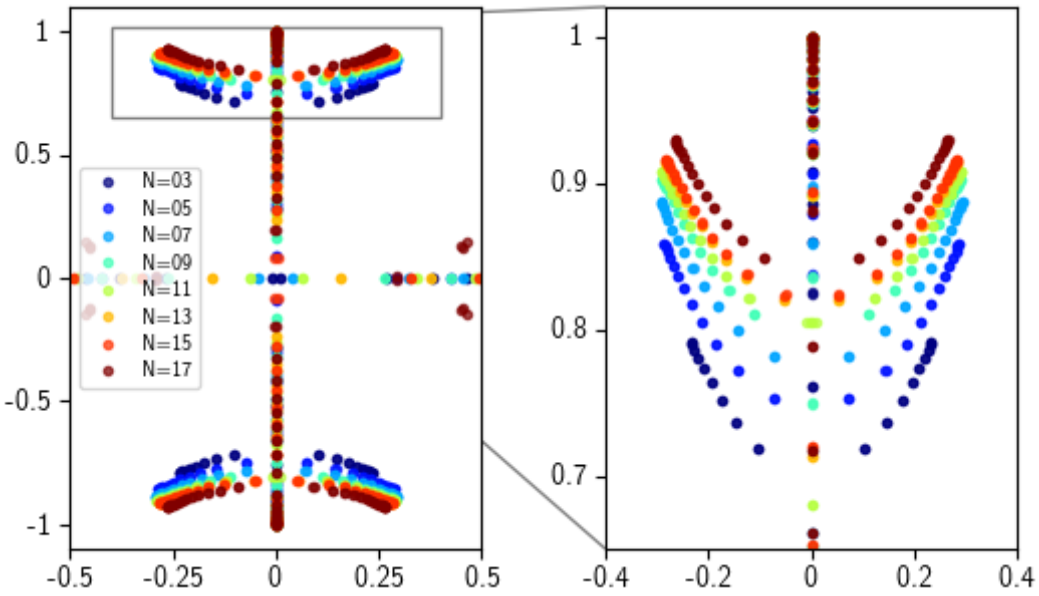

FIGURE 3.32: Local IST spectra of the local high-amplitude structure which emerges as a regularisation of the gradient catastrophe with different solitonic content (from 3 to 17 solitons). (left) the full IST spectra, (right) zoomed around the unstable band. The vertical axis corresponds to the imaginary part of ξ, while horizontal to its real part.

and the value of amplitude at the point of the gradient catastrophe as the value of background. The fit with Peregrine perfectly represents the main part of the local structure even with the very high value of ϵ (see for example Fig. 3.8).

3.3.4 IST of the experimental data

Now, having the criteria for the identification of the local structures, we are able to make a connection between the data obtained with deterministic initial conditions and measured experimentally in the framework of integrable turbulence. For the analysis, we will use already presented experimental data.

We will start from the local Peregrine-like structure used for the nonlinear holography (see Fig. 3.17)c,d. The result is shown in Fig. 3.33. On the left side normalized power profile is depicted. The window for the IST spectrum computation is chosen around the local maxima of the pedestal (shown by red). The corresponding IST portrait is plotted on the right side. We observe all the signatures of the local Peregrine-like structure, but with the visible band deformation. Nevertheless, the portrait can be compared with the one obtained numerically for the deterministic initial conditions. Figure 3.34 shows this comparison. By red the same spectrum as in the Fig. 3.33 is depicted (colour is preserved), by blue crosses we replot the spectrum from Fig. 3.32 for N =5. The spectrum depicted by blue is scaled in horizontal direction in order to provide the comparison. As reader can see this two spectra are almost identical except the band deformation. We can suppose that the

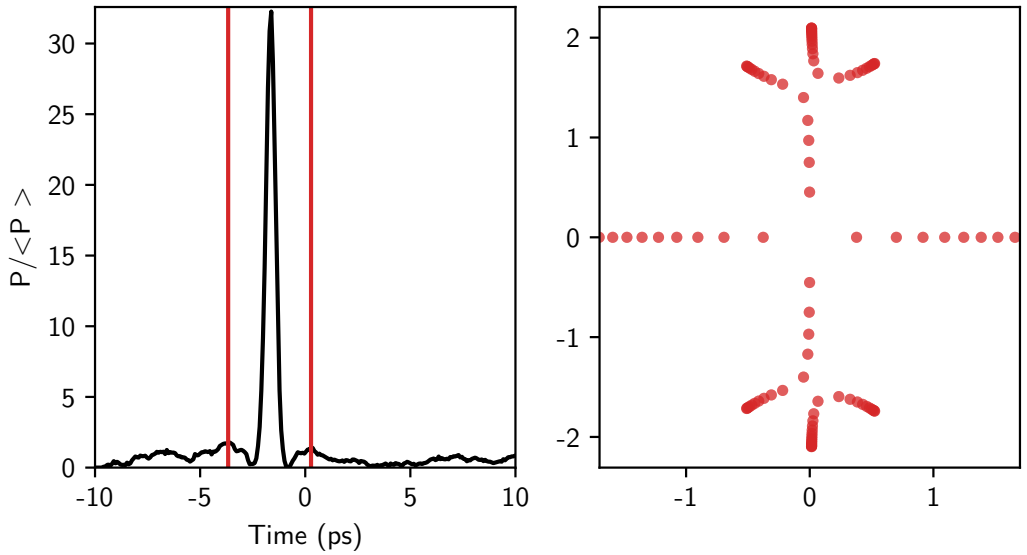

FIGURE 3.33: IST of the experimental data. For the investigation the data from the Fig. 3.17c,d is taken. (left) normalized power profile (black) and the window for IST analysis (red). (right) corresponding IST spectrum. The vertical axis corresponds to the imaginary part of ξ, while horizontal to its real part.

structures have the similar nature. Therefore, the Tovbis-Bertola scenario can be observed experimentally in the integrable turbulence governed by focusing 1-D NLS equation. This is also confirmed by the nonlinear holography approach.

However, due to the nonsmoothness of the partially-coherent initial conditions and interaction with neighbours, the bands can be even more deformed. For example the coherent structure which was shown before in Fig. 3.15e. Corresponding IST portrait is depicted in Fig. 3.35. We can see that the bands are completely separated. At the same time, the curvature of the spines noticeably increased.

We can experct observations of more complex higher genus solutions, for example at the point of collision of two breathers [119], but this will be the topic of further investigations.

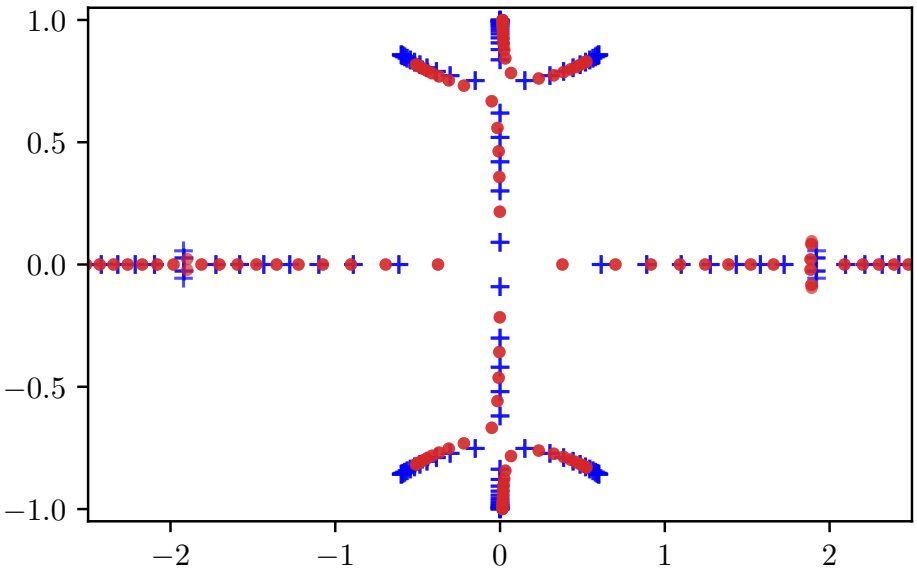

FIGURE 3.34: Comparison of the local IST spectra of experimentally measured data and numerically obtained from deterministic initial conditions. (red dots) the same spectrum as in the Fig. 3.33, (blue crosses) from Fig. 3.32 for N =5. The spectra are scaled in order to provide the comparison.

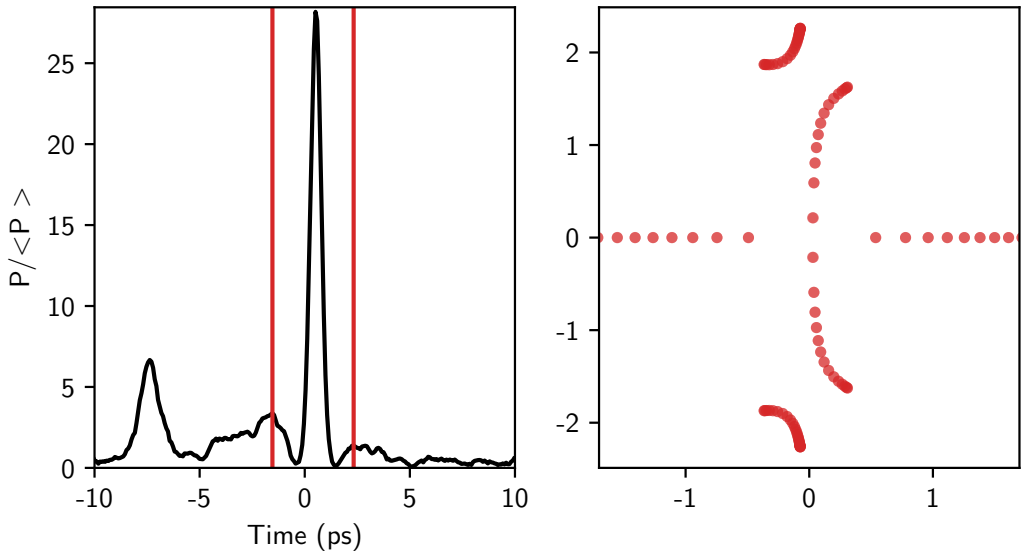

FIGURE 3.35: IST of the experimental data. The data is taken from the Fig. 3.15e. (left) normalized power profile (black) and the window for IST analysis (red). (right) corresponding IST spectrum. The vertical axis corresponds to the imaginary part of ξ, while horizontal to its real part

Chapter 4

Integrable turbulence in the defocusing NLS model

In this chapter, we will study the dynamics of partially-coherent light in nonlinear media with normal dispersion. The model of such media is the defocusing Nonlinear Schrodinger equation. Despite the visual similarity (defocusing NLS differs from the focusing simply by a sign before the dispersion term) properties of these systems are very different. The most important difference is the absence of the modulation instability in the defocusing case and, hence, the rich dynamics related to that.

However, the defocusing system also supports (dark) solitons [64, 246, 247] and cnoidal waves (periodic stationary solutions). There is also a process of regularisation of the gradient catastrophes by emerging of so-called Dispersive Shock Waves (DSW), also called undular bores [110]. All these phenomena are expected to be observed in the integrable turbulence behind the 1-D defocusing NLS model.

As a guideline, we will follow the same question as in the previous chapters: what is the link between the global statistics and the local dynamics? As stated in the first chapter, our goal is to fill the gap between the understanding of the emergence of coherent structures and the emergence of non-Gaussian statistics. In the defocusing regime of 1-D NLS, the coherent structures are for instance the DSWs or the dark and grey solitons.

We will provide extended numerical simulations of the defocusing integrable turbulence in order to identify all possible mechanisms. Further, we will study each of them separately with deterministic models. This will allow us to recognize and distinguish all possible scenarios, which could be observed in experimental data obtained with the Heterodyne Time Microscope. As in the previous chapter, we will provide the IST analysis of the experimental data as well as the fitting with the exact solutions of the 1-D defocusing NLS.

4.1 Numerical study of the 1-D defocusing NLS integrable turbulence

This section is dedicated to numerical studies of the integrable turbulence behind the defocusing NLS model. Using the step-adaptive numerical solver

we will provide first the simulations of the partially-coherent light propagation with parameters close to experimental ones. Then, we will identify origins of the observed phenomena using simplified deterministic models. The process of formation of the Dispersive Shock Waves will be studied on the example of a simple double pulse signal. Also, we will consider the possibilities of the dark solitons formation in the integrable turbulence. Finally, we will examine the evolution of statistical variables.

4.1.1 Simulations of the partially-coherent light propagation in 1-D defocusing NLS system

The partially-coherent light propagation in media governed by the 1-D defocusing NLS model differs from the corresponding focusing dynamics. It was shown in [128–130] that the DSW generation takes place as a regularisation of the gradient catastrophe caused by collision of two neighbour pulses[1]. Indeed, the defocusing dynamics leads to the pulse broadening and, hence, the gradient catastrophe happens not in the center (for the pulses without chirp) as it is in the focusing regime. Depending on the proximity of a neighbour humps we can expect to observe either the nonlinear interference between humps or the wave braking of a single hump. However, we will see later that in the case of partially-coherent waves the two pulse collision occurs earlier. Also, we will demonstrate that the defocusing dynamics leads to the inevitable spectrum broadening. Finally, it will be shown that kurtosis of the power probability density function decreases simultaneously with the increasing spectral width[2].

Here, we will provide systematic numerical simulations and see how change of the nonlinearity affects the dynamics. The way we provide the numerical simulations is very similar to the one explained in Sec. 3.2.1.1. We will employ the step-adaptive method by decomposing the NLS equation into a system of linear equations. As before, we start from partially-coherent waves with Gaussian statistics for real and imaginary parts. In order to produce, the partially-coherent initial conditions we will add uniformly distributed from -π to π random phases in Fourier space. This will guarantee us the periodic boundary conditions.

The defocusing NLS can be written in the form:

$$i\frac{\partial A}{\partial z} - \frac{\beta_2}{2}\frac{\partial^2 A}{\partial t^2} + \gamma|A|^2 A = 0 \tag{4.1}$$

where as usual the $\beta_2 > 0$ is the second-order dispersion and γ is the nonlinearity. As we can see, the equation 4.1 is written in the form used in nonlinear fiber optics, indeed, differs from the focusing one 3.1 only by the sign before the dispersion term.

[1] Here it is important to point out that pulse collision is not the only one mechanism of the DSW generation. More about DSW in 1-D NLS system (and not only) can be found in the review [110].

[2] The exact relation between RMS spectral width and the fourth order moment of $|A|$ can be found in [241].

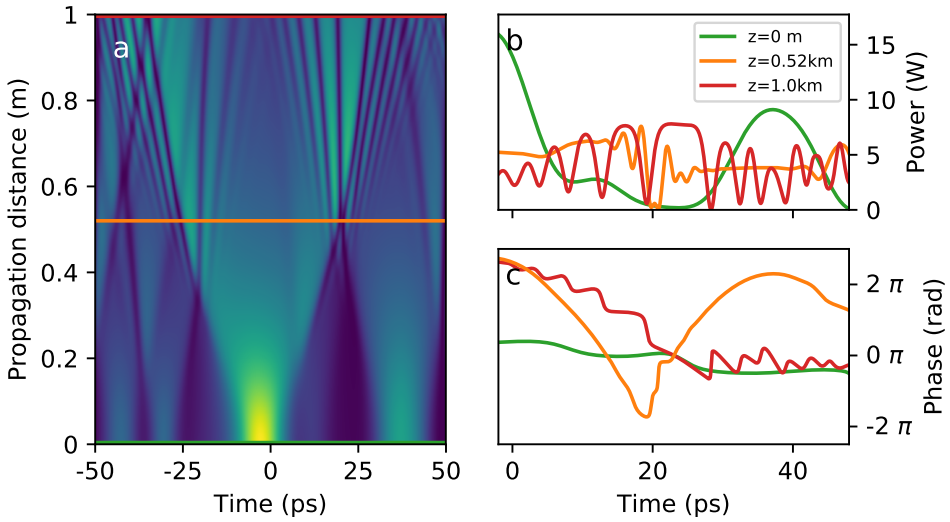

FIGURE 4.1: Simulations of the partially-coherent wave propagation in the defocusing NLS system. Simulation parameters are close to the experimental ones: β_2 = 22 ps^2/km and $\gamma = 3\ W^{-1}km^{-1}$, average power $P_0 = 4.5\ W$ and spectral width $\Delta\nu = 0.05\ THz$. (a) Spatio-temporal diagram. Green,orange and red lines correspond to 0, 0.5 and 1 km respectively. Orange line shows the distance at which the double shock happens. (b) Power profile is zoomed around the double shock area. Colours are preserved. (c) The same for the phase profile.

These simulations are intended for a clear interpretation of the experimentally measured data. In the experiments, we studied three main zones of parameters: the case of weak nonlinearity when the spectral with of the partially-coherent wave was 0.5 THz, intermediate case 0.1 THz and strongly nonlinear 0.05 THz. The power was the same for all the three cases: 4.5 W. Parameters of the single-mode fiber were: β_2=22 ps^2/km, $\gamma = 3\ (Wkm)^{-1}$ and the length 900 m. The fiber parameters are measured as in the previous experiments with the focusing fiber (see Appendix B). The numerical simulations will be provided using the *exactly same parameters*.

Figure 4.1 shows the simulations of the partially-coherent light propagation having an initial spectral width at the half maximum 0.05 THz and average power 4.5 W. The spatio-temporal diagram depicted in Fig. 4.1a shows a typical example of such propagation. In the initial conditions made of the linear superposition of interdependent Fourier components, several humps are randomly distributed in position and amplitude. The two small amplitude humps on the left (from -50 to -25 ps) create a narrow deepening between each other while propagating. This structure (which is similar to a dark soliton [24, 103] as we will show later) preserves its shape for the long distance, even after collisions with other dark structures. Another important event occurs on the right side of the diagram. Two higher amplitude humps collide at the distance z = 0.52 km. As it was mentioned above the defocusing dynamics leads to the gradient catastrophe at the point of collision and its regularisation with the Dispersive Shock Waves [129, 130]. We made three cross-sections of the spatio-temporal diagram: at the initial step, at the point

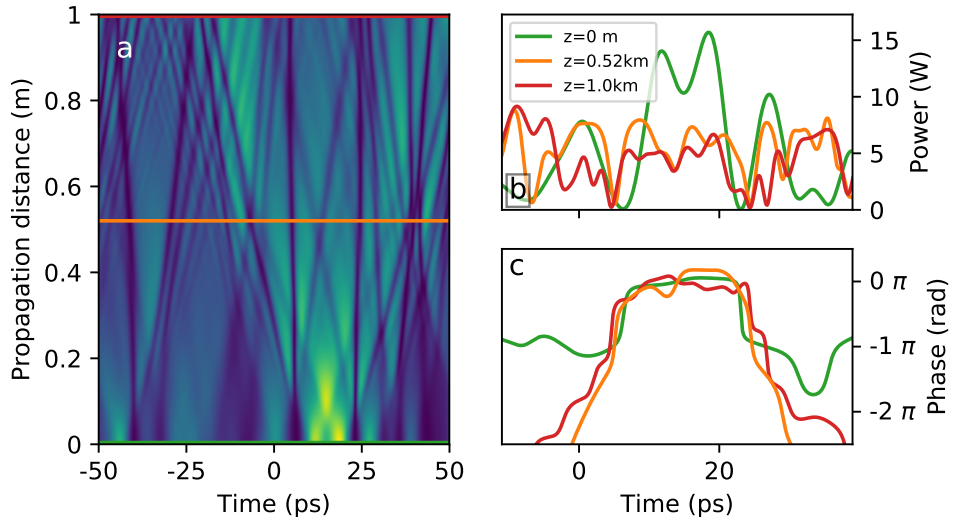

FIGURE 4.2: Simulations of the partially-coherent wave propagation in the defocusing NLS system. Simulation parameters are close to the experimental ones: β_2 = 22 ps^2/km and γ = 3 $W^{-1}km^{-1}$, average power P_0 = 4.5 W and spectral width $\Delta\nu$ = 0.1 THz. (a) Spatio-temporal diagram. Green,orange and red lines correspond to 0, 0.52 and 1 km respectively. Orange line shows the distance at which the double shock happens. (b) Power profile is zoomed around the double shock area. Colours are preserved. (c) The same for the phase profile.

of collision (z=0.52 km) and at the end of the diagram (z=1 km). Corresponding power and phase profiles around the point of collision are depicted in Fig. 4.1b,c. As one can notice at the collision point (orange) the phase as well as power experience an abrupt change of the derivative sign, this is the signature of the catastrophe and ensuing regularisation. By the red, the DSWs are depicted. In some literature, this process is also called nonlinear interference of the dispersive waves [127, 128]. Power profile demonstrates the structure of the DSW. It consists of the main 'plateau' and oscillating wings. The minimum of the power of the first localised structure on right side of the plateau is zero, in the terminology adopted in the field of DSW this point called the vacuum point [113, 212]. The phase profile shows that the plateau has non-zero speed (the corresponding phase has a well-seen angle). This is consistent with the spatio-temporal diagram which shows that plateau moves to the right. Also, the oscillating parts of the DSW have non-zero velocities. Indeed, the oscillations diverge in different directions from the plateau. Detailed study of the gradient catastrophe (infused by two humps collision) will be presented in the Sec. 4.1.2.3.

On the Fig. 4.2 similar diagram for a less nonlinear regime is depicted. For this simulation we used the partially-coherent wave with 0.1 THz spectral width and 4.5 W average power. In this case similar events can be observed: collisions of the neighbour humps due to the defocusing dynamics which leads to the generation of the trains of localised structures as well as generation of separate dark structures due to fulfilment of specific criteria at the initial stage.

The process of creation of the localised dark structures (solitons) will be

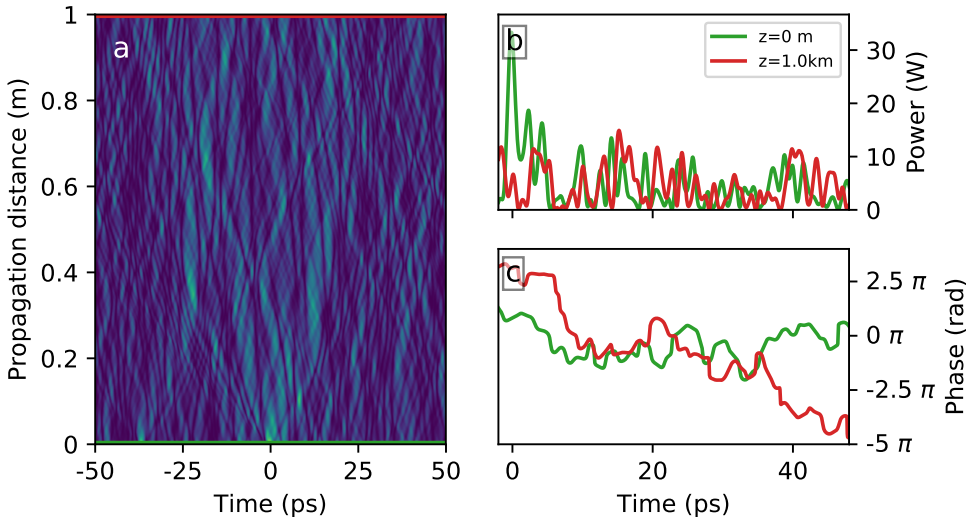

FIGURE 4.3: Simulations of the partially-coherent wave propagation in the defocusing NLS system. Simulation parameters are close to the experimental ones: β_2 = 22 ps^2/km and γ = 3 $W^{-1}km^{-1}$, average power $P_0 = 4.5\ W$ and spectral width $\Delta\nu = 0.5\ THz$. (a) Spatio-temporal diagram. Green and red lines correspond to 0 and 1 km respectively. (b) Power profile is zoomed around the double shock area. Colours are preserved. (c) The same for the phase profile.

considered in details in Sec. 4.1.2.1. Less nonlinear initial conditions propagated over the same distance give more information about the stationary stage of the defocusing integrable turbulence. Indeed, in this case, collisions occur in a shorter propagation distance and the system has more 'time' to achieve equilibrium. This fact can be immediately seen by following the kurtosis evolutions with the propagation distance[3]. Reader can notice that the process of generation of the trains of the coherent structures at the collision points leads to the state similar to so-called soliton gas [248] made, in this case, from randomly distributed interacting dark solitons [247]. An interesting event which can be observed in this diagram occurs between 0 and 25 ps. Here we can see three humps: one of the high power (15 W) and two of lower (8-10 W). It is very common in the partially coherent initial conditions to have a π phase jump between neighbour humps, the reason for this is the areas between humps where power falls down to zero. Plots on the right side of the Fig. 4.2b,c show the power and phase profiles at different positions: z=0 km (green), z=0.52 km (orange) and z=1 km (red). One can notice that the initial phase profile contains the π phase jump symmetrically from both sides of the central hump. The spatio-temporal diagram shows that these initial conditions lead to the generation of two dark co-propagating localised structures. It also can be seen on the power profiles plot. Indeed, the orange line (z= 0.52 km) has deepnesses (dark solitons) around the points (t=5 and 25 ps) of zeros of the initial function (green). The shape and positions of the coherent structures are preserved during the propagation even after several collisions with other structures and decreasing background level [247] (red line).

[3]Corresponding plot will be demonstrated in Sec. 4.1.3.

Finally, we consider the regime of weaker nonlinearity. Corresponding numerically computed spatio-temporal diagram is shown in Fig. 4.3a. In this case, we don't see distinctly the process generation of the DSWs. Initially, humps have a smaller size (proportional to one over the spectral width) and intervals between each other comparable with a typical size of the dark soliton for these conditions. This leads to the immediate generation of coherent structures. These structures start to mix and interact with each other and with the dispersive waves creating a state similar to a dense dark soliton gas. Further decreasing of the nonlinearity will lead to a state where only dispersive waves are presented. In this way, the system goes very rapidly to the stationary state. The power and phase profiles (see Fig. 4.3b,c) at the stationary state (z=1 *km*) almost indistinguishable from the ones at the beginning of propagation. However, the statistical studies will show the rapid but minor decreasing of the value of kurtosis (see Sec. 4.1.3).

4.1.2 DSW and dark solitons as fundamental bricks of the 1-D defocusing NLS integrable turbulence

As we have seen from the numerical studies, the spatio-temporal dynamics of the partially-coherent waves in the defocusing NLS can be decomposed into the four principal building blocs: quasi-linear dynamics of the dispersive waves, generation of a single dark soliton, appearance of the modulated nonlinear wave trains (DSW) due to the gradient catastrophe at the point of collision of two humps and interaction of all components mentioned above. If the first mechanism can be considered as trivial[4], the DSW and single soliton generation have to be studied carefully. That is why in this section we propose to consider deterministic models which could shed some light on these processes.

4.1.2.1 Black, grey and high order solitons

Let's first discuss the structure of the solitonic solutions in the defocusing NLS. As it was mentioned before, the 1-D defocusing NLS governed systems don't support the pulse-like stationary solutions called bright solitons. Instead, they have solutions which can be seen as a dip on the finite background in the intensity profile. These solutions are called *black* (if the dip goes down to zero intensity) and *grey* solitons. Also, like the focusing counterpart, defocusing NLS supports multisoliton solutions.

As we showed in Ch. 1, for the 1-D defocusing NLS written in the dimensionless form:

$$i\frac{\partial u}{\partial t} - \frac{1}{2}\frac{\partial^2 u}{\partial x^2} + |u|^2 u = 0 \tag{4.2}$$

[4]Here we have to mention that the defocusing dynamics of a single bell-like hump leads to the formation of the dispersive shock waves due to the wave breaking process [249–251]. However, in the partially-coherent case, the collision happens earlier than the waves breaking.

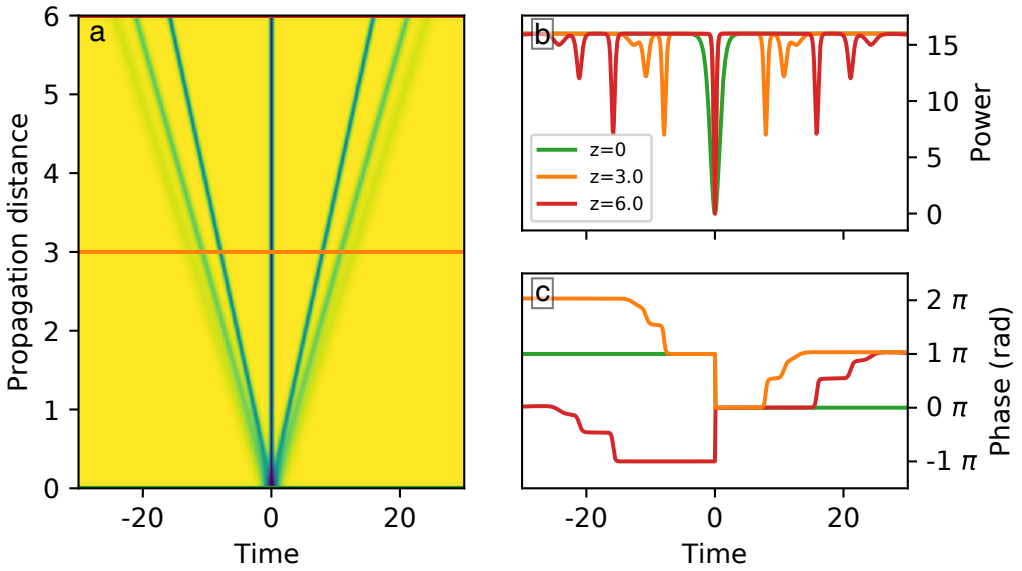

FIGURE 4.4: Simulations of the mulisoliton propagation in the defocusing NLS system, $u(0,x) = Ntanh(x)$ with $N = 4$ in this case. Simulations provided for the dimensionless 1-D NLS 4.2. (a) Spatio-temporal diagram. Green, orange and red lines correspond to 0, and 6 nonlinear lengths respectively. (b) Power profile around zoomed around the double shock area. Colours are preserved. (c) The same for the phase profile.

The general formula for the dark soliton is following:

$$u(0,x) = \eta[Btanh(\xi) - i\sqrt{1-B^2}] \tag{4.3}$$

where $\xi = \eta B(x - x_0)$, parameter B is the deepness of the dip (B=1 gives the black soliton, B=0 - continuous wave), η defines the background amplitude, x_0 is the initial shift.

Also, the 1-D defocusing NLS has multisoliton solutions. In the simplest case, it is similar to the focusing. If the fundamental black soliton can be expressed as follows: $u(0,x) = tanh(x)$. The multisoliton solution is simply: $u(0,x) = Ntanh(x)$, where $2N-1$ will give the number of generated solitons. The Fig. 4.4 shows numerically computed dynamics of the multisoliton with N=4. Spatio-temporal diagram Fig. 4.4a shows the evolution of the initial dip ($u(0,x) = 4tanh(x)$) on the background of amplitude 4 (in normalised units). As we can see, three pairs of gray solitons separate from the central black soliton while propagating. In Fig. 4.4b,c the power ($|u|^2$) and phase profiles at three different propagation dispenses are depicted. The initial dip (green) is wider than the general black soliton solution for this level of background. It has the sharp phase jump of π as the fundamental soliton. The phase of the grey solitons propagating to the right has the same shape but different signs than ones propagating to the left.

4.1.2.2 IST approach to the characterisation of the dark solitons

The most illustrative way to describe the full dark soliton family in the 1-D defocusing NLS is the IST representation. The approach for solving Zakharov-Shabat problem in the defocusing case is similar to the focusing one. In order to find the IST spectrum, we will employ the Fourier collocation method described in Sec. 3.3. The ZS problem itself is changed as follows:

$$\begin{bmatrix} i\partial_x & u \\ u^* & -i\partial_x \end{bmatrix} Y = \xi Y \tag{4.4}$$

As we can see, the change of sign in the equation leads to qualitatively different scattering problem. Indeed, the matrix in the equation 4.4 has a very remarkable property: it is Hermitian. Therefore, the eigenvalues are *real*.

As we mentioned in the prevention section the defocusing NLS has a multisoliton solution in the form $u(0,x) = Ntanh(x)$. In order to illustrate the inverse scattering approach, we calculated the IST spectra of the multisoliton solution with N from 0 to 10 with a step 0.5. Corresponding data is plotted in the Fig. 4.5.

The spectrum of the plane wave is continuous. It is situated from minus infinity to infinity with a gap in the center [5]. A width of the gap is given by the wave amplitude. For example, a plane wave with amplitude 1 will be represented by a continuous IST spectrum with the gap from -1 to 1. A discrete eigenvalue (as in the focusing case) represents the soliton. Discrete eigenvalues are situated inside the gap. Its position inside the gap represents the depth of the gray soliton. If the discrete eigenvalue situated at zero (in the center of the gap) it represents a back soliton.

As we can see in Fig. 4.5, when $N = 1$ (green) we observe a gap of the width 2 (from -1 to 1) and one discrete point in the center which corresponds to the black soliton. Increasing N, we observe that the number of discrete eigenvalues in the IST spectrum also increase. New eigenvalues appear closer to the gap edge and therefore represents gray solitons of different depth. The example of $N = 4$ (yellow), considered before (see Fig. 4.4), is represented by the gap of the width 8 (from -4 to 4) and 7 discrete points (the central point is double). This corresponds exactly to the situation we observed in the spatio-temporal diagram: one black soliton and 6 grays. The gray soliton has 3 different widths and symmetrically move away from the center.

4.1.2.3 Dispersive Shock Wave formation via two pulse collision

As we have seen before, in the case of the partially-coherent wave propagation in the media governed by 1-D defocusing NLS, the process of two humps collision plays a crucial role. Indeed, due to the defocusing dynamics initially separated humps increase their temporal width until the moment of collision, which leads to the double shock [129, 130]. The more rigorously, the

[5] In the case when the wave will have a group velocity mismatch the gap will be shifted from the center. The direction of the shift depends on the sign of mismatch.

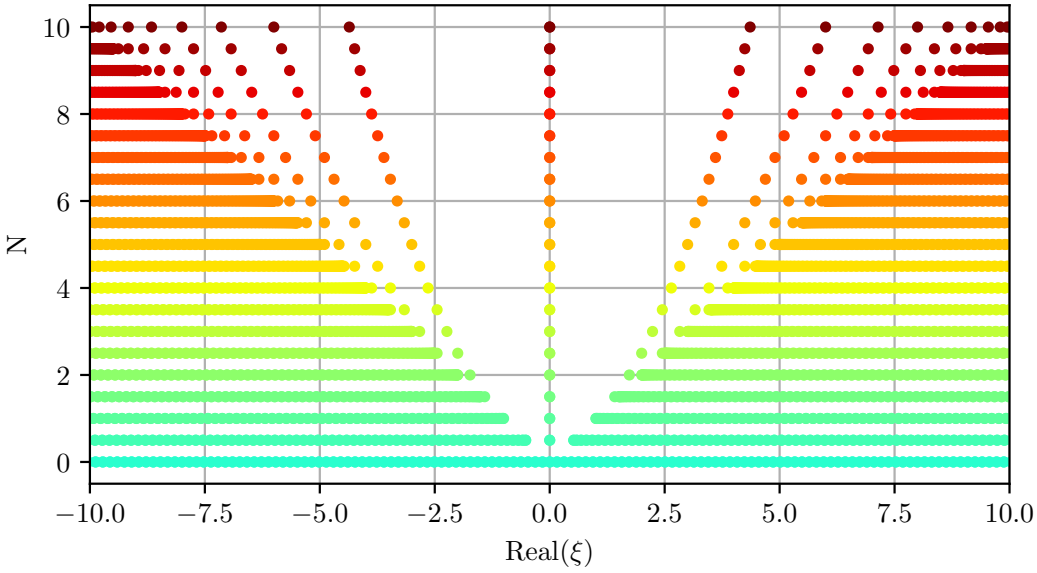

FIGURE 4.5: IST spectra of N soliton solutions

double shock is the gradient catastrophe in intensity or phase which happens at the point of collision. In the defocusing NLS, the gradient catastrophe is regularised by generation of the Dispersive Shock Waves. The DSW can be considered as a modulated train of dark solitons. The modulated parameters can be the amplitude, frequency or the mean value. It can be characterised with at least two speeds of propagation: one of the leading edge and one of the trailing [110].

The one simplest deterministic model for studying the double shock generated DWS is the two bell-like pulses with variable separation. This model was widely studied in optics as a way of generating a train of the dark solitons in 1-D defocusing NLS [126, 252] and related systems [253, 254].

Detailed consideration of this mechanism was provided after its observation in the Bose-Einstein condensate [255]. In the cold atom domain, the phenomenon is known as nonlinear interference. The theoretical studies provided in [127] using IST and later in [128] using Whitham averaging theory[6] show that in the case when two identical, quasi one-dimensional Bose-Einstein condensates: (1) the process of generation of the train of dark solitons happens symmetrically (2) the speed and modulation of the wave train depends on the initial separation of the two packets. These conclusions can be adopted for the study of two interacting pulses in the 1-D defocusing NLS governed media.

In order to illustrate these statements we provided numerical simulation of the 1-D defocusing NLS. We took two identical Gaussian pulses and simulated their evolution in changing only the initial separation distances. We

[6]Whitham averaging theory is one of the main tools for studying the DSW dynamics. However, this theory will not consider in this manuscript. For the detailed description see the following articles [110, 111].

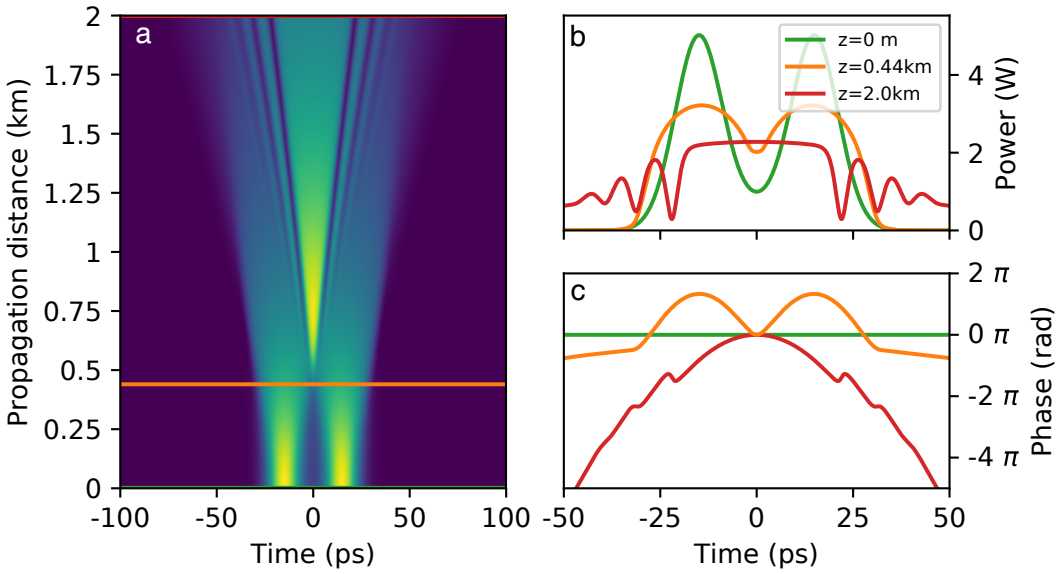

FIGURE 4.6: Simulations of the double pulse signal propagation in the defocusing NLS system. Simulation parameters are close to the experimental ones: $\beta_2 = 22$ ps^2/km and $\gamma = 3$ $W^{-1}km^{-1}$, peak power $P_0 = 5$ W and separation 30 ps. (a) Spatio-temporal diagram. Green, orange and red lines correspond to 0, 0.44 and 2 km respectively. (b) Power profile is zoomed around the double shock area. Colours are preserved. (c) The same for the phase profile

used the 1-D defocusing NLS adopted in optics (see Eq. 4.1) with the parameters of the real experiments: β_2=22 ps^2/km, $\gamma = 3$ $(Wkm)^{-1}$. Pulses were given by the formula $A(0,t) = a(exp[-(t-\Delta)^2/2\sigma^2] + exp[-(t+\Delta)^2/2\sigma^2])$, where $a^2 = 5$ W, $\sigma^2 = 75$ ps^2 and $\Delta = 15, 25$ and 50 ps - half of the separation.

Results of the simulations are presented in Fig. 4.6, 4.7 and 4.8. First, let's consider the case when the separation is small: 30 ps between the pulses' maxima. The spatio-temporal diagram is depicted in Fig. 4.6a. The power and phase profiles are plotted in Fig. 4.6b,c respectively. As one can see from the initial power profile, the pulses are not completely separated and the central point power is approximately 1 W. By orange, we depicted the profiles in the point of beginning of the shock formation. The power profiles, as well as the phase profile, consist of two symmetrical humps. The sign of the phase gradient shows that at the moment of shock the system tends to push the two humps together[7]. After the moment of shock, we observe the formation of the plateau in the center and DSW on its sides (see the red lines). The phase profile and well as spatio-temporal diagram show that all the DSW have non-zero speed and the plateau is increasing its size while propagation.

The next figure 4.7 shows the same pulses, but more separated initially in time. Precisely, the separation distance is 50 ps. At this distance, the double pulse signal already has an area where the power goes down to zero. As we

[7]Indeed, NLE equation includes the group velocity dispersion, therefore the linear dispersion relation is $k = \omega^2\beta_2/2$. Therefore, group velocity is $1/v_g = dk/d\omega = \omega\beta_2$. So the phase gradient $d\phi/dt$ which is instantaneous frequency. Finally, different signs of the phase gradient correspond to the opposite group velocities.

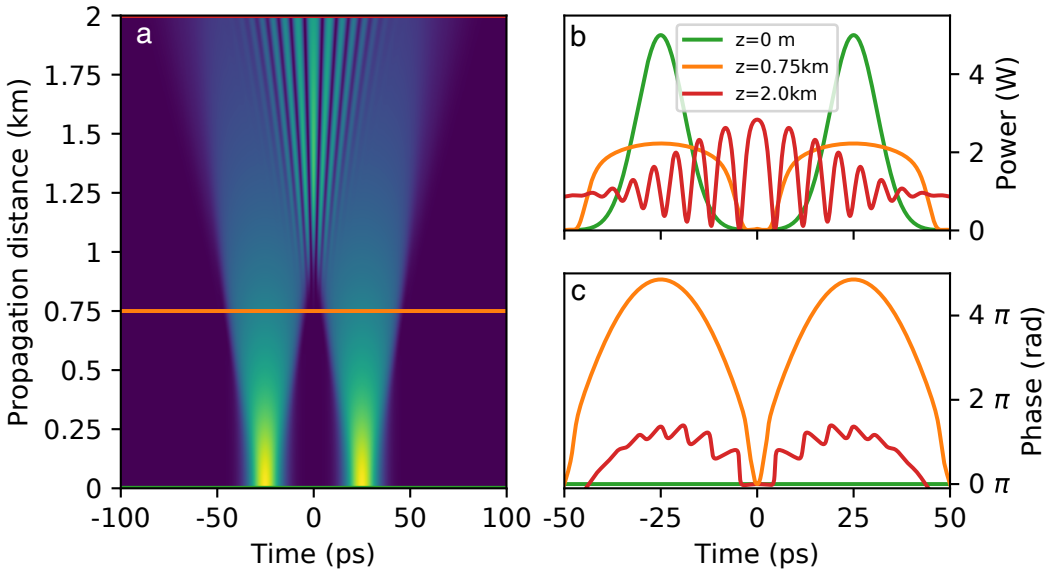

FIGURE 4.7: Simulations of the double pulse signal propagation in the defocusing NLS system. Simulation parameters are close to the experimental ones: $\beta_2 = 22$ ps^2/km and $\gamma = 3$ $W^{-1}km^{-1}$, peak power $P_0 = 5$ W and separation 50 ps. (a) Spatio-temporal diagram. Green, orange and red lines correspond to 0, 0.75 and 2 km respectively. (b) Power profile is zoomed around the double shock area. Colours are preserved. (c) The same for the phase profile.

can see the spatio-temporal diagram (Fig. 4.7a) shows that dynamics significantly changed. Indeed, here we do not observe the formation of the central plateau, while the frequency of coherent dark structures is visibly increased. Also, remarkable change is the constant phase around the central point (t=0 ps) which means that there is no repulsive dynamics in this area. At the same time, the change of the sign of the phase derivative close to the point of double shock (see the orange line) becomes faster.

Finally, we will consider the case of the large initial separation: 100 ps. Results of the simulation are presented in Fig. 4.8. Here we observe the dynamics similar to the previous separation distance, but showing even more distinctly the mentioned properties. The central peak became indistinguishable from its neighbours. *The duration of all dark coherent structures visibly decreased with increasing separation time*. This point will be crucial for understanding of the presence of different scales in the experimental data recorded with the same statistical parameters. Also, remarkable is the number of vacuum points. If in the first case we didn't observe any of them during the given propagation distance, in the second case we have seen two vacuum points around the central point, the last case demonstrates approximately ten of them. As in the previous case, velocity of the dark structures in the central part of the wavetrain is close to zero.

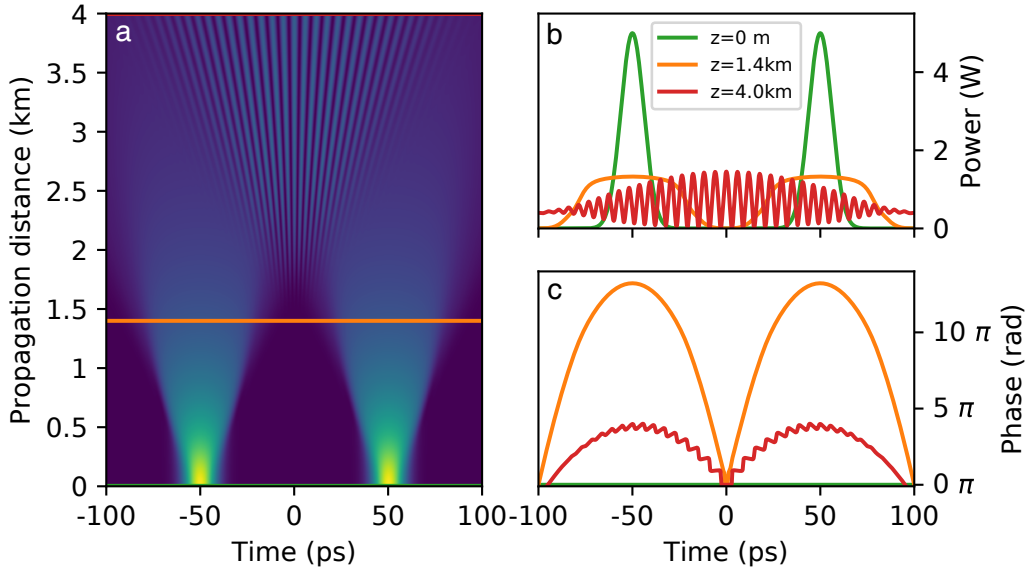

FIGURE 4.8: Simulations of the double pulse signal propagation in the defocusing NLS system. Simulation parameters are close to the experimental ones: $\beta_2 = 22$ ps^2/km and $\gamma = 3$ $W^{-1}km^{-1}$, peak power $P_0 = 5$ W and separation 100 ps. (a) Spatio-temporal diagram. Green, orange and red lines correspond to 0, 1.4 and 4 km respectively. (b) Power profile is zoomed around the double shock area. Colours are preserved. (c) The same for the phase profile.

4.1.2.4 Generation of the dark solitons

Presented simulations of the partially-coherent light dynamics in 1-D defocusing NLS system revealed the possibility of the single dark soliton generation (for example see Fig. 4.2). From the first look, this process does not seem to be probable, because the dark soliton is a very particular exact solution of the 1-D defocusing NLS equation. However, this phenomenon can be observed in the numerical simulations more often than one would expect (Fig. 4.1, 4.2). In this section, we present a deterministic model which shows one of the possible scenarios of the coherent solitary structures generation.

As one could notice, in Fig. 3.12, where the experimentally recorded partially-coherent initial conditions are depicted, it is very likely to find areas where the phase experiences the π phase jump. For example, in Fig. 3.12b we see three separate humps and two phase jumps in the area where power goes to zero. Standard random linear superposition of waves with Gaussian statistics (partially-coherent initial conditions) creates favourable conditions for generation of the dark (and even black) solitons.

Figure 4.9 shows one of the possible scenarios of generation of the dark soliton. As an initial condition, we created two humps with sharp phase jump between them (Fig. 4.9b,c - green lines). For simulations we used real experimental parameters: β_2=22 ps^2/km, $\gamma = 3\ (Wkm)^{-1}$. The spatio-temporal diagram (Fig. 4.9a) demonstrates the evolution of such initial conditions. As we can see, defusing dynamics leads to the gradient catastrophe (around point z=0.25 km). It is similar to the cases shown in the previous section, however, the phase jump between humps destroys the symmetry of DSW

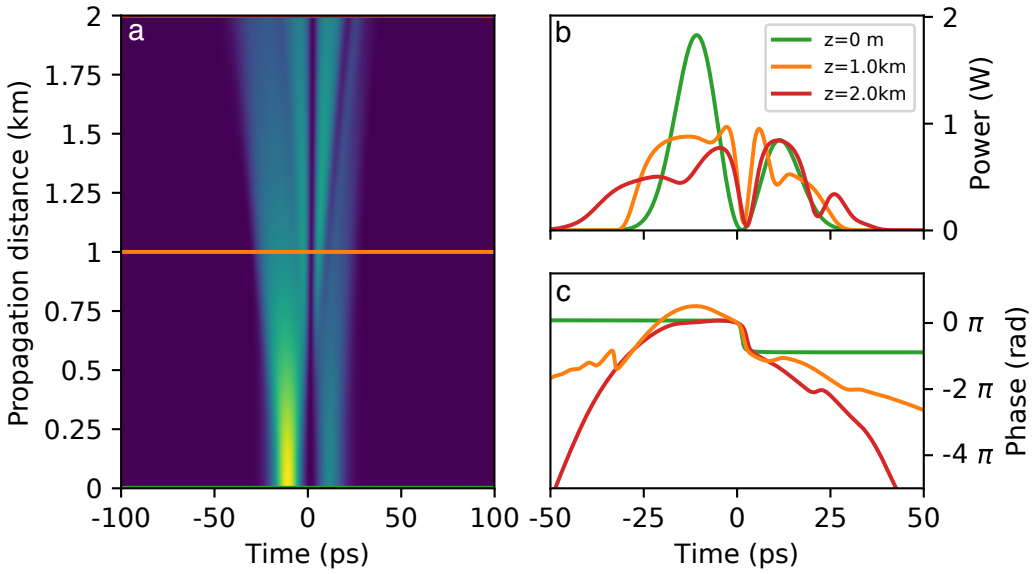

FIGURE 4.9: Typical scenario of generation of the dark soliton in the defocusing integrable turbulence.

generation. The phase was particularly chosen in order to shift one of the dark solitons to the center, as it was expected the needed phase equals to π. Resulting dynamics is very similar to one of the multisoliton solution (two solitons in this case) on the finite width background [247]. Indeed, as we can see from the diagram, there are two satellite gray solitons of the low deepness generated. Remarkably, this effect is present even if the pulses have equal amplitudes[8]. Further increasing of the power of the pulses will lead to the generation of new satellite gray solitons.

4.1.3 Statistical approach to the 1-D defocusing NLS integrable turbulence

We start as in the previous chapters (see in particular section 3.2) with the signal having Gaussian statistics for the real and imaginary part of the field, i.e. exponential distribution for the intensity. It is well established that the defocusing dynamics leads to the low-tail probability density function [125]. In other words, the probability of observation of the high-amplitude structures is lower than initially.

As in the focusing case, information about the fourth order moments of the probability density function can be used to make some assumptions about the light behaviour. Figure 4.10 shows the fourth order moment defined as in Sec. 3.2.2 as a function of propagation distance. Taking the Gaussian shape of the spectrum we varied its width $\Delta\nu$, keeping the average power constant. We studied three experimental parameters considered before: $\Delta\nu = 0.05$ (blue line), 0.1 (orange) and 0.5 (green) THz, all with average

[8]Exactly these initial conditions were used for the experimental observation of the dark solitons in [126].

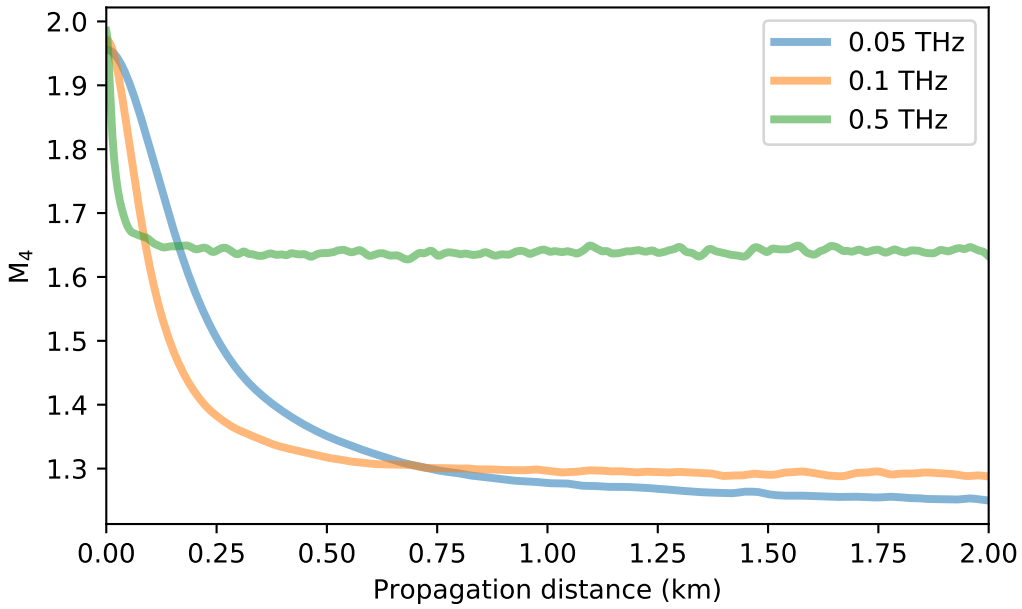

FIGURE 4.10: The fourth order moments ($M_4[X] = E[(X)^4]/(E[(X)^2])^2$) of the partially-coherent initial condition as a function of the propagation distance. The average power is 4.5 W, spectral widths 0.05 (blue line), 0.1 (orange) and 0.5 (green) THz.

power 4.5 W. We provided averaging over 100 realisations of the partially-coherent initial conditions for each parameter. The simulation box was 300 ps with the discretization step 0.1 ps.

From the Fig. 4.10 we can make several straightforward conclusions: (i) the transient regime of the statistics is shorter in the case of the weakest nonlinearity , (ii) the value of the kurtosis at the stationary state is smaller for the more nonlinear regime. This behaviour of the system can be understood taking into the account the fact that there is a typical distance associated with the neighbour humps collision. Indeed, as we have seen in Fig. 4.1, 4.2 and 4.3, all dynamics globally can be divided on the before and collision parts. However, we do not observe any signature of this event in the evolution of kurtosis. Fig. 4.10 demonstrates monotonous decay of the kurtosis for all considered parameters. Therefore, evolution of another quantity has to be studied.

Here we would like to state a conjecture which is in a good agreement with our observations: *the typical distance at which the double shock occurs is directly correlated with the point where the FWHM of the spectrum has its maximum*. The comparison of the kurtosis and FWHM of the spectrum evolution is presented in Fig. 4.11. The orange line shows the kurtosis of the partially-coherent wave with spectral widths 0.1 THz and average power 4.5 W. The maximum of the FWHM of the spectrum is shown by the black dashed line. The FWHM of the spectrum for the given propagation distance was computed by averaging the power spectra of 100 realisations and fitting it with the Gaussian function. We extracted the standard deviation σ and transformed it to the FWHM by computing $2\sigma\sqrt{2log(2)}$. As we can see the FWHM of the spectrum curve has a well-seen maximum. The distance which

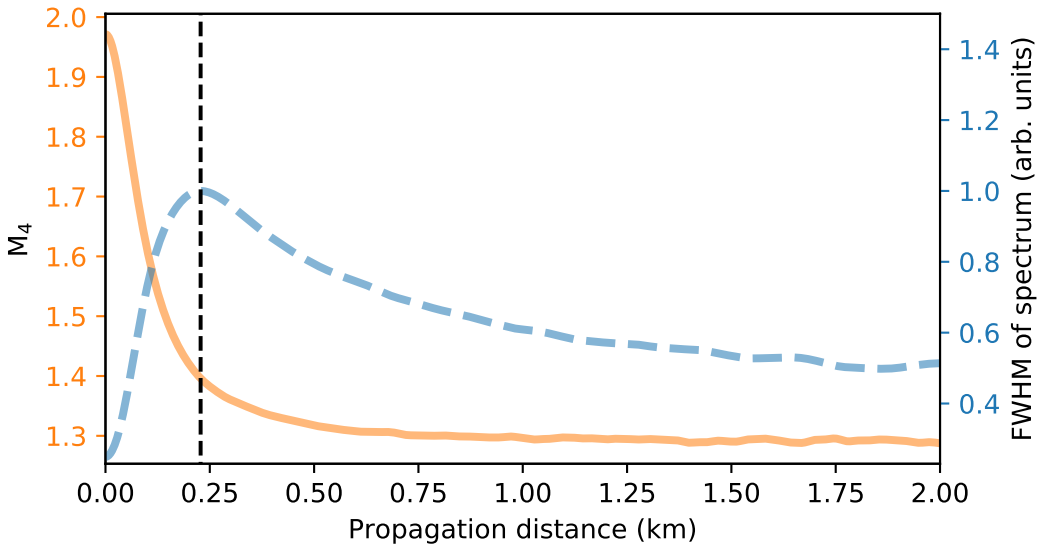

FIGURE 4.11: Comparison of he fourth order moment (orange) and the FWHM of the spectrum (blue) plotted as a function of the propagation distance. The average power of the partially-coherent initial conditions is 4.5 W, spectral widths - 0.1 THz. Black line shows the position of the maximum of the blue curve (z = 0.23 km).

corresponds to this maximum represents with a good agreement the typical collision point observed in the numerical. This can be seen, for example, in Fig. 4.2. Also, Fig. 4.7 and 4.8 show that the phase gradient is the highest at the collision point, which signifies about increased spectral width. Remarkably, the evolution of the standard deviation of the spectrum itself (not the Gaussian fit) is directly proportional to the kurtosis (see [241]) and, hence, does not have overshot. The corresponding spectra and Gaussian fits can be found in Appendix E.

Finally, I would like to recall that the stated observation is a conjecture, which has to be rigorously proved. However, it goes beyond the framework of this manuscript and will be the subject of further investigations.

4.2 Experimental investigation the defoctusing NLS integrable turbulence by using Heterodyne Time Microscope

In this section, we will provide the experimental evidence of the phenomena discussed above. Using the Heterodyne Time Microscope, we recorded the partially-coherent light of different spectral widths at the output of the 900 m-long fiber with normal dispersion ($\beta_2 > 0$). We will demonstrate typical recorded data and provide a comparison with the results of numerical simulations presented in the previous section in order to understand the underlying mechanisms. Also, we will compare experimental data with the

exact solutions of the 1-D defocusing NLS and demonstrate the applicability of the local IST analysis for identification of the recorded structures.

4.2.1 Zoology in the defocusing regime of NLS integrable turbulence

In order to confirm observations and conjectures obtained from numerical simulations, we present in this section snapshots of experimentally recorded partially-coherent light propagating in the defocusing media. The recording was provided with the HTM. However, we have shown in the previous chapter that it could be successfully done using the SEAHORSE. We demonstrate here phase and amplitude profiles of three different sets of the recorded frames. Each set corresponds to one of initial conditions: $\Delta\nu = 0.05$, 0.1 and 0.5 THz. Average power was set to be the same in all the experiments: 4.5 W. We recorded the snapshots by sets of 50,000 frames each. In this section, we demonstrate only the most illustrative or typical snapshots selected manually.

The procedures of generation of the initial signal, the setup calibration and tuning were the same as in the previous chapter. The fiber parameters were measured in separate experiments and compared with the numerical simulations (see Appendix B). We remind that the typical shape of the random phase and amplitude of the initial conditions recorded in the experiments is similar to ones presented in Fig 3.12 in the previous chapter.

The numerical simulations of the partially-coherent wave propagation(for example Fig. 4.1), demonstrated the important role of the double shock in the nonlinear dynamics. The double shock leads to the generation of the Dispersive Shock Waves: the train of modulated in depth and separation solitary dark waves. As we have seen in the Sec. 4.1.2.3, the initial separation of the humps can lead to the formation of different time scales, changing the modulation parameters of the DSW. Finally, in Sec. 4.1.2.4 we demonstrated how phase shift between neighbour humps can lead to the generation of the isolated dark solitons.

We start with the most nonlinear case. Figures 4.12 and 4.13 show the experimentally recorded snapshots of the random wave having 0.05 THz spectral width and average power 4.5 W, propagated in 900 m fiber. These experimental parameters correspond to parameters of the numerical simulations presented the in the section 4.1.1 (see Fig. 4.1). In the first row, the output snapshots of the Heterodyne Time Microscope are depicted. The second one shows the reconstructed phase and the third one - the power profile. The procedure of the phase and power reconstruction from the recorded snapshots can be found in Sec. 2.3.3.

Figure 4.12 demonstrates different variations of the process of the DSW formation on the sides of a plateau (see the Fig.4.1b,c). One can recognize the plateau that appears as a result of the nonlinear collision of two close humps discussed in section 4.1.2.3. The size of the plateau can depend on many factors: separation and amplitude of the initial humps, chirp, interaction with other neighbour humps. In the case of the partially coherent wave, we can

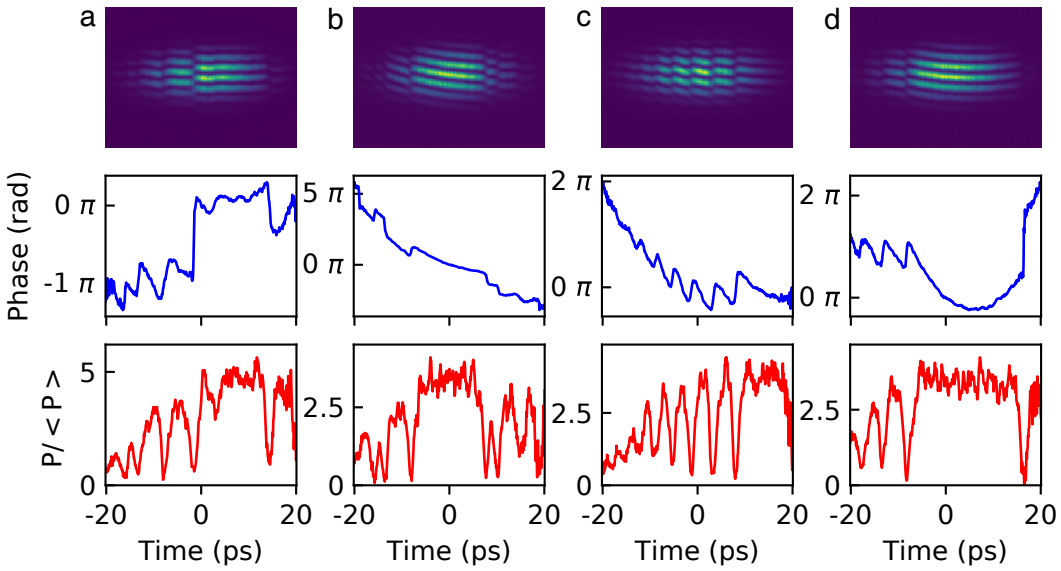

FIGURE 4.12: Experimentally recorded with HTM partially-coherent waves propagated in 900 m fiber with normal dispersion. The initial spectral with is 0.05 THz, average power 4.5 W. (first row) snapshots recorded directly with the HTM. (second and third rows) reconstructed phase and power profiles.

have a big variety of the initial conditions, therefore we observe the plateaus of different sizes surrounded by many non-periodical DSW. In Fig. 4.12a,b typical snapshots containing the plateau are depicted. One can see the good resemblance to the profiles obtained numerically. Fig. 4.12c confirms that non-perturbed DWS can be observed even in the developed stage of the integrable turbulence. In the last figure 4.12d a long plateau of 19 ps is shown.

Also, experimental data show that we can observe completely different time scales with the same type of random wave. As we demonstrated using the deterministic model (see Sec. 4.1.2.3), large separation between the initial humps leads to the generation of the very dense train of periodical nonlinear waves. Indeed, besides the data shown in Fig. 4.12 we can find fast oscillating profiles. Figure 4.13 demonstrates the recorded data containing such dense wave trains. As we can see from the power and amplitude profiles, each oscillation, indeed, has the characteristic phase jump, so it can be considered as a dark soliton locally. The value of the phase jump depends on the deepness of the grey soliton as it is predicted by the Eq. 4.3. Remarkably, in Fig. 4.13c we observe the case when the modulated nonlinear wave train contains many vacuum points. This can be signatures of large separation between the initial hump created this nonlinear wave.

However, the nonlinear holography technique (see Sec. 3.2.1.6) is not applicable to the developed stage of the defocusing integrable turbulence. In the recorded window we will always find wave trains, presented just partially. Hence, the full information will be always missing. Therefore, the initial conditions cannot be reconstructed in this way.

Increasing the spectral width we obtain more complex profiles for the same propagation distance. Experimental data which corresponds to initial FWHM 0.1 THz is depicted in Fig. 4.14. We observe less ordered pictures due

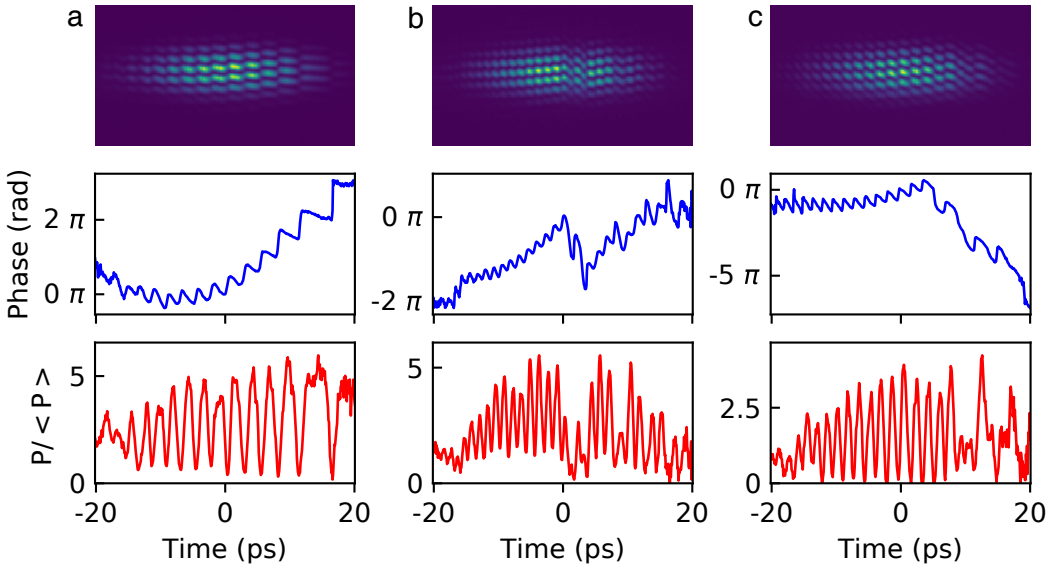

FIGURE 4.13: Experimentally recorded with HTM partially-coherent waves propagated in 900 m fiber with normal dispersion. Exactly the same experimental parameters as in Fig. 4.12 are used, however in this figure we present data that contains fast oscillating wavetrains.

to the fact that the two pulse collision happens (in average) earlier than in the previous case. So the system has more propagation distance to the recording point and, hence, DSW produced by different humps collision have a chance to mix and interfere. However, we still can recognise the dark solitons with all corresponding features.

The experimentally recorded data for the random wave having widest initial spectrum is presented in Fig. 4.15. We can see that presented profiles are very similar to the data recorded without any nonlinear propagation. This signifies that we are close to the weakly nonlinear regime (however, presence of the coherent structures signifies that the weakly nonlinear regime is not achieved), which is also can be seen from the statistical analysis (see Fig. 4.10). However, the presence of the dark solitons in the range of parameters has to be investigated.

4.2.2 Experimental data analysis

In this section, we will provide a comparison between the recorded experimental data and analytical solutions of the defocusing NLS. For this purpose, we have chosen among all the recorded data the frames containing well distinguishable dark solitons. As we have seen in the previous section, it is more likely to observe well separated dark solitons using the initial conditions having the narrowest spectral width: 0.05 THz. In order to prove that the experimental data can be well fitted by the solution Eq. 4.3, we have chosen frames which contain black and gray solitons.

The result of analysis is depicted in Fig. 4.16. The part of the figure marked by (a) corresponds to the analysis of the black soliton, (b) - a gray one. As before, the first row contains the snapshots recorded with HTM, the

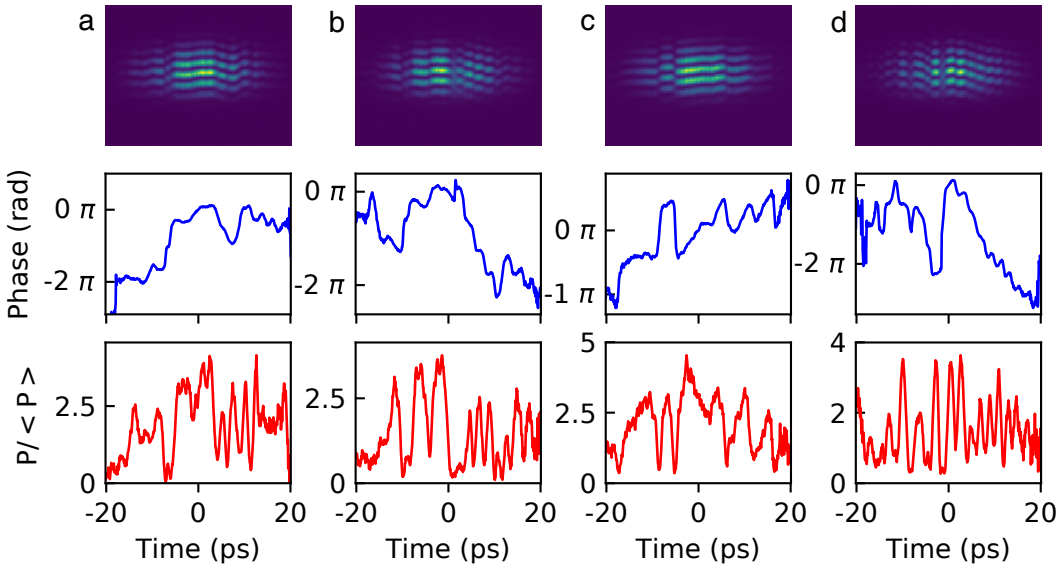

FIGURE 4.14: Experimentally recorded with HTM partially-coherent waves propagated in 900 m fiber with normal dispersion. Spectral width is 0.1 THz, average power is 4.5 W. (first row) snapshots recorded directly with the HTM. (second and third rows) reconstructed phase and power profiles.

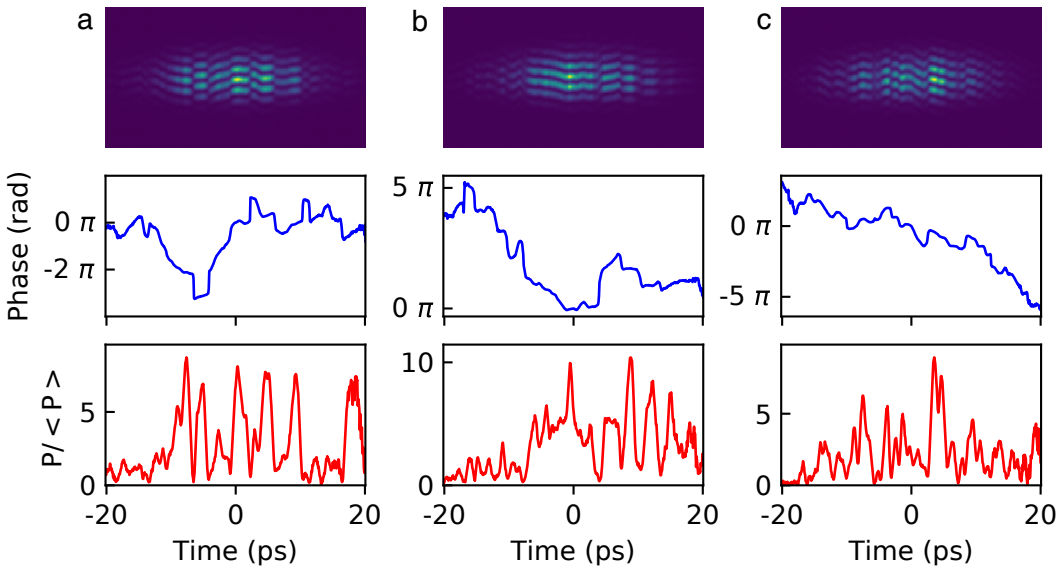

FIGURE 4.15: Experimentally recorded with HTM partially-coherent waves propagated in 900 m fiber with normal dispersion. Spectral width is 0.5 THz, average power is 4.5 W. (first row) snapshots recorded directly with the HTM. (second and third rows) reconstructed phase and power profiles.

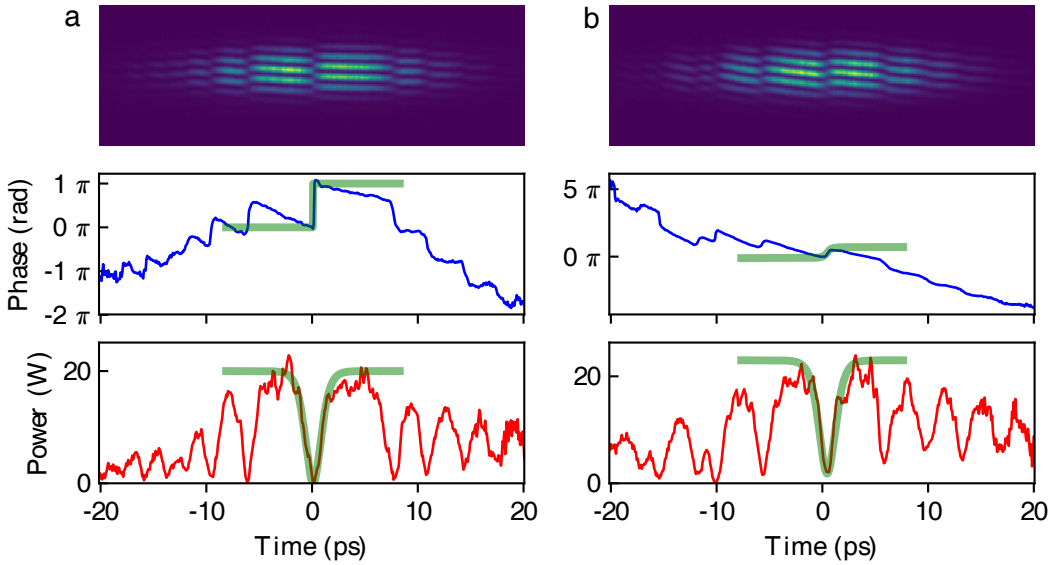

FIGURE 4.16: Fit of the experimentally recorded data with the Eq. 4.3. The experimental data is recorded for the initial random wave having 0.05 THz and average power 4.5 W. Green lines show the fit for the black (a) and gray (b) soliton.

second - phase profile, the third one - power profile. In Fig. 4.16a the green line represents the fit, made with $u(\tau, 0) = Ntanh(\tau)$. The exact solution was renormalized to the dimensional form as follows: $t = \tau\sqrt{\beta_2/(2\gamma P_0)}$. The only one adjusted parameter was N - the background amplitude. From the Fig. 4.16a we can report that the good agreement of the exact solution with the experimental data was observed. The difference in the phase profiles just a consequence of the non-zero speed of the experimental dark soliton. Figure 4.16b shows a gray soliton comparison with the Eq. 4.3 written in the dimensional form. In this case, the adjustable parameters were background amplitude and the soliton deepness. In this case, the experimental data can be fitted with a good accuracy as well.

Having the phase and power profiles we are able to provide the local analysis of the experimentally measured data using the IST technique. The procedure is similar to one shown in Sec. 3.3.4. However, as we demonstrated before the ZS spectrum lies only on the real axis due to the fact that the matrix in the corresponding scattering problem (see Eq. 4.4) is Hermitian.The IST spectrum of the experimental data plotted in Fig. 4.16a is shown in Fig. 4.17. We provided the local analysis in the region fitted by the analytical expression (green line in Fig. 4.16a). The IST spectrum shows the presence of one almost black soliton on the background 1.5 in normalized units. This confirms our conjecture that the collision of two neighbour humps leads to the appearance of the modulated nonlinear wavetrain (DSW) which locally can be seen as a sequence of dark solitons.

Finally, I would like to summarize the main results of this chapter. First of all, the direct observations of the partially-coherent light propagation in the system governed by the 1-D defocusing NLS equation were provided. We observed nonlinear wavetrains recorded with the same initial conditions, but

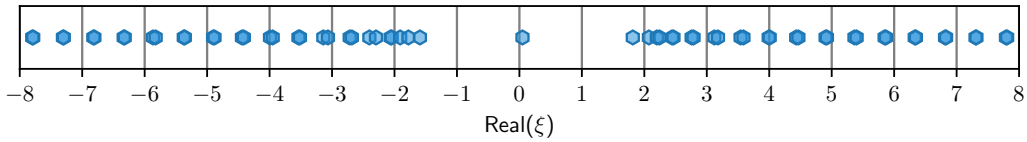

FIGURE 4.17: IST spectrum of the experimentally recorded data depicted in Fig. 4.16a

having different oscillation scales. Numerical simulations of the partially-coherent wave propagation with periodic boundary conditions showed that the origin of such wavetrains is the nonlinear interference of two neighbour humps. We considered a deterministic model of two pulses in order to explain such effect. It is known for a long time that the initial separation between two humps strongly influences the time scale of the nonlinear waves generated after the collision. This explanation was adopted for the case of the partially-coherent light propagation in the 1-D defocusing NLS systems.

Chapter 5

Conclusions and perspectives

This work is dedicated to the experimental fiber optics and numerical studies of the integrable turbulence in a system governed by focusing and defocusing 1-D NLS equation.

In Chapter 1, we provided basics of the theory of integrable systems. Introducing the stochastic initial conditions into an integrable system we enter the domain of integrable turbulence. We showed the key differences between integrable turbulence and conventional theory of weak turbulence. We considered in details the case of integrable 1-D Nonlinear Schrödinger (NLS) equation. Since one of our objectives was to build connections between the local dynamics and statistical descriptions of the systems governed by NLS, we discussed its exact solutions and method of integration called Inverse Scattering Transform. Among the exact solutions, there is a family called solitons on the finite background that plays an important role being a possible prototype of the ocean Rogue waves. The applications NLS to other real physical systems was discussed as well. We pointed out the complexity and importance of using the periodic boundary conditions in the investigation of the integrable turbulence, especially using Inverse Scattering Transform. Finally, considered dominating mechanics of focusing and defocusing 1-D NLS equation such as modulation instability, gradient catastrophe and dispersive shock waves formation.

In Chapter 2, we made a short review of the ultrafast measurement techniques which demonstrate the necessity of the development of a new approach. We biased our new measurement technique on the duality between spatial and temporal imaging. The essential of the temporal imaging are given at the beginning of the chapter as well. Using this well-known approach, we first extended it in order to construct a Time Microscope for the efficient power profile measurement with both high resolution and dynamics. The high dynamical range was obtained employing a sensitive sCMOS camera. The detailed explanation of the experimental procedures are given in Section 2.2.2. Then, using the second dimension of the camera, we established the heterodyne measurements of the phase. In order to verify the accuracy of measurements, we provided versatile tests including the power spectrum reconstruction. Measuring the resolution curve we found an asymmetry in the behaviour of the system which appears when the dispersion of the signal changes. We examined this effect by introducing higher order dispersion terms into the numerical model of the Time Microscope. This investigation showed the crucial influence of the third-order dispersion which

acts similar to the conventional optical aberrations. Finally, we proposed the modification of the Heterodyne Time Microscope which overcomes the resolution limit using the digital holography approach. The technique, which we called SEAHORSE (Spatial Encoding Arrangement with Hologram Observation for Recording in Single-shot the Electric field), demonstrated the possibilities to register in single-shot the power and phase profiles with resolution 80 fs over the window of 40 ps.

In Chapter 3, we revised the results obtained in the semi-classical limit of the focusing NLS equation. By means of the numerical simulations and experimental studies of the deterministic initial conditions, we demonstrated the universality of emergence of the Peregrine soliton as a regularisation of the gradient catastrophe. Experimental work with Optical Sampling Oscilloscope showed that these results are valid even in a range of parameters far from the considered limit. While numerical investigations proved that the Peregrine soliton can be observed even in the focusing dynamics of completely solitonless initial conditions.

At the next step, we provided the direct experimental observations of the partially-coherent waves propagation in the optical fiber governed by 1-D focusing NLS with the Heterodyne Time Microscope. We observed a big variety of the coherent structures which appear at the transient and stationary stage of the integrable turbulence. For some range of parameters, the localised Peregrine soliton was often found in the experimental data. Having the access to the complex envelop of the signal we used a solver of the 1-D NLS equation to reconstruct the initial conditions that lead to the localised Peregrine soliton. We proved that it appears from a single hump which can be often found in the partially-coherent initial conditions. Assuming that in the focusing regime every isolated initial hump can be considered separately, we employed an analytical expression obtained in the semi-classical regime for a rapidly decaying initial hump. With this expression, we managed to compute numerically the distribution of the maximum compression points of the Peregrine solitons along the propagating distance for the partially-coherent initial conditions. We discovered that the maximum of the distribution of the compression points coincides exactly with the maximum of the fourth order moment of the amplitude, which corresponds to the case when probability to observe high amplitude structure is the highest. This brings the conjecture that due to its universal nature the localised Peregrine soliton is the main origin of the 'heavy-tailed' statistics in the transient regime of the integrable turbulence.

Finally, using the local periodical IST analysis, we identified the recorded localised Peregrine solitons as genus 2 solutions and showed corresponding IST portraits.

In Chapter 4, we studied the integrable turbulence in the defocusing case. We provided the direct observations of the partially-coherent light propagation in the system governed by the 1-D defocusing NLS. We observed the emergence of nonlinear wavetrains having different oscillation scales with the same initial parameters. In order to investigate the origin of this phenomenon, we provided numerical simulations of the partially-coherent light

propagation with periodic boundary conditions. We observed that there are two main mechanisms dominating in the range of realistic parameter: dark solitonic structure generation due to the π phase jump often presented in the considered initial conditions and generation of the dispersive shock waves as a result of nonlinear interference of two neighbour humps. The appearance of different time scales was explained using a simplified deterministic model which considers only two humps. It was known before that two humps colliding generate a nonlinear wavetrain as a regularisation of the double-sided gradient catastrophe and the oscillation scale of the wavetrain strongly depends on the initial separations of two humps.

We also provided the statistical analysis of this system and showed the evolution of the fourth order moment of the field. However, the moment of collisions of two neighbour humps, which we expected to observe (in analogy with the moment of the gradient catastrophe in the focusing case), was not pronounced. Nevertheless, we found the evolutions of the FWHM of the spectrum reflects this moment quite well. In the end, we showed that the local IST analysis can be used for identification of the experimentally recorded structures in the defocusing case as well.

By this, the study of the integrable turbulence in the NLS governed systems cannot be considered as a complete. In some sense it is inverse. The results and conjectures presented in the given manuscript show new insights that can serve as a starting point for construction of the full statistical theory. Despite some already existing parts, like the case of the weak nonlinearity, there are many challenging open questions. Today, there are some promising approaches for the description of the condensate and partially-coherent wave dynamics separately. For example, application of the soliton gas theory (which is not well studied itself in the experimental fiber optics). Therefore, first possible step to the unification of the integrable turbulence theory is a careful study of the transition between the condensate and the partially-coherent wave, already started by Akhmediev and co-authors in [120, 121].

Another major direction of possible future studies, could be the construction of the statistical theory in the framework of the IST with the finite-gap potentials. The global IST spectrum is a constant of motion and, therefore, distribution of the eigenvalues on the complex plane can possibly give estimates of statistical parameters at the stationary state of the integrable turbulence. Inability to study theoretically the infinite temporal window limit obliges us to use the periodic boundary conditions and therefore to work in the finite-gap paradigm. As we already mentioned, application of the finite-gap theory is a very challenging task. However, if this theory can be constructed, the IST spectrum reconstruction from an experimentally recorded signal is quite achievable, as we demonstrated in the current manuscript.

Appendix A

Thermal Lensing in the Treacy compressor

Measurements of the high power signal with the Time Microscope faces several problems. One of crucial problems which directly affects the recorded signal profile is the thermal lensing effect. Indeed, the thermal lens makes the signal beam uncollimated. Therefore, the waist of the beam going to be shifted out of optimal position inside the crystal. On the Fig. A.1, A.2, A.3 measurements of the beam profile at the far-field zone are depicted. Far-field zone is found in the focal plane of a lens of 5 m-long focal distance placed right after the compressor. Measurements provided with a phosphor coated silicon CCD-based profiler Spiricon-Ophir. Pictures obtained for Spectrogon PC 0600 NIR gratings.

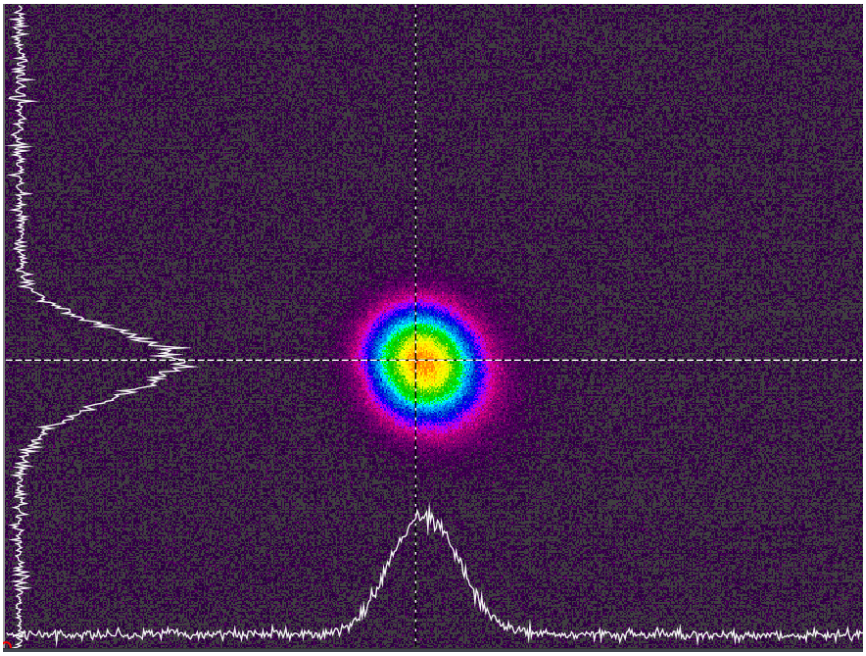

FIGURE A.1: Average power 0.5 W.

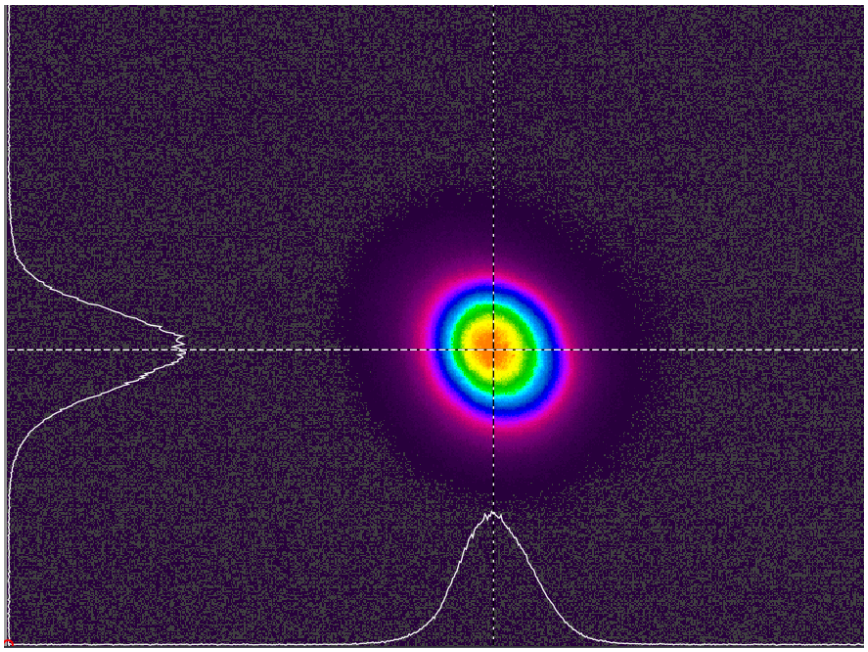

FIGURE A.2: Average power 2 *W*.

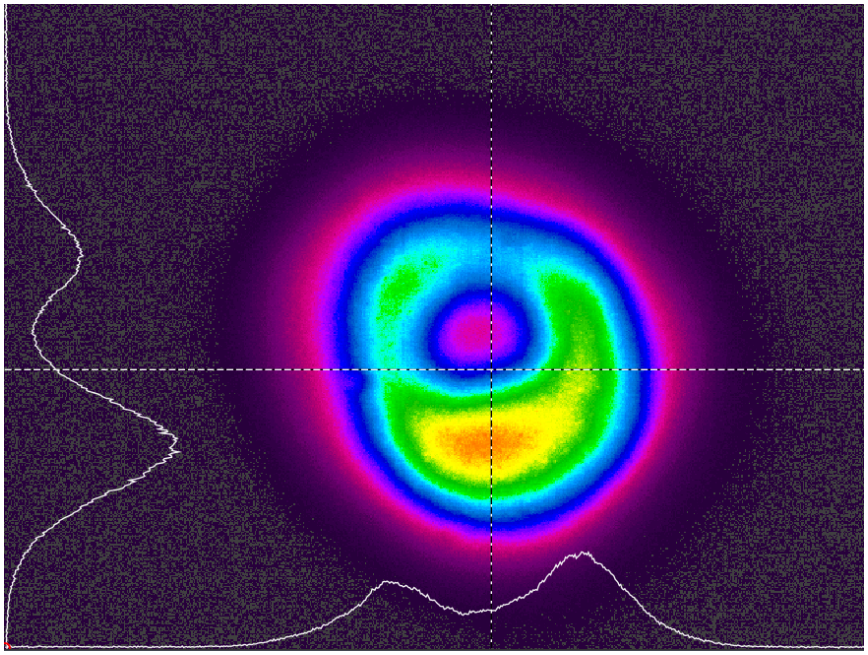

FIGURE A.3: Average power 7.1 *W*.

Appendix B

Estimates of non-linear and dispersion coefficients of the PM fiber

We provided the estimates of the nonlinear coefficient of optical fiber by providing a separate experiment. We injected a 200 fs with P_{avg} = 400 mW and repetition rate 80 MHz pulse into a short (typically 2 m) fiber and measured input and output spectra. For the anormal dispersion fibers ($\beta_2 < 0$) we simply provided comparison with fiber parameter of which we already know. As a reference we took a standard SMF 28 fiber. We recorded the input and output spectra and tried to match by changing the power injected to the fiber under investigation. The comparison is shown in Fig. B.1. This gave us the first estimates that were confirmed by the numerical simulations. For the normal dispersion fiber ($\beta_2 > 0$) due to the absens of reference only numerical simulations were provided (see Fig. B.2). Extended numerical simulations, recording for the normal dispersion fiber and figures presented below were made by Simonne Guilbert during her maser thesis.

The dispersion curve was obtained experimentally in IRCICA, subdivision of PhLAM laboratory of University Lille 1, by Remi Habert.

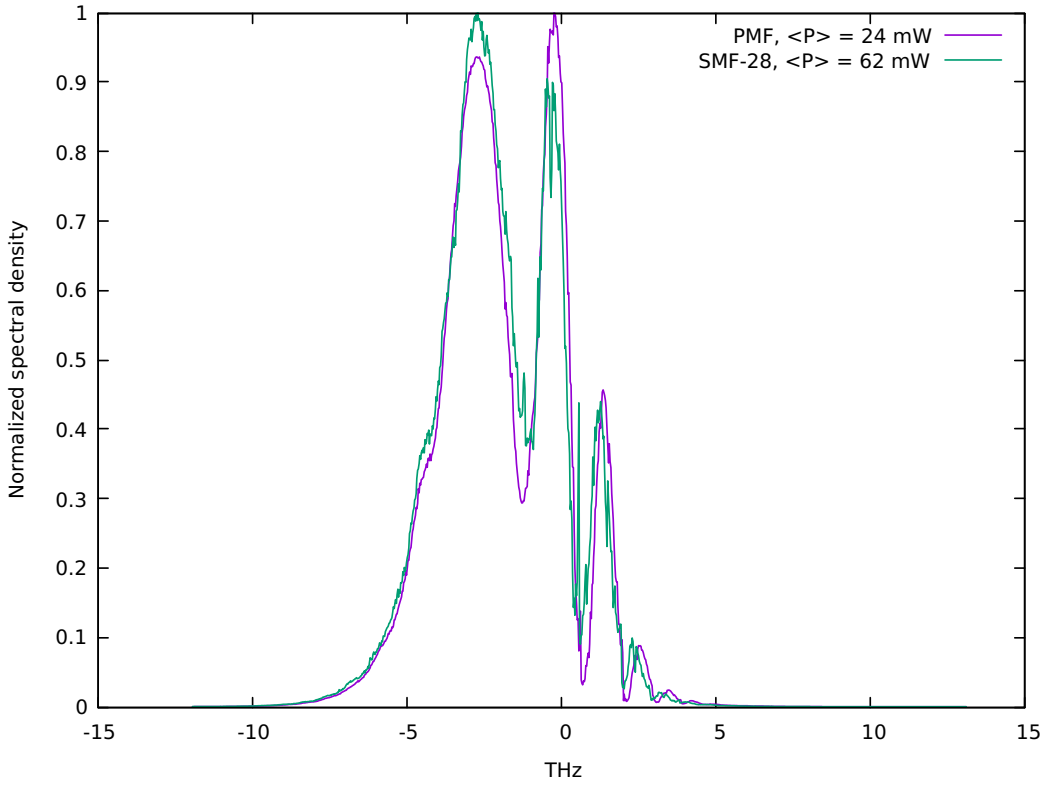

FIGURE B.1

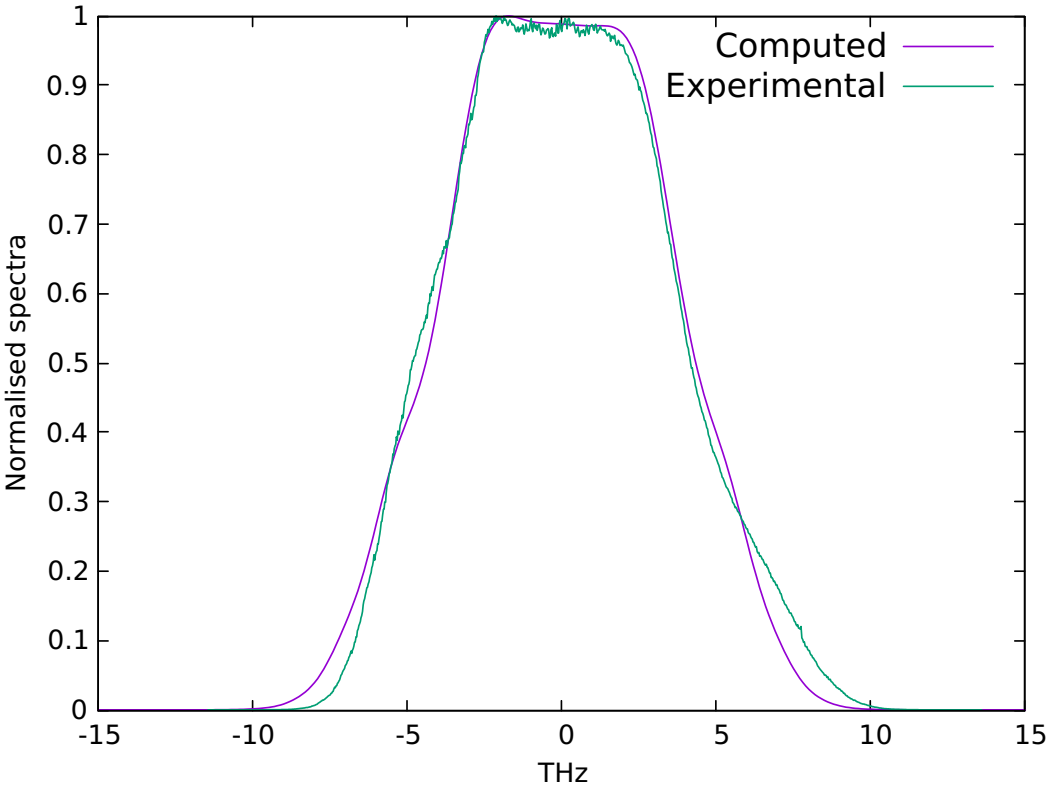

FIGURE B.2: Experimental and computed spectra, P_{max} of the pulse 3886 W.

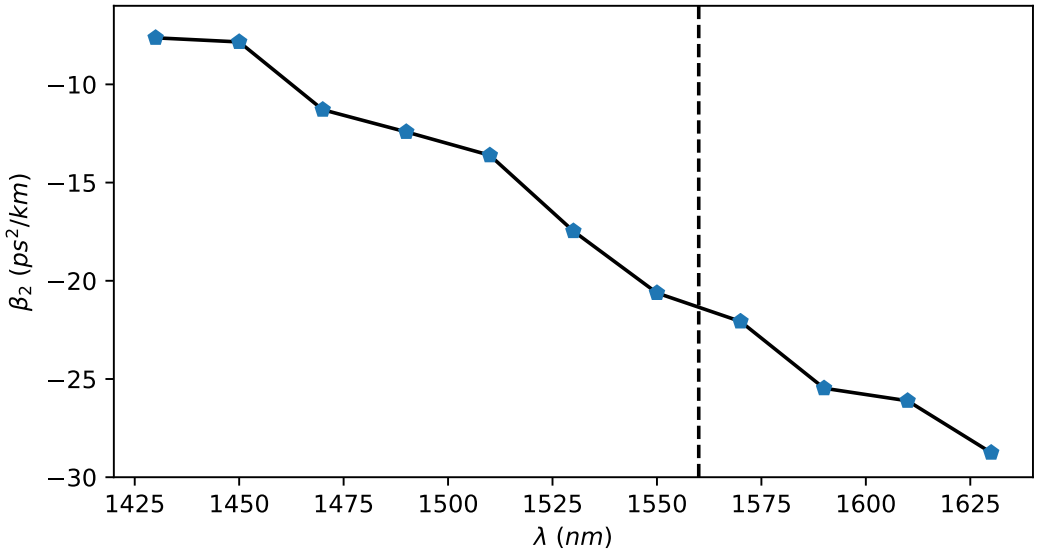

FIGURE B.3: Experimentally measured dispersion of the PMF Fibercore HB-1550T. Dashed line corresponds to the signal wavelength in the experiments.

Appendix C

Change of variables in NLS equation

In the present manuscript we used different forms of the NLS eqquations. For the sake of clarity, we provide here a summery of the changes of variables needed to obtain one or another form. The changes are depicted in Fig. C.1. On the figure: P_0- peak power of pulse or average power of partially-coherent wave, T_0 - typical pulse duration or timescale, $L_D = T_0^2/\beta_2$ - linear length, $L_{NL} = 1/\gamma P_0$ - nonlinear length, $\epsilon = \sqrt{L_{NL}/L_D} = \sqrt{|\beta_2|/\gamma P_0 T_0^2}$.

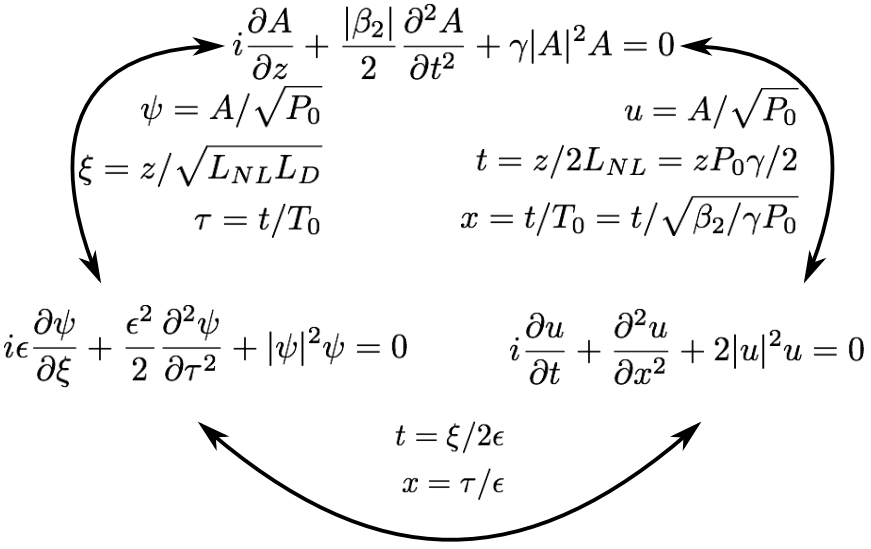

FIGURE C.1: Change of variables for NLS equation used in the manuscript.

Appendix D

Intrapulse stimulated Raman scattering effect on the random wave propagation

Here we present the comparison of the experimentally measured data using HTM and numerical simulations. So the propagation equation used in simulation is following:

$$i\frac{\partial A}{\partial z} + \frac{|\beta_2|}{2}\frac{\partial^2 A}{\partial t^2} + \gamma|A|^2 A - \gamma T_R A\frac{\partial |A|^2}{\partial t} = 0$$

where T_R is the ceffitient proportional to the slope of the Raman gain [21]. For the numerical simulations we used following parameters: β_2 = -22 ps^2/km and γ = 2.4 $W^{-1}km^{-1}$ and T_R = 3 fs.

The intrapulse stimulated Raman scattering term is added to the propagation equation *only for the last plot* in the Fig. D.1. The rest is the completely the same as presented in Fig. 3.15.

Also we present here some additional snapshots recorded with HTM with a high power initial conditions P_0 = 4.5 W $\Delta\nu$ = 0.1 THz (see Fig. D.2,D.3). It is clear that our experiment no longer described by the 1-D NLS equation. We clearly observe the frequency downshift which is represented by the phase inclination. Also the detected coherent structures can be split by the considered effect into several structures with smaller size.

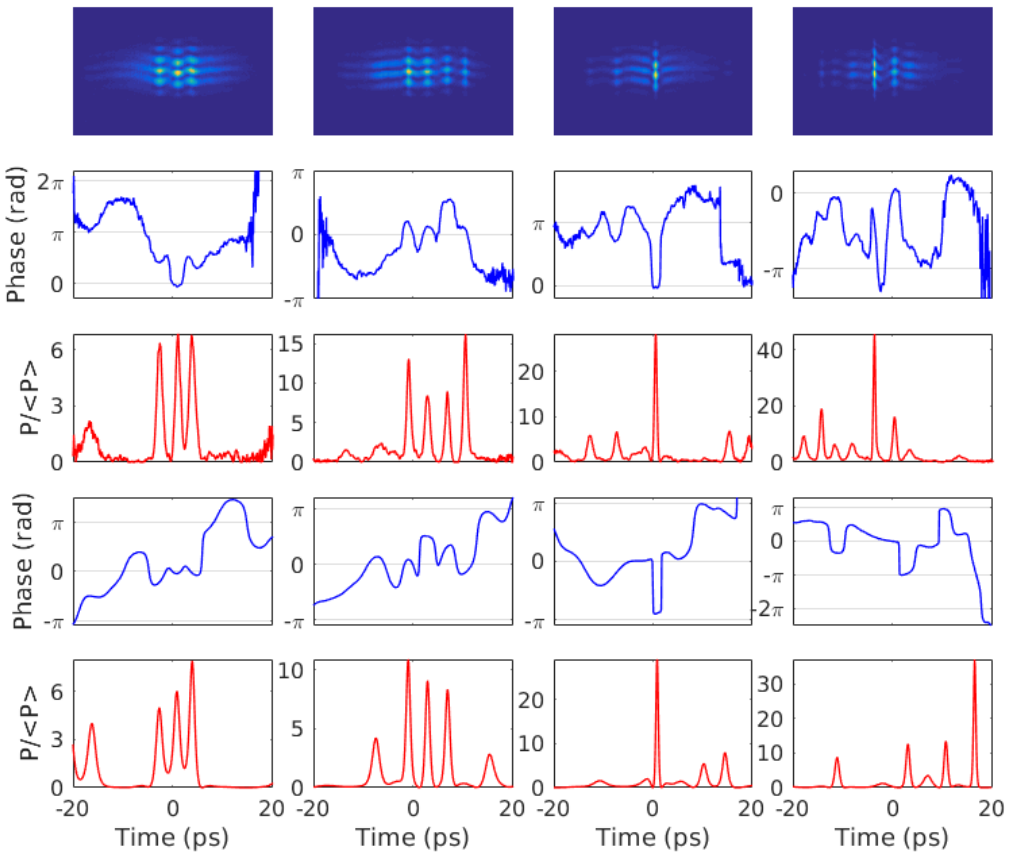

FIGURE D.1: Comparison of the numerical simulations and HTM measured signal.

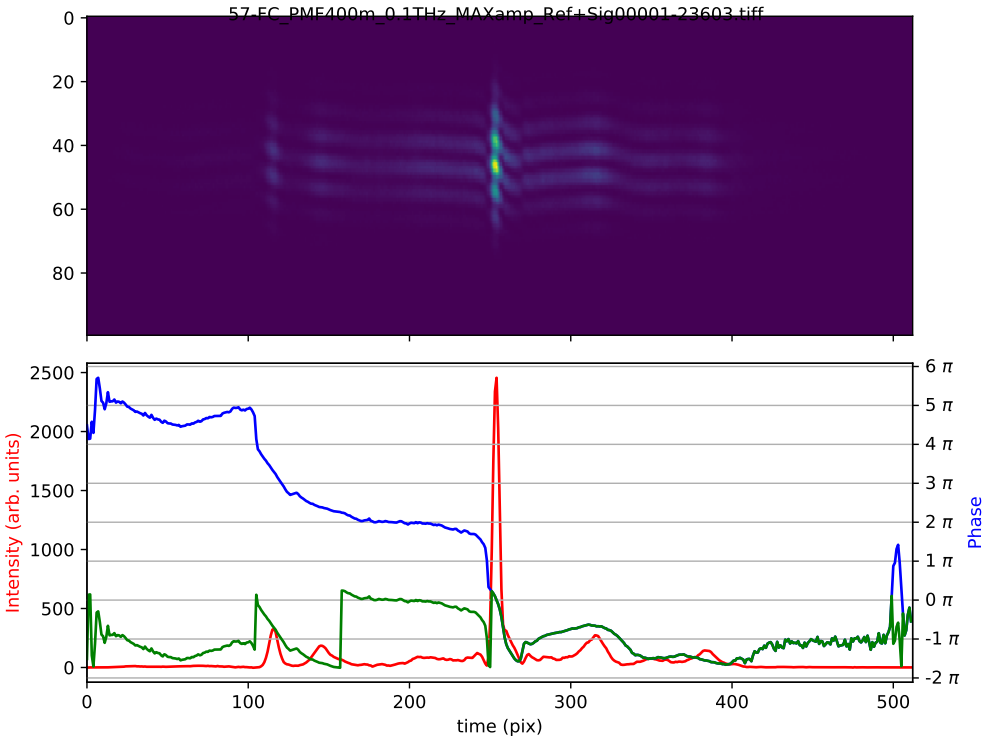

FIGURE D.2: Additional snapshot recorded with the HTM. Partially-coherent light having $P_0 = 4.5\ W$ $\Delta\nu = 0.1\ THz$.

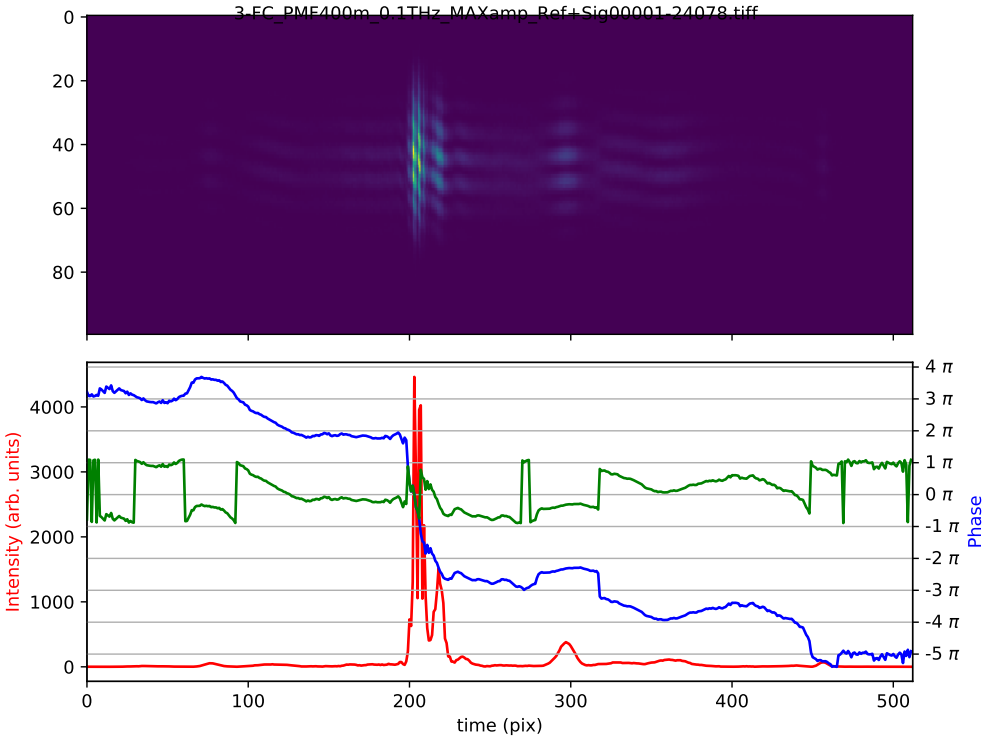

FIGURE D.3: Additional snapshot recorded with the HTM. Partially-coherent light having $P_0 = 4.5\ W$ $\Delta\nu = 0.1\ THz$.

Appendix E

Evolution of the spectra of the partially-coherent wave in defocusing system.

Here, we present the comparison of the numerically computed spectra of the partially-coherent wave propagated in the defocusing system. The parameters of the initial conditions: spectral widths - 0.1 THz, average power 4.5 W. The spectrum is computed at three different distances 0, 0.27 and 1.9 km. Fibber parameters: β_2=22 ps^2/km, γ = 3 $(Wkm)^{-1}$. As we can see, the spectra computed at z = 0.27 and 1.9 km are almost indistinguishable in the log-scale, while the FWHM is obviously different. Therefore, dynamics of RMS and FWHM of the spectrum is not the same.

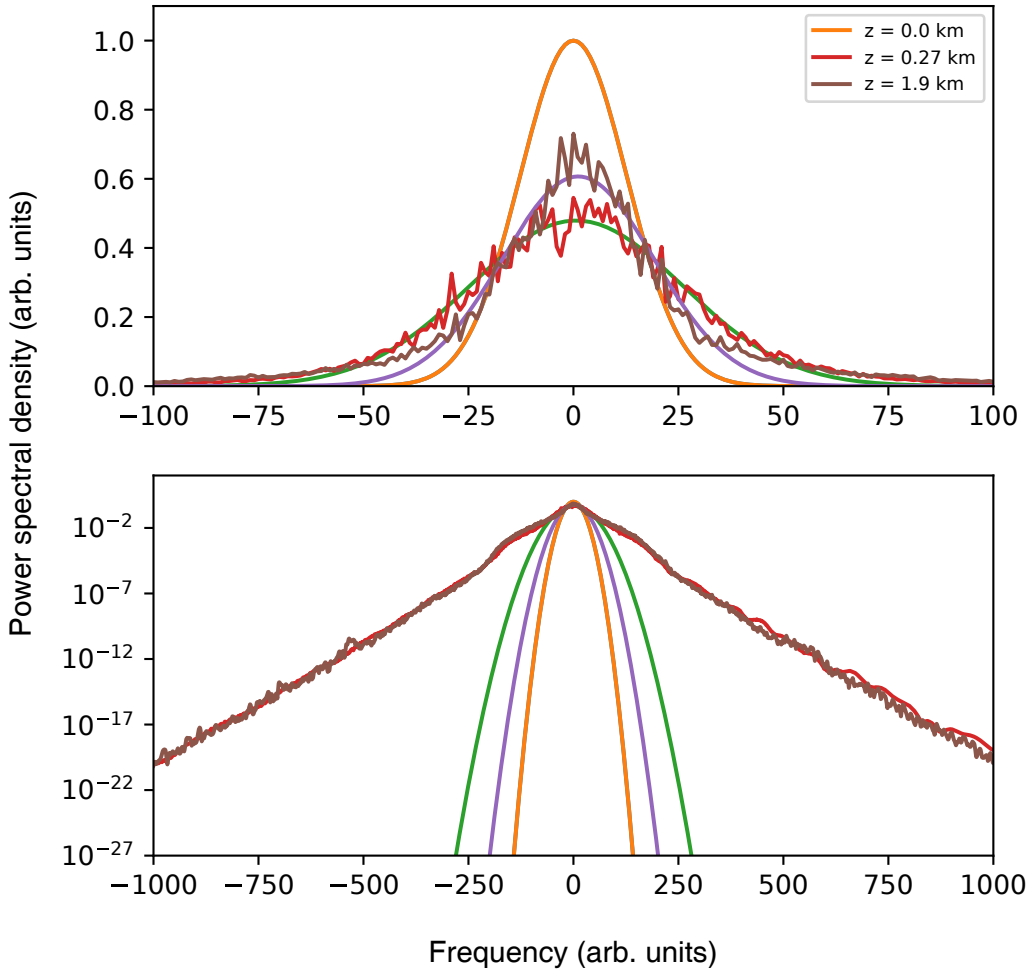

FIGURE E.1: Numerical studies of the evolution of the spectra in defocusing media. The average power of the partially-coherent initial conditions is 4.5 W, spectral widths - 0.1 THz. Distances 0, 0.27 and 1.9 km. Bottom plot shows the same data but in the log-scale.

Author's publications

- Tikan, A., Bielawski, S., Szwaj, C., Randoux, S. and Suret, P. "Single-shot measurement of phase and amplitude by using a heterodyne time-lens system and ultrafast digital time-holography." *Nat. Photon*. **12**, 228–234 (2018).
- El Koussaifi, R. et al. "Spontaneous emergence of rogue waves in partially coherent waves: A quantitative experimental comparison between hydrodynamics and optics." *Phys. Rev. E* **97**, 012208 (2018).
- Tikan, A. et al. "Universality of the Peregrine Soliton in the Focusing Dynamics of the Cubic Nonlinear Schrödinger Equation." *Phys. Rev. Lett*. **119**, 033901 (2017).
- Vatnik, I. D., Tikan, A., Onishchukov, G., Churkin, D. V. and Sukhorukov, A. A. "Anderson localization in synthetic photonic lattices." *Sci. Rep*. **7**, 1–6 (2017).
- Tikan, A., Vatnik, I. D., Churkin, D. V. and Sukhorukov, A. A. "Deriving eigenmode excitation spectrum of synthetic photonic lattices by means of optical heterodyning." *Laser Phys*. **27**, 026203 (2017).
- Suret, P. et al. "Single-shot observation of optical rogue waves in integrable turbulence using time microscopy." *Nat. Commun.* **7**, 13136 (2016).

Attended Seminars/Conferences/Workshops

- (O) S. Bielawski, A. Tikan, R. El Koussaifi, F. Gustave, S. Bielawski, C. Szwaj, S. Randoux, M. Onorato, G. El and P. Suret, Real-time Measurements, Rogue Phenomena, and Single-Shot Applications, Photonics West, San Francisco, 2018

- (I) S. Randoux, A. Tikan, R. El Koussaifi, F. Gustave, S. Bielawski, C. Szwaj, S. Randoux, M. Onorato, G. El and P. Suret, Integrable turbulence: a review of recent results, Workshop on "Dispersive equations with random initial data", Bristol, UK, January 10-12th, 2018

- (I)P. Suret, R. El Koussaifi, A. Tikan, C. Evain, C. Szwaj, S. Bielawski and S. Randoux, Direct observation of optical Rogue Waves in integrable turbulence by using Time Microscopy, Nice Optics, October 26-28 2016, Nice, France

- (P) A. Tikan, C. Billet, A. Tovbis, G. El, M. Bertola, et al., "Le soliton de Peregrine comme structure universelle de la compression d'impulsion dans les fibres optiques", Rencontres du Non-Linéaire, Mar 2017 , Paris, France

- (I) P. Suret, R. El Koussaifi, A. Tikan, M. Onorato and S. Randoux, "Proprietes statistiques des ondes non lineaires unidirectionnelles : une comparaison experimentale entre hydrodynamique et optique", Mini Colloque des Rencontres du Non Lineaire, Paris, Mar 2017

- (O) P. Suret, R. El Koussaifi, A. Tikan, C. Evain, C. Szwaj, S. Randoux, and S. Bielawski, "Single-shot observation of rogue waves in optical turbulence by using Time Microscopy," in 2017 European Conference on Lasers and Electro-Optics and European Quantum Electronics Conference, (Optical Society of America, 2017)

- (PD) P. Suret, R. El Koussaifi, A. Tikan, C. Evain, C. Szwaj, S. Randoux, and S. Bielawski, "Single shot observation of rogue waves in optical turbulence by using Time Microscopy," in 2017 European Conference on Lasers and Electro-Optics and European Quantum Electronics Conference, (Optical Society of America, 2017)

- (O) C. Billet, A. Tikan, G. El, A. Tovbis, M. Bertola, T. Sylvestre, F. Gustave, S. Randoux, G. Genty, P. Suret, and J. M. Dudley, "Universal Peregrine Soliton structure in optical fibre soliton compression," in 2017 European Conference on Lasers and Electro-Optics and European Quantum Electronics Conference, (Optical Society of America, 2017)

- (P) R. El Koussaifi, A. Tikan, M. Onorato, S. Randoux, and P. Suret, "Propagation of incoherent waves having a JONSWAP spectrum in an optical fiber and in a wave tank: deviations from Gaussian statistics and rogue waves", Extreme Events and Rogue Waves Seminar (International Wilhelm and Else Heraeus Seminar), May 30 - June 3 2016, Bad Honnef, Germany

- (O) P. Suret, R. El Koussaifi, A. Tikan, P. Walczak, C. Evain, C. Szwaj, S. Bielawski and S. Randoux, "Optical Rogue Waves in integrable turbulence: direct observation by using Time Microscopy and study of the statistical properties", Extreme Events and Rogue Waves Seminar (International Wilhelm and Else Heraeus Seminar), May 30 - June 3 2016, Bad Honnef, Germany

- (P) A. Tikan, S. Bielawski, R. El Koussaifi, C. Evain, M. Le Parquier, S. Randoux, C. Szwaj et P. Suret, "Coherent structures generated from random initial conditions in the one-dimensional Nonlinear Schrödinger Equation", Rencontres du Non Lineaire, Paris, Mar 2016

- (P) R. El Koussaifi, M. Onorato, S. Randoux, A. Tikan et P. Suret, "Experiences de propagation d'ondes partiellement coherentes : comparaison entre optique et hydrodynamique", Rencontres du Non Lineaire, Paris, Mars 2016

- I. D. Vatnik, A. M. Tikan, D. V. Churkin, A. A. Sukhorukov."Anderson localization of light in synthetic photonic lattices", Spatiotemporal Complexity in Nonlinear Optics (SCNO), Aug. 31 2015-Sept. 4 2015

- (O) A. M. Tikan. "Study of the effect of Anderson localization in synthetic photonic lattices", 53rd International Students Scientific Conference, Novosibirsk, v. Quantum Physics, p. 105 2015

- (P) I. D. Vatnik, A. M. Tikan, D. V. Churkin, A. A. Sukhorukov. "Anderson Localization In Optical Mesh Lattices Realized In Time Domain", Lasers and Electro-Optics Europe (CLEO EUROPE/IQEC), materials conference, Munich (ICM), Germany (2015)

- I. D. Vatnik, A. M. Tikan, D. V. Churkin, A. A. Sukhorukov."Anderson Localization in Synthetic Photonic Lattices". CLEO: 2015 - Laser Science to Photonic Applications, materials conference, San Jose, USA 2015

(P) - poster

(O) - oral contribution

(I) - invited talk

(PD) - post deadline

Bibliography

[1] V. E. Zakharov. "Turbulence in integrable systems". In: *Studies in Applied Mathematics* 122.3 (2009), pp. 219–234.

[2] U. Frisch. *Turbulence: the legacy of A. N. Kolmogorov*. Cambridge university press, 1995.

[3] M. J. Ablowitz and H. Segur. *Solitons and the inverse scattering transform*. Vol. 4. Siam, 1981.

[4] S. Novikov et al. *Theory of solitons: the inverse scattering method*. Springer Science & Business Media, 1984.

[5] British Association for the Advancement of Science., J. Robison, and J. Scott Russell. *Report of the Committee on Waves: appointed by the British Association at Bristol in 1836 [and consisting of Sir J. Robison and J. Scott Russell]*. London: Printed by R. and J.E. Taylor, 1838, 417–496 p.

[6] D. J. Korteweg and G. De Vries. "XLI. On the change of form of long waves advancing in a rectangular canal, and on a new type of long stationary waves". In: *The London, Edinburgh, and Dublin Philosophical Magazine and Journal of Science* 39.240 (1895), pp. 422–443.

[7] E. Fermi et al. "Studies of the nonlinear problems". In: (1955).

[8] A.C. Scott, F.Y.F. Chu, and D.W. McLaughlin. "The soliton: A new concept in applied science". In: *Proceedings of the IEEE* 61.10 (1973), pp. 1443–1483.

[9] P. G. Drazin and R. S. J.son. *Solitons: an introduction*. Vol. 2. Cambridge university press, 1989.

[10] A. Degasperis and S. Lombardo. "Integrability in Action: Solitons, Instability and Rogue Waves". In: *Rogue and Shock Waves in Nonlinear Dispersive Media*. Ed. by M. Onorato, S. Resitori, and F. Baronio. Cham: Springer International Publishing, 2016, pp. 23–53.

[11] C. S. Gardner et al. "Method for solving the Korteweg-deVries equation". In: *Physical Review Letters* 19.19 (1967), pp. 1095–1097.

[12] H. Washimi and T. Taniuti. "Propagation of Ion-Acoustic Solitary Waves of Small Amplitude". In: *Physical Review Letters* 17 (19 1966), pp. 996–998.

[13] L. V. Wijngaarden. "On the equations of motion for mixtures of liquid and gas bubbles". In: *Journal of Fluid Mechanics* 33.3 (1968), pp. 465–474.

[14] L. G. Redekopp and P. D. Weidman. "Solitary Rossby Waves in Zonal Shear Flows and Their Interactions". In: *Journal of the Atmospheric Sciences* 35.5 (1978), pp. 790–804.

[15] B. B. Kadomtsev and V. I. Petviashvili. "On the stability of solitary waves in weakly dispersing media". In: *Soviet Physics Doklady* 15.6 (1970), pp. 539–541.

[16] V. E. Zakharov and A. B. Shabat. "A scheme for integrating the nonlinear equations of mathematical physics by the method of the inverse scattering problem. I". In: *Functional Analysis and Its Applications* 8.3 (1974), pp. 226–235.

[17] M. J. Ablowitz et al. "Method for Solving the Sine-Gordon Equation". In: *Physical Review Letters* 30 (25 1973), pp. 1262–1264.

[18] V. E. Zakharov and A. B. Shabat. "Exact theory of two-dimensional self-focusing and one- dimensional self-modulation of waves in nonlinear media". In: *Soviet Physics JETP* 34.1 (1972), pp. 62–69.

[19] A. R. Osborne. *Nonlinear Ocean Wave and the Inverse Scattering Transform*. Elsevier, 2002.

[20] C. Kharif, E. Pelinovsky, and A. Slunyaev. *Rogue Waves in the Ocean*. Springer, 2009, pp. 63–89.

[21] G. P. Agrawal. *Nonlinear Fiber Optics*. Academic Press, Oxford, England, 2013.

[22] A.K. Zvezdin and A.F. Popkov. "Contribution to the nonlinear theory of magnetostatic spin waves". In: *Soviet Physics JETP* 57.2 (1983), pp. 350–355.

[23] A. Hasegawa and F. Tappert. "Transmission of stationary nonlinear optical pulses in dispersive dielectric fibers. I. Anomalous dispersion". In: *Applied Physics Letters* 23.142 (1973), pp. 142–144.

[24] A. Hasegawa and F. Tappert. "Transmission of stationary nonlinear optical pulses in dispersive dielectric fibers. II. Normal dispersion". In: *Applied Physics Letters* 23.4 (1973), pp. 171–172.

[25] S. V. Manakov. "On the theory of two-dimensional stationary self-focusing of electromagnetic waves". In: *Soviet Physics JETP* 38.2 (1974), pp. 248–253.

[26] C. R. Menyuk. "Stability of solitons in birefringent optical fibers. II. Arbitrary amplitudes". In: *Journal of the Optical Society of America B* 5.2 (1988), pp. 392–402.

[27] S. Nazarenko. *Wave Turbulence*. Springer Science & Business Media, 2011.

[28] A. I. Dyachenko and V. E. Zakharov. "Is free-surface hydrodynamics an integrable system?" In: *Physics Letters, Section A: General, Atomic and Solid State Physics* 190.July (1994), pp. 144–148.

[29] V. E. Zakharov, V. S. L'vov, and G. Falkovich. *Kolmogorov spectra of turbulence I: Wave turbulence*. Springer Science & Business Media, 1992.

[30] R. Peierls. "Zur Theorie der elektrischen und thermischen Leitfahigkeit von Metallen". In: *Annalen der Physik* 396.2 (1930), pp. 121–148.

[31] A. A. Vedenov. "Theory of a Weakly Turbulent Plasma". In: *Reviews of Plasma Physics: Volume 3*. Ed. by M. A. Leontovich. Boston, MA: Springer US, 1967, pp. 229–276.

[32] G. M. Zaslavskii and R. Z. Sagdeev. "Limits of statistical description of a nonlinear wave field". In: *Soviet Physics JETP* 25 (1967), pp. 718–724.

[33] K. Hasselmann. "On the non-linear energy transfer in a gravity wave spectrum.Part 2. Conservation theorems; wave-particle analogy; irreversibility". In: *Journal of Fluid Mechanics* 15.2 (1962), pp. 273–281.

[34] V. E. Zakharov and N. N. Filonenko. "Energy spectrum for stochastic oscillations of the surface of a liquid". In: *Doklady Akademii Nauk* 170.6 (1966), pp. 1292–1295.

[35] S. Dyachenko et al. "Optical turbulence: weak turbulence, condensates and collapsing filaments in the nonlinear Schrödinger equation". In: *Physica D: Nonlinear Phenomena* 57.1-2 (1992), pp. 96–160.

[36] P. Suret, A. Picozzi, and S. Randoux. "Wave turbulence in integrable systems: nonlinear propagation of incoherent optical waves in single-mode fibers". In: *Optics Express* 19.18 (2011), p. 17852.

[37] A. Picozzi et al. "Optical wave turbulence: Towards a unified nonequilibrium thermodynamic formulation of statistical nonlinear optics". In: *Physics Reports* 542.1 (2014), pp. 1–132.

[38] P. A. E. M. Janssen. "Nonlinear Four-Wave Interactions and Freak Waves". In: *Journal of Physical Oceanography* 33.4 (2003), pp. 863–884.

[39] V. E. Zakharov. "Stability of Periodic Waves of Finite Amplitude on the Surface of a Deep Fluid". In: *Zhurnal Prildadnoi Mekhaniki i Tekhnicheskoi Fiziki* 9.2 (1968), pp. 86–94.

[40] V. E. Zakharov, F. F. Dias, and A. Pushkarev. "One-dimensional wave turbulence". In: *Physics Reports* 398.1 (2004), pp. 1–65.

[41] C. Connaughton et al. "Condensation of classical nonlinear waves". In: *Physical Review Letters* 95.26 (2005), pp. 1–4.

[42] J. W Goodman. *Statistical optics*. J. Wiley & Sons, 2015.

[43] D. S. Agafontsev and V. E. Zakharov. "Integrable turbulence and formation of rogue waves". In: *Nonlinearity* 28.8 (2015), pp. 2791–2821.

[44] V. E. Zakharov and L. A. Ostrovsky. "Modulation instability: The beginning". In: *Physica D: Nonlinear Phenomena* 238.5 (2009), pp. 540–548.

[45] Y. Bromberg et al. "Hanbury Brown and Twiss interferometry with interacting photons". In: *Nature Photonics* 4.10 (2010), pp. 721–726.

[46] S. Derevyanko and E. Small. "Nonlinear propagation of an optical speckle field". In: *Physical Review A - Atomic, Molecular, and Optical Physics* 85.5 (2012), pp. 1–9.

[47] M. Onorato et al. "Freak waves in random oceanic sea states". In: *Physical Review Letters* 86.25 (2001), pp. 5831–5834.

[48] M. Onorato et al. "Observation of strongly non-Gaussian statistics for random sea surface gravity waves in wave flume experiments". In: *Physical Review E - Statistical, Nonlinear, and Soft Matter Physics* 70.6 2 (2004), pp. 1–4.

[49] J. C. Dainty. *Laser speckle and related phenomena*. Vol. 9. Springer science & business Media, 2013.

[50] M. Onorato et al. "Rogue waves and their generating mechanisms in different physical contexts". In: *Physics Reports* 528.2 (2013), pp. 47–89.

[51] H. C. Longuet-Higgins. "The intersection of potential energy surfaces in polyatomic molecules". In: *Proceedings of the Royal Society A* 344.1637 (1975), pp. 147–156.

[52] R. El Koussaifi et al. "Spontaneous emergence of rogue waves in partially coherent waves: a quantitative experimental comparison between hydrodynamics and optics". In: *Physical Review E* 97.1 (2017), p. 012208.

[53] P. Walczak, S. Randoux, and P. Suret. "Optical rogue waves in integrable turbulence". In: *Physical Review Letters* 114.14 (2015), pp. 33–35.

[54] D. R. Solli et al. "Optical rogue waves." In: *Nature* 450.7172 (2007), pp. 1054–1057.

[55] N. Akhmediev et al. "Recent progress in investigating optical rogue waves". In: *Journal of Optics (United Kingdom)* 15.6 (2013).

[56] J. M. Dudley et al. "Instabilities, breathers and rogue waves in optics". In: 8.10 (2014), pp. 755–764.

[57] S. Wabnitz et al. "Roadmap on optical rogue waves and extreme events". In: *Journal of Optics* 18 (2016).

[58] V. E. Zakharov. "Stability of periodic waves of finite amplitude on the surface of a deep fluid". In: *Journal of Applied Mechanics and Technical Physics* 9.2 (1968), pp. 190–194.

[59] R. El Koussaifi et al. "Spontaneous emergence of rogue waves in partially coherent waves: A quantitative experimental comparison between hydrodynamics and optics". In: *Physical Review E* 97.1 (2018).

[60] L. Shemer, A. Sergeeva, and A. Slunyaev. "Applicability of envelope model equations for simulation of narrow-spectrum unidirectional random wave field evolution: Experimental validation". In: *Physics of Fluids* 22.1 (2010), pp. 1–9.

[61] A. Chabchoub, N. P. Hoffmann, and N. Akhmediev. "Rogue wave observation in a water wave tank". In: *Physical Review Letters* 106.20 (2011), pp. 2–5.

[62] P. Janssen. *The interaction of ocean waves and wind*. Cambridge University Press, 2004.

[63] G. L. Lamb Jr. *Elements of soliton theory*. New York, Wiley-Interscience, 1980.

[64] A. Chabchoub et al. "Experimental observation of dark solitons on the surface of water". In: *Physical Review Letters* 110.12 (2013), pp. 1–5.

[65] G. O. Ludwig, J. L. Ferreira, and Y. Nakamura. "Observation of ion-acoustic rarefaction solitons in a multicomponent plasma with negative ions". In: *Physical Review Letters* 52.4 (1984), pp. 275–278.

[66] W. M. Moslem et al. "Dust-acoustic rogue waves in a nonextensive plasma". In: *Physical Review E - Statistical, Nonlinear, and Soft Matter Physics* 84.6 (2011), pp. 1–7.

[67] V. Konotop and M. Salerno. "Modulational instability in Bose-Einstein condensates in optical lattices". In: *Physical Review A* 65.2 (2002), 021602 (1–4).

[68] W. Bao. *The nonlinear Schrödinger equation and applications in Bose-Einstein condensation and plasma physics*. World Scientific, 2007, pp. 141–239.

[69] E. A. Kuznetsov and M. D. Spector. "Modulation instability of soliton trains in fiber communication systems". In: *Theoretical and Mathematical Physics* 120.2 (1999), pp. 997–1008.

[70] D. S. Agafontsev and V. E. Zakharov. "Integrable turbulence generated from modulational instability of cnoidal waves". In: *Nonlinearity* 29.11 (2016), pp. 3551–3578.

[71] V. E. Zakharov and L. A. Ostrovsky. "Modulation instability: The beginning". In: *Physica D: Nonlinear Phenomena* 238.5 (2009), pp. 540–548.

[72] V.I. Bespalov and V.I. Talanov. "Filamentary Structure of Light Beams in Nonlinear Media". In: *Soviet Physics JETP* 3 (1966), pp. 471–476.

[73] L. A. Ostrovskii. "Propagation of wave packets and space-time self-focusing in a nonlinear medium". In: *Soviet Physics JETP* 24.4 (1967), pp. 797–800.

[74] V. I. Karpman. "Self-modulation of nonlinear plane waves in dispersive media". In: *Soviet physics JETP* 6 (1967), pp. 829–832.

[75] T. Taniuti and H. Washimi. "Self-trapping and instability of hydromagnetic waves along the magnetic field in a cold plasma". In: *Physical Review Letters* 21.4 (1968), pp. 209–212.

[76] T. Brooke Benjamin and J E Feir. "The disintegration of wave trains on deep water". In: *Journal of Fluid Mechanics* 27.3 (1967), pp. 417–430.

[77] K. Tai, A. Hasegawa, and A. Tomita. "Observation of modulational instability in optical fibers". In: *Physical Review Letters* 56.2 (1986), pp. 135–138.

[78] K. Tajima. "Self-Amplitude Modulation in PSK Coherent Optical Transmission Systems". In: *Journal of Lightwave Technology* 4.7 (1986), pp. 900–904.

[79] P. K. Shukla and J. J. Rasmussen. "Modulational instability of short pulses in long optical fibers." In: *Optics letters* 11.3 (1986), p. 171.

[80] M. J. Potasek. "Modulation instability in an extended nonlinear Schrödinger equation." In: *Optics Letters* 12.11 (1987), pp. 921–3.

[81] M. N. Islam, S. P. Dijaili, and J. P. Gordon. "Modulation-instability-based fiber interferometer switch near 1.5 microm." In: *Optics letters* 13.6 (1988), pp. 518–20.

[82] G. Cappellini and S. Trillo. "Third-order three-wave mixing in single-mode fibers: exact solutions and spatial instability effects". In: *Journal of the Optical Society of America B* 8.4 (1991), p. 824.

[83] S. Trillo and S. Wabnitz. "Dynamics of the nonlinear modulational instability in optical fibers." In: *Optics letters* 16.13 (1991), pp. 986–8.

[84] B. Kibler et al. "Observation of Kuznetsov-Ma soliton dynamics in optical fibre". In: *Scientific Reports* 2 (2012), pp. 1–5.

[85] B. Kibler et al. "The Peregrine soliton in nonlinear fibre optics". In: *Nature Physics* 6.10 (2010), pp. 790–795.

[86] M. Erkintalo et al. "Higher-order modulation instability in nonlinear fiber optics". In: *Physical Review Letters* 107.25 (2011), pp. 14–18.

[87] V. E. Zakharov and A. A. Gelash. "Superregular solitonic solutions: a novel scenario of the nonlinear stage of Modulation Instability". In: *Nonlinearity* 27.4 (2014), pp. 1–41.

[88] V. E. Zakharov and A. A. Gelash. "Nonlinear stage of modulation instability". In: *Physical Review Letters* 111.5 (2013), pp. 1–5.

[89] S. Toenger et al. "Emergent rogue wave structures and statistics in spontaneous modulation instability". In: *Scientific Reports* 5.1 (2015), p. 10380.

[90] M. Närhi et al. "Real-time measurements of spontaneous breathers and rogue wave events in optical fibre modulation instability". In: *Nature Communications* 7 (2016), p. 13675.

[91] B. Kibler et al. "Superregular breathers in optics and hydrodynamics: Omnipresent modulation instability beyond simple periodicity". In: *Physical Review X* 5.4 (2015), pp. 1–12.

[92] P. G. Grinevich and P. M. Santini. "The finite gap method and the analytic description of the exact rogue wave recurrence in the periodic NLSCauchy problem. 1". In: *Nonlinearity* 31.11 (2018), pp. 5258–5308.

[93] N. N. Akhmediev and V. I. Korneev. "Modulation instability and periodic solutions of the nonlinear Schrödinger equation". In: *Theoretical and Mathematical Physics* 69.2 (1986), pp. 1089–1093.

[94] D. H. Peregrine. "Water waves, nonlinear Schrödinger equations and their solutions". In: *The Journal of the Australian Mathematical Society. Series B. Applied Mathematics* 25.1 (1983), pp. 16–43.

[95] E. A. Kuznetsov. "Solitons in a parametrically unstable plasma". In: *Doklady Akademii Nauk* 236 (1977), pp. 575–577.

[96] Y. Ma. "The Perturbed Plane-Wave Solutions of the Cubic Schrödinger Equation". In: *Studies in Applied Mathematics* 60.1 (1979), pp. 43–58.

[97] N. Akhmediev, A. Ankiewicz, and M. Taki. "Waves that appear from nowhere and disappear without a trace". In: *Physics Letters, Section A: General, Atomic and Solid State Physics* 373.6 (2009), pp. 675–678.

[98] N. Akhmediev, A. Ankiewicz, and J. M. Soto-Crespo. "Rogue waves and rational solutions of the nonlinear Schrödinger equation". In: *Physical Review E - Statistical, Nonlinear, and Soft Matter Physics* 80.2 (2009).

[99] N. Akhmediev, A. Ankiewicz, and M. Taki. "Waves that appear from nowhere and disappear without a trace". In: *Physics Letters, Section A: General, Atomic and Solid State Physics* 373.6 (2009), pp. 675–678.

[100] V. I. Shrira and V. V. Geogjaev. "What makes the Peregrine soliton so special as a prototype of freak waves?" In: *Journal of Engineering Mathematics* 67.1 (2010), pp. 11–22.

[101] V. E. Zakharov and A B Shabat. "Interaction between solitons in a stable medium". In: *Soviet Physics JETP* 64.5 (1973), pp. 1627–1639.

[102] K. J. Blow and N. J. Doran. "Multiple dark soliton solutions of the nonlinear Schrödinger equation". In: *Physics Letters* 107A.2 (1985), pp. 55–58.

[103] P. Emplit et al. "Picosecond steps and dark pulses through nonlinear single mode fibers". In: *Optics Communications* 62.6 (1987), pp. 374–379.

[104] D. Krokel et al. "Dark-Pulse Propagation in Optical Fibers". In: *Physical Review Letters* 60.1 (1988), pp. 29–32.

[105] A. M. Weiner et al. "Experimental observation of the fundamental dark soliton in optical fibers". In: *Physical Review Letters* 61.21 (1988), pp. 2445–2448.

[106] S. Burger et al. "Dark solitons in bose-einstein condensates". In: *Physical Review Letters* 83.25 (1999), pp. 5198–5201.

[107] A. Amo et al. "Polariton superfluids reveal quantum hydrodynamic solitons". In: *Science* 332.6034 (2011), pp. 1167–1170.

[108] A. V. Gurevich and L. P. Pitaevskii. "Nonstationary structure of a collision less shock wave". In: *Soviet Physics JETP* 38.2 (1974), pp. 291–297.

[109] G. B. Whitham. *Linear and nonlinear waves*. Vol. 42. J. Wiley & Sons, 2011.

[110] G. El and M. A. Hoefer. "Dispersive shock waves and modulation theory". In: *Physica D: Nonlinear Phenomena* 333 (2016), pp. 11–65.

[111] A. V. Gurevich and A. L. Krylov. "Dissipationless shock waves in media with positive dispersion". In: *Soviet Physics JETP* 65.5 (1987), pp. 944–953.

[112] G. A. El et al. "Decay of an initial discontinuity in the defocusing NLS hydrodynamics". In: *Physica D: Nonlinear Phenomena* 87.1-4 (1995), pp. 186–192.

[113] G. Xu et al. "Dispersive Dam-Break Flow of a Photon Fluid". In: *Physical Review Letters* 118.25 (2017), pp. 1–5.

[114] R. M. Miura. "Korteweg-de Vries equation and generalizations. I. A remarkable explicit nonlinear transformation". In: *Journal of Mathematical Physics* 9.8 (1968), pp. 1202–1204.

[115] M. Wadati. "The modified Korteweg-de Vries equation". In: *Journal of the Physical Society of Japan* 34.5 (1973), pp. 1289–1296.

[116] B. A. Dubrovin, V. B. Matveev, and S. P. Novikov. "Non-linear equations of Korteweg-de Vries type, finite-zone linear operators, and Abelian varieties". In: *Russian mathematical surveys* 31.1 (1976), pp. 59–146.

[117] Y. Ma and M. J. Ablowitz. "The periodic cubic Schrodinger equation". In: *Studies in Applied Mathematics* 65.2 (1981), pp. 113–158.

[118] J. S. Blakemore. "ELECTRONS IN METALS". In: *Solid State Physics*. 2nd ed. Cambridge University Press, 1985, pp. 149–292.

[119] S. Randoux, P. Suret, and G. A. El. "Inverse scattering transform analysis of rogue waves using local periodization procedure". In: *Scientific Reports* 6.1 (2016), p. 29238.

[120] J. M. Soto-Crespo, N. Devine, and N. Akhmediev. "Integrable Turbulence and Rogue Waves: Breathers or Solitons?" In: *Physical Review Letters* 116.10 (2016), pp. 1–5.

[121] N. Akhmediev, J. M. Soto-Crespo, and N. Devine. "Breather turbulence versus soliton turbulence: Rogue waves, probability density functions, and spectral features". In: *Physical Review E* 94.2 (2016), pp. 1–10.

[122] J. T. Manassah. "Self-phase modulation of incoherent light". In: *Optics Letters* 15.6 (1990), p. 329.

[123] B. Dubrovin, T. Grava, and C. Klein. "On universality of critical behavior in the focusing nonlinear Schrödinger equation, elliptic umbilic catastrophe and the Tritronquée solution to the Painlevé-I equation". In: *Journal of Nonlinear Science* 19.1 (2009), pp. 57–94.

[124] M. Bertola and A. Tovbis. "Universality for the Focusing Nonlinear Schrödinger Equation at the Gradient Catastrophe Point: Rational Breathers and Poles of the Tritronquée Solution to Painlevé I". In: *Communications on Pure and Applied Mathematics* 66.5 (2013), pp. 678–752.

[125] S. Randoux et al. "Nonlinear random optical waves: Integrable turbulence, rogue waves and intermittency". In: *Physica D: Nonlinear Phenomena* 333 (2016), pp. 323–335.

[126] J. E. Rothenberg and H. K. Heinrich. "Observation of the formation of dark-soliton trains in optical fibers." In: *Optics letters* 17.4 (1992), pp. 261–263.

[127] W. M. Liu, B. Wu, and Q. Niu. "Nonlinear effects in interference of bose-einstein condensates". In: *Physical Review Letters* 84.11 (2000), pp. 2294–2297.

[128] M. A. Hoefer, P. Engels, and J. J. Chang. "Matter-wave interference in Bose-Einstein condensates: A dispersive hydrodynamic perspective". In: *Physica D: Nonlinear Phenomena* 238.15 (2009), pp. 1311–1320.

[129] C. Conti et al. "Observation of a gradient catastrophe generating solitons". In: *Physical Review Letters* 102.8 (2009), pp. 25–28.

[130] J. Fatome et al. "Observation of optical undular bores in multiple four-wave mixing". In: *Physical Review X* 4.2 (2014), pp. 48–52.

[131] L. F. Mollenauer, R. H. Stolen, and J. P. Gordon. "Experimental Observation of Picosecond Pulse Narrowing and Solitons in Optical Fibers". In: *Physical Review letters* 45.13 (1980), pp. 1095–1098.

[132] M. A. Duguay and J. W. Hansen. "Optical sampling of subnanosecond light pulses". In: *Applied Physics Letters* 13.5 (1968), pp. 178–180.

[133] D. J. Kane and R. Trebino. "Characterization of Arbitrary Femtosecond Pulses Using Frequency-Resolved Optical Gating". In: *IEEE Journal of Quantum Electronics* 29.2 (1993), pp. 571–579.

[134] R. Trebino. *Frequency-resolved optical gating: the measurement of ultrashort laser pulses*. Springer Science & Business Media, 2012.

[135] T. C. Wong, M. Rhodes, and R. Trebino. "Single-shot measurement of the complete temporal intensity and phase of supercontinuum". In: *Optica*. Vol. 1. 2. 2014, p. 973209.

[136] T. H. Maiman. "Stimulated optical radiation in Ruby". In: *Nature* 187.4736 (1960), pp. 493–494.

[137] J. Hecht and A. Street. "A short history of laser development Short history of laser development". In: *Optical Engineering* 49.September 2010 (2010), pp. 99–122.

[138] R. W. Hellwarth and F. J. McClung. "Giant Pulsations from Ruby". In: *Bulletin of the American Physical Society* 6.August 1961 (1961), p. 414.

[139] L. E. Hargrove, R. L. Fork, and M. A. Pollack. "Locking of hene laser modes induced by synchronous intracavity modulation". In: *Applied Physics Letters* 5.1 (1964), pp. 4–5.

[140] W. E. Lamb. "Theory of an Optical Maser". In: *Physical Review* 134.6A (1964), A1429–A1450.

[141] P. F. Moulton. "Spectroscopic and laser characteristics of Ti:Al_2O_3". In: *Journal of the Optical Society of America B* 3.1 (1986), p. 125.

[142] I. A. Walmsley and C. Dorrer. "Characterization of ultrashort electromagnetic pulses". In: *Advances in Optics and Photonics* 1.2 (2009), p. 308.

[143] J. A. Armstrong. "Measurement of picosecond laser pulse widths". In: *Applied Physics Letters* 10.1 (1967), pp. 16–18.

[144] L. P. Barry et al. “Autocorrelation of ultrashort pulses at 1.5 μm based on nonlinear response of silicon photodiodes”. In: *Electronics Letters* 32.20 (1996), pp. 1922–1923.

[145] K. L. Sala, G. A. Kenny-Wallace, and G. E. Hall. “CW Autocorrelation Measurements of Picosecond Laser Pulses”. In: *IEEE Journal of Quantum Electronics* 16.9 (1980), pp. 990–996.

[146] D. T. Reid et al. “Roadmap on ultrafast optics”. In: *Journal of Optics (United Kingdom)* 18.9 (2016), pp. 1–32.

[147] R. A. Fisher and J. A. Fleck. “On the phase characteristics and compression of picosecond pulses”. In: *Applied Physics Letters* 15.9 (1969), pp. 287–290.

[148] E. B. Treacy. “Measurement and interpretation of dynamic spectrograms of picosecond light pulses”. In: *Journal of Applied Physics* 42.10 (1971), pp. 3848–3858.

[149] J. L. A. Chilla and O. E. Martinez. “Analysis of a Method of Phase Measurement of Ultrashort Pulses in the Frequency Domain”. In: *IEEE Journal of Quantum Electronics* 27.5 (1991), pp. 1228–1235.

[150] J. L. Chilla and O. E. Martinez. “Direct determination of the amplitude and the phase of femtosecond light pulses.” In: *Optics letters* 16.1 (1991), pp. 39–41.

[151] J. L. A. Chilla and O. E. Martinez. “Frequency domain phase measurement of ultrashort light pulses . Effect of noise”. In: *Optics Communications* 89 (1992), pp. 434–440.

[152] K. W. DeLong et al. “Pulse retrieval in frequency-resolved optical gating based on the method of generalized projections.” In: *Optics letters* 19.24 (1994), pp. 2152–2154.

[153] P. Sidorenko et al. “Ptychographic reconstruction algorithm for frequency resolved optical gating: super-resolution and extreme robustness: erratum”. In: *Optica* 4.11 (2017), p. 1388.

[154] T. Zahavy et al. “Deep Learning Reconstruction of Ultra-Short Pulses”. In: Dlps (2018), pp. 1–6.

[155] R. Trebino et al. “Measuring ultrashort laser pulses in the time-frequency domain using frequency-resolved optical gating”. In: *Review of Scientific Instruments* 68.9 (1997), pp. 3277–3295.

[156] C. Iaconis and I. A. Walmsley. “Spectral phase interferometry for direct electric-field reconstruction of ultrashort optical pulses”. In: *Optics Letters* 23.10 (1998), p. 792.

[157] M. Rhodes, Z. Guang, and R. Trebino. “Unstable multipulsing can be invisible to some ultrashort pulse measurement techniques”. In: *Proceedings SPIE* (2016), 97320R.

[158] C. Dorrer et al. "Single-shot real-time characterization of chirped pulse amplification systems using spectral phase interferometry for direct electric-field reconstruction". In: *Optics Letters* 24.11 (1999), pp. 1644–1646.

[159] E. M. Kosik et al. "Interferometric technique for measuring broadband ultrashort pulses at the sampling limit". In: *Optics Letters* 30.3 (2005), p. 326.

[160] A. S. Wyatt et al. "Sub-10 fs pulse characterization using spatially encoded arrangement for spectral phase interferometry for direct electric field reconstruction". In: *Optics Letters* 31.12 (2006), p. 1914.

[161] J. D. McGee, J. Beesley, and A. D. Berg. "A dynamic electron image information store". In: *Journal of Scientific Instruments* 43 (1966), pp. 153–159.

[162] D. J. Bradley, B. Liddy, and W. E. Sleat. "Direct linear measurement of ultrashort light pulses with a picosecond streak camera". In: *Optics Communications* 2.8 (1971), pp. 391–395.

[163] J. Itatani et al. "Attosecond Streak Camera". In: *Physical Review Letters* 88.17 (2002), p. 4.

[164] *Hamamatsu streak cameras*. https://www.hamamatsu.com/eu/en/product/photometry-systems/streak-camera/index.html.

[165] B. H. Kolner and M. Nazarathym. "Temporal imaging with a time lens". In: *Optics Letters* 14.12 (1989).

[166] K. Goda and B. Jalali. "Dispersive Fourier transformation for fast continuous single-shot measurements". In: *Nature Photonics* 7.2 (2013), pp. 102–112.

[167] P. Ryczkowski et al. "Real-time full-field characterization of transient dissipative soliton dynamics in a mode-locked laser". In: *Nature Photonics* 12.4 (2018), pp. 221–227.

[168] C. Lei and K. Goda. "The complete optical oscilloscope". In: *Nature Photonics* 12.4 (2018), pp. 190–191.

[169] G. Yang et al. "Gerchberg–Saxton and Yang–Gu algorithms for phase retrieval in a nonunitary transform system: a comparison". In: *Applied Optics* 33.2 (1994), pp. 209–218.

[170] A. Mahjoubfar, C. L. Chen, and B. Jalali. "Design of Warped Stretch Transform". In: *Scientific Reports* 5 (2015), pp. 1–15.

[171] B. Alonso et al. "Spatiotemporal amplitude-and-phase reconstruction by Fourier-transform of interference spectra of high-complex-beams". In: *Journal of the Optical Society of America B* 27.5 (2010), p. 933.

[172] G. Steinmeyer. "A review of ultrafast optics and optoelectronics". In: *Journal of Optics A: Pure and Applied Optics* (2003).

[173] C. V. Bennett and B. H. Kolner. "Upconversion time microscope demonstrating 103x magnification of femtosecond waveforms". In: *Optics Letters* 24.11 (1999), pp. 783–785.

[174] B. H. Kolner. "Space-Time Duality and the Theory of Temporal Imaging". In: *IEEE Journal of Quantum Electronics* 30.8 (1994), pp. 1951–1963.

[175] C. Bennett and B. Kolner. "Principles of parametric temporal imaging-part I : System configuration". In: *IEEE journal of quantum electronics* 36.4 (2000).

[176] C. V. Bennett. "Parametric Temporal Imaging and Aberration Analysis". PhD thesis. 2000.

[177] S. A. Akhmanov et al. "Nonstationary nonlinear optical effects and ultrashort light pulse formation". In: *IEEE Journal of Quantum Electronics* 4.10 (1968), pp. 598–605.

[178] S. A. Akhmanov, A. P. Sukhorukov, and A. S. Chirkin. "Nonstationary phenomena and space-time analogy in nonlinear optics". In: *Soviet Physics JETP* 28.4 (1969), pp. 748–757.

[179] W. J. Caputi. "Stretch: A time-transformation technique". In: *IEEE Transactions on Aerospace and Electronic Systems* AES-7.2 (1971), pp. 269–278.

[180] P. Naulleau and E. Leith. "Stretch, time lenses, and incoherent time imaging." In: *Applied optics* 34.20 (1995), pp. 4119–28.

[181] J. D. Jackson. *Classical electrodynamics*. Wiley, 1999.

[182] J. W. Goodman. *Introduction to Fourier optics*. Roberts and Company Publishers, 2005.

[183] R. W. Boyd. *Nonlinear optics*. Academic press, 2003.

[184] M. A. Foster et al. "Silicon-chip-based ultrafast optical oscilloscope". In: *Nature* 456.7218 (2008), pp. 81–84.

[185] M. A. Foster et al. "Silicon-chip-based ultrafast optical oscilloscope". In: *Nature* 456.6 (2008).

[186] R. Salem et al. "Optical time lens based on four-wave mixing on a silicon chip." In: *Optics letters* 33.10 (2008), pp. 1047–1049.

[187] R. Salem et al. "High-speed optical sampling using a silicon-chip temporal magnifier". In: *Optics Express* 17.6 (2009), pp. 4324–4329.

[188] D. H. Broaddus et al. "Temporal-imaging system with simple external-clock triggering." In: *Optics express* 18.13 (2010), pp. 14262–14269.

[189] *PicoLuz Ultrafast Temporal Magnifier*. https://www.thorlabs.com/newgrouppage9.cfm?objectgroup_id=5282. Online; accessed 9-May-2018.

[190] P. Suret et al. "Single-shot observation of optical rogue waves in integrable turbulence using time microscopy". In: *Nature Communications* 7 (2016), p. 13136.

[191] D. Strickland and G. Mourou. "Compression of amplified chirped optical pulses". In: *Optics Communications* 56.3 (1985), pp. 219–221.

[192] M. Cavagna. "Réalisation d'un laser fibré femtoseconde". MA thesis. Univ. Lille 1, 2015.

[193] H. A. Haus et al. "Stretched-pulse additive pulse mode-locking in fiber ring lasers: theory and experiment". In: *IEEE Journal of quantum electronics* 31.3 (1995), pp. 591–598.

[194] E. B. Treacy. "Optical Pulse Compression With Diffraction Gratings". In: *IEEE Journal of Quantum Electronics* 5.9 (1969), pp. 454–458.

[195] E. B. Treacy. "Measurement of picosecond pulse substructure using compression techniques". In: *Applied Physics Letters* 14.3 (1969), pp. 112–114.

[196] C. Chen et al. "A New ultra-violet SHG crystal beta-BaB2O4". In: *Scientia Sinica* 18 (1985), p. 235.

[197] V. G. Dmitriev, G. G. Gurzadyan, and D. N. Nikogosyan. *Handbook of nonlinear optical crystals*. 3rd. Vol. 64. Springer-Verlag Berlin Heidelberg, 1999.

[198] C. V. Bennett and B. H. Kolner. "Aberrations in temporal imaging". In: *IEEE Journal of Quantum Electronics* 37.1 (2001), pp. 20–32.

[199] M. Miyagi and S. Nishida. "Pulse spreading in a single-mode optical fiber due to third-order dispersion: effect of optical source bandwidth." In: *Applied optics* 18.13 (1979), pp. 2237–2240.

[200] A. Tikan et al. "Single-shot measurement of phase and amplitude by using a heterodyne time-lens system and ultrafast digital time-holography". In: *Nature Photonics* 2 (2018).

[201] C. V. Bennett. *Ultrafast chirped optical waveform recorder using a time microscope*. 2015.

[202] P. Bowlan et al. "Crossed-beam spectral interferometry: a simple, high-spectral-resolution method for completely characterizing complex ultrashort pulses in real time". In: *Optics Express* 14.24 (2006), p. 11892.

[203] P. Gabolde and R. Trebino. "Single-shot measurement of the full spatio-temporal field of ultrashort pulses with multi-spectral digital holography". In: *Optics Express* 14.23 (2006), p. 11460.

[204] U. Schnars and W. Jüptner. "Direct recording of holograms by a CCD target and numerical reconstruction". In: *Applied Optics* 33.2 (1994), pp. 179–181.

[205] N. June, J. O. Soc, and T. Kreis. "Digital holographic interference-phase measurement using the Fourier-transform method". In: *Journal of the Optical Society of America A* 3.6 (1986).

[206] U. Schnars et al. *Digital holography*. Springer, 2015, pp. 39–68.

[207] D. Gabor. "A New Microscopic Principle". In: *Nature* 161 (1948).

[208] E. N. Leith and J. Upatnieks. "Reconstructed wavefronts and communication theory". In: *JOSA* 52.10 (1962), pp. 1123–1130.

[209] J. W. Goodman and R. W. Lawrence. "Digital image formation from electronically detected holograms". In: *Applied Physics Letters* 11.1967 (1967), pp. 77–79.

[210] M. K. Kim. *Digital Holographic Microscopy*. Springer, 2011, pp. 149–190.

[211] E. Madelung. "Quantum Theory in Hydrodynamical Form". In: *Zeitschrift für Physik* 40.October 1926 (1927), pp. 1–4.

[212] A. Moro and S. Trillo. "Mechanism of wave breaking from a vacuum point in the defocusing nonlinear Schrödinger equation". In: *Physical Review E - Statistical, Nonlinear, and Soft Matter Physics* 89.2 (2014), pp. 1–10.

[213] S. Randoux et al. "Optical Random Riemann Waves in Integrable Turbulence". In: *Physical Review Letters* 118.23 (2017), pp. 2–6.

[214] S. A. Akhmanov, A. P. Sukhorukov, and R. V. Khokhlov. "Self-focusing and self-trapping of intense light beams in a nonlinear medium". In: *Soviet Physics JETP* 23.6 (1966), pp. 1025–1033.

[215] A. V. Gurevich and A. B. Shvartsburg. "Exact solutions of the equations of nonlinear geometric optics". In: *Soviet Physics JETP* 31.6 (1970), pp. 1084–1089.

[216] P. Suret et al. "Rogue waves in integrable turbulence: semi-classical theory and fast measurements". In: *Nonlinear Guided Wave Optics*. 2053-2563. IOP Publishing, 2017, 12-1 to 12-32.

[217] A. Tovbis, S. Venakides, and X. Zhou. "On semiclassical (zero dispersion limit) solution of the focusing nonlinear Schrödinger equation". In: *Communications on Pure and Applied Mathematics* 57 (2004), pp. 877–985.

[218] B. Kibler et al. "The Peregrine soliton in nonlinear fibre optics". In: *Nature Physics* 6.10 (2010), pp. 790–795.

[219] S. Randoux et al. "Nonlinear spectral analysis of Peregrine solitons observed in optics and in hydrodynamic experiments". In: (2018), pp. 1–13.

[220] T. R. Taha and M. Ablowitz. "Analytical and numerical aspects of certain nonlinear evolution equations. II. Numerical, nonlinear Schredinger equation". In: *Journal of Computational Physics* 55.2 (1984), pp. 203–230.

[221] J. Hult. "A Fourth-Order Runge – Kutta in the Interaction Picture Method for Simulating Supercontinuum Generation in Optical Fibers". In: *Journal Of Lightwave Technology* 25.12 (2007), pp. 3770–3775.

[222] A. Tikan et al. "Universality of the Peregrine Soliton in the Focusing Dynamics of the Cubic Nonlinear Schrödinger Equation". In: *Physical Review Letters* 119.3 (2017).

[223] F. Baronio et al. "Solutions of the Vector Nonlinear Schrödinger Equations: Evidence for Deterministic Rogue Waves". In: *Physical Review Letters* 109 (4 2012), p. 044102.

[224] E. P. Gross. "Structure of a quantized vortex in boson systems". In: *Il Nuovo Cimento (1955-1965)* 20.3 (1961), pp. 454–477.

[225] L. P. Pitaevskii. "Vortex lines in an imperfect bose gas". In: *Soviet Physics JETP* 13.2 (1961).

[226] J. A. Fleck, J. R. Morris, and M. D. Feit. "Time-Dependent Propagation of High Energy Laser Beams through the Atmosphere". In: *Applied Physics* 10 (1976), pp. 129–160.

[227] A. Chabchoub et al. "Hydrodynamic supercontinuum". In: *Physical Review Letters* 111.5 (2013), pp. 1–5.

[228] A. Hasegawa. "Generation of a train of soliton pulses by induced modulational instability in optical fibers". In: *Optics letters* 9.7 (1984), pp. 288–290.

[229] P. Colman et al. "Temporal solitons and pulse compression in photonic crystal waveguides". In: *Nature Photonics* 4.December (2010).

[230] M. D. Pelusi, Y. Matsui, and A. Suzuki. "Pedestal Suppression from Compressed Femtosecond Pulses Using a Nonlinear Fiber Loop Mirror". In: *IEEE Journal of Quantum Electronics* 35.6 (1999), pp. 867–874.

[231] B. Barviau, S. Randoux, and P. Suret. "Spectral broadening of a multimode continuous-wave optical field propagating in the normal dispersion regime of a fiber." In: *Optics letters* 31.11 (2006), pp. 1696–1698.

[232] L. Mandel and E. Wolf. *Optical coherence and quantum optics*. Cambridge university press, 1995.

[233] D. Soh et al. "The effect of dispersion on spectral broadening of incoherent continuous-wave light in optical fibers". In: *Optics Express* 18.21 (2010), pp. 22393–22405.

[234] R. H. Stolen. "Nonlinearity in Fiber Transmission". In: *Proceedings of the IEEE* 68.10 (1980), pp. 1232–1236.

[235] G. P. Agrawal. "Effect of intrapulse stimulated Raman scattering on soliton-effect pulse compression in optical fibers". In: *Optics Letters* 15.4 (1990), p. 224.

[236] M. Tsang, D. Psaltis, and F. G. Omenetto. "Reverse propagation of femtosecond pulses in optical fibers." In: *Optics letters* 28.20 (2003), pp. 1873–1875.

[237] C. Barsi, W. Wan, and J. W. Fleischer. "Imaging through nonlinear media using digital holography". In: *Nature Photonics* 3.4 (2009), pp. 211–213.

[238] A. S. Goy and D. Psaltis. "Imaging in focusing Kerr media using digital reverse propagation". In: *Physical Review A* 83.031802 (2011), pp. 1–4.

[239] N. Akhmediev, A. Ankiewicz, and M. Taki. "Waves that appear from nowhere and disappear without a trace". In: *Physics Letters, Section A: General, Atomic and Solid State Physics* 373.6 (2009), pp. 675–678.

[240] N. Akhmediev, J. M. Soto-Crespo, and A. Ankiewicz. "Extreme waves that appear from nowhere: On the nature of rogue waves". In: *Physics Letters, Section A: General, Atomic and Solid State Physics* 373.25 (2009), pp. 2137–2145.

[241] M. Onorato et al. "On the origin of heavy-tail statistics in equations of the Nonlinear Schrödinger type". In: *Physics Letters, Section A: General, Atomic and Solid State Physics* 380.39 (2016), pp. 3173–3177.

[242] A. Chabchoub. "Tracking Breather Dynamics in Irregular Sea State Conditions". In: *Physical Review Letters* 117.14 (2016), pp. 1–6.

[243] J. Satsuma and N. Yajima. "B Initial Value Problems of One-Dimen sional Self-Modul ation of Nonlinear Waves in Dispersive Media". In: *Supplement of the Progress of Theoretical Physics* 55 (1974), pp. 284–306.

[244] J. Yang. *Nonlinear waves in integrable and nonintegrable systems*. Vol. 16. Siam, 2010.

[245] M. J. Ablowitz et al. "Long time dynamics of the modulational instability of deep water waves". In: *Physica D* 152-153 (2001), Physica D.

[246] Y. Kivshar and B. Luther-Davies. "Dark optical solitons: Physics and applications". In: *Physics Report* 298.2-3 (1998), pp. 81–197.

[247] W. J. Tomlinson et al. "Dark optical solitons with finite-width background pulses". In: *Journal of the Optical Society of America B* 6.3 (1989), p. 329.

[248] G. A. El and A. M. Kamchatnov. "Kinetic equation for a dense soliton gas". In: *Physical Review Letters* 95.20 (2005), pp. 1–4.

[249] W. J. Tomlinson, R. H. Stolen, and A. M. Johnson. "Optical wave breaking of pulses in nonlinear optical fibers". In: *Optics Letters* 10.9 (1985), pp. 457–459.

[250] J. E. Rothenberg and D. Grischkowsky. "Observation of the formation of an optical intensity shock and wave breaking in the nonlinear propagation of pulses in optical fibers". In: *Physical Review Letters* 62.5 (1989), pp. 531–534.

[251] D. Anderson, M. Desaix, and M. Lisak. "Wave breaking in nonlinear-optical fibers". In: *Journal of the Optical Society of America B* 9.8 (1992), pp. 1358–1361.

[252] J. A.R. Williams et al. "The generation of quasi-continuous trains of dark soliton-like pulses". In: *Optics Communications* 112.5-6 (1994), pp. 333–338.

[253] T. Marest et al. "Emission of dispersive waves from a train of dark solitons in optical fibers". In: *Optics Letters* 41.11 (2016), pp. 2454–7.

[254] C. Finot, J. Dudley, and G. Millot. "Generation of dark solitons by interaction between similaritons in Raman fiber amplifiers". In: *Optical Fiber Technology* 12.3 (2006), pp. 217–226.

[255] M. R. Andrews et al. "Observation of interference between two bose condensates". In: *Science* 275.5300 (1997), pp. 637–641.